Spin Relaxation and Coherence in Molecular Nanomagnets and Molecular Spin Qubits

Tesis Doctoral (Octubre 2019)

VNIVERSITAT DE VALÈNCIA

Instituto de Ciencia Molecular (ICMol)

Universitat de València

Luis Escalera Moreno

Programa de Doctorado en Nanociencia y Nanotecnología

Dirigida por:

Prof. Eugenio Coronado Miralles

Dr. Alejandro Gaita Ariño

D. **EUGENIO CORONADO MIRALLES**, Profesor Catedrático del Departamento de Química Inorgánica de la Universitat de València y D. **ALEJANDRO GAITA ARIÑO**, doctor por la Universitat de València.

CERTIFICAN: Que la presente memoria, titulada: "**Spin Relaxation and Coherence in Molecular Nanomagnets and Molecular Spin Qubits**", corresponde a la Tesis Doctoral de **LUIS ESCALERA MORENO** y ha sido desarrollada bajo su dirección en el Instituto de Ciencia Molecular, autorizando mediante este escrito la presentación de la misma para optar al grado de Doctor.

En Paterna, a 15 de octubre de 2019.

Prof. Eugenio Coronado Miralles Dr. Alejandro Gaita Ariño

Luis Escalera Moreno

The more I learn, the more I realize how much I don't know.

Apocryphal

Als meus pares

Al meus iaios

Agradecimientos

Después de varios años y de tantas vivencias en un mismo lugar de trabajo, es inevitable el surgimiento de amistades y relaciones personales con la gente que rodea a uno mismo. Personas que afortunadamente, al margen de los duros momentos, han sabido poner un toque de esperanza y ánimo al arduo camino que conlleva la realización de una tesis doctoral, y a las que por tanto merece la pena agradecer su positiva actitud con algunas palabras.

En primer lugar, se me viene a la cabeza el inicio de mi andadura por el ICMol. Debo agradecer al profesor Antonio Marquina, de la Facultad de Matemáticas de la UV, por confiar y creer en mí, quien me recomendó y se puso en contacto con Eugenio Coronado. A Eugenio agradecerle que me hiciera un hueco en su grupo de investigación desde el primer día cuando me entrevisté con él, con el fin de darme una oportunidad de demostrar mi valía. También agradecerle su actuación como guía durante todo este tiempo aconsejando las formas más oportunas de darle la mayor visibilidad a mi trabajo, sea haciendo todo lo posible por publicar en revistas de considerable impacto o proponiéndome como ponente en charlas tanto contribuidas como invitadas.

Fue ese primer día cuando Eugenio me presentó a quienes en adelante serían mis compañeros de trabajo, y debo confesar que no pude tener mayor suerte de haber llegado a este gran equipo. A Álex Gaita agradecerle ser un supervisor cercano y muy amable, gran persona, entusiasta y siempre dispuesto a escuchar y ayudar en todo. Tampoco olvidar su preocupación constante durante mi recuperación tras la lesión de menisco y nuestra estancia en Basilea. A Salva Cardona agradecerle su ayuda durante mis primeros días para situarme en el grupo, tanto echándome una mano con trámites como prestándome material para leer y estudiar. Y, por supuesto, cómo olvidar aquellos días de congreso callejeando por Santiago de Compostela con él y su pareja Pilar. A Modesto agradecerle ser una persona cercana a la que poder siempre consultar abiertamente cuestiones y problemas en relación a mis investigaciones. Agradecerle también el haberme brindado la oportunidad de asistir como oyente a sus clases de Química de Coordinación, donde disfruté y aprendí a partes iguales. Y no podría olvidarme de José Jaime Baldoví, con quien he labrado una gran amistad que espero perdure durante mucho tiempo y en la que, además de nuestro gusto por la ciencia, compartimos otros intereses como la historia y la

cultura. Agradecerle también haberme hecho partícipe de sus ideas sobre nanoimanes moleculares, las cuales posteriormente permitieron expandir mi tesis más allá del horizonte previsto, dándole así mayor cuerpo y alcance. Que casualmente los dos seamos de la misma localidad -Játiva- algo tenía que significar.

Otra etapa que recuerdo con cariño es la que comprendió mi paso por la zona de los químico-físicos en el ICMol durante la realización de mi máster en química teórica. Allí tuve la ocasión de conocer más gente que también me han hecho crecer como persona y científico. A Pepe Sánchez debo agradecerle su bondad y amabilidad a la hora de recibirme y asesorarme en su máster, así como su preocupación tras mi operación de menisco. También reconocerle como excelente y competente gestor en la administración de dicho máster en Valencia. A Dani Roca agradecerle su cercanía y profesionalidad de quien ciertamente pude aprender bastante sobre cálculos de primeros principios durante mis inicios. A Enrique Ortí y Rosendo Pou, grandes profesores y mejores personas, agradecerles su interés, disposición y estima hacia mí. Manifestar también mi alegría por el reencuentro con Juan Aragó tras varios años desde cuando Rosendo nos presentó en mi primer año de universidad, con quien he establecido una magnífica colaboración que estoy seguro será ciertamente fructífera. Agradecer también a Jesús Cerdà por su simpatía y su desinteresada disposición a echar siempre un cable donde y cuando haga falta. De esta etapa, no me perdonaría olvidarme de otra gran persona a la que tuve la suerte de conocer, Nico Suaud. Quiero agradecerle su amistad, así como el haber cuidado tan bien de mí durante mi estancia en su laboratorio de Toulouse, donde aprendí mucho con él y tuve también la oportunidad de conocer de su mano a excelentes profesores como Nathalie Guihéry y Jean Paul Malrieu. Es un gusto para mí trabajar en equipo con él en forma de colaboración y verle cada vez que nos visita en Valencia.

Naturalmente, también quiero mencionar especialmente a aquellas personas que componen mi entorno de trabajo más cercano. A Helena Prima, Lorena, Silvia, Ziqi, Aman y, aunque sea en la distancia, pero no por ello menos importante, Joana, gracias por vuestra amistad e incondicional apoyo. Confío en que sigamos saliendo de vez en cuando junto con Álex, Salva y José a comer y cenar para desconectar un poco del trabajo, que también está bien y merece la pena.

Igualmente, quisiera también recordar tanto a compañeros de la UIMM y del ICMol como a otros científicos de otros grupos, a quienes admiro y ha sido un placer conocer, y con quienes es un gusto conversar por todo lo que he aprendido y puedo seguir aprendiendo de ellos. Gracias a Gonzalo, Carlos Martí, Guille, Efrén, Yan, Alicia, Mónica, Helena Pinilla, Miguel, Alejandra, Boris Tsukerblat, Hans Güdel, Fernando Luis, Steve Hill,… También mencionar a los profesores de la facultad de física de la UV Eugenio Roldán, Antonio Pich y Armando Pérez, quienes me acogieron de muy buen gusto como oyente en sus clases y se interesaron por mis investigaciones. Por supuesto, tampoco olvidarme de mis compañeros doctorandos con quienes he compartido tantos buenos momentos durante este periodo: Samuel, Marc, Garín, Ramón, Miguel, Verónica, Eugenia, Safaa,… También mencionar y agradecer a todas las personas encargadas de mantener el buen funcionamiento y gestión de nuestro grupo y del instituto, de quienes siempre he recibido un trato amable, profesional y competente: Paco, Manuel, Estela, Ruth, Fina, Mayte,…

Por último, también mencionar a mis padres Luis y Elena a quienes debo agradecer todo por haberme dado todo cuanto he necesitado, por su apoyo, por creer en mí, y estar siempre ahí incondicionalmente. Y dedicar esta tesis doctoral a mi abuelo materno Antonio, por convertirme en la persona que soy gracias a él, a quien admiré y sigo admirando, de quien nunca me olvido y del que siento sus fuerzas allá donde esté. Sé que habría sido un orgullo para ti haber asistido al acto de defensa de mi tesis doctoral. Gracias por todo y por siempre.

"…it seems that the laws of physics present no barrier to reducing the size of computers until bits are the size of atoms, and quantum behaviour holds dominant sway."

R. P. Feynman (1985)

Table of Contents

Abstract

One of the most promising building-blocks for storage and processing of information are the so-called molecular nanomagnets and molecular spin qubits. These zero-dimensional molecular systems exhibit interesting magnetic phenomena, where information is encoded in their spin energy levels. Because of the practical inability to fully isolate a quantum-mechanical system, uncontrolled interactions with the surrounding environment can damage the information either stored or under processing in these systems. Thus, in order to build molecular nanomagnets and spin qubits able to satisfy even the most demanding challenges either current or future, one first needs to develop a rational framework to know how to design a given system as decoupled from the detrimental effects of its environment as possible.

In this dissertation, we conduct a theoretical exploration of some of the most important mechanisms that contribute to spin relaxation, i.e., the collapse of the information stored and processed in the above-mentioned systems. We aim to develop first-principles and efficient methodologies devoted first to quantify the damage of these mechanisms, and then to provide synthetic rules to re-design and improve a given system at the lab stage. We will apply and test our novel methods to a representative set of the most interesting and promising molecular nanomagnets and spin qubits. For the purpose of facilitating a systematic use of these methods to any interested researcher, we also develop and provide a computational framework that incorporates the theoretical models herein developed.

List of Publications

2015

J. J. Baldoví, S. Cardona-Serra, J. M. Clemente-Juan, L. Escalera-Moreno, A. Gaita-Ariño, G. Mínguez Espallargas, Quantum Error Correction with magnetic molecules, *EPL*, 2015, **110**(3), 33001. (Chapter 7)

2016

S. Cardona-Serra, L. Escalera-Moreno, J. J. Baldoví, A. Gaita-Ariño, J. M. Clemente-Juan, E. Coronado, SIMPRE1.2: Considering the hyperfine and quadrupolar couplings and the nuclear spin bath decoherence, *J. Comput. Chem.*, 2016, **37**(13), 1238. (Chapter 3)

A. Gaita-Ariño, H. Prima-García, S. Cardona-Serra, L. Escalera-Moreno, L. E. Rosaleny, J. J. Baldoví, Coherence and organisation in lanthanoid complexes: from single ion magnets to spin qubits, *Inorg. Chem. Front.*, 2016, **3**, 568.

2017

L. Escalera-Moreno, N. Suaud, A. Gaita-Ariño, E. Coronado, Determining Key Local Vibrations in the Relaxation of Molecular Spin Qubits and Single-Molecule Magnets, *J. Phys. Chem. Lett.*, 2017, **8**(7), 1695. (Chapter 4)

2018

L. Escalera-Moreno, J. J. Baldoví, A. Gaita-Ariño, E. Coronado, Spin states, vibrations and spin relaxation in molecular nanomagnets and spin qubits: a critical perspective, *Chem. Sci.*, 2018, **9**, 3265. (Chapter 4)

L. E. Rosaleny, S. Cardona-Serra, L. Escalera-Moreno, J. J. Baldoví, V. Gołębiewska, K. Wlazło, P. Casino, H. Prima-Garcia, A. Gaita-Ariño, E. Coronado, Peptides as Versatile Platforms for Quantum Computing, *J. Phys. Chem. Lett.*, 2018, **9**(16), 4522.

2019

L. Escalera-Moreno, J. J. Baldoví, A. Gaita-Ariño, E. Coronado, Exploring the high-temperature frontier in molecular nanomagnets: from lanthanides to actinides, *Inorg. Chem.*, 2019, **58(18)**, 11883 (Forum Article). (Chapter 4)

L. Escalera-Moreno, A. Gaita-Ariño, E. Coronado, Decoherence from dipolar interspin interactions in molecular spin qubits, *Phys. Rev. B.*, 2019, **100**, 064405. (Chapter 5)

L. Escalera-Moreno, J. J. Baldoví, Unveiling the effect of magnetic noise in the coherence of single-molecule quantum processors, *Front. Chem.*, 2019, **7**, 662. (Chapter 5)

In preparation or under peer-review

L. Escalera-Moreno, J. J. Baldoví, A. Gaita-Ariño, E. Coronado, SIMPRE 2.0. In preparation. (Chapter 3)

L. Escalera-Moreno, M. Amoza, A. Gaita-Ariño, E. Ruiz, E. Coronado, VOPc, $[VO(dmit)_2]^{2-}$, $[V(dmit)_3]^{2-}$. In preparation. (Chapter 4)

L. Escalera-Moreno, Jose J. Baldoví, A. Gaita-Ariño, E. Coronado, Design of high-temperature f-block molecular nanomagnets through the control of vibration-induced spin relaxation. Under peer-review in *Chem. Sci.* (Chapter 4)

L. Escalera-Moreno, P. Fernández-Acebal, H. Prima-García, A. Gaita-Ariño, E. Coronado, Coherence and Rabi Oscillations in GdW_{30}. In preparation. (Chapter 5)

L. Escalera-Moreno, A. Gaita-Ariño, E. Coronado, Atomic Clock Transitions in HoW_{10}. In preparation. (Chapter 6)

J. López-Cabrelles, L. Escalera-Moreno, H. Prima-García, G. Mínguez Espallargas, A. Gaita-Ariño, E. Coronado, Quantum coherence in a MOF with up to 9 potentially distinguishable qubits. Submitted to *Dalton Trans.*

Block 0.

Introduction

1

Motivation

1.1 Unsolved Problems

There is no doubt that nowadays we all live immersed in the so-called information age. Every day, big data archives flow all around the world at a speed which would have been unconceivable just a few decades ago. Together with the need of storing and carrying larger amounts of information, there also exists an increasing interest to achieve a larger computational power able to satisfy even the most demanding challenges of current interest for society and industry. Among these challenges, one can find for example the simulation of new materials both for technological gadgets and for space aircrafts, or the *in-silico* test of new drugs that help to control and cure the diseases that affect human beings. These needs are pushing and will keep doing it until they are all covered.

The rise in the computing capacity of standard computers over the last few decades has been possible as technology has been able to fabricate smaller transistors to fit a larger number of them in a processing chip. To get some idea, every two years the number of transistors in a microprocessor is approximately multiplied by two. This is what is known as Moore's law, named after the co-founder of Intel Gordon Moore, who established this empirical observation in 1965. Nonetheless, it is clear that this relentless miniaturization of transistors will end up by reaching the nanoscale, where classical physics is not valid anymore and the laws of quantum physics enter at play instead.

Inside this context, it is worth wondering whether the properties of quantum systems could be harnessed to build a quantum processor and process information. Indeed, this idea was already proposed first by P. Benioff in 1980

and then by R. P. Feynman in the first conference of Physics of Computation at the Massachusetts Institute of Technology in 1981.[1,2] These proposals would have remained just an anecdote were it not for the fact that, in 1994, P. Shor devised the first quantum algorithm able to conduct prime factorization of large integer numbers in polynomial time,[3,4] which outperforms the exponential time taken in classical computers. This fact represented the proof-of-concept of the enormous advantages that a quantum computer could bring respect to classical computing, and since then it has drawn the attention of an increasing number of researchers all around the world interested in contributing to the development of quantum computing.

The next natural step is to ask which kind of hardware should be employed either to store information in it or to implement a given quantum algorithm. While at present certain physical systems can be identified as prime candidates, it is equally essential to pursue this goal on a broad basis of competing approaches by allowing hybridization and cross fertilization between different fields (e.g., quantum optics, atomic physics, as well as solid state physics). Some of the most commonly studied hardware proposals are those based on: cold ion traps,[5–11] nuclear magnetic resonance,[12–21] cavity quantum electrodynamics,[22–30] linear optics,[31] quantum dots,[32–39] phosphorus-donors in silicon,[40–45] Josephson junctions,[46–54] endohedral fullerenes,[55–59] and nitrogen-vacancy centers.[60–69] In addition, the emerging research field of nanoscience and nanotechnology is also providing alternative approximations. The building-blocks for quantum hardware would be the so-called molecular nanomagnets,[70–79] and molecular spin qubits,[80–89] which will be subject of study in this dissertation.[90–94] The former could be used as classical memories for information storage, and the latter constitutes the most elementary unit for quantum processing.

Although there exists a plethora of promising candidates for hardware, the goal of building multi-purpose quantum computers able to efficiently solve intractable problems on classical computers seems to be nowadays out of reach. Before achieving this goal, several challenges both fundamental and technological should first be overcome, being decoherence and scalability two of the most representative. The fact of being quite hard to decouple a given quantum-mechanical system from its environment is related with the former, namely, uncontrolled interactions with the aforementioned system will damage -in a certain timescale- the information encoded in the form of qubits. These are

the most basic pieces of any quantum processor, and will be introduced in chapter 2. On the other hand, the execution of algorithms able to perform tasks of increasing complexity will require the interplay of a larger number of qubits while keeping quantum information unaltered. This is what scalability refers to. There do already exist several small-scale prototypes working with a few qubits,[4,18,95,96] which are proving that quantum computing is becoming a reality. Nonetheless, only the attainment of a quantum processor able to deal with large enough numbers of qubits will make quantum computing a tool worth paying attention when it comes to solve problems of interest for society and industry.

1.2 Goals

One of the current key goals is to unveil the role of the different decoherence mechanisms acting on molecular spin qubits, in order to establish general and rational synthetic rules at the lab stage that allow reaching long enough phase memory times. This characteristic time determines the timescale for quantum information survival, and will be introduced in chapter 2. To reach this goal, the theoretical approximation is proving to be an indispensable tool on how to gain increasing insight. Thus, one of the main goals of this dissertation will be to develop an *ab initio* framework devoted to provide first a quantitative estimate of the impact of the most important decoherence mechanisms on the phase memory time; and then a guide of chemical modifications in the geometrical structure of a given molecular spin qubit to increase its phase memory time. All in all, the key goal consists in unveiling the explicit structure-property relation in molecular spin qubits, where the property is the phase memory time, in order to elaborate a general recipe for building a molecular spin qubit with the desired phase memory time.

An important class of magnetic systems that will be subject of study in this dissertation are single-ion molecular nanomagnets based on lanthanides and uranium. The target relaxation mechanism to focus on in these systems will be the one derived from the spin-vibration coupling, which contributes to destroy information saved in the form of bit at high enough working temperatures. Motivated by the fact that state-of-the-art theoretical methods are still too computationally demanding, the second main goal will be to develop a first-principles inexpensive methodology that allows a generalized and efficient evaluation of spin-vibration coupling in single-ion molecular nanomagnets

based on lanthanides and uranium. This methodology should also be able to provide insight on how the structure of a given molecular nanomagnet has to be chemically modified to improve the magnet performance.

To ensure a systematic and practical application of the methods herein developed, the third main goal will be to build a computational framework in the form of a software package where all these methods will be implemented. This code will be used in a representative set of potential molecular spin qubits and molecular nanomagnets.

1.3 Organization of the Thesis

This dissertation is broken down into three main blocks as follows.

The first block "Computational Development" is aimed at describing the computational framework in the form of a practical and useful software that can be provided to any interested researcher. All the models presented in the second block are updates that have been implemented on the original code SIMPRE developed prior to this dissertation. The first updated version of this code that was developed and published within the present work is SIMPRE1.2, and is presented in chapter 3. Besides, in this chapter we will also introduce the newest version SIMPRE2.0.

The second block "Theoretical Development and Applications" is focused on presenting the theoretical models developed herein and which are devoted to unveil the impact of some of the most important spin relaxation mechanisms acting on molecular spin qubits and molecular nanomagnets, namely, "Spin-vibration Coupling" in Chapter 4 and "Magnetic Noise" in Chapter 5. These models will be applied to several potential molecular spin qubits and molecular nanomagnets of current interest in order to extract a list of chemical modifications on the molecular structures that could help to improve the performance of these systems.

In the third and last block "Current Challenges", some open problems and current challenges of wide interest in the field of molecular spin qubits are presented and discussed. In chapter 6 "Atomic Clock Transitions in HoW_{10}" we propose a novel approach based on the introduction of transition probabilities to reproduce the magnetic field dependence of the phase memory time of a

molecular spin qubit exhibiting a particularly interesting phenomenon, namely, atomic clock transitions. In chapter 7 “Quantum Error Correction” we will study Tb^{3+}-based polynuclear magnetic molecules whose energy scheme allows defining up to nine qubits. Then, we will discuss on the possibility of implementing in it some algorithms such as the Shor’s three- and nine-qubit quantum error correction codes.

2

Molecular Nanomagnetism and Electron Paramagnetic Resonance

2.1 Molecular Nanomagnets and Molecular Spin Qubits

The aim of this section is to introduce the physical systems that will be subject of study in the next chapters, namely, molecular nanomagnets and molecular spin qubits. For that, we will firstly review the main advantages of quantum computation schemes in order to motivate the applicability of these systems in quantum information processing.

Classical vs quantum computing

Nowadays, we all are used to employ computers in our daily life, which exploit classical electronics to store and compute information under the rules of the so-called Boolean logics. Particularly, in 1937 Alan Turing established the basics of classical computing by introducing the concept of universal computer, also known as Turing machine.[97] Ten years later, scientists from the University of Pennsylvania built the first electronic computer, ENIAC, able to perform arithmetic operations with numbers of up to ten digits.[98] As technology is improved, it is possible to increase the performance of classical computers, which relies in our ability of further miniaturizing the transistors of processing chips by exploiting advances in nanotechnology. If this miniaturization keeps going on, these electronic components will unavoidably reach the atomic scale as predicted by the abovementioned Moore's law. Thus, data processing is destined to eventually meet quantum physics towards a common discipline in

which information would be stored in components of quantum nature and processed under the laws of quantum physics.[99]

The proposal raised by Feynman in 1981 was that of building a universal quantum simulator in order to study and understand complex quantum systems that are intractable by classical computers.[100,101] A quantum simulator is a quantum system with a well-understood and fully controllable dynamics that can be unequivocally mapped onto the one of a target system.[102–106] Thus, there is no need to solve the complex dynamics of the target system anymore, since it can be simulated with a much simpler system.

"Trying to find a computer simulation of physics seems to me to be an excellent program to follow out…the real use of it would be with quantum mechanics…nature isn't classical…and if you want to make a simulation of nature, you'd better make it quantum mechanical, and by golly it's a wonderful problem, because it doesn't look so easy." R. P. Feynman (1981)

Quantum simulation represents one of the most powerful uses of quantum computing and one of the biggest advantages over classical computers.[107–110] Functional quantum simulators would allow the development of new materials, a deeper understanding of high-temperature superconductivity, or a fine description of chemical compounds and chemical reactions.[111–114] For example, to simulate the dynamics of n independent spin-1/2 systems in a classical computer, one would need to store and manipulate a vector of 2^n components, something impractical as soon as $n > 20$. Instead, a quantum simulator would require a vector of only n components to define the system state. Importantly, this proves the significant increase in computational efficiency, since the exponential scaling of the problem to solve is replaced by a linear scaling.

Exploiting the properties of quantum world can provide advantages not found in classical computers that are harnessed even by nature, such as the use of quantum-based avian compasses by migratory birds.[115] This quantum potential is also extended to information processing. As mentioned above, P. Shor devised a quantum algorithm able to perform prime factorization of integer numbers in polynomial time, which contrasts with the exponential time taken by classical computers. Interestingly, the success of some encryption methods

in providing privacy for online operations, such as RSA protocols, relies on the inability of factorizing large integer numbers within a reasonable time by classical computers. However, even a moderately-sized quantum computer would be able to perform these factorizations and thus break the cryptographic systems that have resisted attacks even from the most powerful classical computers.

Fortunately, the quantum principles exploited to achieve an unprecedented computational power also provide new methods to protect information transmission, namely, quantum cryptography. This discipline was originally introduced by S. Wiesner,[116] and subsequently developed by C. Bennett and G. Brassard.[117–120] The key to this novel approach relies on the uncertainty principle which would make information eavesdropping be impossible without a high chance of irreversibly disturbing the sent message. Nowadays, there already exist implementations of quantum cryptography in the form of quantum key distribution marketed by companies such as MagiQ and id Quantique. Previously, large-scale experiments proved reliable key distribution across a distance of up to several tens of kilometers and under diverse atmospheric conditions.[121–123] Eventually, quantum cryptography could replace current cyphering protocols, although recent simulations suggest that RSA protocols could resist attacks even from highly scalable quantum computers.[124]

Another important problem whose efficient implementation is due to quantum principles is that of searching for a specific entry in a disordered database. Indeed, in 1996 L. Grover devised a quantum algorithm able to accomplish this task much faster than any classical computer could do.[125,126] Particularly, if the database contains n entries, the average number of algorithmic operations to perform before succeeding scales with $\sqrt{n}$ instead of n as found in classical algorithms. Grover's algorithm works by creating a superposition of all entries where each on them has the same probability of appearing after performing a projective measurement. Then, the probability of a successful measurement is increased by submitting this superposition to a series of quantum operations devoted to find the target entry from an input feature. Successful implementations of this algorithm were already achieved on nuclear magnetic resonance setups and, more recently, in single magnetic molecules.[15,127]

Quantum computers

Quantum computing is intended to perform well-defined tasks by storing and manipulating information in the form of a determined number of minimal quantum registers known as qubits. A well-defined task requires (i) to know what input we need, (ii) to define what output we want to get, (iii) to be successfully finished within a finite time. During this process, the input qubits are properly manipulated through a sequence of steps known as logical gates to obtain an output. Qubits are the quantum version of bits, the building blocks of classical computers. A bit, or binary digit, is a system with two well-characterized states denoted as 0 and 1, and is the minimum amount of information to deal with. There exist several options of implementing a bit by means of diverse magnitudes such as charges, voltages, or electric currents. In this last case, the state 0 could be assigned to a flowing current below a given threshold, while the state 1 would require a current above the threshold.

The key to a bit is that its value is necessarily either 0 or 1 without any further possibility. Instead, a qubit exploits quantum superposition to produce a general state whose value, the minimum amount of information in a quantum computer, is simultaneously 0 and 1. Of course, any projective measurement on the qubit must be avoided as long as one needs to keep the superposition. This general state is written in the form of a ket $|\Psi\rangle$ as a linear combination of the orthonormal elements $|0\rangle$ and $|1\rangle$, i.e., $\langle i|j\rangle = \delta_{ij}$ where δ_{ij} is the Kronecker's delta:

$$|\Psi\rangle = \alpha|0\rangle + \beta|1\rangle \qquad \textbf{Eq. 1}$$

In **Eq. 1**, α and β can be any combination of complex numbers such that $|\alpha|^2 + |\beta|^2 = 1$. A quantum computer is a device that exploits quantum superposition to process information with a much more efficient time scaling compared to classical computers. For instance, an exponential scaling can be turned into a polynomial scaling as mentioned above. This has a decisive impact on the execution time and memory requirement: a quantum technology computer will be able to perform tasks utterly intractable on any conceivable

non-quantum hardware. Indeed, classical computers use a series of bits to constitute a memory register where information is stored. While a classical register of *n* bits represents *n* values as a unique assignment of each bit to 0 or 1, a quantum register with *n* qubits can represent up to the whole set of 2^n values if each qubit is found in state superposition. Thus, the computation is simultaneously performed on all possible combinations of values $(\nu_1,\ldots\nu_n)$ with ν_i = 0, 1, while a classical computer would only be able to deal with one combination at a given time.

A simple illustration of quantum operations on qubits is provided by the CNOT logical gate, which will be presented in chapter 7. This gate flips the value of the target qubit whenever the value of the control qubit is 1, and does not produce any effect on the target qubit whenever the control value is 0. Let us consider that the control qubit is in state superposition $|\Psi_c\rangle = \alpha|0\rangle + \beta|1\rangle$, and the target qubit is $|\Psi_t\rangle = |0\rangle$. The joint state is written as $|\Psi_c\rangle \otimes |\Psi_t\rangle = (\alpha|0\rangle + \beta|1\rangle) \otimes |0\rangle = \alpha|00\rangle + \beta|10\rangle$, where the first position in the ket stands for the control value and the second position represents the target value. Since $|\Psi_c\rangle$ contains both $|0\rangle$ and $|1\rangle$, which is the result of applying a CNOT gate on $|\Psi_t\rangle = |0\rangle$? Is it $|\Psi_t\rangle = |0\rangle \rightarrow |0\rangle$? Is it $|\Psi_t\rangle = |0\rangle \rightarrow |1\rangle$? The right answer is neither of them but both results at once: $|\Psi_c\rangle \otimes |\Psi_t\rangle \rightarrow |\Psi\rangle = \alpha|00\rangle + \beta|11\rangle$. Indeed, whenever the control value is 0, the target value will remain unaltered with its original value 0. On the contrary, if the control value is 1, the target value will turn into 1. Hence, $|\Psi\rangle$ is an entangled state since a measurement to know the control value will unavoidably determine the target value. For instance, if the former is found to be 0, the latter must be necessarily 0 since its original value was 0. In other words, an entangled state cannot be written as a product of two factors where each one depends only on a single qubit.

Qubit states are physically defined in the form of discrete configurations found in quantum-mechanical systems such as the ones mentioned in chapter 1. For instance, one qubit can be embodied in the superposition of two non-degenerate energy levels labeled as $|0\rangle$ and $|1\rangle$. In the general case of implementing *n* qubits one would require 2^n levels, which are now labeled as $|x_1 \ldots x_n\rangle$ with $x_j \in \{0,1\}$. This set of levels constitutes the so-called computational space in which the algorithm will be conducted by driving a series of allowed

and addressable transitions between these levels. Importantly, the computational space must fulfil some important requirements to avoid a bad implementation of the *n* qubits. On one hand, this space must be well-isolated so that other energy levels cannot interfere while performing the computation. On the other hand, any transition must be distinguishable from the rest in order not to drive more than one at once.

Scalability and decoherence

In the pursuit of building a general-purpose quantum computer, it will be useful to follow a guide of minimum requirements for any physical implementation, since nowadays only small prototypes working with a limited number of qubits are available.[4,18,95,96] These requirements were established in 2000 by D. DiVincenzo and read as follows:[128]

1. A scalable physical system that allows controlling an increasing number of well-characterized qubits as needed.
2. The ability to reliably initialize each qubit to a known state.
3. Decoherence times longer than the logical gate running times.
4. A universal set of logical gates.
5. The capability to read the result of any given computation by performing projective measurements of the qubit states onto the basis set $\{|0\rangle,|1\rangle\}$.

Basically, a quantum computation initializes the qubits, manipulates them in a coherent evolution, i.e. by preserving quantum superpositions, and reads out the final result. Each given algorithm is composed of a sequence of logical gates that ends in a finite time. In principle, since there is an infinite number of algorithms one would also require an infinite set of gates to cover the realization of all possible computational tasks. Fortunately, it can be proven that every logical gate can be reproduced with an arbitrary precision by a finite set of gates known as universal set of logical gates. There exist several universal sets and they will be introduced in chapter 7.

Building a general-purpose quantum computer with a high enough number of qubits requires overcoming important challenges such as scalability and

quantum decoherence. As far as the former is concerned, a quantum computer is intended to efficiently solve intractable problems in classical computers, such as prime factorization of large integer numbers or simulation and modelling of complex physical systems. As mentioned, a potential quantum computer should coherently deal with a large enough number of qubits to conduct non-trivial quantum algorithms of wide interest. Moreover, interfaces with direct relevance for quantum communication will need to be developed for connecting quantum computers in secure networks to allow task parallelization. At this point, we recall the quantum cryptography protocols introduced above.

A moderate goal to achieve in the middle term would be to develop specific-purpose quantum processors with a few tens of qubits to demonstrate the experimental feasibility of implementing quantum algorithms and simulation, with emphasis on potential scalability. In particular, the so-called NISQ (Noisy Intermediate-Scale Quantum) technology is proving that this goal could become a reality.[129] Depending on the sophistication in the experimental implementation and on how restrictive the required conditions are, it often happens that certain qubits of a given physical nature may be more appropriate than others to conduct a specific task. Thus, it is likely that there will not be a single winner in this race, i.e., different quantum technologies where qubits of different nature interact with each other could be complementary. Of course, this fact should eventually lead to a rather highly-interdisciplinary research with a well-coordinated effort.

Hence, an extra requirement should be added to the Di Vincenzo's list, namely, when dealing with mixed setups, qubits coming from different architectures -also known as stationary qubits- will need to be efficiently interconverted. In other words, the information carried by a qubit in a given architecture should be faithfully transmitted into another qubit of different nature. In this sense, the so-called flying qubits would be responsible for carrying the relevant information between stationary qubits in different architectures.[130] For instance, one could foresee that, while quantum operations take place in a given part of the device, a qubit could be coherently transferred to a magnetic molecule in the form of a photon for a storage time. Then, the molecule could be subjected to a quantum error correction protocol and, finally, the protected qubit would be coherently transferred back again to a photon to be re-introduced in the quantum algorithm under execution.

Concerning decoherence, quantum-mechanical systems are not closed but they are coupled and irreversibly interact with their environment. Indeed, all environmental degrees of freedom not included in the model Hamiltonian are not under any active control and hence will act as a noise that results in the destruction of quantum superpositions. This process is known as quantum decoherence and is one of the main roadblocks to overcome before successfully implementing any computational process.[131–133] In most of cases, it is not possible a total suppression of decoherence and current efforts are intended to find optimal physical systems in which this detrimental effect is minimum.

As mentioned, quantum information is encoded in the form superpositions. Thus, quantum coherence is the ability to keep these superpositions intact, while decoherence would be the process whereby uncontrolled environmental interactions destroy them in a given timescale known as decoherence time. This process prevents the quantum system from evolving according to the model Hamiltonian. In other words, the evolution of the quantum algorithm will be different as expected from the logical gate sequence. Any attempt at manipulating qubits leads to what some scientists refer to as the yin-yang of quantum computing: on one hand, qubits must weakly interact with their environment in order to avoid decoherence. On the other hand, they must also strongly interact both with each other to conduct logical gates and with the controlled external stimuli that is applied to manipulate them and run the given algorithm.[134] As it can be seen, quantum computing can become pretty much elusive because of the difficulty of simultaneously controlling certain degrees of freedom while preventing environmentally-induced decoherence. The experimental challenge is to find physical systems with the required nonlinear interactions for computation and simultaneously easily accessible from outside without a rapid loss of quantum coherence.[135]

In principle, as far as we are unable to control and suppress decoherence, large-scale quantum computing could remain as a distant dream. Nonetheless, by developing clever schemes scientists are also finding ways not to necessarily fight decoherence but just to reverse and fix its detrimental effects. Some of these methods are collectively known as quantum error correction and will be introduced in chapter 7. These error correction schemes are based on entangling the qubit containing the relevant information with a set of ancillary qubits. Then, after sending all of them through a noisy channel, any error produced on the logical qubit will be accordingly corrected to restore its original state.

Molecular spin qubits

The physical systems we will focus on in the next chapters are magnetic molecules -which means presence of unpaired electrons- where a single metal ion is coordinated by a set of ligands. In these systems, qubits are encoded in the spin energy levels, which can be among the several $2S+1$ projections of the ground electron spin quantum number S. These are the so-called molecular spin qubits mentioned in chapter 1. The most simple situation is the one of a ground spin doublet $S = 1/2$ under a static magnetic field, where the $|0\rangle$ and $|1\rangle$ states of the single qubit are defined as the non-degenerate $m_s = \pm 1/2$ components. In case of Ln^{3+} ions where the spin-orbit coupling is larger than the ligand field effect, S must be replaced by the quantum number J, which also incorporates the quantum number L of the orbital angular momentum. The possible values of J are $|L+S|,\ldots,|L-S|$, and the ground value is determined by the Hund rule: $J = |L-S|$ if the 4f-shell is less than half-filled, $J = |L-S|$ whenever this shell is more than half-filled, and $J = S$ for half-filled 4f-shells, such as in Gd^{3+} and Eu^{2+}. If the nucleus of the metal ion is magnetic with a ground spin quantum number I and is coupled to the electron spin via hyperfine coupling, the $2I+1$ projections will produce $(2J+1)(2I+1)$ electronuclear spin states. Hence, nuclear spins can also be employed to define qubits. The standard experimental technique employed to drive these magnetic systems across their spin levels and thus perform quantum algorithms will be described in section 2.2.

Within solid-state spin systems, the molecular strategy presents one interesting advantage, namely, the power of chemical design to conduct fine-tune synthesis *à la carte* of molecules with the desired properties. This can be initially accomplished by varying key parameters as a result of an appropriate design.[136] Indeed, this approach often allows gradually changing one of these parameters inside a series of molecules. Thus, one can systematically study the effect of this given property on a target property with the aim of understanding how to produce optimal systems through a rational design. Equally important, another important possibility is the use of polynuclear magnetic molecules, i.e. with several metal ions, for implementing two- or three-qubit logical gates. In this case, one needs to achieve magnetically distinguishable metal centers so that they can be selectively addressed. This in turn means different coordination environments, which can be obtained through a careful ligand design.[81,137] For

these particular purposes, the field of molecular magnetism has produced a vast set of tools to design and study magnetic molecules over the last few decades. Experimental working conditions can also be tuned to produce optimal results on a given molecule, such as a large number of long-lived Rabi oscillations (see section 2.2).[138]

The nature of decoherence mechanisms depends on the physical candidate for quantum hardware. Particularly, three main mechanisms can be found in the case of molecular spin qubits.[139] As depicted in **Fig. 1**, these are: (i) coupling with vibration bath, (ii) coupling with surrounding magnetic nuclei (nuclear spin bath), (iii) coupling between different magnetic molecules containing qubits (electron spin bath).

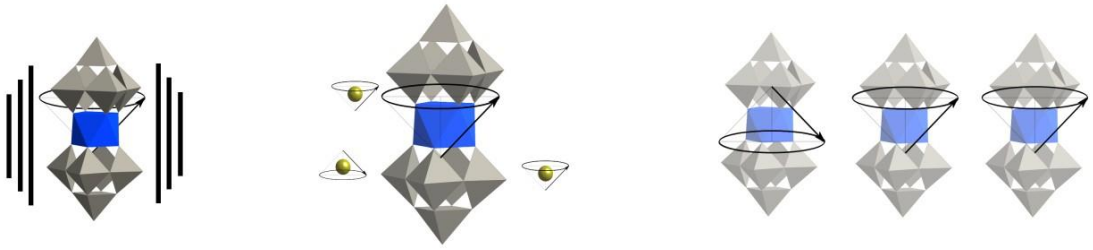

Fig. 1 Main decoherence mechanisms in molecular spin qubits represented as an arrow in a selected single-ion magnetic polyoxometalate. Left: coupling with vibration bath, center: coupling with surrounding magnetic nuclei (nuclear spin bath), right: coupling between different magnetic molecules (electron spin bath).

The mechanism (i) has to do with the interaction between spin and vibrational degrees of freedom via spin-orbit coupling, and will be studied in chapter 4. The mechanisms (ii) and (iii) could be merged into a unique one as their origin arises in both cases from the coupling between magnetic dipoles, which can be either the molecules encoding the qubits or surrounding magnetic nuclei. They both will be studied in chapter 5 under the name of magnetic noise.

In the pursuit of scalable architectures for quantum information processing, molecular spin qubits are also pushing to become potential candidates. Scalability could be achieved by combining these solid-state qubits with others degrees of freedom such as nuclear spins, electron charge, optical photons, and superconducting qubits.[140] Thus, the key strengths of different qubit implementations -including coherent storage of qubits for times exceeding

seconds, fast qubit manipulation, single-qubit measurement, and scalable methods for entangling spatially separated matter-based qubits- could be brought altogether to pave the road for practical solid-state quantum technologies.

Even in the case of only using spin-based qubits, particular architectures for scalability have been introduced and studied over the last few years. Finding them is crucial as the ultimate goal of multipurpose architectures devoted to implement generic algorithms will require moving from ensemble experiments with randomly distributed spin qubits, to spatially organizing close magnetic entities in periodic arrays to allow controlled inter-qubit communications for logical gates, see also chapter 7.[81,141,142] Of course, in order to be practical, qubits would also need to be arbitrarily initialized, coherently manipulated, efficiently measured and also scalable to large numbers. While this is still hard to reach for molecule-based spin qubits, important proposals involving molecular spin ensembles are already advancing in that direction.[143,144] Indeed, these proposals are based on superconducting coplanar waveguide resonators with arrays of nanoscopic constrictions where the spin ensembles are deposited, see **Fig. 2**.[145] By reducing the size of the center line, it is possible to significantly increase the magnetic field magnitude in the vicinity of each given constriction. Thus, provided a high enough coupling spin-constriction is achieved, this setup has been proposed to spatially organize small magnetic entities such as single molecular crystals and even individual molecules or ions, communicated via the aforementioned waveguides in all cases. A first notable example was provided by locally implanting rare-earth ions in a substrate of Al_2O_3 which are in addition coupled to superconducting NbN lumped-element micro-resonators.[146] Simultaneously, thorough studies were conducted to simulate the use of molecular spins acting as qubits coupled to the mentioned nano-constrictions.[147,148] Importantly, by using sets of realistic parameters, they concluded that both strong and ultra-strong couplings could be achieved when using molecular ensembles of spin qubits and even individual molecular spins. This would allow using molecular qubits either for storage or processing of quantum information in these potential scalable architectures.

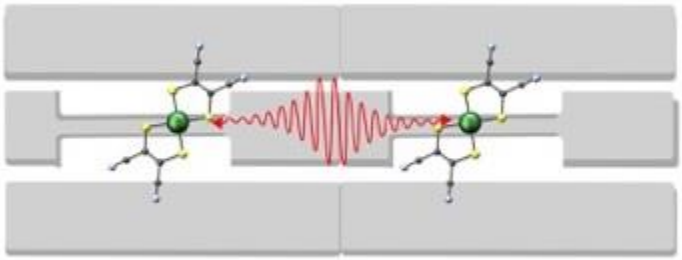

Fig. 2 Superconducting coplanar waveguides (grey) that connect pairs of molecules deposited on nanoscopic constrictions through resonant photons (red). Credits to Dr. Salvador Cardona-Serra.

A rather different approach to look for scalability is that based on biomolecules as building-blocks. Their exploration as versatile platforms opens the door to a detailed engineering of them, thanks to techniques developed in molecular biology such as recombinant protein technology or CRISPR-CAS9.[149,150] For instance, DNA origami was successfully employed to control the spatially positioning of functional materials by self-assembly and ordering gold nanoparticles.[151,152] Moreover, linear self-assembling peptides were shown to form a variety of stable and versatile nanostructures useful for the rational design of functional devices.[153] Hence, it is likely that the bio-nanotechnological strategy could eventually be applied in the quest for scalability in quantum computing. As a matter of fact, spin-carrying metalloproteins were already probed by manipulating their quantum states via multifrequency pulsed EPR methods,[154] while triple-stranded metallo-hellicates were suggested as addressable electron spin qubits to implement Lloyd's quantum computer proposal.[155–157] More recently, molecular chemistry has provided an example of a new organic building-block whose control and readout is conducted by using a nitrogen-vacancy center in diamond, namely, a synthetic polyproline with electron spins localized on attached molecular side groups.[158] Importantly, although only very few of these spin systems were addressed, this work does show that the use of spin-labeled peptides can become a potential resource for molecular-based scalable networks engineered with well-established chemical methods. In addition, the use of peptidic spin qubits could benefit from the possibility of systematic property optimization: whether one is interested in quantum coherence or in any other specific related effect, the rational procedure to improve the desired property would be to perform a screening of a

combinatorial peptide library, i.e. to make combinations of substitutions of individual amino acids in the sequence to obtain progressively better properties.

Molecular nanomagnets

Quantum computing exploits state superposition for data processing but yet it is also possible to harness complementary quantum systems to store information in the form of classical bits. These systems are known as molecular nanomagnets and are characterized by a bistable ground spin state at zero magnetic field that can be used as an information bit. Unlike conventional bulk magnets, their magnetic properties have a molecular origin. This means that collective long-range magnetic ordering of magnetic moments is not necessary for bistability and the characteristic molecular magnetic behavior appears even at high dilutions in a diamagnetic matrix.[159] Herein, we provide a general introduction aimed at establishing the basics that will allow us focusing on our main goal, namely, to study the vibration-induced spin relaxation that spoils bit information encoded in molecular nanomagnets. Thus, after identifying the most relevant vibrations for relaxation, it will possible to propose a rational molecular re-design in order to block them and improve the magnet performance. This last part will be thoroughly conducted in chapter 4 with a case study.

Molecular nanomagnets are zero-dimensional magnetic clusters where either a single metal ion or a group of them is coordinated by a set of ligands.[160–162] The former are known as single-ion magnets (SIMs), while the latter are single-molecule magnets (SMMs). Among the metal ions, the most commonly employed were firstly transition metals and subsequently trivalent lanthanides, such as Mn^{3+}, Mn^{4+}, Tb^{3+}, Dy^{3+}. The characteristic feature of molecular nanomagnets is the presence of a bistable ground spin state at zero field separated by a potential barrier, which gives rise to a slow loss of net magnetization and thus to a memory effect in the form of magnetic hysteresis. Hereunder, we will focus on Ln^{3+}-based SIMs as they are currently the last frontier under exploration and are drawing an unprecedented interest.[163–165]

Let us first proceed by describing the electronic structure, namely, the corresponding Hamiltonian $\hat{H}$ that determines energies and wave-functions, see **Fig. 3**. The first two factors $\hat{H}_{kin} + \hat{H}_{e-n}$ are the electron kinetic energy and

electron-nucleus attraction operators of the free metal ion. These factors define the ground electron configuration which in this case is of the form [Xe]$4f^n$, where *n* is the number of electrons in the 4f outer shell. The *n* electrons are distributed in the seven 4f orbitals that arise from the seven projections m_l = -3, -2, -1, 0, +1, +2, +3 of the quantum number l = 3. Note that due to the Pauli exclusion principle only two electrons with opposite $m_s = \pm 1/2$ projections can fit in a given orbital at most. The following factor to include, the electron-electron repulsion operator $\hat{H}_{e-e}$ with a magnitude lesser than that of $\hat{H}_{kin} + \hat{H}_{e-n}$, makes all the possible distributions of the *n* electrons in the seven 4f orbitals not to have the same energy. Each given distribution is known as term and the so-called Hund's rules determine the lowest one in energy. To determine the number of terms for a given configuration, one has to compute the binomial coefficient 2(2l+1)!/e!(2(2l+1)-e)!, where *e* is the number of electrons and l = 3 in this case.

Since Ln^{3+} ions are polyelectronic, the quantum numbers l, m_l, m_s that arise from solving the Schrödinger equation for a hydrogen-like ion are not well-defined. Instead, new quantum numbers must be introduced to characterize the terms present in many-electron systems. Indeed, these are the quantum numbers *S*, *L* of the total spin and orbital angular momenta, respectively. A given term characterized with given values of *S*, *L* is denoted as ^{2S+1}L, where 2*S*+1 is the spin multiplicity and *L* is replaced by a certain letter depending on its value. As with the quantum number *l*, the values 0, 1, 2, 3, 4, 5, 6, 7… of *L* correspond to the letters *S*, *P*, *D*, *F*, *G*, *H*, *I*, *K*… For a given electron distribution in the seven 4f orbitals, i.e. a term, *S*, *L* are calculated just by adding up the values of m_s and m_l of each electron. Note that the doubly-occupied orbitals do not contribute to *S* as the opposite projections $m_s = \pm 1/2$ cancel with each other, but do contribute with $2m_l$ to *L*. To determine the ground term in energy, we apply the Hund's rules. First, the electrons are distributed such that 2*S*+1 is maximized. This means that the electrons must occupy the maximum number of orbitals with m_s = +1/2 projection. Only when there are more than seven electrons these orbitals could be completed with a new m_s = -1/2 electron. The second rule is applied only if several terms have the same maximum spin multiplicity. In this case, the ground term is the one with the largest value of *L*. For that, one places the first electron in the orbital with m_l = +3, the second one in the orbital with m_l = +2, and so on until the last electron is placed in the orbital with m_l = -3. Whenever

the ion contains more than seven 4f electrons, the eighth electron would be placed again in the orbital with $m_l = +3$ and so on once again.

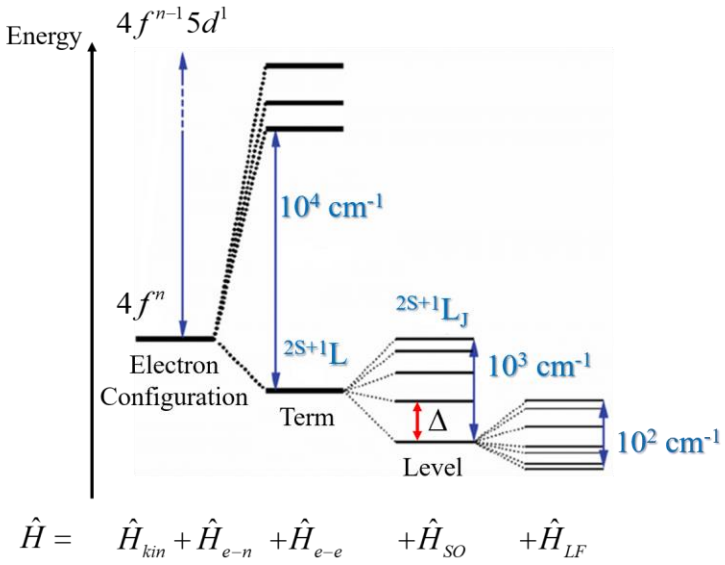

Fig. 3 Russell-Saunders coupling scheme as different interactions of decreasing magnitude are added to the full Hamiltonian $\hat{H}$, see main text. The wavenumbers shown are typical magnitude orders of the splitting energies. In the systems of our interest, the gap Δ between the ground and first excited levels will be large enough as compared to the thermal energy $k_B T$.

The following factor to include in the full Hamiltonian is the spin-orbit interaction $\hat{H}_{SO}$, which couples S, L in a new quantum number J that characterizes the total angular momentum. This interaction splits each term into $(2S+1)(2L+1)$ levels denoted as $^{2S+1}L_J$ with allowed values $J = |L+S|,\ldots,|L-S|$. For a given term with values S, L, the ground level is determined by applying the third Hund's rule. If the 4f shell is less than half-filled, the level with the smallest value of J lies lowest in energy. Instead, if the shell is more than half-filled, the ground level will be the one with the largest value of J. In the particular case of a half-filled shell, $L = 0$ and thus $J = S$ corresponds to the ground level. The validity of Hund's rules relies on assuming that the repulsion between the 4f electrons is greater enough than the spin-orbit coupling, which is considered as a safe estimate for trivalent lanthanide ions due to the compact nature of the 4f orbitals. In this case, once any other interaction is smaller than

the spin-orbit coupling, the scheme followed to derive the several terms and levels is known as Russell-Saunders or *LS* coupling scheme.

Up to this point, we have been describing the electronic structure of a free Ln^{3+} ion. The next step is to discuss the effect of a given Ln^{3+}-coordinating ligand set, i.e. the ligand field interaction $\hat{H}_{LF}$, on the levels $^{2S+1}L_J$. In most of cases, the energy gap Δ between the ground and first excited levels will be larger enough than the thermal energy k_BT below room temperature. Hence, the ground level will be the one mostly populated. If, in addition, the $\hat{H}_{LF}$ magnitude is below enough that of $\hat{H}_{SO}$, the ground level is split into $2J+1$ states according to the several projections $m_J = -J,\ldots,+J$ with a negligible interference from excited levels. Under these conditions, we will focus only on this low-lying multiplet to describe the electronic structure and the magnetic properties of Ln^{3+}-based SIMs. Whenever J is a half-integer number, these states will appear in the form of degenerate spin doublets in virtue of the so-called Kramers theorem. In some particular cases where the metal ion environment is highly symmetric, this degeneracy could be even higher. When dealing with $4f^4$, $4f^5$, $4f^6$ configurations, i.e. Pm^{3+}, Sm^{3+}, Eu^{3+}, it is possible to find that $\hat{H}_{SO} \approx \hat{H}_{LF}$ instead of $\hat{H}_{SO} \gg \hat{H}_{LF}$. Thus, one will have to bear mind the possible limitations of the Russell-Saunders scheme and the crystal field effective approach in these situations (see chapter 4). Anyway, Eu^{3+} is not under consideration on our side as its ground level $^7F_0$ has a $J = 0$ quantum number, which makes this ion be inappropriate to display SIM behavior.

In order not to solve the full Hamiltonian $\hat{H}$, the standard procedure consists in mapping this ground multiplet onto an effective $(2J+1)$-sized Hamiltonian. This is the so-called Crystal Field Hamiltonian $\hat{H}_{CF}$, **Eq. 2**, which is built in the ket basis set $\{|m_J\rangle\}$ and depends only on spin degrees of freedom through the extended Stevens operators $\hat{O}_k^q$.[166] All the effects derived from the interactions $\hat{H}_{kin}$, $\hat{H}_{e-n}$, $\hat{H}_{e-e}$, $\hat{H}_{SO}$ are encoded in the crystal field parameters B_k^q (CFPs), which reproduce the state energies of the ground $^{2S+1}L_J$ level multiplet. Importantly, symmetric metal-coordinating environments will make some CFPs be negligible thus simplifying **Eq. 2**. There exist two main strategies to determine the CFPs involving both first-principles and experimental approaches. On one hand, after building the full Hamiltonian $\hat{H}$ one could compare the $(2J+1)$-sized

submatrix associated to the ground level ${}^{2S+1}L_J$ with the Crystal Field Hamiltonian matrix, **Eq. 2**, in the ket basis set $\{|m_J\rangle\}$. Since $\hat{H}_{CF}$ is Hermitian, this gives rise to a set of $J(2J+1)$ independent linear equations that can be uniquely solved to determine the CFPs if there does not exist overparameterization.[167–169] On the other hand, it is also possible to exploit experimental data such as spectroscopically-determined energy differences between low-lying states by UV-vis spectroscopy or magnetic properties.[170–176] In this case, one proceeds iteratively by varying the CFPs until getting an accurate match between the calculated energies by diagonalizing **Eq. 2** and the experimental ones. Alternative techniques such as EPR spectroscopy are also available and are routinely employed to obtain the CFPs as we will explain in section 2.2.

$$\hat{H}_{CF} = \sum_{k=2,4,6} \sum_{q=-k}^{+k} B_k^q \hat{O}_k^q \qquad \textbf{Eq. 2}$$

Once the CFPs are known, $\hat{H}_{CF}$ is diagonalized to obtain $2J+1$ states with energies E_i and wave-functions $|\psi_i\rangle$ as a linear combination of the ket basis set $\{|m_J\rangle\}$. An important parameter is the energy difference between the ground and most excited states, known as zero field splitting (ZFS), see **Fig. 4**. To define a classical magnetic memory in the form of information bit, this low-lying electronic structure must contain a ground spin doublet, which can be non-degenerate but yet with a rather small gap. As mentioned above, this is often encountered in the case of ground levels ${}^{2S+1}L_J$ with a half-integer quantum number J. Instead, an integer J splits into an odd number of states and thus can give rise either to a singlet or to a doublet as a ground spin state. Under this situation, one should engineer the ligand environment to stabilize the spin doublet.

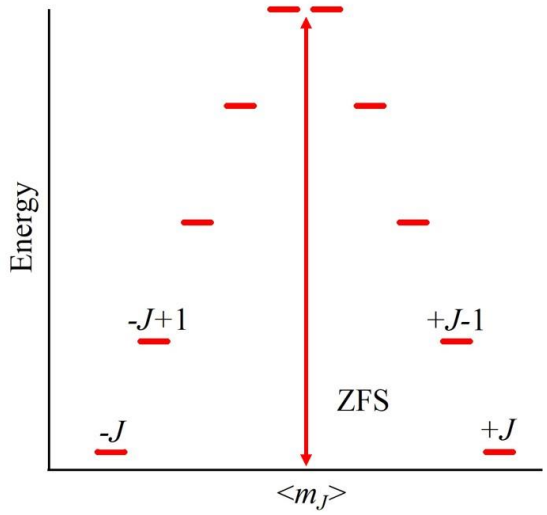

Fig. 4 Archetypal energy representation of the $2J+1$ states associated to the ground level ${}^{2S+1}L_J$ in a molecular nanomagnet. These states are commonly sorted from left to right with increasing expected m_J. For the sake of simplicity, it has been considered that $\langle m_J \rangle = m_J$ in this hypothetical example.

In an ensemble of a given molecular nanomagnet at thermal equilibrium, the population $0 \leq p_i \leq 1$ of each state obeys the Boltzmann law. By applying an external magnetic field, one of the two ground states is stabilized via Zeeman effect and, for a low enough temperature, it will become mostly populated with $p_{i0} \approx 1$. In other words, the sample is magnetized and thus we have *written* an information bit in the state i_0. After turning the field off, the population distribution in which $p_{i0} \approx 1$ and $p_i \approx 0$ for $i \neq i_0$ is not the most stable thermodynamic situation anymore. Therefore, the ensemble will evolve until reaching again the original Boltzmann population in each state. This process is known as magnetic relaxation and, of course, its detrimental effect is that of destroying the stored bit information. The key point is the timescale, characterized by the temperature-dependent relaxation time τ, in which this relaxation takes place. With a large τ, the information will be retained for long enough so that the given nanomagnet can display a potential applicability. Herein, we will focus on the relaxation induced by a thermal bath of vibrations. This becomes the relaxation source limiting τ as thermal energy is increased,

and hence still hampers the use of molecular nanomagnets at more practical temperatures.

This relaxation source involves quanta of vibrational energy, known as phonons, resonant with the energy gaps between pairs of states. Thus, when the field is turned off, a series of phonon absorptions and emissions drives the spin population from the initial state i_0 through the whole $^{2S+1}L_J$ ground multiplet until reaching the thermal equilibrium. The transition rate per unit time $\gamma_{i\rightarrow f}$ between two given states *i* and *f* with wave-functions $|\psi_i\rangle$ and $|\psi_f\rangle$ depends on their energy difference and on the strength coupling between spin and vibration degrees of freedom. On one hand, the larger this energy difference is the smaller $\gamma_{i\rightarrow f}$ will be. That is why ligand sets are often optimized to maximize the ZFS for a given metal ion. Firstly, this was tackled by serendipity but over the last few years theoretical methods are proven to be an indispensable tool for a proper rational design.[71,177–182] These tools have allowed an important increase in the ZFS from some hundreds until few thousands of wavenumbers.[162,164,165,183]

On the other hand, the coupling strength usually becomes smaller if the $\hat{J}_z$ operator expectation values computed at $|\psi_i\rangle$, $|\psi_f\rangle$ are different enough. Note that in the particular case in which $|\psi_i\rangle$, $|\psi_f\rangle$ coincide with given kets $|m_J^i\rangle$, $|m_J^f\rangle$, these expectation values are m_J^i, m_J^f, resp. This means that one should look for molecular nanomagnets where the ground spin doublet is the one corresponding to the states $|\psi_\uparrow\rangle$, $|\psi_\downarrow\rangle$ with $\hat{J}_z$ expectation values closest to ±*J*, the highest values in magnitude that m_J can attain. Indeed, if we consider the initial spin population in the $|\psi_\uparrow\rangle$ state, the reversal of part of it until reaching $|\psi_\downarrow\rangle$ can also happen directly without spin flux through intermediate states. Thus, to minimize this direct process it is also advisable to use Ln^{3+} ions among the ones with a large ground *J* quantum number, which in turn maximizes the difference between +*J* and -*J*. That is why ions such as Tb^{3+}, Dy^{3+} and Ho^{3+} with a more than half-filled 4f shell are preferred, as in virtue of the third Hund's rule the ground *J* corresponds to the maximum value |*L*+*S*|. Instead, Ln^{3+} ions with less than seven 4f electrons stabilize the minimum value |*L*-*S*| as a ground *J*.

All in all, the strategy historically explored to rise the timescale for the spin reversal has been (i) to use Ln^{3+} ions with a large ground *J* and (ii) to search for coordination spheres to further maximize the ZFS. This is the expected

procedure to follow if one assumes that the most likely relaxation pathway consists in a sequence of unit steps through states with increasing expectation values $-J \rightarrow -J+1 \rightarrow ... \rightarrow +J-1 \rightarrow +J$. In this case, the spin population has first to overcome a potential energy barrier given by the ZFS to be reversed, see **Fig. 4**. Nevertheless, there also exists a non-negligible probability for the spin population to tunnel the barrier through excited states without reaching the top of the aforementioned barrier. To minimize this effect, it is important to achieve wave-functions $|\psi_i\rangle$ with a $|m_J\rangle$ basis ket mix as little as possible, for example, with a proper symmetry in the donor-atom distribution around the Ln^{3+} ion. Whenever this tunneling happens, a large ZFS is ineffective at avoiding relaxation and hence any attempt devoted to increase the potential barrier will not produce a significant change in τ anymore. Thus, once the electronic structure is properly addressed, one should now focus on optimizing those molecular features that are limiting the relaxation time. Since the main goal is to design nanomagnets working at higher temperatures, an important part of the invested energy in driving the spin population will undoubtedly stem from vibration modes. In fact, current theoretical methods are intended to guide synthetic efforts at the lab stage by identifying the key molecular vibrations that promote magnetic relaxation. This approach is already producing positive results,[164,165] as with this information one can conduct an *ad hoc* re-design of the ligand environment in order to remove or decouple the relevant vibrations.

Vibration-induced magnetic relaxation can take place through different mechanisms whose prevalence depends on the working temperature range. At low temperatures, there exists a restricted number of available phonons as only low-energy phonons are significantly populated. Thus, the spin in the initial state i_0 can hardly be promoted to higher excited states before decaying towards the other barrier side. Instead, the spin will tunnel the barrier and reach a few low-lying states through a direct process driven by phonons whose frequency matches the energy gap between the two given states. Whenever this mechanism is dominant, the magnetic relaxation rate τ^{-1} will show a proportional dependence with temperature T of the form $\tau^{-1} = AT$, where A is a constant.

At higher temperatures, mechanisms involving more than one phonon gain importance, mainly, the so-called Orbach and Raman processes. The former consists in a step-by-step sequence of direct transitions in which the spin is first

promoted to higher excited states by phonon absorption and then decays towards the other barrier side by phonon emission. This essentially resembles Arrhenius-like processes where reactants must first overcome a potential barrier before reaching the products. In this case, since the barrier crossing can be produced below the highest excited state via quantum tunneling, the barrier height Δ is often found to be smaller than the ZFS and does not necessarily coincide with any intermediate excited state.[184] The dependence of τ^{-1} in a temperature range where the Orbach process dominates is exponential-like $\tau_0^{-1}\exp(-\Delta/k_BT)$, where τ_0^{-1} is the attempt rate at crossing the barrier. In a Raman process, the spin transition between two given states is not direct but through an intermediate state. Two phonons are involved with a frequency difference coinciding with the transition energy. The temperature dependence of τ^{-1} follows a potential evolution of the form $\tau^{-1} = BT^{n+7}$, where B is a constant while the exponent n is 0 for an integer J and ±2 for a half-integer J. The expression of τ^{-1} as a function of temperature including the three processes introduced above is given **Eq. 3**. This expression is often used to fit the experimental thermal evolution of τ^{-1} by varying A, B, τ_0^{-1}, Δ as free parameters.[185]

$$\tau^{-1} = AT + BT^n + \tau_0^{-1}\exp(-\Delta/k_BT) \qquad \textbf{Eq. 3}$$

Eq. 3 can also be complemented with a temperature-independent rate τ_{QTM}^{-1} accounting for quantum tunneling of magnetization between the states $|\psi_\uparrow\rangle$, $|\psi_\downarrow\rangle$, which may operate at low enough temperatures.[185] Unlike the direct process, this is an energy-conserving spin flip-flop event. Hence, neither phonons nor excited states are involved and no energy is exchanged with the environment. The origin of this tunneling can be found in transverse interactions that couple the states $|\psi_\uparrow\rangle$, $|\psi_\downarrow\rangle$ in symmetric $|\psi_\uparrow\rangle+|\psi_\downarrow\rangle$ and antisymmetric $|\psi_\uparrow\rangle-|\psi_\downarrow\rangle$ mixes of different energy. Their energy gap, known as tunneling splitting, is proportional to the spin flip-flop rate between $|\psi_\uparrow\rangle$ and $|\psi_\downarrow\rangle$.[185] These interactions include effective transverse magnetic fields and/or hyperfine couplings with surrounding magnetic nuclei. To suppress the former, nanomagnets are diluted into a diamagnetic matrix composed of isostructural

molecules of yttrium (the most commonly used), lanthanum or lutetium. On the contrary, the latter plays the dominant relaxation role in diluted samples and persists even at very low temperatures. To avoid the limited coercivity derived from this mechanism, a small static magnetic field is usually applied to remove the degeneracy between the states $|\psi_{\uparrow}\rangle$, $|\psi_{\downarrow}\rangle$. Since the spin flip-flop is an event that requires energy conservation, the action of this field should lower the probability of tunneling. Nevertheless, even in nuclear-spin-free nanomagnets one still observes a limited coercivity,[186,187] which points to the existence of more causes behind quantum tunneling of magnetization close to zero field not yet unveiled. A measure to figure out the importance of tunneling in relaxation consists in checking the magnitude of the perpendicular Landé factor $g_{\perp}$ associated to the ground spin doublet $|\psi_{\uparrow}\rangle$, $|\psi_{\downarrow}\rangle$. As a matter of fact, this is responsible for the molecular spin sensitivity to transverse magnetic fields, and that is why nanomagnets are designed with a highly-axial ground Landé *g* tensor.[188,189]

On the other hand, *n* is quite often also used as a free parameter and it is common to obtain fitting values differing from the expected ones: 5, 7, 9. First of all, note that there can exist frontier temperature ranges of coexistence between two competing mechanisms. This fact highlights the importance of fitting the experimental τ^{-1} evolution by using **Eq. 3** instead of performing a separate fit for each term, as this last procedure has historically led to significant errors when identifying the dominant relaxation mechanism at each temperature range. In second place, the derivation of **Eq. 3** relies on some approximations and assumptions, namely, perturbation theory up to second order and a Debye-like phonon density of states ρ.[185] The Debye model assumes a quadratic dependence of $\rho \sim \omega^2$ with the phonon frequency ω. A legitimate question is to what extent the Debye model can be reliable employed for molecular crystals. This model has been extensively used to model a plethora of inorganic crystals whose paramagnetic entities are single ions but not coordinated by a ligand set of molecular nature. Moreover, while it is widely accepted that the observed ρ follows the Debye-like behavior up to an energy of about 20 cm^{-1}, this phonon density becomes smaller than expected as the energy is further increased.[190] Importantly, the use of a wrong phonon density can lead to failed predictions of magnetic relaxation times at high temperatures where we are now turning our

attention,[191] and that is why state-of-the-art theoretical methods are trying to incorporate the real phonon spectrum. This issue will be addressed in chapter 4.

2.2 Electron Paramagnetic Resonance

In this section we provide an introduction to the basics of Electron Paramagnetic Resonance (EPR) and the experiments required to characterize the physical systems described in section 2.1.[192] This discussion is divided into two parts. First, we will go over continuous wave EPR (cw-EPR) which allows determining the electronic structure, and then we will focus on pulsed EPR as a routine tool used to drive and probe the quantum coherence of molecular spin qubits. Since quantum information is encoded in the spin phase, decoherence in molecular qubits will appear in the form of spin dephasing.

Continuous wave EPR

In the previous section we have introduced the target systems that will be subject of study, namely, molecular nanomagnets and molecular spin qubits. These zero-dimensional entities are characterized by having a given number of open-shell electrons which give rise to a set of spin states. Their energies and wave-functions can be determined by means of first-principles calculations, i.e., by solving a Schrödinger-like equation where the main physical interactions such as electron-electron repulsion and spin-orbit coupling are included. This equation involves a Hamiltonian that depends on both spatial and spin degrees of freedom. Nonetheless and as presented previously, in the case of our target systems it is possible to model their spin state scheme by introducing the Crystal Field Hamiltonian which depends only on spin operators and all the effects derived from the spatial operators are encoded in the CFPs. These parameters can also be determined via first-principles calculations but herein we will explain how they can be experimentally obtained by exploiting EPR spectroscopy. This step is crucial since after accessing these parameters one can then diagonalize the Crystal Field Hamiltonian and thus calculate all the physical observables.

Roughly speaking, a standard EPR spectrometer consists in two parallel coils that surround a resonant cavity placed in between them, see **Fig. 5**. An electric

current flowing through these coils generates a static magnetic field that covers the whole cavity, which at the same time is illuminated with an electromagnetic radiation of a frequency in the microwave range. The sample to be probed is placed inside the cavity, and its temperature can be controlled by means of a cryostat that makes use of an external liquid helium tank. A computer connected to the spectrometer takes charge of controlling its functioning by setting the relevant parameters and collecting the experimental data.

Fig. 5 Basic picture of a standard EPR spectrometer. Note the two parallel coils and the thick pipeline carrying liquid helium to the cavity.

Depending on the frequency employed in the cavity, which lies inside the range of the microwave radiation, EPR spectroscopy is classified in different bands, see **Table. 1**. The most popular ones and widely employed are the X and Q bands.

Table. 1 Classification of the different EPR bands according to their radiation frequency. Note that these values are just estimates, the real frequency in a given experiment depends on the settings of the spectrometer and can vary around a small neighborhood of the value displayed in the table.

Band	L	S	C	X	P	K	Q	U	V	E	W	F	D
***ν*/GHz**	1	3	4	10	15	24	35	50	65	75	95	111	140
***ν*/cm^{-1}**	0.03	0.01	0.13	0.33	0.5	0.8	1.18	1.67	2.17	2.5	3.13	3.7	4.76

The magnetic field direction is constant and perpendicular to the coil plane and yet it is possible to modify its magnitude. In virtue of the Zeeman effect, this field interact with the molecular spin states and will change its energy scheme. To account for this coupling, the Crystal Field Hamiltonian needs to be complemented with a Zeeman term $\hat{H}_{zee}$, which for a weak magnetic field (below 1 T) takes the expression in **Eq. 4**.

$$\hat{H}_{zee} = \mu_B \vec{B} \cdot g \cdot \vec{J} \qquad \textbf{Eq. 4}$$

In **Eq. 4**, μ_B is the Bohr magneton, $\vec{B} = \left(B_x, B_y, B_z\right)$ is the magnetic field vector, g is the electron Landé tensor (a 3x3-sized symmetric matrix), and $\vec{J} = \left(\hat{J}_x, \hat{J}_y, \hat{J}_z\right)$ is the electron spin operator. In the case of a spin with $J > 1/2$, g is often replaced by the scalar isotropic value corresponding to the free-ion value g_J, and the magnetic anisotropy is thus accounted for by the Crystal Field Hamiltonian. On the other hand, when the spin quantum number is $J = 1/2$ -either real or effective- and hence the Crystal Field Hamiltonian vanishes, the g tensor is diagonalized to obtain three eigenvalues g_1, g_2, g_3. Then, the corresponding eigenvectors can be used to define three orthonormal axis X, Y, Z. For instance, after considering the map $g_1 = X$, $g_2 = Y$, $g_3 = Z$, **Eq. 4** becomes:

$$\hat{H}_{zee} = \mu_B \left(g_1 B_x \hat{J}_x + g_2 B_y \hat{J}_y + g_3 B_z \hat{J}_z\right) \qquad \textbf{Eq. 5}$$

The Crystal Field Hamiltonian can also be complemented with other interactions such as the hyperfine coupling $\hat{H}_{hy}$ between the electron and nuclear spins of the single metal ion in the magnetic molecule. This interaction is expressed as:

$$\hat{H}_{hy} = \vec{J} \cdot A \cdot \vec{I} \qquad \textbf{Eq. 6}$$

In **Eq. 6**, $\vec{I} = \left(\hat{I}_x, \hat{I}_y, \hat{I}_z\right)$ is the nuclear spin operator, and A is the hyperfine coupling tensor (a 3x3-sized symmetric matrix). $\hat{H}_{hy}$ is often re-written as a function of the eigenvalues A_1, A_2, A_3 of A. Indeed, in the case of a spin with $J > 1/2$, it is assumed that the preferred anisotropy axis -employed to define the Z direction- of the given magnetic molecule coincides with one of the eigenvectors of A. Hence, the two remaining eigenvectors must coincide with the X and Y directions. For instance, by considering the map $A_1 = X$, $A_2 = Y$, $A_3 = Z$, $\hat{H}_{hy}$ becomes:

$$\hat{H}_{hy} = A_1 \hat{J}_x \hat{I}_x + A_2 \hat{J}_y \hat{I}_y + A_3 \hat{J}_z \hat{I}_z \qquad \textbf{Eq. 7}$$

In the case of a spin with $J = 1/2$ -either real or effective-, it is common to assume that both the eigenvectors of g and A coincide. Hence, **Eq. 5** and **Eq. 7** can be employed altogether and are added to produce the spin Hamiltonian. The expressions in **Eq. 5** and **Eq. 7** can be simplified in the case of a more restricted anisotropy. For instance, an axial anisotropy implies that two eigenvalues are equal while the remaining one is different. Let us consider that $g_1 = g_2 \neq g_3$ and $A_1 = A_2 \neq A_3$. The equal and different values are commonly renamed as $g_{\parallel} = g_3$, $g_{\perp} = g_1 = g_2$, $A_{\parallel} = A_3$, $A_{\perp} = A_1 = A_2$, and the eigenvectors corresponding to $g_{\parallel}$, $A_{\parallel}$ are associated to the Z direction. Since $g_1 = g_2$ and $A_1 = A_2$, one can use interchangeably the two remaining eigenvectors to associate the X and Y directions. Of course, we can also come across the isotropic situation in which

all the eigenvalues are equal $g_1 = g_2 = g_3$, $A_1 = A_2 = A_3$. In this case, the three eigenvectors are interchangeable when associating the spatial directions *X*, *Y*, *Z*.

In a common cw-EPR experiment, the magnitude $B = |\vec{B}|$ of the static magnetic field is swept inside a given range while the sample is continuously illuminated with microwave radiation of a fixed frequency *v*. As mentioned, the action of this field is to change the spin energy scheme as its magnitude is increased. When the energy gap $\Delta E = E_2 - E_1$ between two given spin states is close to match the irradiation frequency *v*, the molecule absorbs a quantum of light and the spectrometer records that resonance in the form of a signal peak in the cw-EPR spectrum, see **Fig. 6**. For instance, in the simplest case of a system with a ground spin doublet *S* = 1/2 -where all CFPs vanish- and by considering $\hat{H}_{hy} = 0$, there exist two energy states labeled as spin up with m_s = +1/2 and spin down with m_s = -1/2, which are degenerate at *B* = 0. For weak magnetic fields, this degeneracy is removed and the energies $E_{\pm 1/2}$ of these levels follow the straight lines $E_{\pm 1/2} = \mu_B g B m_s$ as in **Fig. 6**, where *g* is here the Landé factor for the given spin doublet.

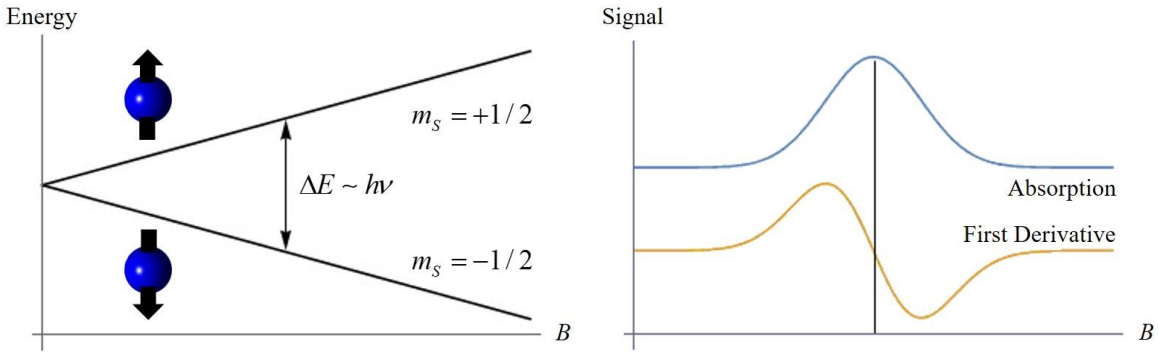

Fig. 6 Left: Energy scheme of a spin doublet labeled with the projections m_s = ±1/2 as a function of the magnetic field magnitude *B*. The resonance is produced when the irradiation frequency *v* closely matches the energy gap Δ*E*. Right: cw-EPR spectrum where the resonance can be recorded as an absorption or as the first derivative of this absorption. Signal in arbitrary units.

Note that the finite lifetime of excited states leads to an uncertainty in their energies. Thus, the resonance condition and the subsequent absorption of one photon does not require a strict match $\Delta E = h\nu$. Indeed, a more realistic picture to describe the light-matter interaction needs to introduce an absorption probability, which depends on how close ΔE is to $h\nu$ and attains its maximum value at $\Delta E = h\nu$. This would explain the rather wide and rounded peak in **Fig. 6**, which would become narrow and sharp under the roughest approximation where the only allowed values for this probability is 0 ($\Delta E \neq h\nu$) and 1 ($\Delta E = h\nu$). Moreover, when probing an ensemble of molecules instead of a single one there can also exists a complementary effect involved in widened peaks of a cw-EPR spectrum. Indeed, local inhomogeneities such as lattice strains and/or local magnetic fields produced by neighboring magnetic entities can give rise to different energy gaps in different copies of the same molecule for each given value of B. Thus, the resonance condition in which ΔE is close to match $h\nu$ arises in a static field window rather than in a specific value. Nevertheless, since all molecules are not equally affected by these inhomogeneities if for instance they are all not equally oriented and are magnetically anisotropic (the case of microcrystalline powders and frozen solutions), it turns out that most of them attain the maximum in the absorption probability at a given B_0 and produce a maximum in the EPR signal at that field. As B becomes smaller or greater than B_0, there exist a lesser number of resonant molecules which produce a lower signal. All these individual signals of decreasing intensity, which are already broadened by energy-time uncertainty, overlap with each other and the spectrometer records their envelope in the form of a widened peak as depicted in **Fig. 6**.

A general molecular magnetic system with a ground electron spin quantum number J will give rise to a more complex spin energy evolution with B, and thus will produce a more sophisticated cw-EPR spectrum. It is possible to simulate this spectrum by means of an iterative procedure in which the parameters of the complemented Crystal Field Hamiltonian are varied until obtaining the best fit. To accomplish this purpose, the software package EASYSPIN is often employed.[193] This is one of the standard procedures to experimentally determine the magnetic anisotropy parameters by exploiting EPR spectroscopy, which subsequently allows diagonalizing the given Hamiltonian and thus obtaining all physical observables of the molecule -either nanomagnet or spin qubit- including its spin energies.

Pulsed EPR

Unlike cw-EPR spectroscopy, in a standard pulsed EPR experiment the static field magnitude is fixed at a given value where a resonance in the cw-EPR spectrum is observed. Now, instead of continuously illuminating the molecular sample, we will rather apply a sequence of finite microwave pulses. These typically take between 10 and 100 ns depending on the pulse and on the radiation intensity, and their oscillating magnetic component is responsible for exciting the spin. By making use of a vast variety of pulse sequences, it is possible to gain extensive knowledge on structural and dynamical properties of a given magnetic sample, as well as drive quantum algorithms. Although it will not be covered in this dissertation, it is equally worth mentioning that spin qubits can also be excited and coherently manipulated by means of oscillating electric fields.[194,195]

In the previous section, we presented the qubit as a well-characterized two-level system whose wave-function $|\Psi\rangle = \alpha|0\rangle + \beta|1\rangle$ is a quantum superposition between two orthonormal computational states $|0\rangle$ and $|1\rangle$. The normalization condition $|\alpha|^2 + |\beta|^2 = 1$ restricts the values that the coefficients α and β can take and, more importantly, allows a geometrical re-interpretation of the qubit as a point on the surface of the unit sphere. Indeed, note that $|\alpha|^2 + |\beta|^2 = 1$ is the equation of the unit sphere where α and β are complex coefficients. Thus, we can re-write the qubit wave-function in terms of spherical coordinates depending on the zenithal $0 \leq \theta \leq \pi$ and azimuthal $0 \leq \varphi \leq 2\pi$ angles:

$$|\Psi\rangle = \cos\left(\frac{\theta}{2}\right)|0\rangle + e^{i\varphi}\sin\left(\frac{\theta}{2}\right)|1\rangle \qquad \textbf{Eq. 8}$$

Such a geometrical interpretation of the qubit constitutes the so-called Bloch Sphere as depicted in **Fig. 7**. The computational states $|0\rangle$ and $|1\rangle$ correspond to the north and south poles of the sphere, and can be respectively recovered with the values $\theta = 0$ and $\theta = \pi$ regardless the value of φ. Any other combination

between θ and φ gives rise to a superposition of $|0\rangle$ and $|1\rangle$. In particular, the combinations with the same weight in $|0\rangle$ and $|1\rangle$ are achieved in the sphere equator and correspond to $\theta = \pi/2$.

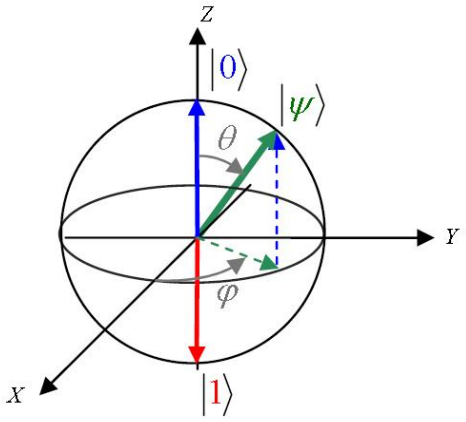

Fig. 7 Geometrical interpretation of the qubit as a point $|\Psi\rangle$ on the surface of the Bloch Sphere. This point is parametrized in terms of the zenithal θ and azimuthal φ angles. Note that the $|0\rangle$ and $|1\rangle$ computational states correspond to the north and south poles of the sphere, resp.

The Bloch Sphere becomes a useful tool when it comes to visualize the effect of a microwave pulse on the qubit wave-function $|\Psi\rangle$. Indeed, let us consider that the molecular sample is magnetized, with a magnetization vector $\vec{M}$, by applying a static field defining the *Z* direction. Since the spin states $|0\rangle$ and $|1\rangle$ are not degenerate, at thermal equilibrium most of molecules occupy the lowest state in energy, say $|0\rangle$. Of course, the larger the energy gap between $|0\rangle$ and $|1\rangle$ is, the more molecules will occupy the $|0\rangle$ state. Nonetheless, since we are working under a fixed static field, enlarging this gap would not be a practical option and other techniques devoted to transfer population to a given state such as the ones discussed in chapter 8 should be employed.

By applying a pulse of a proper length *t*, the molecular population is promoted to the $|1\rangle$ state and $\vec{M}$ is rotated 180 degrees around an axis contained

in the *XY* plane. Likewise, one could also promote this population to the $|0\rangle$ state if all of it were initially at the $|1\rangle$ state. In terms of the Bloch Sphere, the qubit wave-function $|\Psi\rangle$ has changed from $|0\rangle$ to $|1\rangle$ via a rotation of 180 degrees, and that is why this is called a π pulse. On the other hand, the application of a pulse with a length *t*/2 tips or rotates $\vec{M}$ by 90 degrees around the same axis contained in the *XY* plane. This means that the qubit wave-function becomes an equally-weighted superposition $|\Psi\rangle = \left(|0\rangle + e^{i\varphi}|1\rangle\right)/\sqrt{2}$, and is now found at some point of the Bloch Sphere equator. Since $|0\rangle$ was the initial state, this is known as a π/2 pulse and constitutes a routine tool to generate quantum superpositions from basis states. As a matter of fact, the π and π/2 pulses are of a key importance when implementing logical gates in quantum algorithms by means of pulse EPR spectroscopy, see chapter 7.

A simple experiment devised to rotate the magnetization vector $\vec{M}$ in a controlled manner, and thus to prove that the qubit can be placed in state superposition, consists in driving Rabi oscillations. First, we apply a static magnetic field defining the *Z* direction with magnitude B_0. This magnetizes the sample with $\vec{M}$ pointing in this direction. By starting always from this initial situation, the application of a microwave pulse with an increasing length rotates $\vec{M}$ around an axis contained in the *XY* plane by an increasing angle (nutation). The direction of this axis is the propagation direction of the pulse, which in turn often defines the *X* axis direction. Hence, the orthonormal direction both to *X* and *Z* defines the *Y* axis direction. In the Bloch Sphere, the qubit is being driven between the $|0\rangle$ and $|1\rangle$ states and attaining a state superposition whenever the pulse length is not an integer multiple of the π-pulse length, see **Fig. 8**. In the experiment, the *z*-component M_z of $\vec{M}$ is measured and plotted against increasing pulse lengths, which gives rise to an oscillatory pattern as depicted in **Fig. 8** known as Rabi oscillations. Let us recall that the microwave pulse is an electromagnetic wave that harmonically oscillates with time. Thus, the oscillation frequency, known as Rabi frequency Ω_R, is proportional to the magnitude B_1 of the magnetic field that composes this wave as $\Omega_R = \mu_B g B_1 / \hbar$, where $\hbar$ is the reduced Planck's constant and *g* is the Landé factor associated to the spin doublet whose states have been labeled as $|0\rangle$ and $|1\rangle$.

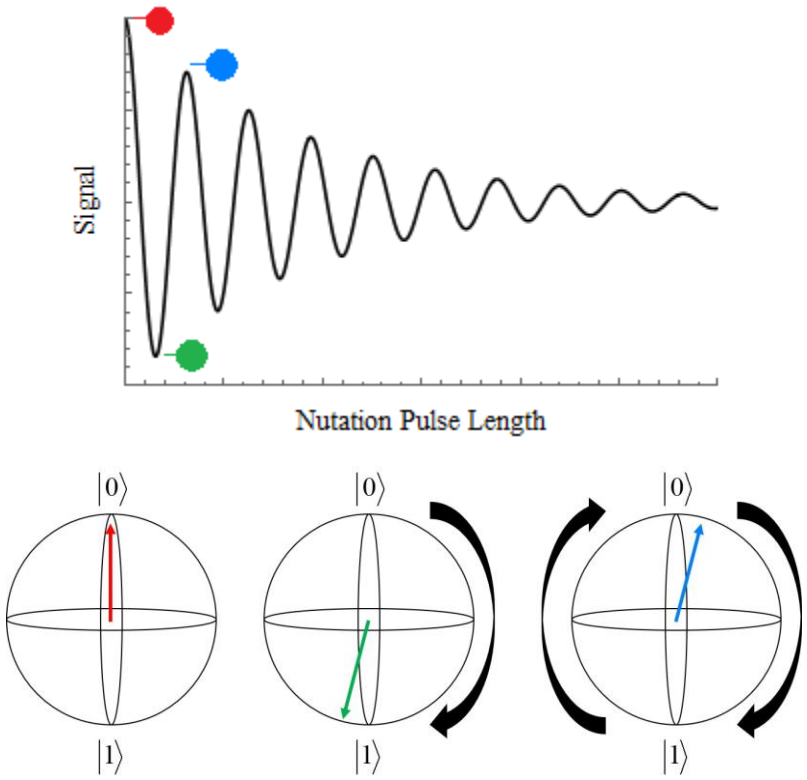

Fig. 8 Top: Damped oscillatory pattern of Rabi oscillations. Signal in arbitrary units. Bottom: Different qubit states in the Bloch Sphere for different nutation pulse length.

The striking feature in **Fig. 8** is the damped behavior of these oscillations. Indeed, let us recall that $\vec{M}$ is proportional to the sum of all molecular magnetic dipolar moments $\vec{\mu_i}$ inside a given volume *V*. Importantly, note that what standard EPR spectrometers detect are macroscopic magnitudes such as $\vec{M}$. A non-damped oscillation would require a nutation of each $\vec{\mu_i}$ at the same speed. Nevertheless, the appearance of local magnetic fields because of the presence of neighboring spins and spatial inhomogeneities both in B_0 and B_1 makes each molecule feel a rather different effective B_1^i. Thus, each $\vec{\mu_i}$ rotates at a different frequency and this results in a collective dephasing. After applying a pulse with a length equal to a π-pulse length (green dot in **Fig. 8**), not all $\vec{\mu_i}$ point in the same direction and hence the magnitude of $\vec{M}$ is now smaller than before applying the pulse. As the pulse length is increased, this dephasing process is more important and M_z becomes smaller. For a long enough length, one finds the same number of $\vec{\mu_i}$ pointing in the two directions of the *Z* axis and M_z

vanishes. The decay of Rabi oscillations is produced at a constant rate $\Gamma = 2\pi/T_{dep}$, where T_{dep} determines the characteristic timescale of the dephasing process; the evolution of these oscillations is modulated by a decaying exponential function as $\exp(-t/T_{dep})\cos(\Omega_R t)$, where t is the pulse length. Of course, to keep control on the qubit states while conducting a quantum algorithm, one will need first to minimize the dephasing process as much as possible by properly designing the molecular ensemble.

Pulse EPR spectroscopy can also be exploited to extract information related to the characteristic timescales that determine the spin relaxation dynamics. Two important parameters that characterize two important spin relaxation processes are the so-called spin-lattice T_1 and spin-spin T_2 relaxation times. Indeed, let us recall that once a static magnetic field defining the Z direction is applied, the magnetization vector $\vec{M}$ is reoriented until reaching a new thermal equilibrium in which $\vec{M}$ points in the static field direction. After applying a microwave pulse contained in the XY plane whose magnetic component tips $\vec{M}$, T_1 determines the timescale taken by $\vec{M}$ to become again aligned with the static field direction. Thus, spin-lattice relaxation is related to magnetic field fluctuations perpendicular to the static magnetic field that tip $\vec{M}$ around axes contained in the XY plane until recovering its equilibrium direction. For instance, one can tip $\vec{M}$ by 90 degrees with a $\pi/2$-pulse and then track the magnetization magnitude M_z in the Z direction. The plot of M_z against time will show an evolution that can be fitted to $M_z = M_0(1-\exp(-t/T_1))$ and allows extracting T_1, where M_0 is the magnetization magnitude in the Z direction before tipping $\vec{M}$. It is also possible to tip $\vec{M}$ by 180 degrees with a π-pulse and then perform the same tracking of M_z to extract T_1. In this case, if we think of the two opposed directions $\vec{M}$ and $-\vec{M}$ along the Z axis as the two states of a classical bit, what is being measured is the lifetime of the information saved in this bit in the form of $-\vec{M}$ direction. The T_1 relaxation process depends on temperature and involves an energy exchange between the molecule and the crystal lattice, which proceeds through excitation of phonon modes until the energy is dissipated towards a thermal reservoir. This can be the heat bath that surrounds the sample in the experimental setup.

On the other hand, the T_2 relaxation time characterizes the evolution timescale of the magnetization magnitude in the XY plane until recovering the thermal equilibrium. After tipping $\vec{M}$ by 90 degrees with a $\pi/2$-pulse, the

molecular spins rotate or precess around the Z axis at a speed determined by the so-called Larmor frequency $\Omega_L = \mu_B g B_0 / \hbar$, where B_0 is the static field magnitude. As explained above, magnetic field spatial inhomogeneities parallel to the static field direction give rise to a distribution in the Larmor frequency and each spin precesses at a different speed. This results in a spin dephasing that lead to a loss of net magnetization in the XY plane as all spin projections on this plane will eventually point in random directions and cancel each other. If for instance the magnetization magnitude M_x is tracked in the X direction against time, we will find an evolution than can be fitted to a decaying exponential $M_x = M_0 \exp(-t/T_2)$ that will allow us extracting T_2. Since quantum information is stored in the form of superposition between two states, namely $\vec{M}$ and $-\vec{M}$ directions, the T_2 relaxation time can be related to the lifetime of this information encoded, in this case, as a superposition contained in the XY plane. Unlike the T_1 process, none energy exchange with the crystal lattice is involved in the T_2-mediated relaxation. Moreover, T_1 and T_2 timescales are rather different and, in particular, spin-spin relaxation quite often proceeds much faster than spin-lattice processes, i.e., $T_2 << T_1$. In other words, by the time $\vec{M}$ is reoriented in the Z direction, the net magnetization in the XY plane has already been completely lost since much before. Nevertheless, especially at high enough temperatures, T_1 can approach T_2 and become similar. Since T_1 is an upper bound of T_2, rising T_2 to preserve quantum information for a longer time could first require to find strategies to increase T_1 depending on the experimental conditions such as temperature.

There exists an alternative EPR experiment that can be performed to determine the survival timescale of quantum information encoded as a state superposition. This consists in a two-pulse sequence with a variable inter-pulse delay time τ, known as Hahn echo sequence, see **Fig. 9**. The characteristic timescale derived from this experiment is called phase memory time T_m and will be the one we will use to discuss the systems presented in the next chapters. Importantly, T_2 and T_m aim to qualitatively describe the same relaxation process. Nevertheless, their determination involves rather different experiments and hence should not be confused. As a matter of fact, T_m is found to be a lower bound of T_2 and they both do not necessarily attain the same numerical value under the same experimental conditions. Of course, T_1 is also an upper bound of T_m.

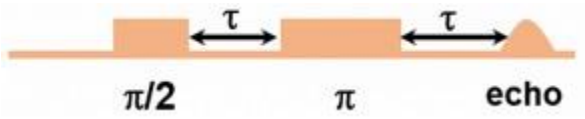

Fig. 9 Hahn echo sequence with an inter-pulse delay time τ between π/2 and π pulses. After a subsequent delay time τ, the EPR spectrometer records a magnetization peak known as echo.

In this two-pulse experiment, a static magnetic field defining the *Z* axis is applied to magnetize the sample -an ensemble of molecular spins- in the field direction, **Fig. 10 (A)**. This stabilizes most of the molecular population in the ground spin state labeled as $|0\rangle$ in the Bloch sphere. Then, a π/2-pulse is applied along the *X* axis to rotate the magnetization vector $\vec{M}$ by 90 degrees, **Fig. 10 (B)**. Before applying the next pulse, there exists a waiting time τ that results in a collective spin dephasing, **Fig. 10 (C)** and **(D)**. Indeed, once the π/2-pulse tips the individual molecular spins, they all will precess around the static field direction. Nevertheless, as explained above, magnetic field fluctuations along this direction produce a distribution of Larmor frequencies due to the presence of nearby magnetic entities such as magnetic nuclei. Thus, these spins will precess at different angular speeds both clockwise and anti-clockwise. After this waiting time, also known as delay time, a π-pulse is applied to rotate all individual spins by 180 degrees, **Fig. 10 (E)**. If the delay time has not been too long to cause an important dephasing, these spins will now precess in opposite direction and, after the same waiting time τ, some of them will converge to a common axis contained in the *XY* plane. This convergence, also known as refocusing, results in a magnetization peak in the *XY* plane recorded by the spectrometer in the form of echo signal, **Fig. 10 (F)** and **(G)**. Since not all individual spins are refocused, this net *XY*-magnetization is of course lesser than the initial one right after the π/2-pulse. The longer the delay time is, the more spins become dephased and a lesser number of them will be refocused; this results in a smaller in-plane magnetization. For a long enough delay time after the π/2-pulse, all spins point in all directions contained in the *XY* plane and they will do so after applying the π-pulse. Hence, no echo signal will be detected anymore. An exponential-like decay is often expected when plotting the echo

signal against the total delay time 2τ, which allows extracting the phase memory time T_m by fitting this decay to a function proportional to $\exp(-2\tau/T_m)$.

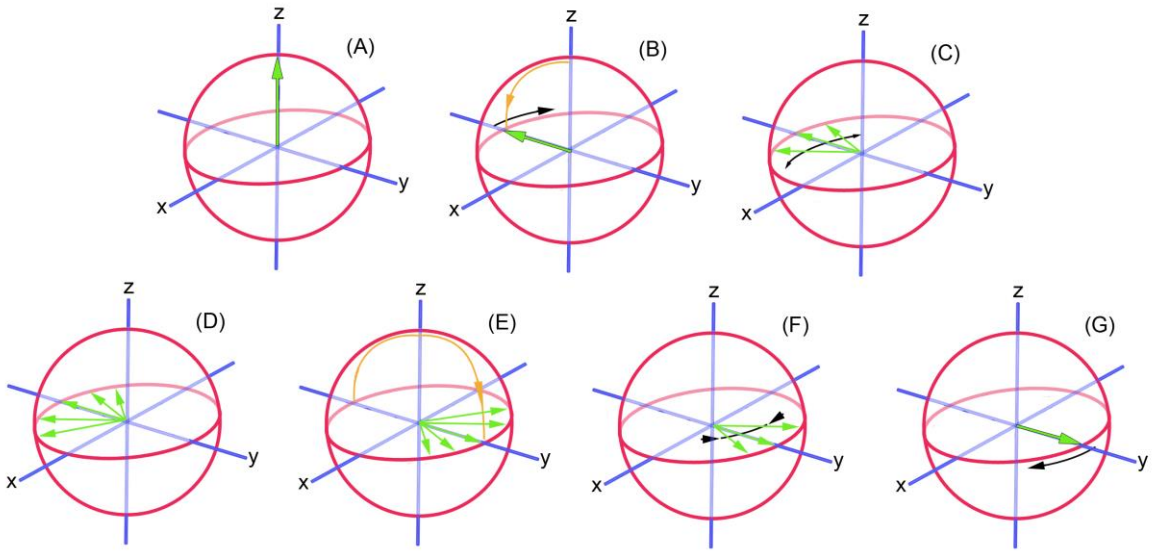

Fig. 10 Consecutive steps in the Hahn echo sequence. (A): a static magnetic field defining the *Z* axis is applied, and the magnetization vector is aligned in this direction. (B): a $\pi/2$ pulse tips the magnetization by 90 degrees. (C) and (D): spins precess at different Larmor frequencies due to magnetic field fluctuations parallel to the *Z* axis (dephasing). (E): after a delay time τ, a π pulse rotates each spin by 180 degrees. (F) and (G): some spins are refocused and, after a new delay time τ, an in-plane magnetization peak is registered in the form of echo signal. The plot of this echo against increasing delay times allows determining the phase memory time T_m of the spin qubit. Credits to Dr. Aaron Filler. CC BY-SA 3.0. https://upload.wikimedia.org/wikipedia/en/b/b6/Spin_Echo_Diagram.jpg Spin Echo Diagram.

The phase memory time T_m can initially be dependent on temperature or not depending on which are the mechanisms involved in causing the spin dephasing. That is why T_m is often determined at different temperatures to get insight on the possible mechanisms that limit this characteristic relaxation time. A temperature-independent evolution is often related to a dephasing whose main cause is the presence of magnetic nuclei or other paramagnetic entities, such as nuclear or electron spin diffusion.[196] On the other hand, a temperature dependence in T_m is most likely indicating a vibration-induced dephasing, for example, at low nuclear spin concentrations or at high enough temperature.[196]

In this case, it is useful and routine to measure T_1 inside the given temperature range to check whether it is limiting T_m or not due to the thermal activation of phonon modes.

Note that the phase memory time T_m is the result of applying a very particular pulse sequence, namely, the Hanh echo sequence. This experiment gives us information on the qubit lifetime in this specific two-pulse algorithm. Of course, the useful and interesting algorithms devised for practical purposes will involve much more sophisticated pulse sequences with more than one qubit at play; thus, the question we should really ask is whether the given qubit will be able to keep its state superposition before the algorithm of our interest ends. This initially prevents the definition of T_m from becoming universal, in the sense that a spin qubit with a long T_m will not necessarily behave with such a good performance when working as a piece of the selected algorithm. Hence, although it is true that finding strategies to increase T_m has provided us with an unprecedented and necessary insight to partially block dephasing mechanisms, there is currently a "the more the better" fever which should come to an end eventually as we are able to integrate spin qubits in complex algorithms, especially because some of the longest T_m reported so far have been measured under experimental conditions that are not necessarily the most suitable to fabricate quantum devices. A likely more useful and realistic magnitude to measure the performance of the spin qubits involved in a given algorithm could be that of quantum fidelity. Roughly speaking, one could repeat the same algorithm either on several copies of the device at once or several times on the same device, and then check how the ensemble of results compares statistically to the expected one if no dephasing is at play.

From the experimental side, the determination of the dephasing mechanism that limits T_m under given working conditions can be accomplished by analyzing the shape of the Hahn echo decay. In some cases, more than one mechanism could be involved in the dephasing and one will need to collect additional experimental data to identify them. For instance, this can consist in a series of comparative measurements where spin concentration, microwave frequency and temperature are individually varied. A possible Hahn echo curve can consist in the superposition of two exponential decays, where the echo signal I is fitted to a biexponential function with two different phase memory times $T_{m,f}$ and $T_{m,s}$:

$$I(2\tau) = I(0) + C_f \exp\left(-2\tau / T_{m,f}\right) + C_s \exp\left(-2\tau / T_{m,s}\right) \qquad \textbf{Eq. 9}$$

In **Eq. 9**, $T_{m,f}$ and $T_{m,s}$ describe two different dephasing mechanisms working at different timescales. Particularly, $T_{m,f}$ stands for the fast dephasing working at short times, while $T_{m,s}$ accounts for the slow dephasing that operates at longer times.[196] The former is often connected with spectral diffusion,[197] the presence of faster relaxing magnetic species such as solvent adducts,[192,198,199] as well as cluster formation by molecular aggregation in frozen solution.[196] This clustering can sometimes be avoided through a quick cooling of the sample, or by using glassing agents such as S_2Cl_2 or glycerol ($C_3H_8O_3$) but with the drawback of introducing some extra magnetic nuclei.[200] On the other hand, the latter is related with the actual spin-spin relaxation process of the probed molecules.

Another important shape that can adopt the Hahn echo curve can be described by a stretched exponential function, which includes the simple exponential decay proportional to $\exp(-2\tau/T_m)$ as a particular case:

$$I(2\tau) = I(0) + C \exp\left(-\left(2\tau / T_m\right)^k\right) \qquad \textbf{Eq. 10}$$

In **Eq. 10**, k is the so-called stretching parameter, whose numerical value is routinely used to identify the main dephasing mechanism at play. Among these mechanisms, one can distinguish two important ones such as physical motion of magnetic nuclei and diffusion processes. In the former case, k lies approximately between 1 and 1.5. This motion can be due to mobile parts both in the molecule and in the solvent matrix that should be replaced by more rigid alternatives to increase T_m. Methyl group vibrations, librations and especially rotations deserve special attention since the latter can take place even at very low temperature via quantum tunneling.[197,201–203] In this case, there exists a series of available options to decrease the dephasing effect derived from methyl groups: (i) fluorination, i.e., to replace ^{1}H by ^{19}F which has similar magnetic properties but its mass is 19 times greater,[136] (ii) to replace the whole -CH_3 by chlorine, which has a much smaller gyromagnetic ratio than ^{1}H thus allowing the construction of bulky ligands with fewer magnetic nuclei,[190] (iii) try to increase the steric hindrance on them whenever they cannot be substituted.[136]

Diffusion processes can be broken down into three main categories, namely, instantaneous diffusion, spectral diffusion, and spin diffusion, which offer a vast variety of Hahn echo decays. Since the excitation width of a microwave pulse can often be narrower than the spectral energy window, not all molecular spins will be necessarily excited. Hence, it is useful to distinguish between excited E and non-excited NE spins to describe these processes as nicely done elsewhere.[204] Instantaneous diffusion involves E-E interactions. Indeed, since spins interact with each other through magnetic dipole interactions, often anisotropic, the tipping of E spins will give rise to an instantaneous change in the local magnetic field that surrounds other E spins. This will add an extra phase to the latter by changing the resonance frequency, and will make their refocusing be different from the expected one.[205] As the field magnitude of a magnetic dipole decays with the third power of distance, a large enough molecular spin concentration is required for instantaneous diffusion to become the main dephasing source.[206] That is the reason why T_m measurements are usually performed at low molecular concentration, although this condition would not be useful at the stage of device design since rather close spin qubits will be required to build logical gates. At high molecular spin concentrations, a stretching parameter k similar to 1 is often expected in **Eq. 10**.

Spectral diffusion has to do with the presence of time-dependent interactions of the molecule with its nearest environment, which in turn will result in a time-dependent transition energy between the two states of the spin qubit. Both linewidth and line shape of the measured absorption spectrum will depend on the environmental fluctuation timescale -the so-called correlation time τ_c- as compared to the EPR experiment timescale t_{EPR}, and on the transition energies available in the sample. If $\tau_c << t_{EPR}$, the spectrometer is not fast enough to resolve each environmental fluctuation and just detects an average transition energy. The result is a homogeneously broadened linewidth proportional to T_m^{-1}, but narrower than that expected from the distribution in the transition energy. This fact is commonly known as motional narrowing, and the broadening is of course a consequence of the energy-time uncertainty: excited energies are blurred because of their finite lifetime. On the other hand, if $\tau_c >> t_{EPR}$, all possible static transition energies are detected, which mainly arise due to the presence of different molecular environments that shift these energies. Of course, since these energies closely lie with each other, the spectrometer will only register the envelop of the individual absorption lines. Moreover, since all

different molecular environments are not equally likely, these lines will display a different absorption intensity that will result in an inhomogeneously broadened envelope. The spectral diffusion process lies between these two limiting cases. Besides environmental fluctuations, other interactions can induce a time-dependence in the transition energy while conducting the Hahn echo sequence. Indeed, if somehow NE spins flip while E spins are being driven, for instance via spin-lattice relaxation, the local change in the surrounding magnetic field of the E spins will give rise to a time-dependent transition energy that irreversibly will contribute to shorten T_m. Spectral diffusion processes can lower k up to 0.5 if τ_c is on the order of the pulse delay.[190]

Spin diffusion also involves E-NE interactions. In particular, pairwise flip-flop events between NE magnetic nuclei in the sample induce changes in the local magnetic field that surround the E molecular spins via dipolar coupling. Thus, a nuclear spin matrix or bath with a high enough concentration is a prerequisite for this dephasing mechanism to become dominant. Whenever the crystal lattice is rigid and instantaneous diffusion does not limit T_m, nuclear spin diffusion often becomes the main dephasing source at low temperatures besides spectral diffusion. In this case, a value between 2 and 2.5 for the stretching parameter k is expected in **Eq. 10**.[190,207,208] Common nuclear flip-flop frequencies lie in the kHz range, i.e., flip-flop events operate in the millisecond timescale.[209] These flip-flop rates are dependent on the microwave pulse frequency ω_{MW} and fortunately can be suppressed under a strong enough nuclear polarization, which means $\hbar\omega >> k_B T$, where T is the working temperature. This condition can for example be attained at millikelvin temperatures and by operating at the standard X and Q bands. Moreover, nuclear spin diffusion can also be quenched inside the so-called diffusion barrier, which is approximately 3-6 Å radius around the molecular spin.[210] Inside this limit, nuclear spins experience strong dipolar couplings that shift their Larmor frequencies and flip-flop processes are inhibited. Recent experiments have shown that the approach of ^{1}H nuclei to spin qubits indeed results in a T_m enhancement for an optimal distance.[211,212] Of course, spin diffusion can also be originated by spins of a non-nuclear nature such as other paramagnetic species in the sample or molecular spins placed in different lattice environments.

Block 1.

Computational Development

3

SIMPRE

This chapter is devoted to describe the computational framework developed and employed to study the molecular systems previously presented. The first step is to describe the spin Hamiltonian that is used to calculate the relevant energy scheme along with the corresponding wave-functions. This consists of the Hamiltonian $\hat{H}_{CF}$ in **Eq. 2** complemented with the terms in **Eq. 5** -the Zeeman interaction $\hat{H}_{zee}$- and **Eq. 7** -the hyperfine coupling interaction $\hat{H}_{hy}$- for $A_{\parallel} = A_3$ and $A_{\perp} = A_1 = A_2$, see chapter 2. The quadrupolar interaction term $\hat{H}_{qu} = P\hat{I}_z^2$, where P is the associated interaction parameter and $\hat{I}_z^2$ is the squared z-component of the Ln^{3+} ion nuclear spin operator, can also be added to $\hat{H}_{CF}$. Thus, our working full spin Hamiltonian $\hat{H}$ is expressed as:

$$\hat{H} = \sum_{k=2,4,6} \sum_{q=-k}^{+k} B_k^q \hat{O}_k^q + \mu_B \left(g_1 B_x \hat{J}_x + g_2 B_y \hat{J}_y + g_3 B_z \hat{J}_z \right) + \\ + A_{\perp} \left(\hat{J}_x \hat{I}_x + \hat{J}_y \hat{I}_y \right) + A_{\parallel} \hat{J}_z \hat{I}_z + P\hat{I}_z^2 \qquad \textbf{Eq. 11}$$

The magnetic field components B_x, B_y, B_z are parameterized in terms of spherical coordinates as $B_x = B\sin\theta\cos\varphi$, $B_y = B\sin\theta\sin\varphi$, $B_z = B\cos\theta$, where B is the field magnitude and $0 \leq \theta \leq \pi$, $0 \leq \varphi \leq 2\pi$ are the zenithal and azimuthal angles, resp. Note that **Eq. 11** will be commonly employed in the case of Ln^{3+}-based single-ion coordination compounds, but of course can also be applied for $J = S = 1/2$ systems in which all CFPs B_k^q vanish. In the general case, a set of

input parameters is firstly required to diagonalize the spin Hamiltonian $\hat{H}$. As previously introduced, these are the Landé factors g_1, g_2, g_3, the axial and perpendicular hyperfine coupling parameters $A_{\parallel}$ and $A_{\perp}$, and the quadrupolar interaction parameter *P*. Regarding the CFPs B_k^q, they can be either externally introduced in the form of input or calculated via an effective model as we will explain below. Once all these parameters are introduced, the (2*J*+1)(2*I*+1)-sized Hamiltonian matrix -built in the $|m_J, m_I\rangle$ ket basis set associated to the ground electron and nuclear spin quantum numbers *J* and *I* of the given Ln^{3+} ion- is subsequently diagonalized.

The diagonalization of **Eq. 11** is conducted by means of a home-made computational package known as SIMPRE -Single-Ion Magnet PREdiction-, which is written in the well-established Fortran programming language. The application of the first versions SIMPRE1.0 and SIMPRE1.1,[213,214] which are previous to the present work and only incorporate the Hamiltonian $\hat{H}_{CF}$ in **Eq. 2**, was intended to determine energies and wave-functions of the ground 2*J*+1 states, as well as to calculate magnetic susceptibility and magnetization curves of Ln^{3+}-based SIMs.[215] When required, these versions have also been accordingly patched to proceed the other way around, namely, to determine the CFPs as free parameters by fitting experimental data such as spectroscopically-determined energies or the aforementioned magnetic properties.[215,216]

The subsequent version SIMPRE1.2, which has been developed and published in this doctorate,[217] includes the extra terms present in **Eq. 11** respect to $\hat{H}_{CF}$. The addition of these hyperfine $\hat{H}_{hy}$ and quadrupolar $\hat{H}_{qu}$ interactions to $\hat{H}_{CF}$ provides now (2*J*+1)(2*I*+1) energies and wave-functions, shown along with the expectation values $\left\{\left\langle \hat{J}_\alpha \right\rangle\right\}_{\alpha=x,y,z}$ and $\left\{\left\langle \hat{I}_\alpha \right\rangle\right\}_{\alpha=x,y,z}$ of the metal ion electron and nuclear spin operators as an output. Of course, the first two versions can be recovered just by setting $B = 0$, $A_{\perp} = 0$, $A_{\parallel} = 0$, $P = 0$. In this case, one will obtain 2*J*+1 energy levels with a degeneracy equal to 2*I*+1. The magnetic field can be set in any direction, but its magnitude must be moderate (0 – 1 T) as the Zeeman interaction $\hat{H}_{zee}$ in **Eq. 11** is used under the weak-field approximation without non-linear dependencies with *B*. Moreover, this version also incorporates a model devoted to provide a theoretical estimate of the phase memory time T_m^n

produced by a nuclear spin bath on a qubit defined in a given single-ion magnetic coordination compound. This model will be applied to some particular systems that will be analyzed in chapters 5 and 6.

This last version has been further improved by incorporating new features and subroutines devoted to (i) estimate the effect of other sources of spin dephasing in molecular qubits and (ii) simulate the vibration-mediated magnetic relaxation in Ln^{3+}-based SIMs. These latest updates, thoroughly described in chapters 4 and 5, will be published in the form of a new version named as SIMPRE 2.0 whose manuscript is currently under preparation and also belongs to this dissertation. In **Fig. 11**, we schematically describe the data flow with a color code selected to identify the new subroutines, inputs and outputs that have been incorporated in each version.

The program starts by reading the input data that has been previously set in simpre.dat and simpre.par files. At this point, prior to diagonalize the spin Hamiltonian in **Eq. 11**, the CFPs can be either read externally by writing them in the input file simpre.cfp or calculated in the subroutines CFP and ROTA such as we will explain below. In the chapters 5 and 6 we will choose the first option as the CFPs therein employed were experimentally determined via cw-EPR spectroscopy. The next step is to build the matrix representations of the hyperfine $\hat{H}_{hy}$ and quadrupolar $\hat{H}_{qu}$ interactions, and this is conducted in the subroutines HYPA, HYPE and QUAD. The last included term is the Zeeman interaction in the subroutine ENE, which subsequently diagonalizes **Eq. 11** and then prints energies and wave-functions in the output file simpre.out along with the expectation values $\left\{\left\langle \hat{J}_\alpha \right\rangle\right\}_{\alpha=x,y,z}$ and $\left\{\left\langle \hat{I}_\alpha \right\rangle\right\}_{\alpha=x,y,z}$. In simpre.par, there exists the option to ask for printing energies and wave-functions calculated at different magnetic field magnitudes B and orientations (θ,φ). In that case, these energies against B and (θ,φ) can be printed column-wise in simpre.ene.out in a much simpler format ready for plotting them.

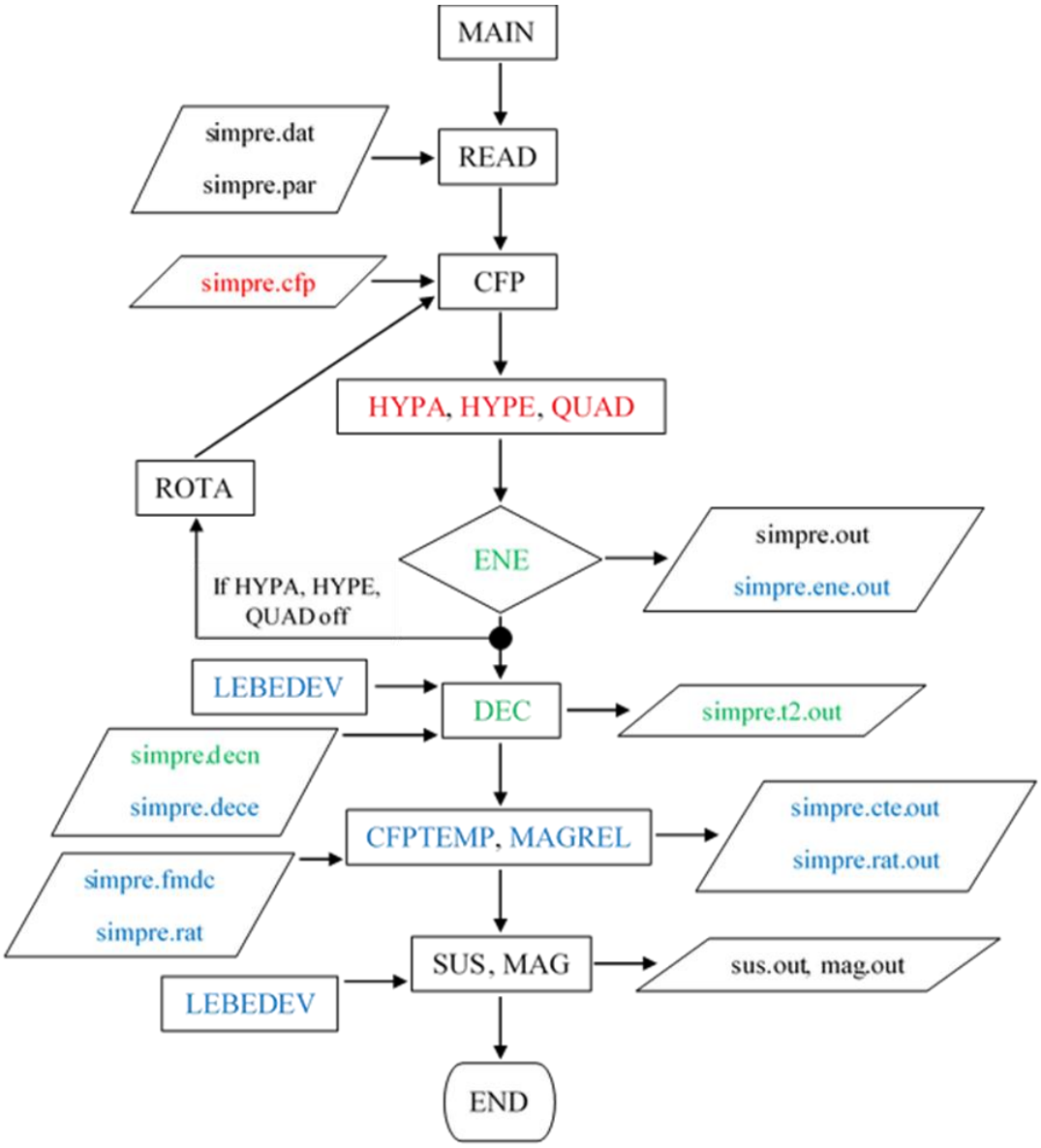

Fig. 11 Flow chart of SIMPRE2.0 version. Subroutine names are written in capital letters. Both input and output names start with the word simpre. Outputs are named with the ending word out. The color code identify the several updates incorporated in each new version. Black: 1.0 and 1.1. Red: 1.2. Green: 1.2 and 2.0. Blue: 2.0. The features in green were introduced for the first time in SIMPRE1.2, and then they were modified and expanded in SIMPRE2.0.

The next subroutines DEC, CFPTEMP, MAGREL, SUS and MAG are optional and thus the preparation of their input files can be avoided. DEC is devoted to estimate the qubit phase memory times T_m^n and T_m^e derived from both

nuclear and electron spin baths resp., see chapter 5. Note that this subroutine can also be applied to powder samples and frozen solutions where molecules are distributed in all possible spatial orientations. Under this situation, the determination of T_m^n and T_m^e may require a mathematical integration over all these orientations, which is conducted by means of the so-called Lebedev rules in the LEBEDEV subroutine as explained in chapter 5. CFPTEMP and MAGREL are in charge of simulating the vibration-induced magnetic relaxation in Ln^{3+}-based SIMs and will be employed in chapter 4, while SUS and MAG calculate magnetic susceptibility and magnetization curves at different temperatures and field magnitudes. Magnetizations are calculated for powder samples and that is why the Lebedev rules need also to be employed in these subroutines.

The radial effective charge model

As mentioned above, SIMPRE can calculate the CFPs B_k^q by means of an effective model known as Radial Effective Charge (REC).[216] This was implemented in the earliest version SIMPRE1.0 prior to this dissertation and hereafter we just reproduce the basis of the model. Indeed, in the case of Ln^{3+} ions, each B_k^q can be rewritten as $a_k A_k^q \langle r^k \rangle$ according to the Stevens formalism,[218] where a_k are the α, β, γ Stevens coefficients, A_k^q are the Stevens parameters, and $\langle r^k \rangle$ is the expected k^{th}-power of the radial distance r in the 4f orbitals. In **Eq. 11**, each $\langle r^k \rangle$ is corrected as $\langle r^k \rangle(1-\sigma_k)$ with the Sternheimer shielding parameters σ_k.[219] Each a_k, $\langle r^k \rangle$, σ_k depends on the Ln^{3+} ion and is tabulated in a subroutine named as LANTA as a function of k. The REC model considers each Ln^{3+}-coordinating atom i (σ-type bond) as an effective point charge with a magnitude $Z_i > 0$ at a distance R_i from the Ln^{3+} ion, and does not take into account any other atom in the ligands. Note that $Z_i > 0$ and R_i do not necessarily have to coincide with formal charges and experimental coordination-bond distances r_i. The Stevens parameters A_k^q are determined by the following relations:[214,220]

$$A_k^0 = \frac{4\pi}{2k+1}\sum_{i=1}^{N}\frac{Z_i e^2 Z_{k0}^c(\theta_i,\varphi_i)}{R_i^{k+1}}\,p_{k0} \qquad \textbf{Eq. 12}$$

$$A_k^q = \frac{4\pi}{2k+1}\sum_{i=1}^{N}\frac{Z_i e^2 Z_{kq}^c(\theta_i,\varphi_i)}{R_i^{k+1}}\,p_{kq} \quad \text{for } q>0 \qquad \textbf{Eq. 13}$$

$$A_k^q = \frac{4\pi}{2k+1}\sum_{i=1}^{N}\frac{Z_i e^2 Z_{k|q|}^s(\theta_i,\varphi_i)}{R_i^{k+1}}\,p_{k|q|} \quad \text{for } q<0 \qquad \textbf{Eq. 14}$$

In **Eq. 12**, **Eq. 13**, **Eq. 14**, N is the number of Ln^{3+}-coordinating atoms, Z_i is the effective charge magnitude, e is the electron charge, R_i , θ_i, φ_i are the spherical coordinates of the effective charge i, p_{k0}, p_{kq}, $p_{k|q|}$ are the prefactors of the spherical harmonics Y_k^q, and Z_{k0}^c, Z_{kq}^c, $Z_{k|q|}^s$ are the tesseral harmonics which are linear combinations of Y_k^q as follows:[221]

$$Z_{kq}^c = \frac{1}{\sqrt{2}}\left(Y_k^{-q} + (-1)^q Y_k^q\right) \quad Z_{k|q|}^s = \frac{i}{\sqrt{2}}\left(Y_k^{-q} - (-1)^q Y_k^q\right) \qquad \textbf{Eq. 15}$$

In simpre.cfp, one can also introduce the CFPs B_{kq} in Wybourne notation. In this case, all CFPs but B_{k0} (k = 2, 4, 6) are complex with real ReB_{kq} and imaginary ImB_{kq} parts. Once these parts are introduced, SIMPRE will convert them into $A_k^q\langle r^k\rangle$ by using conversion factors λ_{kq} -tabulated in the subroutine ENE- as:

$$A_k^0\langle r^k\rangle = B_{k0}/\lambda_{k0}$$
$$A_k^q\langle r^k\rangle = \mathrm{Re}\,B_{kq}/\lambda_{kq} \quad (q>0),\; A_k^q\langle r^k\rangle = \mathrm{Im}\,B_{k|q|}/\lambda_{k|q|} \quad (q<0) \qquad \textbf{Eq. 16}$$

The non-negligible CFPs are determined by the symmetry of the molecule. When using SIMPRE, it is common to determine the point group symmetry by only considering the Ln^{3+}-ion coordination sphere, i.e., the set of effective point charges. Importantly, when dealing with Gd^{3+}-based coordination compounds, one is forced to externally introduce the CFPs in B_k^q notation after determining them by independent methods since the Stevens coefficients for this ion are identically zero. Otherwise, SIMPRE will always provide $2J+1$ degenerate states while experimentally a small ZFS of the order of 1 K is still observed in Gd^{3+}-based SIMs due to a small yet significant magnetic anisotropy.

The diagonalization of $\hat{H}$ in **Eq. 11** produces a set of $(2J+1)(2I+1)$ wave-functions as a linear combination of the ket basis set $\{|m_J, m_I\rangle\}$. As a matter of fact, the numerical values of the CFPs calculated by SIMPRE change after a rotation of the effective point charge coordinates around the Ln^{3+} ion, and this will produce different expressions in each wave-function. Of course, all observables (expectation values) derived from $\hat{H}$ will remain unaltered. For the sake of simplicity and meaningful comparisons, SIMPRE contains the subroutine ROTA which can be used to determine the charge orientation that results in the simplest expression of the ground state wave-function, i.e., the one with the smallest number of significant $|m_J, m_I\rangle$ coefficients. In the latest version of SIMPRE, this option is only available if all the parameters $A_{\parallel}$, $A_{\perp}$, P, B are set to be zero. At each step and after the diagonalization of $\hat{H}$ by ENE, ROTA performs a rotation and then calls the subroutine CFP to re-calculate the CFPs. Subsequently, ENE diagonalizes again $\hat{H}$ to determine the new wave-function expressions. All this iterative procedure can be skipped if the relevant orientation is known beforehand, for example, by using an external program to previously orient the molecule.

As a first approximation to calculate the CFPs, one can use in simpre.dat the experimental positions of the coordinating atoms after setting the coordinate origin at the Ln^{3+}-ion position. Thus, one only needs to decide the value of each charge magnitude Z_i. At this point, one has to find a balance between overparameterization (up to one different Z_i per coordinating atom) and a simple description of the system. In the case of homoleptic systems such as the examples studied in the next chapters, all donor atoms correspond to the same chemical element and an adequate description is often obtained by setting all Z_i

to be the same value Z. In some cases, this ansatz will be too restrictive to properly recover for example covalence effects if important, and may lead to poor results as compared with experimental data. To fix this roadblock, it is still possible to introduce a second parameter that will significantly improve the description of the system properties. This parameter, known as effective radial displacement D_r, see **Fig. 12**, is used to radially get each donor atom closer to the Ln^{3+} ion. Thus, each effective point charge is now placed at a distance $R_i = r_i - D_r$ from the metal ion smaller than r_i. Of course, one could use a different radial displacement for each donor atom but once again, in order to avoid overparameterization, the same collective displacement will be enough in a large majority of cases. The predictive power of the REC model is due to the possibility of associating to each type of ligand a reduced set of effective parameters, namely, Z and D_r. The specific values of these parameters are particular and characterize a given ligand. Therefore, they can be used to predict the energy scheme and magnetic properties when replacing the original Ln^{3+} ion by others.[215,222–224]

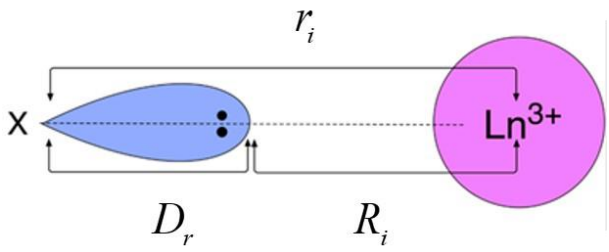

Fig. 12 Lone electronic pair of a donor atom X oriented towards the nucleus of a trivalent lanthanide ion Ln^{3+} (σ-type metal-ligand bond). The effective point charge is located between Ln^{3+} and X at a distance $R_i = r_i - D_r$ from Ln^{3+}, where r_i is the experimental Ln^{3+}-X distance and D_r is the effective radial displacement.

Both Z and D_r can also be used as free parameters to fit experimental data such as magnetic susceptibility, magnetization and/or low-lying energies. In order to obtain these REC parameters for the target compound, we need to vary both of them until obtaining a satisfactory match of a given property P_{ref}. This property can be determined either experimentally as mentioned above or e.g. via first-principles calculations. In the case of Ln^{3+}-based single-ion coordination compounds, a fit of the ground-J multiplet energy states will

always be the desired option. Thus, Z and D_r are scanned in order to achieve the minimum deviation between P_{ref} and the same property P_{fit} calculated by SIMPRE. This deviation is defined in the form of relative error E as in **Eq. 17**, where n is the number of values to fit of the relevant property.

$$E = \frac{1}{n}\sum_{i=1}^{n}\frac{\left[P_{fit,i} - P_{ref,i}\right]^2}{\left[P_{ref,i}\right]^2} \qquad \textbf{Eq. 17}$$

As a starting point for the fitting, or if the REC model is used as a predictive tool when working in absence of experimental data,[224] it is possible to provide a first estimate of D_r and Z in homoleptic compounds by using the following semi-empirical approximate expressions that depend on well-known chemical concepts:[224]

$$D_r \approx \left(\frac{N_L}{V_M}\right)\frac{1}{E_M\left(E_L - E_M\right)}\ , \quad Z = f_{X,CN} / D_r \qquad \textbf{Eq. 18}$$

In **Eq. 18**, N_L is the coordination number of the Ln^{3+} ion, V_M is the valence of Ln^{3+}, i.e. $V_M = 3$, and E_M, E_L are the Pauling electronegativities of Ln and the donor atoms, resp. The effective charge magnitude Z can then be estimated by using the relationship on the right, where $f_{X,CN}$ is a factor that depends on the Ln^{3+} coordination number CN and on the coordinating atoms X.[224] The use of this expression to determine Z is limited since for a given system it requires to know $f_{X,CN}$ in advance. For that, one first has to know the REC parameters of a large enough set of coordination compounds with different Ln^{3+} ion but with the same or similar ligands with the same coordination number.[224] Nevertheless, the values obtained with these two equations are expected to be a very useful tool to address the widespread need for an inexpensive estimation of a starting parameter set in more sophisticated determinations, as well as a route for an inexpensive qualitative prediction of the magnetic properties of f-block SIMs.

All in all, the REC model predictions have been extensively compared against first-principles calculations as well as experimental data,[215,222,225,226] and

have proven to be a competitive tool in terms of efficiency and accuracy. For instance, the comparison between the energies of the ground *J* multiplet obtained with the full Hamiltonian (see Chapter 2) and the ones derived by using $\hat{H}_{CF}$ under the REC model in a Er^{3+}-based SIM showed differences of less than 2 cm^{-1} in each state.[214] These slight differences, that are accompanied by a too high computational cost when using the full Hamiltonian, justify the assumptions that have been taken in the development of the SIMPRE package, which is compatible with its main goal: the prediction of new single-ion molecular derivatives as simple, and computationally inexpensive, as possible. Hence, the main advantage of the REC model is that it allows estimating the CFPs by using the chemical structure of the coordination compound in an inexpensive way. In other words, one can keep the simplicity of the electrostatic model and at the same time reproduce experimental data with a reasonable accuracy.

An illustrative example

As an illustrative purpose, herein we will show an example of a standard CFPs and energies calculation in a $^{167}Er^{3+}$-based magnetic coordination compound once radial displacements D_r and effective charges Z_i are known.[217] The selected molecular compound, $[Er(C_4H_4O_5)_3]^{3-}$ (in short ErODA), consists in a single $^{167}Er^{3+}$ ion surrounded by a ligand environment with nine coordinating oxygen atoms as depicted in **Fig. 13**.

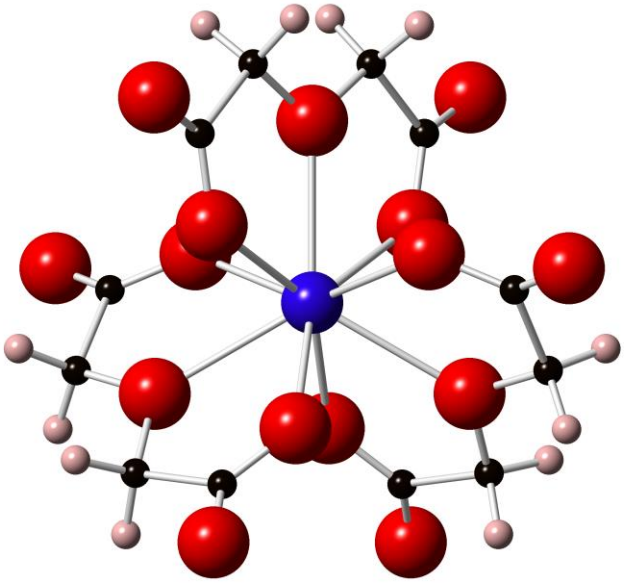

Fig. 13 Ball-and-stick representation of ErODA molecular coordination compound. Blue: Erbium, Red: Oxygen, Black: Carbon, Pale pink: Hydrogen.

From the X-ray experimental geometry of ErODA, the nine coordinating oxygen atoms were firstly directed towards the $^{167}Er^{3+}$ ion with the same radial displacement D_r = 1.100 Å and charge magnitude Z_i = 0.08518 as determined elsewhere.[215] The spherical coordinates (R_i, θ_i, φ_i) of these oxygen atoms after correcting their experimental distance r_i respect to the $^{167}Er^{3+}$ ion are shown in **Table. 2**. After introducing these data in simpre.dat, the most significant CFPs calculated as described above can be found in **Table. 3**.

Table. 2 Spherical coordinates (R_i, θ_i, φ_i) with corrected radial distances R_i of the nine Er^{3+}-coordinating oxygen atoms employed to calculate the CFPs in ErODA compound.

R_i (Å)	θ_i (degrees)	φ_i (degrees)
1.338	90.00	330.00
1.338	90.00	210.00
1.338	90.00	90.00
1.239	46.25	276.72
1.239	133.75	263.28
1.239	133.75	23.28
1.239	46.25	156.72
1.239	46.25	36.72
1.239	133.75	143.28

Table. 3 CFPs calculated by means of the REC model for ErODA compound with the spherical coordinates shown in the above table and a charge Z_i = 0.08518. The remaining CFPs are below 10^{-5} and 10^{-7} cm^{-1} resp.

k	q	$A_k^q \langle r^k \rangle$ (cm^{-1})	B_k^q (cm^{-1})
2	0	29.70522402	0.07544184
4	0	-109.24821295	-0.00485063
4	3	1185.03963107	0.05261581
6	0	-33.04120220	-0.00006839
6	3	465.78993538	0.00096415
6	6	-506.46459015	-0.00104835

The ground Er^{3+} level is $^4I_{15/2}$ which give rise to $2J+1 = 16$ spin-orbit coupled spin states. On the other hand, the nuclear spin quantum number of the ^{167}Er isotope is $I = 7/2$ with $2I+1 = 8$ nuclear states. Thus, the combination of the quantum numbers $J = 15/2$ and $I = 7/2$ results in $(2J+1)(2I+1) = 128$ electronuclear states. Herein, for demonstration purposes we will focus only on

the ground and degenerate spin doublet associated to the Kramers-like $^4I_{15/2}$ level. The coupling with the I = 7/2 nuclear spin of ^{167}Er produces a low-lying energy scheme of 16 electronuclear states as depicted in **Fig. 14**, whose distribution changes as the several interactions $A_{\parallel}$, $A_{\perp}$, P are progressively turned on respect to $\hat{H}_{CF}$. To diagonalize **Eq. 11**, we have used the default Sternheimer shielding parameters for the Er^{3+} ion as well as typical values $A_{\parallel}$ =0.0052 cm^{-1}, $A_{\perp}$ =0.0314 cm^{-1}, P =0.0030 cm^{-1} for Er^{3+}-based coordination compounds.[227] Note that the action of $A_{\parallel}$ on $\hat{H}_{CF}$ is to split the 16 lowest states into 8 degenerate spin doublets equally-spaced in energy. This degeneracy is removed when the perpendicular interaction $A_{\perp}$ is subsequently added. Interestingly, the noticeable effect of the quadrupolar interaction is to alter the spacing between consecutive spin doublets while approximately keeping the same energy gaps.

Note that the first versions 1.0 and 1.1 cannot simulate any split in the ground spin doublet of ErODA as hyperfine and quadrupolar interactions are not implemented. Instead, the latest versions 1.2 and 2.0 devised and developed in this work can now reproduce energy schemes with more fine details. Importantly, this is a crucial feature that will be employed in the chapters 5 and 6 where the qubit states are precisely the result of the coupling between the electron and nuclear spins of the metal ion. Moreover, the energy differences between electronuclear states often lie in the range of X-band frequencies for moderate magnetic fields. Hence, to properly interpret the resonances of cw-EPR spectra one may need to include the hyperfine and quadrupolar interactions in the analysis.

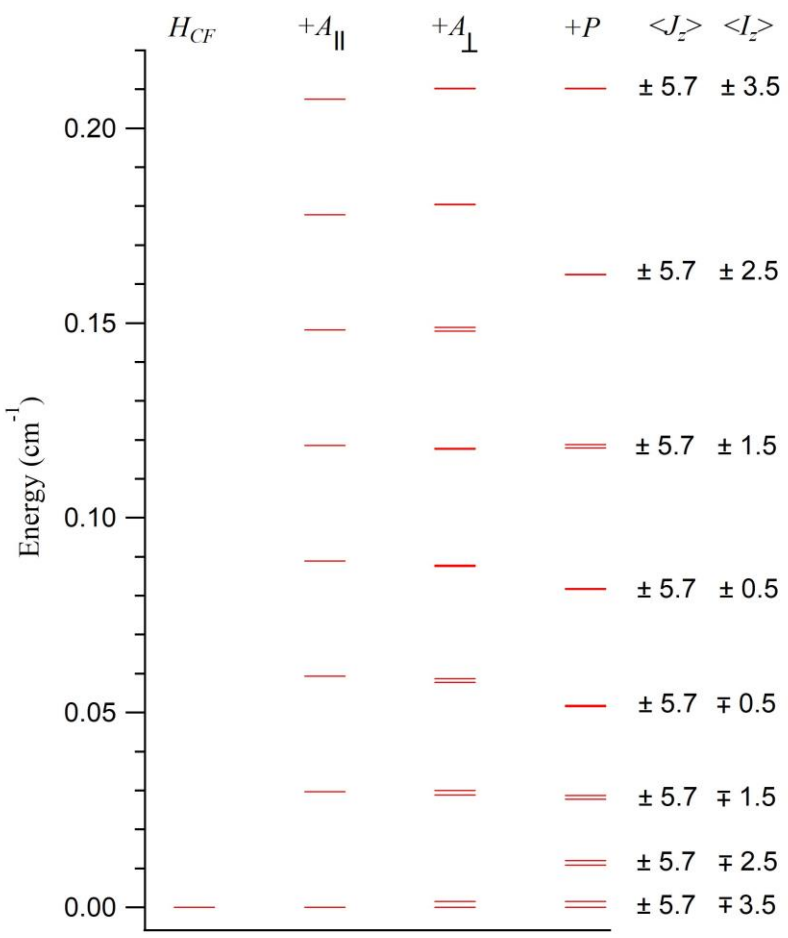

Fig. 14 Energy scheme of the lowest sixteen spin states in the ErODA molecular compound obtained by diagonalizing **Eq. 11** with a zero magnetic field. The effect of the different terms in the spin Hamiltonian is shown from left to right by progressively switching on the parallel hyperfine coupling $A_{\|}$, the perpendicular hyperfine coupling $A_{\perp}$, and the quadrupolar *P* terms. $\langle J_z \rangle$ and $\langle I_z \rangle$ are the expectation values of $\hat{J}_z$ and $\hat{I}_z$.

Block 2.

Theoretical Development and Applications

4

Spin-vibration Coupling

One of the main topics of this dissertation is the understanding of quantum decoherence in molecular spin qubits to minimize its negative effects on quantum information. Decoherence is the collapse of quantum information due to uncontrolled interactions of qubits with their environment. It is of course a major roadblock to overcome in the path to quantum devices, as it creates errors that are challenging to correct while conducting quantum algorithms. We are going to tackle this problem from theory, by developing and applying methods to estimate parameters that describe the relationship between geometric structure and decoherence thus facilitating the design of decoherence-protected spin-based molecular systems.

In this chapter, we will study spin relaxation mediated by lattice and molecular vibrations, which are assumed to be in thermal equilibrium with the sample surrounding (the heat bath). Vibrations are spatial degrees of freedom that can affect the orbital angular momentum and, hence, the molecular spin itself via spin-orbit coupling. Indeed, the vibrations present at a certain temperature, in the form of quanta known as phonons, lead to oscillating electric fields that modulate the crystal field splitting of the paramagnetic species. This modulation is translated into an oscillating magnetic field by spin-orbit coupling (SOC), which can accordingly induce spin transitions.[228] Of course, the selected metal ion determines the SOC magnitude, which in turn will strongly influence spin-lattice relaxation. In particular, a rise in the SOC was found to correlate with a decrease in the spin-lattice relaxation times,[229,230] but not necessarily with the spin-spin relaxation times at low temperature.[231] Hence, low SOC values are favorable to minimize vibration-mediated spin relaxation, and that is why S = 1/2 first-row transition metal ions (V^{4+}, Mn^{2+}, Cu^{2+}), which minimize spin-spin

relaxation compared to $S > 1/2$ systems,[231] are often preferred as potential molecular spin qubits.

As previously discussed, one of the main long-term goals is the achievement of devices able to implement quantum technologies for information storage and processing. In this dissertation, the physical platforms which we are focusing on are spins in molecules but note that the problem of vibrations is general for solid-state devices. Since lattice vibrations couple with spins, we know that spin-lattice relaxation will limit the timescale of quantum information survival as introduced in chapter 2. In other words, T_1 is an upper bound for T_m but, depending on the SOC magnitude, T_1 could be even similar to T_m. Note that this is equally relevant for molecular nanomagnets, where spin relaxation dynamics is determined by the magnetic relaxation time τ. While it is true that vibration-induced relaxation can be minimized by operating at low enough temperature, the current attention is rather being drawn in the opposite direction as practical devices often work at room temperature. Nevertheless, spin-lattice relaxation becomes more important as temperature is raised. In the particular case of molecular spin qubits, this means that T_1 will eventually run over T_m thus preventing quantum information from survival for long enough. Note that this can also happen at low temperature even if ligands are nuclear-spin free.[232] All in all, the key question is clear: how to design molecules with little vibrational spin relaxation at high temperature? This is what motivates the current interest on understanding SOC in magnetic molecules, since short T_1, T_m, τ times still hamper the use of these systems at more practical experimental conditions.

This is still an open problem as we lack a set of well-established design principles aimed to block vibrational relaxation in molecules, where key details may differ depending on each particular chemical structure. Moreover, recent experimental works have evidenced important failures in models that have historically been used to describe lattice vibrations.[184] For instance, the Debye model, known by succeeding at reproducing heat capacities in ionic crystals at low temperature, assumes a quadratic dependence $\rho \sim \omega^2$ of the phonon density of states ρ with the harmonic vibration frequency ω. It is reasonable to expect that such a simple dependence cannot incorporate all vibrational richness of molecular crystals, which fails even in the much simpler ionic crystals at reproducing the T_1 thermal evolution unless the experimental phonon spectrum is used.[191] Indeed, while real phonon spectra do follow the Debye-like quadratic dependence at low frequencies, they mostly deviate from this behavior at higher

energies.[233] Since the target working regime is the high-temperature range, we thus need to drop any guess on the phonon spectrum and, from the theoretical point of view, this means that we have to estimate a first-principles spectrum, i.e., to build a force matrix -often under the harmonic approximation- to diagonalize it and get a finite set of vibrational frequencies, reduced masses and displacement vectors characterizing the so-called vibration normal modes. This calculation constitutes one of the main computational bottlenecks of the methodology that will be presented below. In fact, current models devoted to estimate spin relaxation times still contain additional restrictions -even unrealistic- that limit their performance. These are the following, (i) the assumption whereby each mode couples to the spin with the same strength,[139] and (ii) the presence of semi-empirical parameters such as the Debye temperature and crystal sound velocities.[184] These are roughly estimated or, because of this, more often employed as free parameters to fit experimental data. Moreover, the determined value of the Debye temperature is quite dependent on the experimental technique, which makes it be somewhat meaningless.[184,234] Regarding (i), future methods will have to address each mode individually and be able to calculate its specific coupling strength. All in all, in order to gain in predictive and rationalization power, all these roadblocks should first be overcome within fully *ab initio* approaches.

As a first step to approach this open problem, herein we will focus on developing an *ab initio* methodology to determine the thermal modulation exerted by vibrations on magnetic anisotropy parameters (e.g., CFPs) and hence spin energies. This was pioneered in 1969 by K. N. Shrivastava in magnetically-doped ionic crystals such as Eu^{2+}-doped CaF_2 with phonons modeled according to the Debye model.[235,236] Under his approach, the spin Hamiltonian parameters are expressed as a sum of a static Coulombian term -whose energetic contribution is often determined by hydrostatic pressure measurements- and a dynamic phonon term responsible for changing the magnetic energies. They both arise from electrostatic and spin-phonon interactions, and are dependent on temperature via lattice thermal expansion and Bose-Einstein statistics, resp. Once the thermal evolution of a given parameter is measured, the phonon contribution can be determined just by subtracting the static counterpart. Then, the theoretical expression of this phonon contribution is used to fit its experimental thermal evolution by employing the spin-phonon coupling strength, including possibly the Debye temperature, as a free parameter. This

procedure has produced satisfactory results for instance when modeling the axial zero-field splitting parameter in Cr^{3+}-doped alums, and the electron Landé factor in Mn^{2+}-doped HgSe.[237,238]

In a nutshell, the thermal evolution $B(T)$ of a given magnetic anisotropy parameter in magnetically-doped ionic crystals has been so far written in terms of three additive terms:

$$B(T) = B_{stat}(T) + B_{ac}(T) + B_{op}(T) \qquad \textbf{Eq. 19}$$

These three terms in **Eq. 19** are the static $B_{stat}(T)$ and the dynamic acoustic $B_{ac}(T)$ and optical $B_{op}(T)$ phonon contributions. Acoustic phonons are lattice vibrations that have long wavelengths compared to interatomic distances. On the contrary, optical phonons include all local molecular vibration modes and are higher in energy (typically $10 - 10^3$ cm^{-1}), but yet there also exist many low-energy modes. Thus, these optical phonons can also take the place of acoustic phonons in the Orbach and Raman processes. Indeed, for instance, localized V-S vibrations were reported to contribute in two-phonon relaxation processes in an octahedral V(IV)-dithiolene-based molecule.[239] Nevertheless, optical phonons usually occur at discrete frequencies so that their participation in these mechanisms will depend on the energy coincidence between the spin energy gaps and the phonon frequency (see section 4.3). This may not be the case of librational -small oscillatory rotational motions of a molecule or a side group around the equilibrium position- and similar motions as they often lie close enough in energy to produce a quasi-continuum able to drive most of spin transitions.

The estimation of $B_{stat}(T)$ can be achieved provided one knows the relevant thermal expansion coefficients or by means of semi-empirical point-charge models.[184] On the other hand, the first step to find estimates for the magnitudes B_{ac} and B_{op} has been to assume that they depend on the normal coordinates Q_k of the several normal modes. Then, after implementing a Taylor expansion up to second order in Q_k, it is possible to obtain B_{ac} and B_{op} expressions as a function proportional to the expectation values $\sum_k \langle Q_k \rangle$, $\sum_k \langle Q_k^2 \rangle$. Since these

values are calculated by assuming that phonons are harmonic, $\sum_k \langle Q_k \rangle$ vanishes and each $\langle Q_k^2 \rangle$ is known. Note that this scheme is recovered by the method that we will present below. In the case of B_{op}, optical phonons lie quite close in energy in the vast majority of the studied ionic crystals. Thus, all modes are replaced by a single effective mode with frequency ω_{eff}. As a last step, the sum in B_{ac} is replaced by an integral over the phonon frequency since at not very high temperatures phonons are close enough to form an energy continuum. All these considerations result in the following expressions for $B_{ac}(T)$ and $B_{op}(T)$:

$$B_{ac}(T) = K_{ac} C_{ac} \left(\frac{1}{8} \theta_D^4 + T^4 \int_0^{\theta_D/T} \frac{x^3}{e^x - 1} dx \right) \qquad \textbf{Eq. 20}$$

$$C_{ac} = \frac{\hbar R^2}{2\pi^2 \rho} \left(\frac{2}{3} v_l^{-5} + v_t^{-5} \right) \left(\frac{k_B}{\hbar} \right)^4 \qquad \textbf{Eq. 21}$$

$$B_{op}(T) = K_{op} \frac{\hbar}{2M\omega_{eff}} \coth\left(\frac{\hbar \omega_{eff}}{2k_B T} \right) \qquad \textbf{Eq. 22}$$

In these equations, K_{ac} and K_{op} are the acoustic and optical spin-phonon coupling parameters, θ_D is the Debye temperature -which determines the phonon energy of the minimum wavelength mode in a crystal-, R is an average distance between nearest-neighbor ions, ρ is the crystal density, v_l and v_t are the longitudinal and transverse crystal sound velocities, and M is the crystal mass. As mentioned, the corrections to the Debye-like phonon spectrum, which has been used to derive **Eq. 20** and **Eq. 22**, only become important at high enough temperatures. Nevertheless, this is nowadays the target regime of interest and hence the exact density of phonon states of each particular crystal must now replace the Debye ω^2 value. In fact, this was already stated, somewhat prophetically as we will show below, by Shrivastava in 1969:[235]

"Theoretically probing the high temperature regime would only be possible whenever non-Debye calculations were available, which should be point-to-point calculations."

Since at high temperature higher energy modes become active, it is quite likely that spin relaxation will be mainly promoted by molecular vibrations, which can compete with the Raman mechanism and even dominate the T_1 thermal dependence.[230,240,241] This is what was found in a thorough and systematic study of a series of Cu^{2+} molecular coordination compounds in 2005.[242] Most importantly, therein it was demonstrated one of the main design principles to bear in mind when it comes to lengthen T_1 and ultimately T_m, namely, the key role of molecular rigidity. Indeed, the shortening in T_1 was satisfactorily correlated with a decrease in the ligand rigidity by using apparently more flexible substituents. Since the energy released during the spin relaxation is taken up by the lattice in the form of phonons, a more flexible lattice enhances the probability of spin-lattice relaxation by providing a higher density of available low-energy modes. Thus, trends of increasing spin-lattice relaxation times often correlate with decreasing both flexibility of coordination geometry and mobility in the vicinity of the paramagnetic center as reported in the literature. This important strategy regarding rigidity -but still limited to a small set of systems- is also experimentally being used nowadays to synthesize molecules with a slower spin relaxation.[184,239,243,244]

Our original intention is to develop a systematic methodology suitable for any molecular system, able both to avoid serendipity at the lab stage and to estimate spin-vibration couplings from first-principles. In terms of quantitative calculations, we intend to answer questions such as the following: What does rigidity mean and how it affects spin-vibration coupling and relaxation time? Which are the vibration modes that promote spin relaxation? With it, we expect to aid at guiding experimental synthetic efforts to re-design and optimize the given molecule thus suppressing the detrimental modes. Hopefully, this framework could be used to establish a set of general design principles for the rational design of robust systems against vibration-mediated spin relaxation. As explained above, we will focus on molecular vibrations but yet our method can also incorporate any kind of deformation once its harmonic frequency, reduced

mass and displacement vector is known. Whenever possible, we will also try to connect our conclusions with experimental results.

Derivation of the model and proposed methodology

The proposed methodology as found elsewhere reads as follows.[184,243] Firstly, one considers the relevant set of *N* vibrating atoms. There are many options depending on the goal. For instance, this set can be a whole molecule or just a part of it,[243] but it can also be the unit cell of a molecular crystal.[245] Then, one performs a geometry relaxation of the given atom set until reaching an equilibrium geometry, which lies in a local minimum of the potential energy surface of the given set. If this set is surrounded by other atoms, a relaxation of it in vacuum without considering these other atoms could become quite unrealistic. Depending on the case, a reasonable solution can be to include these surrounding atoms but keeping them frozen while the relevant atom set is relaxed. Of course, the best option would be to relax both the atom set and the surrounding atoms at once as there could be a huge difference between relaxing against rigid or mobile walls. Although this could recover the influence of distant motion on the relevant atom set if important, here we stumble upon an important roadblock, namely, the prohibitive computational cost which limits the maximum number of atoms to relax. Yet, one can relax the whole unit cell of the given crystal by implementing periodic boundary conditions, which aid to recover these distant deforming effects. Nevertheless, under this approach the computational cost may also become prohibitive if too many points in the reciprocal space are explored. Since the main interest is put on molecular vibrations, recent works have been exploring the so-called Γ point which practically incorporates all intramolecular normal modes as well as intermolecular modes if there exists more than one molecule per unit cell.[245]

After performing the relaxation, the next step is to calculate the vibrational normal modes at the equilibrium geometry of the atom set. As a result, one will obtain a set of *R* harmonic frequencies $\nu_1,...,\nu_R$, reduced masses $m_1,...,m_R$, and 3*N*-dimensional displacement vectors $\vec{u}_1,...,\vec{u}_R$ with $\|\vec{u}_k\|=1$, $k = 1,\ldots, R$. If the relaxed atom set is a whole molecular geometry, then $R = 3N\text{-}6$ or $R = 3N\text{-}5$ depending on whether it is non-linear or linear, resp. In particular, the displacement vector of a given mode *k* establishes the spatial directions along

which each atom vibrates around its equilibrium position. This happens according to the expression $\vec{q}_k = \vec{q}_{eq} + Q_k \cdot \vec{u}_k$, where $\vec{q}_k$ is the 3*N*-dimensional Cartesian vector of the atom positions out of their equilibrium positions, $\vec{q}_{eq}$ is the 3*N*-dimensional Cartesian vector of the atomic equilibrium positions, and Q_k is the vibration normal coordinate. This coordinate can take both positive and negative values, while the particular case $Q_k = 0$ for every *k* recovers the equilibrium geometry. Both relaxation geometry and normal mode calculation are nowadays routinely conducted by a plethora of software packages.[246–250]

Secondly, one picks a magnetic property B of the given molecule whose modulation by vibrations is expected to have a decisive impact on spin relaxation. For example, it could be the Landé g factor of an electron spin doublet defining a qubit (sections 4.1, 4.2), or the CFPs in a single-ion molecular nanomagnet (section 4.3). We now assume that B is a function of the several Q_k, i.e., $B = B(Q_1,...,Q_R)$. In principle, this is an unknown expression and that is why a Taylor expansion is performed -which we cut at the second order- around the equilibrium geometry characterized by $Q_1 = ... = Q_R = 0$:

$$B(Q_1,...,Q_R) \approx \left(B\right)_e + \sum_{k=1}^{R}\left(\frac{\partial B}{\partial Q_k}\right)_e Q_j + \frac{1}{2}\sum_{j=1}^{R}\sum_{k=1}^{R}\left(\frac{\partial^2 B}{\partial Q_j \partial Q_k}\right)_e Q_j Q_k \qquad \textbf{Eq. 23}$$

In **Eq. 23**, $\left(B\right)_e$ is the value of B at the relaxed geometry, and the derivatives are also evaluated at this geometry. Of course, one can keep higher-order terms in the expansion as we will explain below. Under the working harmonic approximation, each mode *k* is characterized by a positive integer number n_k that determines its number of quanta with energy $\hbar\omega_k$, where ω_k is the angular frequency of this mode. Thus, let $N = \{n_1,...,n_R\}$ be a given set of vibration quantum numbers. Since normal modes are orthogonal, it is known that the collective vibrational wave-function $\Psi^N(Q_1,...,Q_R)$ is just the product of the individual harmonic wave-functions $\Psi_k^{n_k}(Q_k)$ -with $\left\langle \Psi_k^{n_k} \middle| \Psi_k^{n_k} \right\rangle = 1$- of the *R* modes:

$$\Psi^N(Q_1,...,Q_R)=\prod_{k=1}^{R}\Psi_k^{n_k}(Q_k) \qquad \textbf{Eq. 24}$$

Eq. 24 is now employed to estimate the expectation value $\langle B\rangle^N=\langle\Psi^N|B|\Psi^N\rangle$ of $B(Q_1,...,Q_R)$, where B is substituted by the right side of **Eq. 23**. Note that in this equation the derivatives are just constant numbers; thus, the expectation value is calculated over the variables Q_j and Q_jQ_k. Given the power Q_k^n of a normal mode coordinate Q_k, it can be shown that the expectation value $\langle\Psi^N|Q_k^n|\Psi^N\rangle=\langle\Psi_k^{n_k}|Q_k^n|\Psi_k^{n_k}\rangle$ is zero for *n* odd, while for *n* even is calculated as:

$$\frac{i^n n!}{2^n(n/2)!}\left(\frac{\hbar}{m_k\omega_k}\right)^{n/2}\sum_{\substack{l=0\\ l\equiv n(\mathrm{mod}\,2)}}^{n}(-2)^{l/2}\binom{n/2}{l/2}\binom{n_k+l/2}{n_k} \qquad \textbf{Eq. 25}$$

In **Eq. 25**, $i=\sqrt{-1}$ and the restriction $l\equiv n$ (mod 2) means that *l* has to be such that *n*-*l* is a multiple of 2. Therefore, the expectation values $\langle\Psi^N|Q_j|\Psi^N\rangle$ and $\langle\Psi^N|Q_jQ_k|\Psi^N\rangle$ ($j\neq k$), both equal to $\langle\Psi_j^{n_j}|Q_j|\Psi_j^{n_j}\rangle$ and $\langle\Psi_j^{n_j}|Q_j|\Psi_j^{n_j}\rangle\langle\Psi_k^{n_k}|Q_k|\Psi_k^{n_k}\rangle$ resp., vanish. The only surviving expectation value is of the form $\langle\Psi^N|Q_k^2|\Psi^N\rangle$, i.e., $\langle\Psi_k^{n_k}|Q_k^2|\Psi_k^{n_k}\rangle$, which is $(\hbar/\omega_k m_k)(n_k+1/2)$. By using $\omega_k=2\pi\nu_k$ where ν_k is the linear frequency, we obtain the following estimation of $\langle B\rangle^N=\langle\Psi^N|B|\Psi^N\rangle$:

$$\langle B\rangle^N\approx(B)_e+\sum_{k=1}^{R}\frac{\hbar}{4\pi}\left(\frac{\partial^2 B}{\partial Q_k^2}\right)_e\left(n_k+\frac{1}{2}\right)\frac{1}{\nu_k m_k} \qquad \textbf{Eq. 26}$$

Thirdly, as mentioned at the beginning of the chapter, the vibration bath is thermalized. Thus, to calculate the thermally-expected value $\overline{\langle B\rangle}(T)$ of B at each given temperature *T*, we consider an ensemble of molecules and

implement a Boltzmann average over all possible N sets in terms of the grand canonical ensemble, where the probability $\exp\left(-\left(E_1^{n_1}+...+E_R^{n_R}\right)/k_BT\right)/Z$ of each $\langle B\rangle^N = \langle \Psi^N | B | \Psi^N \rangle$ is determined by the grand partition function Z:

$$\overline{\langle B\rangle}(T) = \frac{\sum_{n_1=0}^{\infty}\cdots\sum_{n_R=0}^{\infty} e^{-\frac{E_1^{n_1}+...+E_R^{n_R}}{k_BT}} \langle B\rangle^N}{\sum_{n_1=0}^{\infty}\cdots\sum_{n_R=0}^{\infty} e^{-\frac{E_1^{n_1}+...+E_R^{n_R}}{k_BT}}} \qquad \textbf{Eq. 27}$$

The variables $E_k^{n_k} = h\nu_k\left(n_k+1/2\right)$ are the harmonic vibrational energies. After replacing $\langle B\rangle^N$ by its estimate in **Eq. 26**, we obtain the following approximate expression for $\overline{\langle B\rangle}(T)$:

$$\overline{\langle B\rangle}(T) \approx \overline{\langle B\rangle}(T=0) + \sum_{k=1}^{R}\frac{\hbar}{4\pi}\left(\frac{\partial^2 B}{\partial Q_k^2}\right)_e \frac{1}{\nu_k m_k}\langle n_k\rangle \qquad \textbf{Eq. 28}$$

In this last equation, $\overline{\langle B\rangle}(T=0)$ is the zero-point contribution, and $\langle n_k\rangle$ is the Bose-Einstein statistics:

$$\overline{\langle B\rangle}(T=0) = \left(B\right)_e + \sum_{k=1}^{R}\frac{\hbar}{8\pi}\left(\frac{\partial^2 B}{\partial Q_k^2}\right)_e \frac{1}{\nu_k m_k} \qquad \textbf{Eq. 29}$$

$$\langle n_k\rangle = \frac{1}{\exp\left(\nu_k/k_BT\right)-1} \qquad \textbf{Eq. 30}$$

The last step consists in calculating the second derivatives $\left(\partial^2 B/\partial Q_k^2\right)_e$ evaluated at the relaxed geometry. For each mode k, one has to generate a set

of distorted geometries $\{\vec{q}_k^{\,i}\}_i$ around the relaxed one by using a given set of both positive and negative values $\{Q_k^i\}_i$ in the expression $\vec{q}_k^{\,i} = \vec{q}_{eq} + Q_k^i \cdot \vec{u}_k$.[184,243] Basically, the minimum value of Q_k is chosen such that it produces a significant enough distortion respect to the relaxed geometry. In other words, the distortion must produce on each Cartesian component of each vibrating atom position a change at least equal to the experimental crystallographic error of the given component. Since each displacement vector is normalized, we have $Q_k^{\min} = \left\| \vec{q}_k^{\min} - \vec{q}_{eq} \right\|$, i.e., $Q_k^{\min} = \sqrt{\sum_{l=1}^{N} \sum_{\alpha=x,y,z} \left(\alpha_k^{l,\min} - \alpha_{eq}^{l} \right)^2}$, where $\left(x_{eq}^{l}, y_{eq}^{l}, z_{eq}^{l} \right)$ is the equilibrium position of the atom *l*, and $\left(x_k^{l,\min}, y_k^{l,\min}, z_k^{l,\min} \right)$ is the distorted position of the atom *l* under the vibrational mode *k* for $Q_k = Q_k^{\min}$. As said, each $\alpha_k^{l,\min} - \alpha_{eq}^{l}$ must equal $\delta\alpha^l$, which is the experimental crystallographic error in the α component of the atom *l*. Thus, we propose that the minimum value $Q_k^{\min}$ for the given vibrational mode *k* be:

$$Q_k^{\min} = \sqrt{\sum_{l=1}^{N} \sum_{\alpha=x,y,z} \left(\delta\alpha^l \right)^2} \qquad \textbf{Eq. 31}$$

Standard X-ray crystallographic techniques do not usually detect hydrogen atoms because of their low electron density, and the relevant post-processing software does not attribute any crystallographic error to the hydrogen atoms in the experimental structure. Hence, we decide not to include any hydrogen atom in the expression of $Q_k^{\min}$. Sometimes, there exist components in the displacement vectors $\vec{u}_k$ that are zero or close enough to zero. This means that some components of some atoms do not change or hardly change from their equilibrium values when the vibrational mode *k* is working. We also decide to exclude from the $Q_k^{\min}$ expression those atom components which do not change or hardly change. To decide which atom components must be excluded, we use a threshold in the corresponding component of the displacement vector. If the absolute value of this component in the displacement vector is not greater than the threshold, we set $\delta\alpha^l = 0$.

On the other hand, we choose the maximum displacement $Q_k^{\max}$ of the distortion coordinate Q_k as the value $Q_k^{\min} \cdot s_k$, where s_k is the natural number such that $Q_k^{\min} \cdot s_k$ is the smallest real number above the classical limit in Q_k corresponding to the ground harmonic vibrational level of the mode *k*. Hence, the number of distorted geometries for each mode *k* is $2 \cdot s_k$, where the values of Q_k are $Q_k^{\min} \cdot j$ with $j = -s_k, -s_k + 1, ..., s_k$. Now, one has to perform a series of point-to-point calculations to determine B at all distorted geometries $\{\vec{q}_k^{\,i}\}_i$ thus producing a set of values $\{B_k^j\}_j$. Depending on the case, this can routinely be conducted by means of software packages such as MOLCAS (section 4.1),[251–253] ORCA (section 4.2),[249,250] or SIMPRE (section 4.3). We then fit the plot $\{B_k^j\}_j$ vs $Q_k^{\min} \cdot j$ to a polynomial $p(Q_k)$ with the smallest degree that provides the best visual and most reasonable fitting. Then, by deriving $p(Q_k)$ twice respect to Q_k and evaluating the result at $Q_k = 0$ we obtain $\left(\partial^2 B / \partial Q_k^2\right)_e$.

All in all, we have obtained an expression, **Eq. 28**, that allows us estimating -up to second order in mode coordinate- the thermal modulation exerted by a set of *R* harmonic vibrations on any given magnetic anisotropy parameter. As it can be seen, there are *R* independent contributions B_k that can be calculated by first-principles methods, one per mode, see **Eq. 32**. In other words, since there are non-crossed derivatives, we can study the individual effect of each mode by separate so that physical interpretations are easier. Therefore, this method allows identifying the most problematic vibrations with the highest $|B_k|$ values, and can be used to gain insight on how to re-design the molecule at the lab stage to obtain more resilient systems against vibration-mediated spin relaxation.

$$B_k = \frac{\hbar}{4\pi}\left(\frac{\partial^2 B}{\partial Q_k^2}\right)_e \frac{1}{\nu_k m_k}\langle n_k \rangle \qquad \textbf{Eq. 32}$$

From **Eq. 32**, each B_k is the product between a factor C_k and the boson number $\langle n_k \rangle$. Each C_k is temperature independent, and defines the spin-vibration

coupling parameter of the mode k, see **Eq. 33**. The boson number $\langle n_k \rangle$ determines the thermal population of the mode k at each given temperature. Hence, the effect of a mode on B -up to second order in mode coordinate- is a balance between how coupled and how populated the mode is. Of course, the optimal situation will be the one in which both coupling and population are low enough.

$$C_k = \frac{\hbar}{4\pi}\left(\frac{\partial^2 B}{\partial Q_k^2}\right)_e \frac{1}{\nu_k m_k} \qquad \textbf{Eq. 33}$$

By inspecting **Eq. 32**, it is already possible to extract some simple conclusions on how to design more robust molecules. As said, B_k is the contribution of the mode *k* at a given temperature, and we want all of them to be as small as possible. On one hand, this can be accomplished if the frequency ν_k is high enough, which means to use rigid molecules such as porphyrines and phthalocyanines (section 4.2).[244,254] In terms of molecular optimization, one first has to visualize which are the atomic movements involved in the detrimental modes. Then, either the environment (section 4.1) or the molecule itself (section 4.3) can be re-designed in order to restrict the relevant movements and hence rise their frequencies.[164,165] Since metal ion motions can also couple to the spin, a complementary strategy can be to use not only rigid molecules but also systems where the metal is encapsulated inside a cage, i.e., with a coordination environment as tight as possible. Some examples of it can be found in nitrogen-doped fullerenes and stapled bis-phthalocyanines.[255–257] On the other hand, reduced masses should also be as large as possible. Let us note that in the simplest case of two atoms with masses m_1 and m_2, the reduced mass $\mu = m_1m_2/(m_1 + m_2)$ is determined by the lightest atom since, if for example $m_1 << m_2$, then $\mu \approx m_1$. Thus, in principle, to avoid small reduced masses, one could try to replace light by heavier atoms with similar nuclear magnetic moment, such as H by F,[136] which can result in an increase of T_m.[258]

As mentioned above, it is possible to keep higher-order terms in the Taylor expansion beyond the second order terms. Nonetheless, this brings two noticeable drawbacks: (i) the increase in the number of point calculations, and

(ii) the appearance of crossed terms that account for the interplay between different modes, which makes physical interpretations be more complicated. For instance, the next non-vanishing term to consider if we keep using the harmonic vibrational wave-function is the fourth order term. Indeed, all three order terms are proportional to $\left(\partial^3 B/\partial Q_k^3\right)_e$, or $\left(\partial^3 B/\partial Q_k^2 \partial Q_j\right)_e$, or $\left(\partial^3 B/\partial Q_k \partial Q_j \partial Q_l\right)_e$ which in any case contain at least one coordinate with an odd power. On the other hand, the surviving four order terms are the ones proportional to $\left(\partial^4 B/\partial Q_k^4\right)_e$ and $\left(\partial^4 B/\partial Q_k^2 \partial Q_j^2\right)_e$, where the latter includes inter-mode crossed interactions. In this case, the estimate of $\langle B\rangle^N$ reads as follows:

$$\langle B\rangle^N = \left\langle \Psi^N \middle| B \middle| \Psi^N \right\rangle \approx (B)_e + \frac{\hbar}{4\pi}\sum_{k=1}^{R}\left(\frac{\partial^2 B}{\partial Q_k^2}\right)_e \left(n_k + \frac{1}{2}\right)\frac{1}{\nu_k m_k} + \\ + \frac{\hbar^2}{128\pi^2}\sum_{k=1}^{R}\left(\frac{\partial^4 B}{\partial Q_k^4}\right)_e \frac{1+2n_k\left(n_k+1\right)}{\left(\nu_k m_k\right)^2} + \frac{\hbar^2}{16\pi^2}\sum_{k=1}^{R-1}\sum_{j=k+1}^{R}\left(\frac{\partial^4 B}{\partial Q_k^2 \partial Q_j^2}\right)_e \frac{\left(n_k+1/2\right)\left(n_j+1/2\right)}{\nu_k m_k \nu_j m_j} \qquad \textbf{Eq. 34}$$

The calculation of $\left(\partial^4 B/\partial Q_k^2 \partial Q_j^2\right)_e$ involves a larger number of point calculations, although the generation of distorted geometries around the relaxed one -where $Q_k = 0$, $Q_j = 0$- is essentially as simple as in the case of derivatives involving only one coordinate. Indeed, one first would apply a distortion along the mode *k* as $\vec{q}_k = \vec{q}_{eq} + Q_k \cdot \vec{u}_k$ respect to $\vec{q}_{eq}$, and the next distortion would be applied by following the mode *j* respect to $\vec{q}_k$ and according to $\vec{q}_{k,j} = \vec{q}_k + Q_j \cdot \vec{u}_j$. The resulting distorted geometry would be determined as $\vec{q}_{k,j}^{\,i} = \vec{q}_{eq} + Q_k^i \cdot \vec{u}_k + Q_j^i \cdot \vec{u}_j$. Then, after calculating B at each $\vec{q}_{k,j}^{\,i}$ and generating a set of values $\left\{B_{k,j}^i\right\}_i$, the two-dimensional plot $\left\{B_{k,j}^i\right\}_i$ vs $\left\{\left(Q_k^i, Q_j^i\right)\right\}_i$ would be fitted to a two-variable polynomial $p\left(Q_k, Q_j\right)$. The derivative $\left(\partial^4 B/\partial Q_k^2 \partial Q_j^2\right)_e$ would be estimated by deriving $p\left(Q_k, Q_j\right)$ twice respect to Q_k, Q_j, and evaluating the result at $Q_k = 0$, $Q_j = 0$.

Although the inclusion of anharmonicity will require to calculate a larger number of parameters, it could be conducted as follows. We can list two

approaches when recalculating $\langle B\rangle^N = \langle \Psi^N | B | \Psi^N \rangle$, namely, (i) to substitute the collective harmonic wave-function in **Eq. 24**, or (ii) to substitute the individual harmonic wave-functions $\Psi_k^{n_k}(Q_k)$ but keeping the form of the new collective wave-function as the product of the individual non-harmonic wave-functions. In both cases, if the anharmonic effects are small enough, one can resort to perturbation theory, where the harmonic energies and wave-functions would be used as a zero-order approximation. In the first case (i), one could calculate a collection *C* of values for the potential energy surface $V(q_1,...,q_R)$ around a local minimum *e*, where q_k is a set of coordinates describing the internal degrees of freedom of the vibrating atom set. Since a derivative is a local concept, it is enough to calculate *C* in a small neighborhood of *e*. Hence, we could determine the several distorted geometries around $q_k = 0$ by employing the displacement vectors $\vec{u}_k$ if the harmonic approximation still applies (i.e., $q_k = Q_k$), or for instance via a molecular dynamics. After taking the energy origin at the minimum, the Taylor expansion around it would read as (let us recall that $(\partial V / \partial q_k)_e = 0$):

$$V(q_1,...,q_R) = \frac{1}{2}\sum_{j=1}^{R}\sum_{k=1}^{R}\left(\frac{\partial^2 V}{\partial q_k \partial q_j}\right)_e q_k q_j + O\left(q^3\right) \qquad \textbf{Eq. 35}$$

If only two and three order terms are kept in **Eq. 35**, we could use C to fit the resultant expression and obtain the corresponding derivatives $(\partial^2 V / \partial q_k \partial q_j)_e$ and $(\partial^3 V / \partial q_k \partial q_j \partial q_l)_e$. Thus, the anharmonicity would be described by the terms proportional to the three order derivatives but, of course, one could use any other alternative parametric expression to model it. With these ingredients, perturbation theory should be able to provide us the collective non-harmonic wave-function Ψ to calculate the matrix elements $\langle \Psi | q_k^n | \Psi \rangle$ and then the expectation value $\langle B \rangle = \langle \Psi | B | \Psi \rangle$. The second case (ii) offers the advantage of always dealing with a single one-dimensional potential energy functions $V_k(q_k)$ at each mode *k*. We could also proceed analogously by determining first the

derivatives $\left(d^l V_k / dq_k^l\right)_e$ with $l \geq 2$ and then employing perturbation theory. Nevertheless, particular expressions to describe anharmonic potential energies around a local minimum were already proposed and thoroughly studied long ago, such as the ones derived from the Kratzer model $V_K\left(q_k\right) = D_k^e\left(1 - q_k^e / q_k\right)^2$ or the well-known Morse model $V_M\left(q_k\right) = D_k^e\left(1 - e^{-a_k\left(q_k - q_k^e\right)}\right)^2$.[259–261] Here, the key point is that the matrix elements $\langle\Psi|q_k^n|\Psi\rangle$ have already been computed.[262–264] In spite of it, both V_K and V_M depend on some parameters such as the equilibrium distance $q_k^e > 0$, the well depth (defined relative to the dissociation situation) $D_k^e > 0$, and $a_k > 0$ determining the well width (the smaller a_k is, the wider the well is), which would have to be previously determined.

4.1 $[Cu(mnt)_2]^{2-}$

The molecular model that we will study by employing the model presented above is a Cu^{2+} complex with formula $[Cu(mnt)_2]^{2-}$, hereafter referred to as **1**, where mnt^{2-} = 1,2-dicyanoethylene-1,2-dithiolate.[207,243] It is depicted in **Fig. 15**, and shows a nearly D_{4h} symmetry in the copper coordination environment. This compound is found in the form of molecular crystal which additionally contains diamagnetic counterions PPh_4^+ (tetraphenylphosphonium) to balance its charge. **1** is magnetic with a ground electron spin doublet S = 1/2 that is used to define one qubit. Importantly, the ligands of **1** contains atoms with no magnetic nuclei or whose magnetic isotopes have a very low occurrence. This allowed measuring a long T_m = 68 μs at 7 K -the latest record when reported in 2014- after counterion deuteration and dissolving **1** and its Ni-based diamagnetic analog in the molar ratio 99.99:0.01. With this promising result, we decided to apply our model to check the role of molecular vibrations on the magnetic anisotropy of **1**.

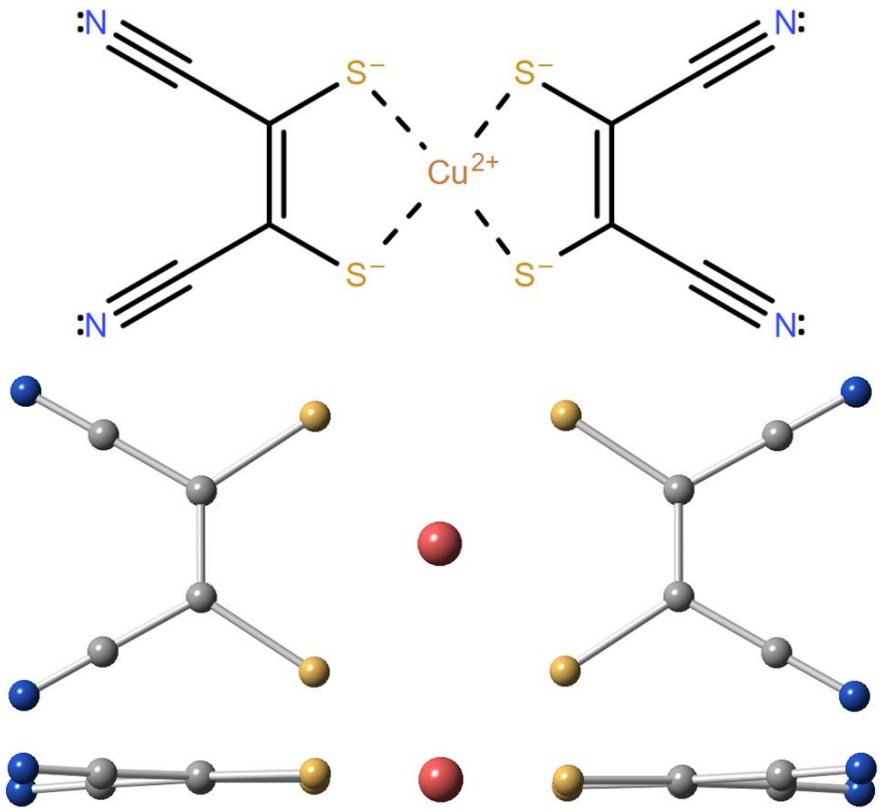

Fig. 15 From top to bottom: Lewis structure, upper view, and side view of the experimental geometry of **1** at 100 K. Orange: Cu, Yellow: S, Grey: C, Blue: N. Note that (i) **1** contains no H atoms, and (ii) **1** is not strictly planar.

Our original motivation is that of studying the temperature sensitivity of the qubit energy gap in **1**, i.e. the energy difference between the states $|0\rangle$ and $|1\rangle$, caused by a thermal bath of molecular vibrations. From a quantum computing point of view, the successful implementation of a given algorithm relies on applying a well-defined pulse sequence between spin states. Nevertheless, vibrations as a non-controlled source of noise could alter the spin energies -as well as the composition of the corresponding wave-functions- at a given time. If the spectrometer frequency $\hbar\omega$ is not accordingly corrected, the new qubit gap $\hbar\omega'$ is not matched anymore, and this would result in an unexpected spin transition with respect to the one referred in the working time-dependent Hamiltonian, **Fig. 16**.

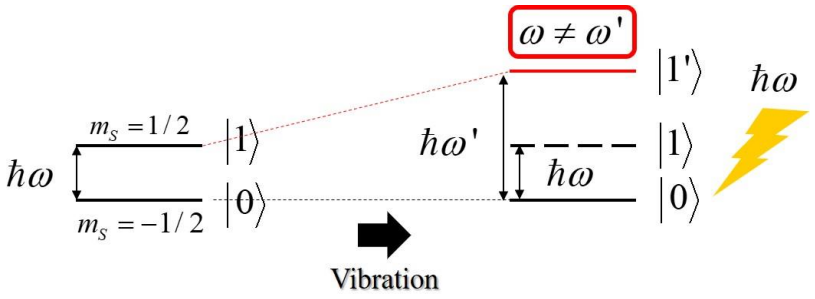

Fig. 16 Change in the qubit energy gap and the wave-function composition caused by non-controlled vibrations while conducting a quantum algorithm. The spectrometer frequency $\hbar\omega$ does not match the new gap $\hbar\omega'$ and the expected spin transition is not produced which thus results in a computational error.

Since from a magnetic point of view **1** can be described as a ground doublet S = 1/2, the spin Hamiltonian becomes rather simple and only contains the Zeeman and hyperfine coupling terms, which are assumed to be axial, see **Eq. 36**.[207] Moreover, the two eigenvectors corresponding to $g_{||}$, $A_{||}$ are assumed to be colinear and this common direction is used to define the Z axis respect to the experimental geometry. Just to showcase our model, we consider a hypothetical experiment with a magnetic field applied in this direction. Hence, B_x = 0, B_y = 0, $B_z = B_0$, where B_0 is the field magnitude. If the Zeeman interaction dominates over the hyperfine coupling for a moderate B_0, the qubit gap Δ is $\mu_B g_{||} B_0$. Since μ_B and B_0 are constants, a change of Δ with temperature will arise, in principle, from the thermal modulation of $g_{||}$ by the vibration bath. Thus, we select $B = g_{||}$ as the target anisotropy parameter.

$$\hat{H} = \mu_B g_{\perp}\left(B_x\hat{S}_x + B_y\hat{S}_y\right) + \mu_B g_{||} B_z\hat{S}_z + A_{\perp}\left(\hat{S}_x\hat{I}_x + \hat{S}_y\hat{I}_y\right) + A_{||}\hat{S}_z\hat{I}_z \qquad \textbf{Eq. 36}$$

Before applying the model and obtaining the relevant results, we need to point out the following consideration. Both the relaxation of the experimental geometry and the distortion of the relaxed geometry produce geometries whose eigenvectors associated to the axial eigenvalues $g_{||}^{rd}$ will surely not coincide with the field direction anymore. Hence, all $g_{||}^{rd}$ need to be corrected to obtain

the values $g_{\parallel}^{rdc}$ acting in the field direction, which are the ones that really determine the qubit gap. This correction is straightforward just by using the invertible matrix G -provided by the employed software package- that diagonalizes the g tensor written in the canonical Cartesian basis set. Indeed, if $diag\left(g_{\perp}^{rd}, g_{\perp}^{rd}, g_{\parallel}^{rd}\right)$ is the diagonal representation in the eigenvector base, then $g = G diag\left(g_{\perp}^{rd}, g_{\perp}^{rd}, g_{\parallel}^{rd}\right) G^{-1}$ and the value $g_{\parallel}^{rdc}$ to pick is just the *zz* component of g. Note that to make the last equality meaningful, the three eigenvectors of g must appear in G with the same order that we have employed to build the diagonal matrix representation $diag\left(g_{\perp}^{rd}, g_{\perp}^{rd}, g_{\parallel}^{rd}\right)$. On the other hand, the three canonical Cartesian vectors will appear in g with the same order as in G. In general, depending on the software, the expression to relate $diag\left(g_{\perp}^{rd}, g_{\perp}^{rd}, g_{\parallel}^{rd}\right)$ and g could be $g = G^{-1} diag\left(g_{\perp}^{rd}, g_{\perp}^{rd}, g_{\parallel}^{rd}\right) G$ instead. These corrected values $g_{\parallel}^{rdc}$ are the ones that we use to represent them against the normal coordinates Q_k.

The relevant atom set to relax is the whole molecule **1**. We first tried to relax the isolated experimental geometry of **1**, as if it were in vacuum. Nevertheless, we found that the relaxed geometry largely deviated from the near planarity of the experimental structure. We thus had to include in the relaxation process the nearest-neighbor counterions, at their experimental positions in the crystal, that surround **1**, see **Fig. 17**. This inclusion recovered the mentioned planarity and produced a more realistic relaxed geometry, but we needed to keep the counterions frozen in order not to reach a prohibitive computational cost. This relaxation and the subsequent normal mode calculation was conducted with the software Gaussian09 by using the so-called Density Functional Theory (DFT).[246] The $g_{\parallel}^{rd}$ calculations both at the relaxed and the distorted geometries were performed with the MOLCAS package as a joint collaboration with Dr. Nicolas Suaud (University Toulouse III Paul Sabatier).[251–253,265]

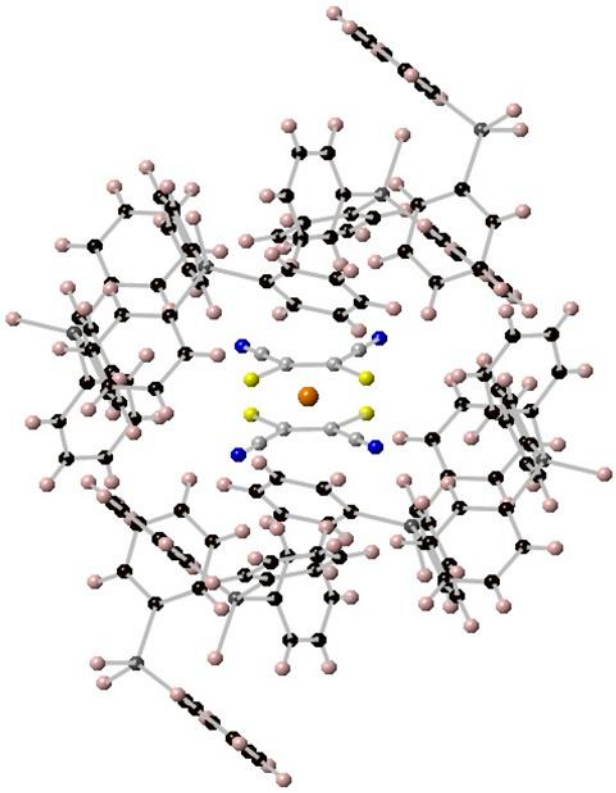

Fig. 17 Frozen nearest-neighbor counterions PPh_4^+ at their experimental crystallographic positions surrounding **1** in the relaxation process. Orange: Cu, Yellow: S, Grey and Black: C, Blue: N, Pale pink: H.

The infrared (IR) spectrum of the molecular crystal containing **1** was experimentally determined in the range 400 - 2500 cm^{-1} by K. Bader et al., see **Fig. 18**, which allows checking the accuracy of our calculated IR spectrum for **1** in that frequency range. Since the experimental geometry of **1** is relaxed while keeping the nearest counterions frozen, the calculated IR spectrum only displays vibrations involving **1**. This means that the non-marked experimental peaks, that correspond to counterion vibrations, do not appear in the calculated spectrum. The experimental marked peaks only correspond to vibrations of **1**. As can be seen, we provide reasonable estimates for the marked peaks with relative errors below 5%. There is no available experimental data below 400 cm^{-1}. Nevertheless, since the calculated peaks in **Fig. 18** (top) approach the experimental ones as frequency is decreased, we expect that this trend also holds below 400 cm^{-1} and hence our calculated far-IR spectrum might be a good estimate of the experimental one.

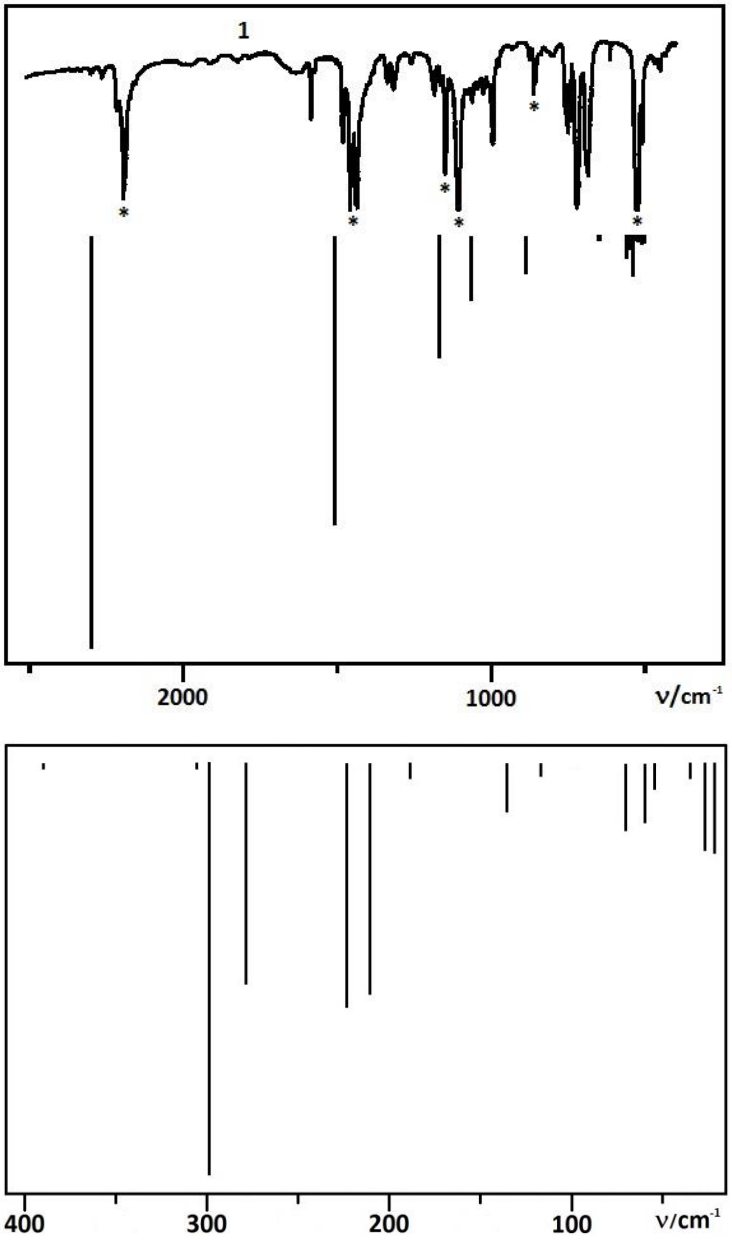

Fig. 18 Top: experimental IR spectrum of the molecular crystal containing **1** (above), and calculated IR spectrum at the relaxed geometry of **1** (below), both in the range 400 – 2500 cm^{-1}. The marked peaks correspond to vibrations of **1**, while non-marked peaks only involve vibrations in the counterion. Vertical scales are in arbitrary units. Bottom: calculated far-IR spectrum at the relaxed geometry of **1** in the range 0 – 400 cm^{-1}.

The calculated far-IR spectrum of **1** in **Fig. 18** (bottom) exhibits a first noticeable gap in between 305 and 390 cm^{-1} corresponding to the modes 25 and

26, resp. In terms of temperature, these frequencies are 439 K and 561 K. Since the upper limit of the experimental temperature range is found at ~300 K, we expect that vibrations beyond the aforementioned gap are not significantly populated. Thus, we only use the first 25 molecular modes in our model, i.e., R = 25. These vibrations do not involve significant covalent bond stretching. Instead, the most significant distortions consist in covalent bond bending along with coordination bond stretching and bending. On the other hand, in **Fig. 19** we show two examples of evolutions $g_{\|}^{rdc} = g_z$ vs Q_k along the modes k = 24 and k = 25 around the relaxed geometry $Q_k = 0$.

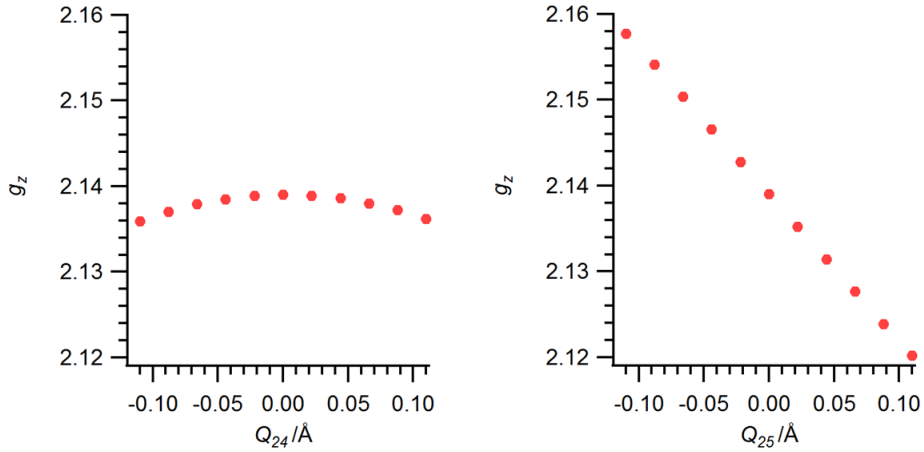

Fig. 19 g_z evolution with Q_{24} (left) and Q_{25} (right) between -0.110 Å and +0.110 Å. The near-linear dependence of g_z with Q_{25} -a breathing vibration- produces a rather small second derivative at Q_{25} = 0. At Q_k = 0 (relaxed geometry), the calculated $(g_z)_e$ is 2.1425.

The determination of $g_{\|}$ in **Eq. 36** -as well as $g_{\perp}$, $A_{\|}$, $A_{\perp}$- was experimentally conducted by K. Bader et al. via cw-EPR X-band (9.47 GHz) spectroscopy on a finely ground powder sample with a molar ratio 98.5:1.5 at T = 5 K ($g_{\|}$ = 2.093 ± 0.002) and T = 294 K ($g_{\|}$ = 2.091 ± 0.002).[207] These two values along with their experimental errors give rise to a variation of $g_{\|}$ in the temperature range 5 K – 294 K relative to T = 5 K that lies inside the interval [-2.9 ‰, 1.0 ‰]. The application of **Eq. 28**, with the joint effect of the first 25 molecular vibrations, produces the values 2.138 and 2.141 at T = 5 K and T = 294 K, resp. This results in a positive relative thermal evolution of 1.4 ‰ that lies close to

the aforementioned interval. Here, one has to notice that a main source of numerical noise is found in the determination of the second derivatives $\left(\partial^2 B / \partial Q_k^2\right)_e$. Indeed, while satisfactory and unequivocal fittings are found for the plots $g_{||}^{rdc} = g_z$ vs Q_k, in which the variation of $g_{||}^{rdc} = g_z$ with respect to $Q_k = 0$ is large enough compared to the noise floor of $g_{||}^{rdc} = g_z$, the fitting procedure is not that unequivocal if this variation becomes comparable to the aforementioned noise floor and can even conditionate the derivative sign. Despite it, the accuracy in the $g_{||}^{rd}$ calculations can be further improved in MOLCAS by employing a procedure developed elsewhere and followed by a DDCI (Difference Dedicated Configuration Interaction) evaluation of the spin-free spectrum.[266,267] This method led to a more accurate value $g_{||}^{rd}$ = 2.099 determined at the experimental geometry of **1** around 100 K, but at a prohibitive computational cost to be applied in a large set of geometries. Yet, our approach to estimate $g_{||}^{rd}$ is satisfactory as compared with standard quantum-chemical calculations.[268–270] In **Fig. 20** we show the B_k contribution of the first 25 vibrational modes of **1**.

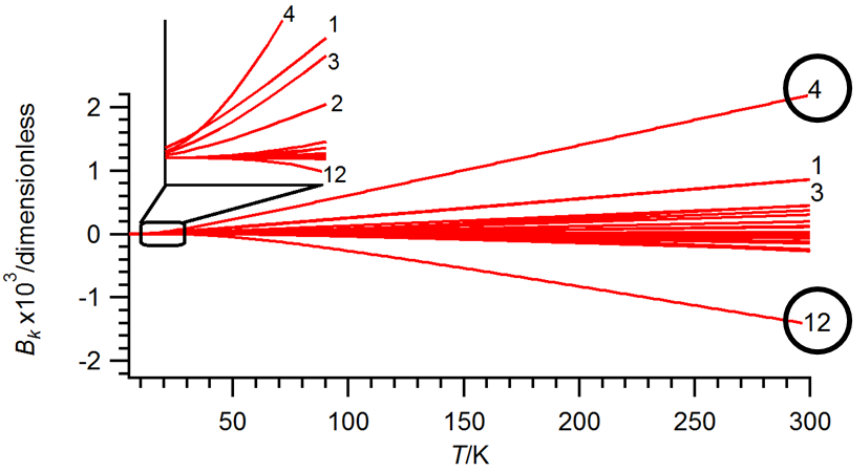

Fig. 20 B_k thermal contributions in **Eq. 32** to $\overline{\langle g_{||} \rangle}(T = 0)$ of the first 25 molecular modes of **1** in the temperature range 5 – 300 K. Inset: zoom-in at the range 10 – 30 K. Note that B_1 and B_3 have very similar thermal evolutions as their slopes only differ in less than 1%.

We clearly see two differentiate modes, 4 and 12 in **Fig. 21**, that display the largest B_k contributions relative to the others in the explored temperature range. These two contributions are essentially similar in magnitude but with opposite sign. This may explain the near thermal-insensitivity of the experimental $g_{\|}$ evolution. Our calculated relative evolution 1.4 ‰ may be positive due to the positive contributions of B_1 and B_3. Contributions from the other modes might have a negligible effect as they basically cancel with each other. Below 10 – 15 K, molecular vibrations are hardly populated (i.e. $\nu_k \gg k_B T$) which expectedly produce rather flat thermal evolutions. On the other hand, at high temperature each B_k acquires a linear evolution. Indeed, as $k_B T$ becomes larger than ν_k, we can approximate $\exp(\nu_k / k_B T) \approx 1 + \nu_k / k_B T$. Hence, the Boson number in **Eq. 32** becomes proportional to T.

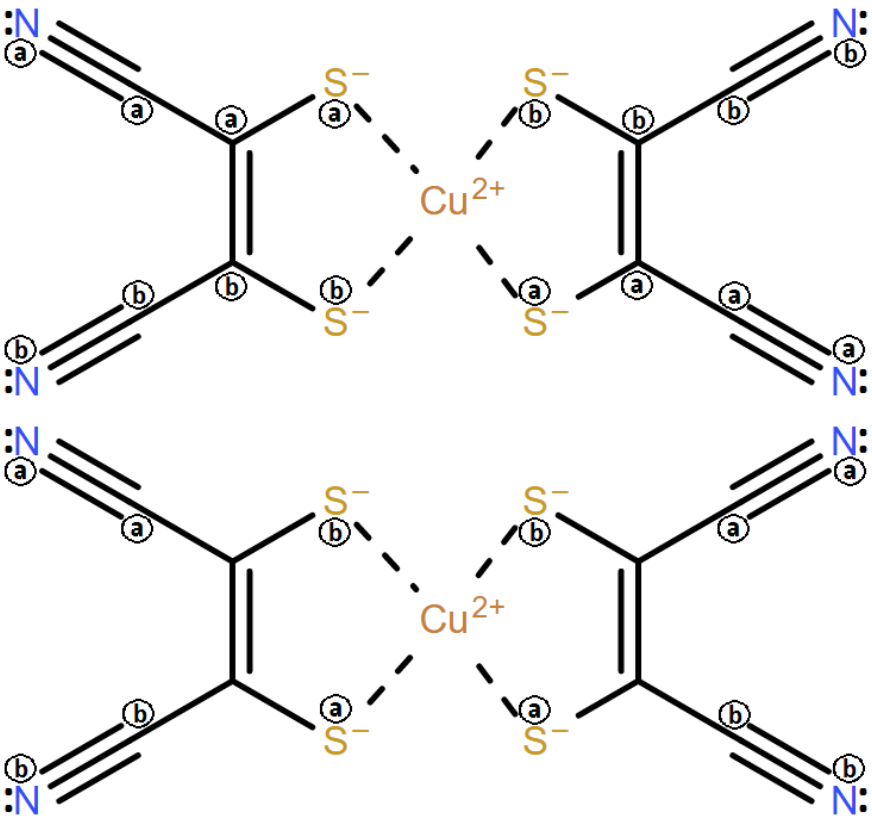

Fig. 21 Out-of-plane vibrational modes 4 (top) and 12 (bottom) of **1**. a-labeled atoms move toward the reader while b-labeled atoms move away from the reader and vice versa.

The mode 4 is an out-of-plane twisting vibration and, since its frequency ν_4 = 34.76 cm^{-1} is relatively low, it is expected to be populated already from low temperature. This mode alters the dihedral angle between the two ligands, which behave almost as rigid planes in this case. On the contrary, the mode 12 has a much higher frequency ν_{12} = 104.16 cm^{-1} and can be seen as an out-of-plane wagging vibration. In this mode, the ligands are twisted and the orientation of the CuS_4 moiety is altered while its square planar structure is maintained. In this particular molecular system, B_4 and B_{12} essentially cancel each other in the explored temperature range but, in other systems, there could have modes with the same sign in B_k producing a much more marked $g_{||}$ thermal dependence. If it had been the case of **1**, we could have proposed some strategies to avoid the out-of-plane movements that characterize the modes 4 and 12. Indeed, for instance, one could think that some kind of physical or chemical pressure -the latter in the form of different or bulkier counterions- applied in the perpendicular direction to the molecular plane should be enough to block them.

In **Fig. 22** we depict the spin-vibration coupling constants C_k of **Eq. 33** for the first 25 modes of **1**. Five of them clearly hold the highest magnitudes, namely: (a) modes 4 and 13, with positive coupling and (b) modes 12, 23 and 24, with negative coupling. Let us recall that the sign of C_k is the sign of the derivative $\left(\partial^2 B / \partial Q_k^2\right)_e$. Thus, positive couplings increase B_k respect to its value at T = 0 K, while the negative ones decrease B_k as temperature is raised. The mode 4 clearly gives the largest positive contribution B_k in the whole temperature range. As mentioned, besides its remarkable coupling, it is a low-frequency mode and hence it becomes populated already from low T. On the contrary, the modes 23 and 24 have larger couplings but their high frequencies ν_{23} = 278.70 cm^{-1} and ν_{24} = 298.81 cm^{-1} make them become significantly populated only at high enough temperature. Ultimately, this fact results in much weaker B_k contributions, which supports the assumption of neglecting in our method any mode with a frequency beyond 300 cm^{-1}. To elaborate further, another striking feature is that, despite the similar coupling constants of the modes 4 and 13 on one hand, and the modes 12 and 24 on the other hand, B_4 and B_{12} are clearly much higher than B_{13} and B_{24}, resp., at each given temperature. Of course, the reason of this behavior is found in the fact that $\nu_{13} \gg \nu_4$ and $\nu_{24} \gg \nu_{12}$. Hence, the modes 4 and 12 are significantly populated before than the modes 13 and 24,

resp. The capability of calculating individual spin-vibration coupling constants offers the possibility to establish priorities on a given set of modes. In other words, it allows deciding which modes should be engineered first whenever they seem to couple similarly.

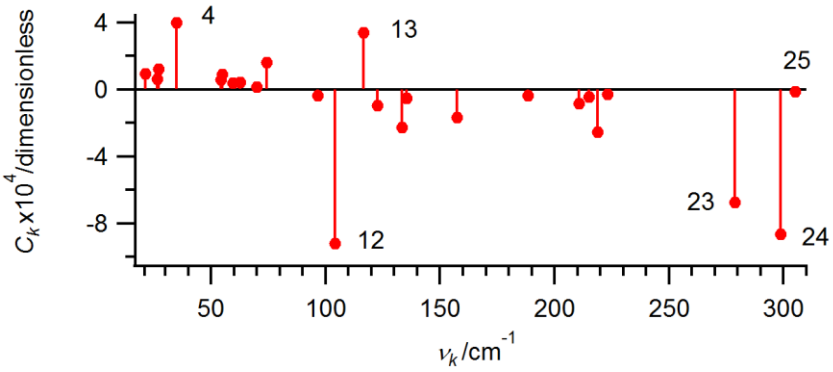

Fig. 22 Spin-vibration coupling constants C_k in **Eq. 33** of the first 25 molecular modes of **1**, which are sorted by increasing frequency from 21 to 305 cm^{-1}.

Interestingly, we identify modes that largely distort the copper coordination sphere but do not couple very much, as well as modes with a significant coupling but altering the coordination sphere very little. The first case is illustrated by the mode 25 when compared to the modes 13, 23 and 24, see **Fig. 23**; while the modes 4 and 12 exemplify the second case. The mode 25 is a breathing vibration in which g_z evolves near-linearly along Q_{25}, see **Fig. 19**. Despite comparable displacements of the coordinating atoms, its second derivative is much smaller than those of the modes 13, 23 and 24, which results in a rather negligible C_{25} as seen in **Fig. 22**. This clearly evidences the crucial role of modes with symmetric movements around the metal ion at producing linear trends in g_z around $Q_k = 0$. Of course, a small $\left(\partial^2 B / \partial Q_k^2\right)_e$ could also be achieved with a near-horizontal evolution of B. In the case $B = g_{||}$, this means to have a highly isotropic magnetic system with a small enough spin-orbit coupling, such as in organic radicals or, among $S > 1/2$ metals, in Mn^{2+}, Fe^{3+} and Gd^{3+}.[138,271] Nevertheless, this strategy should be initially discarded since often magnetic anisotropy is desirable to facilitate qubit addressing or to slow down magnetic relaxation in molecular nanomagnets.[81]

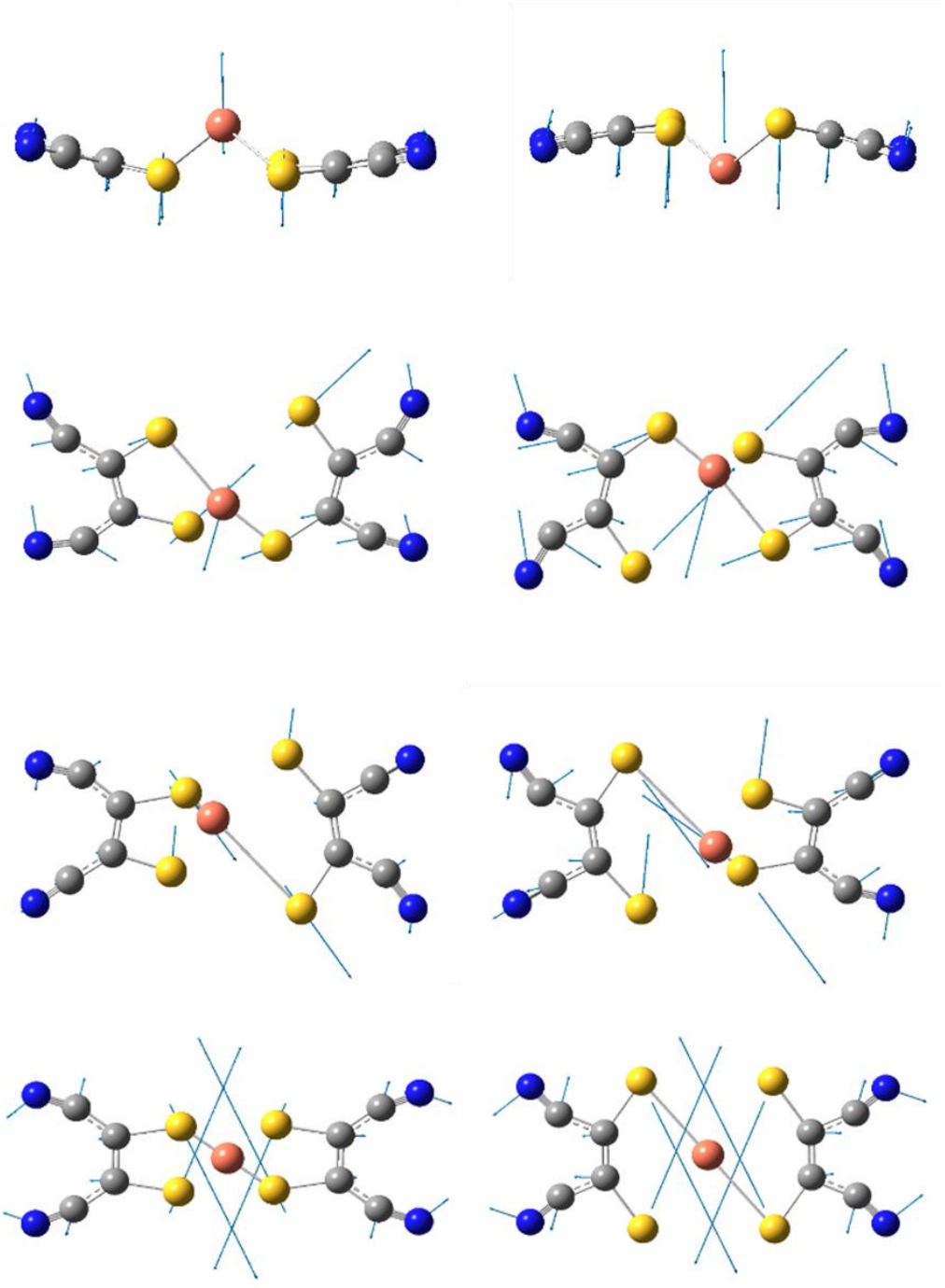

Fig. 23 Pictures of vibrational modes of **1** including displacement vectors (blue arrows): 13 (first row), 23 (second row), 24 (third row), 25 (fourth row). The pictures have been taken for the values of the distortion coordinate Q_k = -1.0 Å (left) and +1.0 Å (right).

To end up, it is worth making an effort to connect our conclusions with the T_1-mediated spin relaxation. In other words, we have found two molecular modes with important B_k thermal evolutions but, does it mean they necessarily determine the experimental T_1 thermal dependence at high temperature? Let us simulate this thermal dependence by assuming three different relaxation mechanisms at play as commonly done in similar coordination compounds with similar T_1 evolutions,[203,234,241,272,273] namely, the direct, Raman, and local mode processes. In this case, the Raman process is rather modeled with a dependence of the form $A_R\left(T/\theta_D\right)^9 I_8\left(\theta_D/T\right)$, where $I_8\left(\theta_D/T\right)$ is the so-called transport integral, see **Eq. 37**. To avoid the numerical evaluation of $I_8\left(\theta_D/T\right)$ which has no analytical solution,[234,274] it is common to use a term of the form $A_R\left(T/\theta_D\right)^n$ where the exponent 9 is substituted by an effective exponent *n* as a free parameter.[234] Yet, if one desires to keep the original term $A_R\left(T/\theta_D\right)^9 I_8\left(\theta_D/T\right)$, there are available phenomenological expressions that reproduce $I_8\left(\theta_D/T\right)$ as a function of θ_D/T for $0.4 \leq \theta_D/T \leq 18$, and can be used to fit T_1 by using θ_D as a free parameter.[234] For $\theta_D/T \gg 1$, we can replace θ_D/T by ∞ and it can be shown that $I_8\left(\infty\right) = 8!$; when $\theta_D/T \ll 1$, I_8 can be approximated as $\left(\theta_D/T\right)^7/7$.[234]

$$I_8\left(\theta_D/T\right) = \int_0^{\theta_D/T} \frac{x^8\, e^x}{\left(e^x-1\right)^2}\, dx \qquad \textbf{Eq. 37}$$

The local mode process, described by the right-most term of **Eq. 38**, represents a mechanism similar to that of Orbach. In fact, the Orbach term is recovered when $\exp\left(\Delta/T\right) \gg 1$. In the present case, the $S = 1/2$ spin is driven from a given m_s projection to the reversed one through an energy barrier that is resonant with a molecular mode of a characteristic energy $k_B\Delta$.

$$\frac{1}{T_1} = A_D T + A_R\left(\frac{T}{\theta_D}\right)^n + A_L \frac{\exp\left(\Delta/T\right)}{\left(\exp\left(\Delta/T\right)-1\right)^2} \qquad \textbf{Eq. 38}$$

We now use **Eq. 38** to fit the experimentally-determined T_1 points of **1** as a function of temperature, see **Fig. 24**.

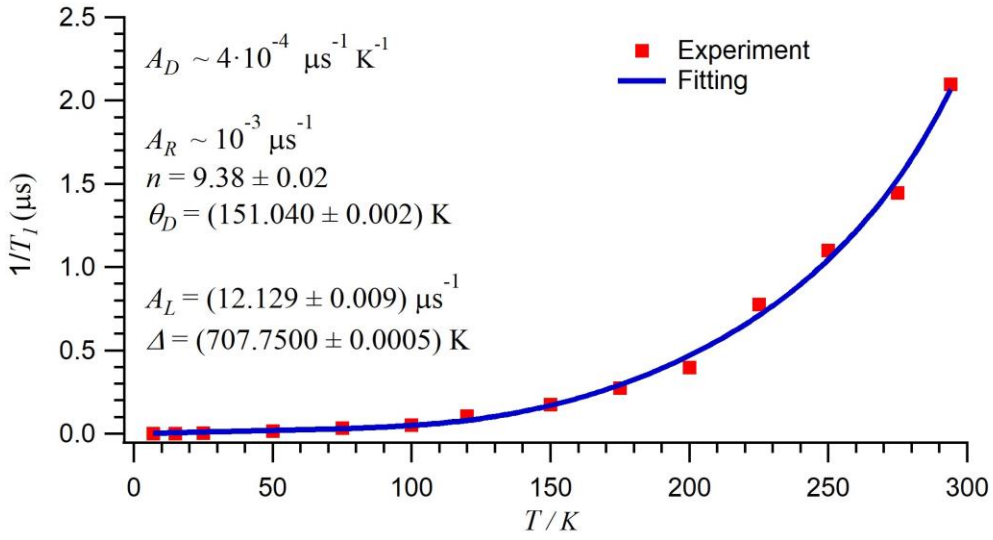

Fig. 24 Fitting (blue curve) to the experimental $1/T_1$ thermal evolution (red points) of **1**,[207] according to **Eq. 38**.

As seen in **Fig. 24**, we note that the experimental T_1 evolution is satisfactorily recovered but, more importantly, both direct and Raman might have a rather negligible role due to their small coefficients A_D and A_R (we just provide their magnitude orders) compared to A_L. The Debye temperature lies among typical values for similar molecular compounds.[203,234,241,272,273] The exponent n is close to 9, which is the expected value for half-integer spins as mentioned in chapter 2. The characteristic energy of the molecular local mode involved is found to be $\Delta \sim 708$ K ~ 492 cm^{-1}. While this is a reasonable and possible value,[203,272] it does not coincide with the frequencies of the modes 4 and 12. Yet, interestingly, in our calculated IR spectrum there do exist two modes with a similar energy, namely, ν_{30} ~ 501 cm^{-1} and ν_{31} ~ 506 cm^{-1}. Thus, although T_1 starts to become similar to T_m from 50 K,[207] which is right the temperature where B_4 and B_{12} acquire a significant contribution in **Fig. 20**, we cannot initially attribute this behavior to the action of the modes 4 and 12 as the whole thermal dependence of T_1 seems to be dominated by a mode with a clearly different frequency. Of

course, to unveil the real role of molecular vibrations, one would have to derive an explicit theoretical expression of T_1 as a function of them, which is something indeed interesting but beyond the scope of the present work.

4.2 $[V(dmit)_3]^{2-}$, $[VO(dmit)_2]^{2-}$, VOPc

In this section, we will apply the model developed and presented above to three $S = 1/2$ V^{4+}- and VO^{2+}-based molecular coordination compounds, namely, $[V(dmit)_3]^{2-}$, $[VO(dmit)_2]^{2-}$, VOPc, where dmit = 1,3-dithiole-2-thione-4,5-dithiolate and Pc = phthalocyanine, hereafter referred to as **2**, **3**, **4**, resp., see **Fig. 25**. All of them encode one molecular spin qubit, and have been characterized via cw- and pulsed-EPR by R. Sessoli et al. Interestingly, some potential results were found.[239,244]

On one hand, the joint study of **2** and **3** revealed the key role of the oxovanadium (vanadyl) VO^{2+} moiety in enhancing quantum coherence up to room temperature. Indeed, after substituting one dmit ligand in **2** by this moiety, **3** shows T_1 and T_m relaxation times of around 3 – 4 μs and 0.7 – 1.0 μs at T = 293 K, resp. Note that this reported T_m, which also relies on the additional benefit provided by using nuclear spin-free ligands, is even higher than the one found in **1** at the same temperature (~0.6 μs), in spite of a much higher electron spin concentration in **3**. Instead, **2** is able to show quantum coherence only up to T = 150 K with T_1 = 0.71 μs which limits T_m at 0.2 μs for the same temperature. Importantly, these results show that rapid decreases in T_1 caused by an efficient spin-vibration coupling -thus hampering the use of spin qubits at high temperatures- can be modulated after uniquely introducing structural modifications as a complementary strategy of reducing the nuclear spin content. In this case, a nearly octahedral environment in **2** is replaced by a square pyramidal in **3**.

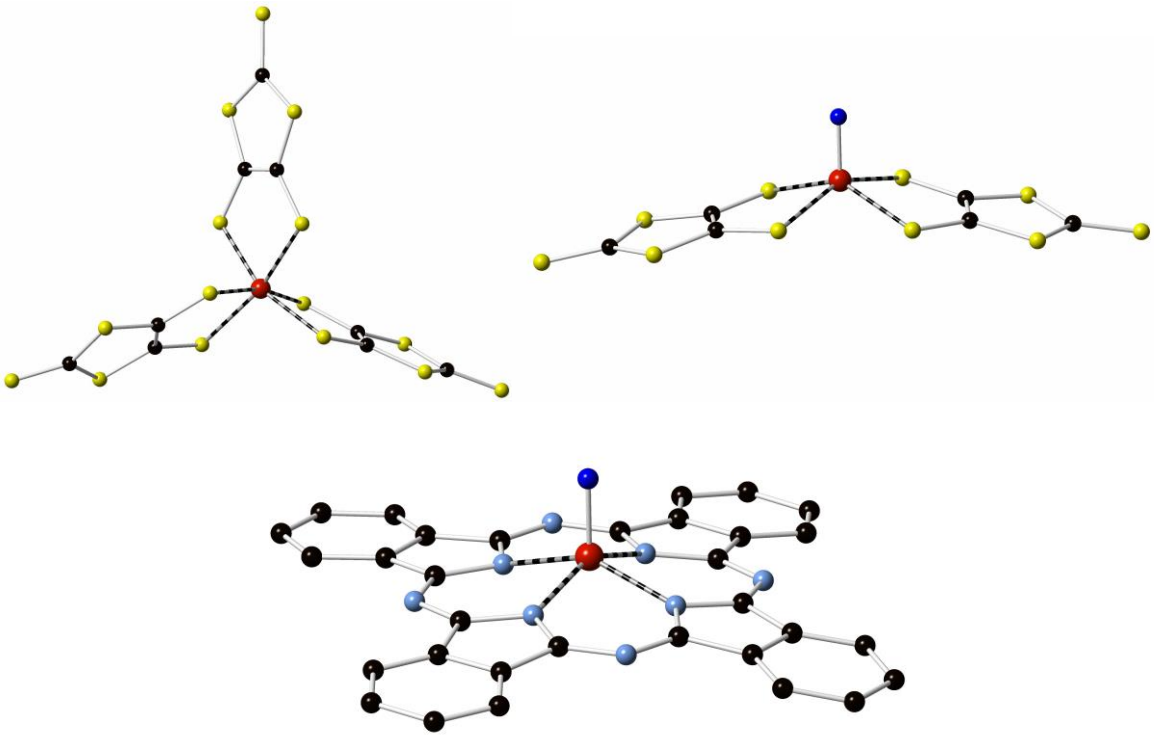

Fig. 25 Top Left: **2**, Top Right: **3**, Bottom: **4**. Red: V, Black: C, Yellow: S, Dark blue: O, Light blue: N. Note that both **2** and **3** do not contain hydrogen atoms. In **4** hydrogen atoms are omitted for clarity.

The importance of the metal coordination symmetry as a major influence on spin relaxation was already noticed long ago in a series of copper(II) coordination compounds, also studied via EPR spectroscopy.[242] Indeed, $1/T_1$ rates were up to six times faster in pseudo-tetrahedral compounds compared to square planar ones. Besides, the relatively higher rigidity found in square planar and octahedral coordination geometries enabled longer relaxation times compared to tetrahedral environments as well as other geometries. On the other hand, **4** is also able to show room-temperature quantum coherence with T_1 = 1.1 μs and T_m = 0.8 μs at T = 300 K. More strikingly, **4** still displays Rabi oscillations at the same temperature despite the nuclear-spin active environment (^{1}H and ^{14}N nuclei) of VO^{2+} thus evidencing again the key role of the vanadyl moiety. These oscillations are also observed in **3** at room temperature but with nuclear-spin free ligands.

Herein, we intend to make a comparison on the quantitative level between **2**, **3**, and **4** in order to find similarities and differences as well as to extract possible correlations to assess the role played by the vanadyl moiety in the spin-lattice relaxation. As mentioned, we will rely on our model applied in section 4.1 but now it will be complemented with a perturbative analysis on the Landé factor $g_{\|}^{rdc}$ up to second order in mode coordinate depending on excitation energies and matrix elements between pairs of the metal-ion 3d orbitals. We will also try to connect our results with experimental facts either to support or discard some conclusions derived from them.

Spin-vibration coupling constants and thermal evolutions

We first proceed by determining spin-vibration coupling constants C_k and individual thermal evolutions B_k in **Eq. 32** and **Eq. 33** of the low-energy molecular modes of **2**, **3**, **4**, see **Fig. 26**, **Fig. 27**, **Fig. 28**. The spin Hamiltonian employed to describe the ground S = 1/2 electronic structure in these three systems is also the one found in **Eq. 36** and we select again $B = g_{\|}$ as the relevant anisotropy parameter to study. The value of $g_{\|}$ in **Eq. 36** was experimentally determined via cw-EPR X-band spectroscopy only at room temperature: 1.985 (**2**), 1.970 (**3**), 1.966 (**4**). Both **2** and **3** are non-neutral molecules thus the crystal contains counter-ions (PPh_4^+, tetraphenylphosphonium) to balance the charge. We again include the nearest-neighbor counter-ions to **2** and **3** but by keeping them frozen in the geometry relaxation. On the contrary, **4** is not charged. In this case, we select a molecule of **4** along with the nearest copies in the crystal; then, the geometry relaxation is conducted while keeping the latter frozen. In fact, we only relaxed the vanadium moiety plus the four vanadium-coordinating nitrogen atoms in order not to increase the computational cost -**4** is a rather medium-sized molecule- and because the focus is put on studying the aforementioned moiety together with the vanadium coordination sphere.

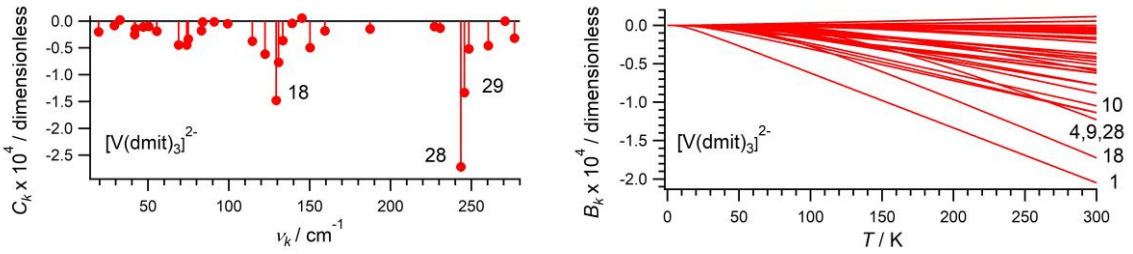

Fig. 26 Left: spin-vibration coupling constants C_k in **Eq. 33** of the first 33 molecular modes of **2** from 19 to 280 cm^{-1}. Right: B_k thermal contributions in **Eq. 32** to $\overline{\langle g_{||} \rangle}(T=0)$ of the first 33 molecular modes of **2** in the temperature range 0 – 300 K.

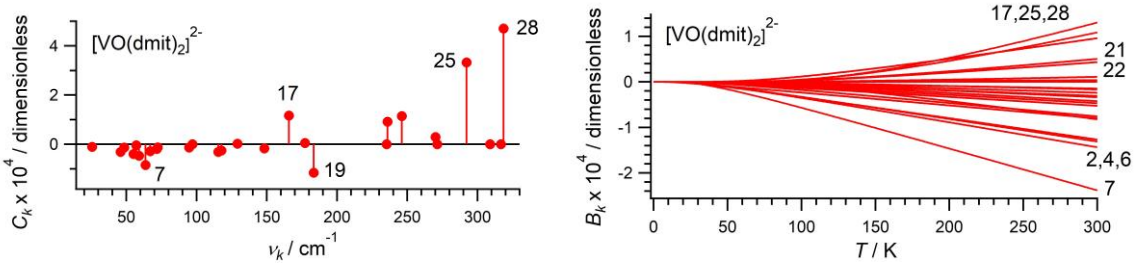

Fig. 27 Left: spin-vibration coupling constants C_k in **Eq. 33** of the first 28 molecular modes of **3** from 25 to 320 cm^{-1}. Right: B_k thermal contributions in **Eq. 32** to $\overline{\langle g_{||} \rangle}(T=0)$ of the first 28 molecular modes of **3** in the temperature range 0 – 300 K.

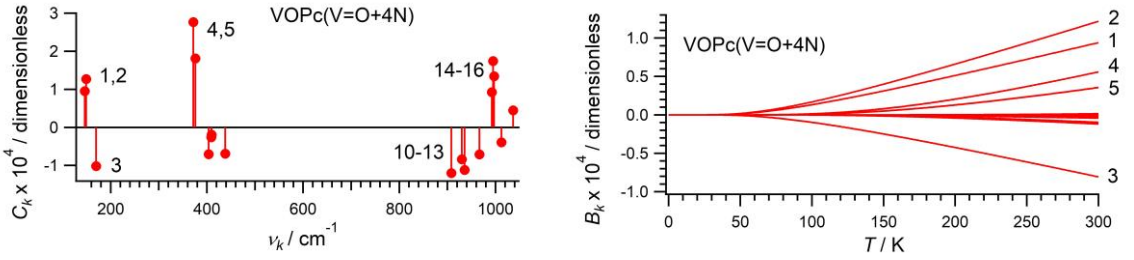

Fig. 28 Left: spin-vibration coupling constants C_k in **Eq. 33** of the 18 molecular modes of **4** from 140 to 1040 cm^{-1}. Right: B_k thermal contributions in **Eq. 32** to $\overline{\langle g_{||} \rangle}(T=0)$ of the 18 molecular modes of **4** in the temperature range 0 – 300 K. In this system, only the vanadyl moiety and the four vanadium-coordinating nitrogen atoms are left to vibrate.

The geometry relaxation and the vibrational spectrum calculation of **2**, **3**, **4** was also performed in the software package Gaussian09 by employing DFT.

On the other hand, the $g_{\parallel}^{rdc}$ determinations both at the relaxed and distorted geometries were conducted now with the code ORCA in collaboration with Prof. Eliseo Ruiz and Martín Amoza (University of Barcelona). The resulting IR spectrum and $g_{\parallel}^{rdc}$ values compared with the experimental data were of better accuracy than that of the ones produced for **1**. For instance, the calculation of $g_{\parallel}^{rdc}$ at the experimental geometries of **2**, **3**, **4** provided the values 1.997, 1.952, 1.963 with relative errors of 0.6%, 0.9%, 0.2%, resp. In addition, the relative errors of the highest calculated frequencies (1012 - 1036 cm^{-1}), namely vanadyl stretching frequencies in **4**, which can be taken as un upper bound for the rest of calculated frequencies as shown above, lie between 0.7 – 3.0%.[275] As done with **1**, we drop all modes of **2** and **3** with a harmonic frequency above ~300 cm^{-1}. In the case of **4** we keep all the 18 modes obtained when only the abovementioned six atoms are left to vibrate even if some modes are beyond the selected frequency limit. We make this decision to include the vanadyl stretching mode despite its large harmonic frequency above 1000 cm^{-1} and because 18 is still a reduced number of vibrations for a moderate computational cost. Note that, unlike **1**, the inclusion of a local mode term does not result in satisfactory fittings when modeling the experimental temperature dependence of $1/T_1$. Instead, it is enough to only consider the direct and Raman terms. As already mentioned above,[211] this means that molecular vibrations in the range 10 – 100 cm^{-1} may play the role of acoustic and optical phonons involved in the Raman process.

Perturbative analysis in mode coordinate

In the perturbative treatment up to second order in mode coordinate of $g_{\parallel}^{rdc}$, the CASSCF wave-functions of the five magnetic molecular orbitals that contain the single V^{4+} valence electron (derived in ORCA by solving the relevant Schrödinger-like equation) are firstly projected onto the model vector space whose basis set is composed of the five vanadium 3d orbitals $|xy\rangle$, $|yz\rangle$, $|xz\rangle$, $|z^2\rangle$, $|x^2-y^2\rangle$. This projection method is known as *ab initio* ligand field theory (AILFT),[276] and allows writing the following simple perturbative expression for $g_{\parallel}^{rdc}$ as a function of each given mode coordinate Q_k :

$$g_{\parallel}^{rdc}(Q_k) \approx \left(g_{\parallel}^{rdc}\right)_e \pm \frac{\zeta}{S}\sum_{i=1}^{4}\frac{\left|\left\langle E_i \left| \hat{L}_z \right| E_0 \right\rangle\right|^2 (Q_k)}{(E_i - E_0)(Q_k)} \qquad \textbf{Eq. 39}$$

In **Eq. 39** there are several variables to describe: $\left(g_{\parallel}^{rdc}\right)_e$ is the value of $g_{\parallel}^{rdc}$ evaluated at the relaxed geometry, ζ is the spin-orbit coupling parameter which is provided by ORCA and changes rather little in a small neighborhood of the relaxed geometry ($(\zeta)_e$= 166.4, 169.7, 179.3 cm^{-1}, for **2**, **3**, **4**, resp.), E_i is the energy of the excited state $|E_i\rangle$ while E_0 is the energy of the ground state $|E_0\rangle$, and $\hat{L}_z$ is the *z*-component of the vanadium orbital angular momentum. In our case, $S = 1/2$ and the sign to choose is the negative one since the V^{4+} 3d shell is less than half-filled. Whenever it is more than half-filled, the sign would be the positive one. In the particular case of a half-filled shell, the second-order perturbative term in **Eq. 39** vanishes. The states $|E_0\rangle$ and $|E_i\rangle$ are linear combinations of the abovementioned basis set whose coefficients are provided by ORCA:

$$\begin{aligned} |E_0\rangle &= c^0_{xy}|xy\rangle + c^0_{yz}|yz\rangle + c^0_{xz}|xz\rangle + c^0_{z^2}|z^2\rangle + c^0_{x^2-y^2}|x^2-y^2\rangle \\ |E_i\rangle &= c^i_{xy}|xy\rangle + c^i_{yz}|yz\rangle + c^i_{xz}|xz\rangle + c^i_{z^2}|z^2\rangle + c^i_{x^2-y^2}|x^2-y^2\rangle \end{aligned} \qquad \textbf{Eq. 40}$$

The matrix elements $\langle E_i|\hat{L}_z|E_0\rangle$ are easily calculated just by knowing the action of $\hat{L}_z$ on each basis set element:[228]

$$\begin{aligned} &\hat{L}_z|xy\rangle = -2i|x^2-y^2\rangle \quad \hat{L}_z|yz\rangle = -i|xz\rangle \quad \hat{L}_z|xz\rangle = i|yz\rangle \\ &\hat{L}_z|x^2-y^2\rangle = 2i|xy\rangle \quad \hat{L}_z|z^2\rangle = 0 \end{aligned} \qquad \textbf{Eq. 41}$$

The resulting squared matrix element $\left|\langle E_i|\hat{L}_z|E_0\rangle\right|^2$ reads as follows, where the asterisk denotes the conjugate complex number:

$$\left|\langle E_i|\hat{L}_z|E_0\rangle\right|^2 =$$

$$\left|2\left(\left(c^i_{xy}\right)^* c^0_{x^2-y^2} - \left(c^i_{x^2-y^2}\right)^* c^0_{xy}\right) + \left(\left(c^i_{yz}\right)^* c^0_{xz} - \left(c^i_{xz}\right)^* c^0_{yz}\right)\right|^2 \qquad \textbf{Eq. 42}$$

In **Table. 4**, we show $\left|\langle E_i|\hat{L}_z|E_0\rangle\right|^2$ and $E_\mathrm{i} - E_0$ of the four excitations $0 \rightarrow i$ for **2**, **3**, **4** at their respective relaxed geometries:

Table. 4 Squared matrix elements (top) and excitation energies (bottom) in **Eq. 39** for **2**, **3**, **4** evaluated at their relaxed geometries (see **Fig. 29**, **Fig. 30**, **Fig. 31**).

		$0 \rightarrow 1$	$0 \rightarrow 2$	$0 \rightarrow 3$	$0 \rightarrow 4$
$\left\|\langle E_i\|\hat{L}_z\|E_0\rangle\right\|^2$	**2**	$8.6 \cdot 10^{-3}$	$2.8 \cdot 10^{-2}$	$9.3 \cdot 10^{-3}$	$1.3 \cdot 10^{-2}$
	3	4.0	$2.3 \cdot 10^{-4}$	$3.0 \cdot 10^{-4}$	$1.2 \cdot 10^{-2}$
	4	$3.0 \cdot 10^{-4}$	$1.9 \cdot 10^{-2}$	3.9	$1.6 \cdot 10^{-3}$
$E_i - E_0$ (cm^{-1})	**2**	8449.1	8463.9	26181.2	26899.3
	3	21358.5	23211.4	23943.9	35088.9
	4	22768.3	23092.0	24684.1	34735.6

Importantly, for compounds **3** and **4** there clearly exists a quotient $\left(\left|\langle E_i|\hat{L}_z|E_0\rangle\right|^2 / (E_i - E_0)\right)_e$ that dominates over the rest, namely, the one corresponding to the excitation $0 \rightarrow 1$ and $0 \rightarrow 3$ resp. since the excitation energies are similar or within the same order of magnitude. On the contrary, although these excitation energies are also similar in **2**, in this case the four quotients are much more similar and none of them can be neglected. Of course,

this fact has to do with the wave-function composition in terms of the basis set elements $|xy\rangle$, $|yz\rangle$, $|xz\rangle$, $|z^2\rangle$, $|x^2-y^2\rangle$ of the ground AILFT state $|E_0\rangle$. Indeed, since $|E_0\rangle$ in **3** and **4** is equal to $|xy\rangle$ and to a combination of $|xy\rangle$ and $|x^2-y^2\rangle$ resp., the non-vanishing matrix elements are only produced with $|E_1\rangle$ and $|E_3\rangle$, which equal $|x^2-y^2\rangle$ and a combination between $|x^2-y^2\rangle$ and $|xy\rangle$, resp., see **Eq. 41** and **Eq. 42**. On the contrary, in **2**, $|E_0\rangle$ is approximately $c^0_{z^2}|z^2\rangle$ with $|c^0_{z^2}|\approx 1$ and, since $\hat{L}_z|z^2\rangle = 0$, the squared matrix elements $|\langle E_i|\hat{L}_z|E_0\rangle|^2$ are rather small but, more importantly, similar in magnitude as shown in **Table. 4**. Hence, while for **3** and **4** all excitations but one can be neglected, see **Eq. 43** and **Eq. 44** resp., in the case of **2** the four excitations must be included in **Eq. 39**.

Compound **3**: $$g_{\parallel}^{rdc}(Q_k) \approx \left(g_{\parallel}^{rdc}\right)_e - 2\zeta \frac{|\langle E_1|\hat{L}_z|E_0\rangle|^2 (Q_k)}{(E_1 - E_0)(Q_k)} \qquad \textbf{Eq. 43}$$

Compound **4**: $$g_{\parallel}^{rdc}(Q_k) \approx \left(g_{\parallel}^{rdc}\right)_e - 2\zeta \frac{|\langle E_3|\hat{L}_z|E_0\rangle|^2 (Q_k)}{(E_3 - E_0)(Q_k)} \qquad \textbf{Eq. 44}$$

The use of **Eq. 39**, **Eq. 43**, **Eq. 44** for **2**, **3**, **4** resp. provide accurate results at estimating the value of $g_{\parallel}^{rdc}(Q_k)$ -determined by ORCA- for $Q_k = 0$ with relative errors between 0.2 and 0.4%. In **Fig. 29**, **Fig. 30**, **Fig. 31**, it is shown the electron probability density of the five AILFT states for **2**, **3**, **4** resp. at their relaxed geometries.

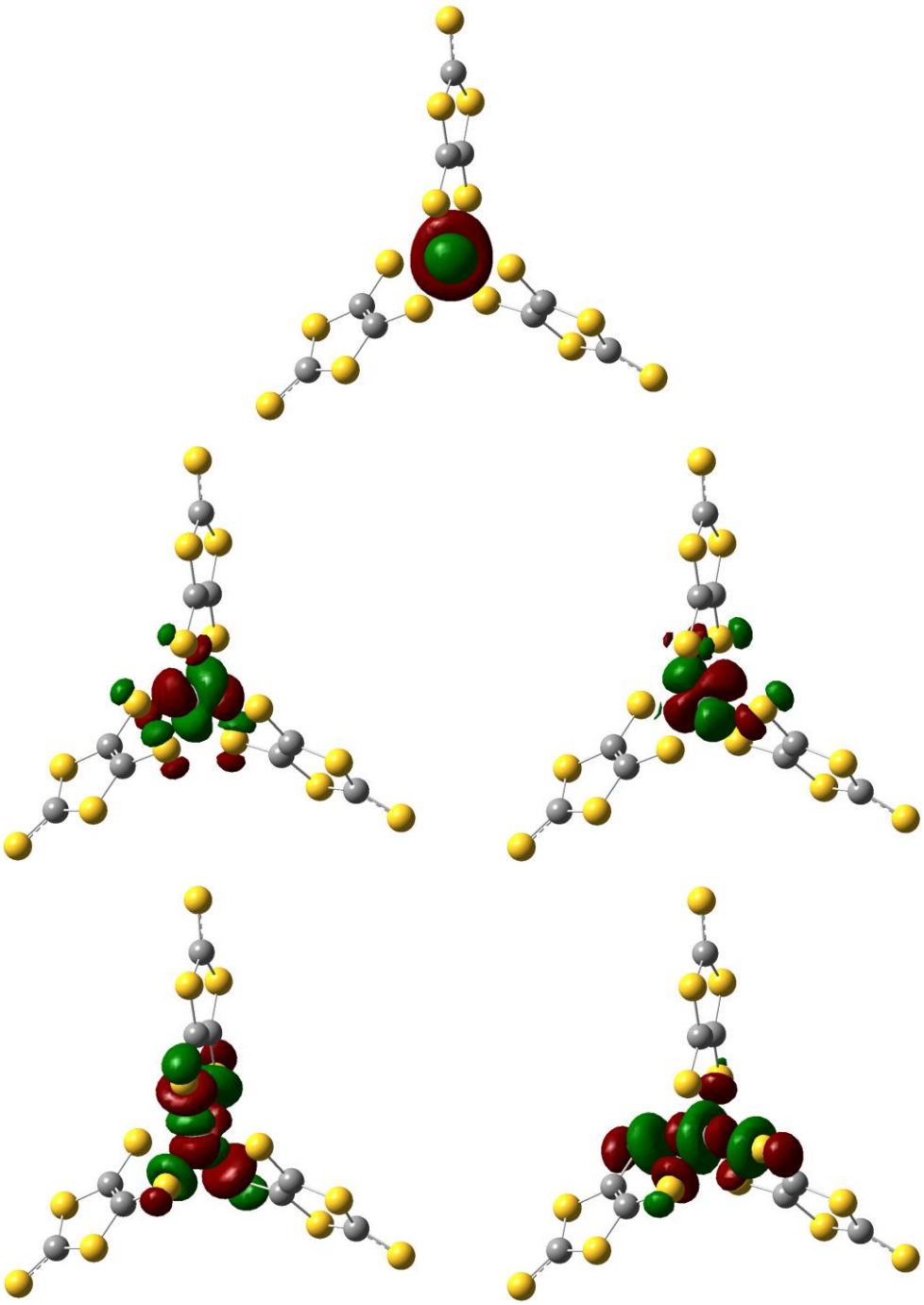

Fig. 29 Electron probability density representation of the five AILFT states at the relaxed geometry of **2**. Top: $|E_0\rangle$, Middle left: $|E_1\rangle$, Middle right: $|E_2\rangle$, Bottom left: $|E_3\rangle$, Bottom right: $|E_4\rangle$. Green and garnet colors denote space regions where the wave-function is positive and negative, resp.

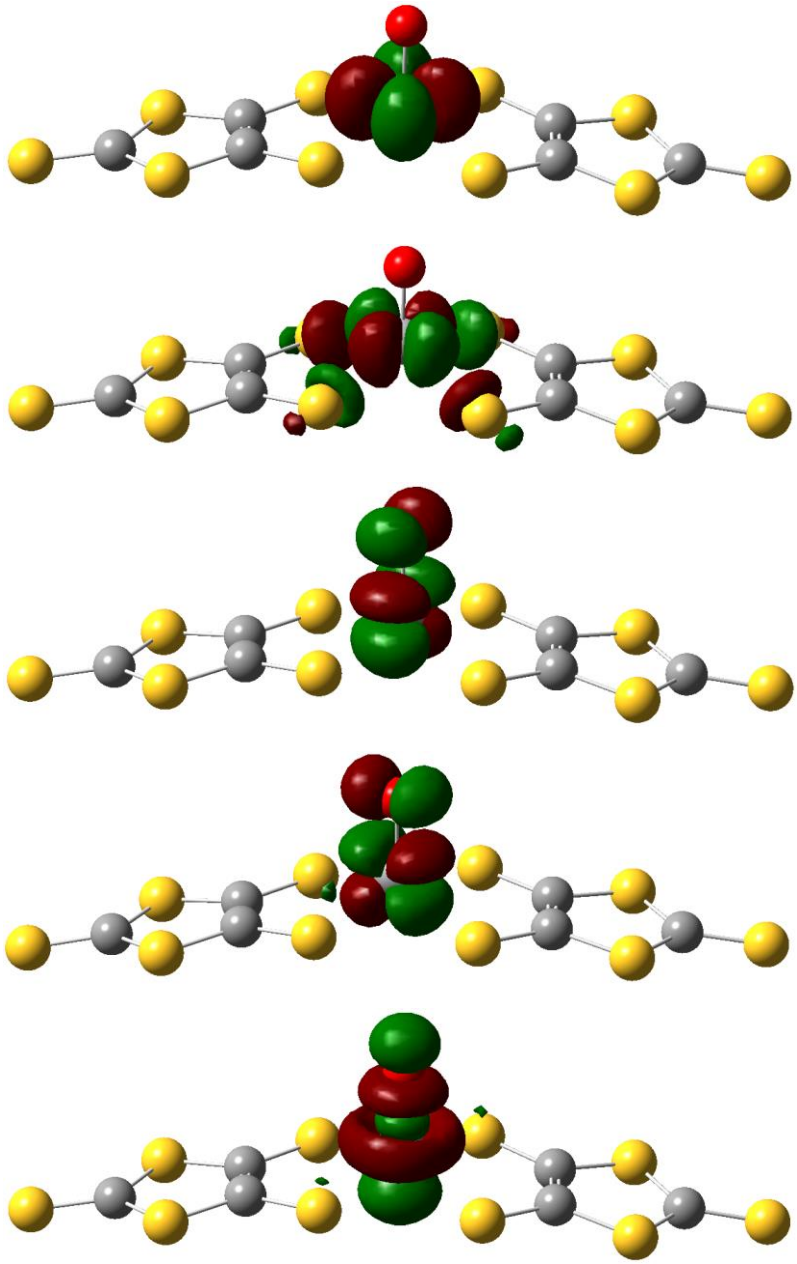

Fig. 30 Electron probability density representation of the five AILFT states at the relaxed geometry of **3**. From top to bottom: $|E_0\rangle$, $|E_1\rangle$, $|E_2\rangle$, $|E_3\rangle$, $|E_4\rangle$. Green and garnet colors denote space regions where the wave-function is positive and negative, resp.

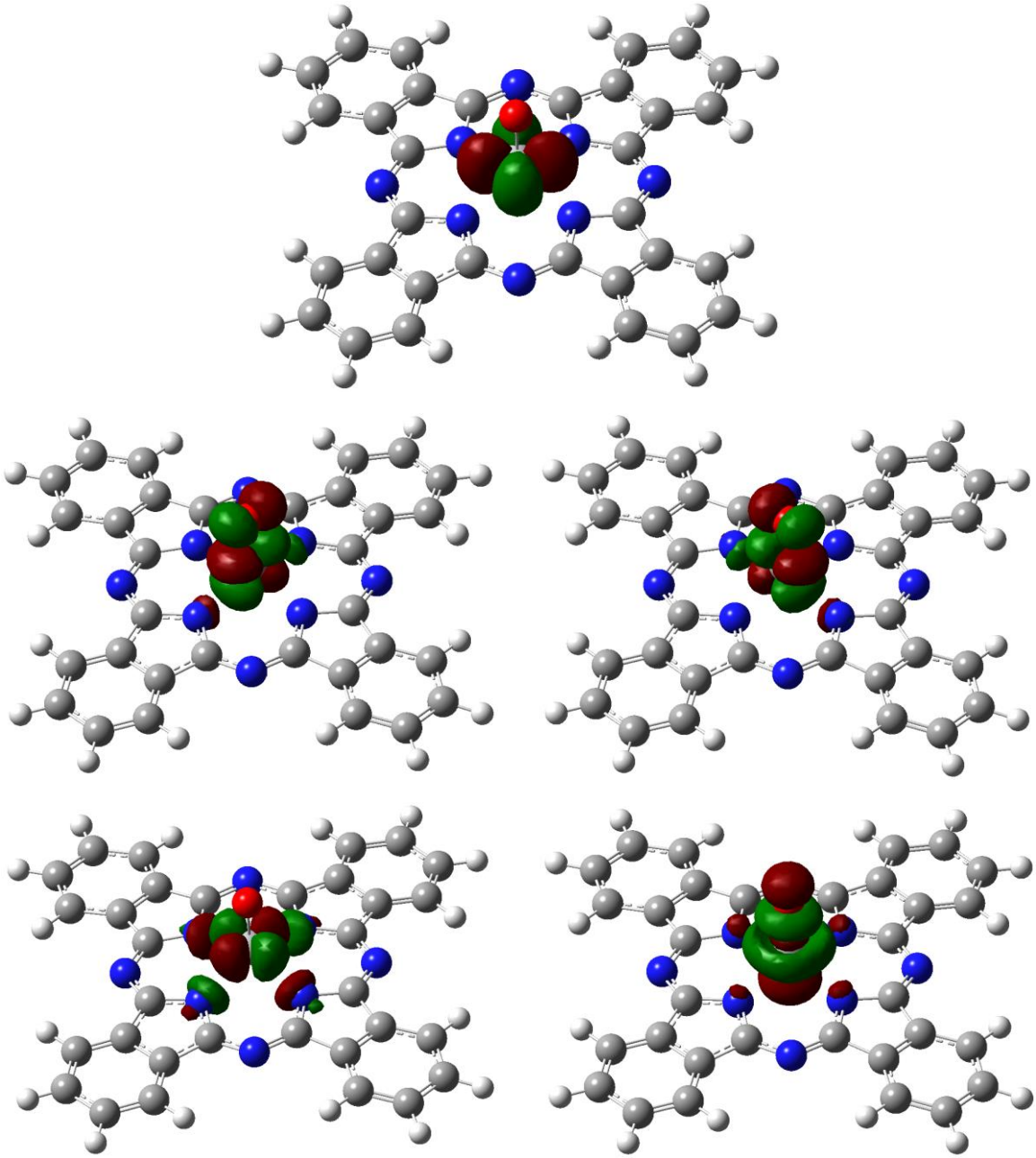

Fig. 31 Electron probability density representation of the five AILFT states at the relaxed geometry of **4**. Top: $|E_0\rangle$, Middle left: $|E_1\rangle$, Middle right: $|E_2\rangle$, Bottom left: $|E_3\rangle$, Bottom right: $|E_4\rangle$. Green and garnet colors denote space regions where the wave-function is positive and negative, resp.

Let us elaborate further on the wave-function composition of the five AILFT states as it was related to the faster spin-lattice relaxation of **2** with respect to **3**

in the experimental study.[239] Indeed, the faster relaxation of **2** was tentatively ascribed to a more pronounced contribution to the ground AILFT state $|E_0\rangle$ (i.e., the SOMO: semi-occupied molecular orbital) by different vanadium 3d orbitals. Instead, as shown above, by employing the same axes definition we found that for **2** and **3** $|E_0\rangle \approx c^0_{z^2}|z^2\rangle$ with $|c^0_{z^2}| \approx 1$ and $|E_0\rangle \approx c^0_{xy}|xy\rangle$ with $|c^0_{xy}| \approx 1$, resp. Hence, the difference between **2** and **3** seems to arise not from the SOMO pureness but rather from which are the vanadium 3d orbitals involved in it. For this, the key chemical factor might be the vanadyl moiety. Respect to **2**, where the SOMO is $\approx|z^2\rangle$, the introduction of this moiety in **3** stabilizes a SOMO that, in general, is a combination between $|xy\rangle$ and $|x^2-y^2\rangle$ depending on the X and Y axes definition. This new composition, besides making $g_{\parallel}^{rdc}(Q_k)$ be determined by a single excitation, seems to be the reason behind the preservation of quantum coherence up to room temperature in **3**. Thus, an important design principle would consist in stabilizing a SOMO mainly composed by a combination between the vanadium orbitals $|xy\rangle$ and $|x^2-y^2\rangle$, while a SOMO $\approx|z^2\rangle$ should be avoided. In this case, it has been achieved by replacing one of the ligands with a vanadyl moiety that results in a square pyramid coordination environment.

Mode analysis and correlations

The analysis of those modes that produce a linear, or near-linear, evolution in $g_{\parallel}^{rdc}(Q_k)$ with the distortion coordinate Q_k -hence, with the beneficial effect of a rather small second derivative of $g_{\parallel}^{rdc}(Q_k)$ respect to Q_k- reveals another correlation. Both in **3** and **4** it is possible to identify up to three of these modes. They involve symmetric motions around the vanadium atom, which may be facilitated by a higher molecular symmetry respect to **2**. For instance, those modes corresponding to **3** involve either joint displacements out of the molecular plane of both carbon and sulphur atoms, or a breathing vibration where the coordinating sulphur atoms move towards and away from the vanadium atom at once. These motions are also found in **4**, where the four vanadium-coordinating nitrogen atoms execute joint back-and-forth movements either out of the molecular plane or in the form of breathing

vibration. Interestingly, it is observed that these particular modes of **3** and **4** are the ones with the most evident linear evolution in the excitation energy 0→1 and 0→3 with the distortion coordinate, resp. This linear correlation between $g_{\|}^{rdc}(Q_k)$ and excitation energy with Q_k seems to be independent from the kind of evolution in the corresponding squared matrix element of **3** and **4**. Yet, the relative variation of the excitation energy in the corresponding range around $Q_k = 0$ is clearly greater than that of the matrix element for each one of these modes. In the compound **2**, it is hard to find this correlation as there is more than one excitation at play.

It is equally interesting to mention that those modes with the highest magnitude of C_k, which are initially the most detrimental ones, also present characteristic atomic motions. As a matter of fact, in all of the three compounds **2**, **3**, **4** these modes are also the ones with the highest magnitude in the second derivative of $g_{\|}^{rdc}(Q_k)$, despite C_k is also a function of the corresponding harmonic frequency and reduced mass. Both in **3** and **4** two of these modes involve a vanadyl swaying combined with approaching/separation of pairs of vanadium-coordinating sulphur atoms in the case of **3**. Besides, in **4** there are two extra modes that involve unsynchronized back-and-forth displacements of the four coordinating nitrogen atoms inside the molecular plane. The abovementioned approaching/separation motions of pairs of coordinating sulphur atoms are also observed in the corresponding modes of **2**. In this compound, other modes involve movements in these coordinating atoms outward and inward the ligand plane both synchronized and unsynchronized.

If the vanadyl swaying is key to relaxation, a possible strategy to further enhance coherence could be to block this motion to increase its energy, for instance, by introducing steric hindrance around it thus making C_k be smaller. Its calculated frequencies in **3** and **4** lie between 300 and 375 cm^{-1}, which may not produce a significant population at low temperature but rather the opposite at higher temperatures. On the other hand, movements in the coordinating sulphur atoms should also be removed and, for that, structures similar to that of phthalocyanine such as porphyrin are initially ideal. Indeed, in these structures the coordinating atoms are bonded to the ligands via two covalent bonds unlike **2** and **3** where there is only a single one. This might result in an increased frequency of the modes involving these movements as can be checked when comparing **4** to **2** and **3**, where the relevant modes of the former are about 700

-750 cm^{-1} higher in energy than those of **2** and **3**, whose frequencies are between 250 and 300 cm^{-1}.

Another point worth mentioning is the relative variation of the squared matrix element respect to its value in $Q_k = 0$. Interestingly, among the modes with the highest relative variation, which show a parabolic evolution, one find those modes with the highest magnitude in C_k. In the particular case of **2** -the fastest relaxing system-, these variations are even much higher with respect to **3** and **4**, and are present in a larger number of modes. Of course, as mentioned, for this larger variation to happen, the composition of the AILFT states plays a key role. Otherwise, if ideally these states were coincident with the vanadium 3d orbitals $|xy\rangle$, $|yz\rangle$, $|xz\rangle$, $|z^2\rangle$, $|x^2-y^2\rangle$, the resulting matrix elements would be rather constants and independent of Q_k. Hence, as can be seen, the compound with the highest relative variations in $\left|\langle E_i|\hat{L}_z|E_0\rangle\right|^2$ around $Q_k = 0$ corresponds to the one with the fastest spin-lattice relaxation at each given temperature.

On the contrary, a rather opposite correlation with respect to the modes with the highest magnitude in C_k is observed in the excitation energies $\Delta E_i = E_i - E_0$ for the three compounds. In particular, the modes of **2** with the highest relative variation in ΔE_i correspond to those with the smallest magnitude of C_k. Nevertheless, in this compound one has to note that the change in $g_{||}^{rdc}(Q_k)$ is mostly determined by the variation of $\left|\langle E_i|\hat{L}_z|E_0\rangle\right|^2$, which is much greater than that of ΔE_i. In **3**, we find the same for those modes with the highest variation in ΔE_i. In fact, among these modes there is one whose evolution in $g_{||}^{rdc}(Q_k)$ is close to be linear. Another important issue in this compound is that $\left|\langle E_i|\hat{L}_z|E_0\rangle\right|^2$ does not determine the evolution in $g_{||}^{rdc}(Q_k)$ anymore, since its relative variation in the relevant modes is at least one order of magnitude below that of ΔE_i. Lastly, **4** follows the same rule but importantly, besides $\left|\langle E_i|\hat{L}_z|E_0\rangle\right|^2$ does not control $g_{||}^{rdc}(Q_k)$ either, the modes with the highest variation in ΔE_i are precisely the ones that show the nearest linear trend in $g_{||}^{rdc}(Q_k)$ with Q_k. This behavior in the three systems seems to be in agreement with the evolution **2** < **3** ≤ **4** from the worst quantum-coherence performance to the best one.

All in all, if there are modes with high C_k among the ones with the highest variation in ΔE_i, there is no need to care about engineering ΔE_i since in this case it does not seem to determine the evolution of $g_{\parallel}^{rdc}(Q_k)$. Instead, whenever ΔE_i does determine the change in $g_{\parallel}^{rdc}(Q_k)$, the modes with the highest variation in ΔE_i seem to be the ones that produce near linear evolutions in $g_{\parallel}^{rdc}(Q_k)$ and hence rather small C_k. Therefore, instead of ΔE_i, the focus should be put on suppressing those factors that can allow changing $\left|\langle E_i|\hat{L}_z|E_0\rangle\right|^2$ with respect to its value at $Q_k = 0$, since a larger variation in this matrix element seems to correlate with a worse performance in the target compound. As noted above, this can be achieved via a proper composition of the five AILFT wave-functions in terms of the orbitals $|xy\rangle$, $|yz\rangle$, $|xz\rangle$, $|z^2\rangle$, $|x^2-y^2\rangle$. In the particular case of the three compounds under study, the introduction of the vanadyl moiety seems to be crucial for it.

As also suggested in the experimental study,[239] it is interesting to compare the frequencies of those modes in **2** and **3** that produce the highest values in C_k ($|C_k \cdot 10^4| \geq 1$) -which may be key for relaxation (see section 4.3)- in order to check the vanadyl rigidity role at increasing the given frequencies from **2** to **3**. In **2**, these frequencies are 129.2, 243.5, 245.7 cm^{-1} with $C_k \cdot 10^4$ = -1.5, -2.7, -1.3, resp. On the other hand, in **3** they are 165.7, 183.4, 246.2, 292.2, 318.5 cm^{-1} with $C_k \cdot 10^4$ = 1.2, -1.2, 1.1, 3.3, 4.7, resp. While the last two modes of **3** are indeed higher in energy than those of **2**, the remaining frequencies (165.7, 183.4, 246.2 cm^{-1}) lie approximately in between the energy limits 129 and 245 cm^{-1} for the frequencies of the modes of **2**. Thus, with not much different values for $B_k = C_k \langle n_k \rangle$ in the range 100 – 200 K where coherence is lost in **2**, the introduction of the vanadyl moiety would initially contribute with a rather limited role in terms of molecular rigidity. In other words, the rigidity in the stretching vibration might not be the only decisive factor behind the enhanced performance in **3** respect to **2**.

4.3 $[U(Cp^{ttt})_2]^+$

In chapter 2, we have talked about some important strategies that have commonly been employed to improve the performance of molecular nanomagnets, namely, (i) the need of a large ground *J* quantum number, (ii) non-mixed wave-functions with a ground spin doublet composed by the projections ±*J*, and (iii) a large energy barrier that separates these two components. This constitutes the so-called static picture, which can be tuned by properly engineering the electronic structure of the low-lying 2*J*+1 states via chemical modification of ligands. Often, this has been enough to systematically increase relaxation times in a given temperature range as well as blocking temperatures, T_b, which importantly determine the highest temperature that still allows observing the magnetic hysteresis loop. Nevertheless, once all the parameters in (i), (ii), (iii) are properly optimized, magnetic relaxation will now be determined by alternative mechanisms, which are the ones that should now be addressed and suppressed. In other words, further optimization of (i), (ii), (iii) will not lead to molecular nanomagnets with a better performance if the parameters involved therein are not limiting the achievement of higher relaxation times and blocking temperatures anymore.[277] As mentioned, one of the main goals nowadays is to develop operative nanomagnets at increasing temperature. This introduces the spin-vibration coupling as one of those new key parameters to optimize, since vibration-mediated magnetic relaxation, e.g. Raman, Orbach and local mode, becomes more important as temperature is raised. If firstly the electronic structure engineering allowed increasing T_b from 2 K to 14 K in the period 2004 – 2011,[160,278] the recent consideration of this additional dynamic picture where spins are coupled to lattice and molecular vibrations have produced an outstanding jump forward both in τ and T_b from 14 K to 60 K and 80 K during the last seven years.[164,165]

These two last compounds are mononuclear Dy-based bis-metallocenium cations, $[Dy(Cp^{ttt})_2]^+$ (T_b = 60 K) and $[Dy(Cp^*)(Cp^{iPr5})]^+$ (T_b = 80 K) (where Cp^{ttt} = $\{C_5H_2{}^tBu_3\text{-}1,2,4\}$, Bu_3 = $C(CH_3)_3$, Cp^* = pentamethylcyclopentadienyl, Cp^{iPr5} = penta-iso-propylcyclopentadienyl), which interestingly do not display an axial symmetry but a rather distorted one, see **Fig. 32**. First-principles calculations provided insight on the spin relaxation pathway among the several low-lying 2*J*+1 states in $[Dy(Cp^{ttt})_2]^+$ and, more importantly, allowed identifying the relevant molecular vibrations involved in driving the spin population across this pathway. The subsequent ligand modification aimed at

removing these vibrations produced the compound $[Dy(Cp^{*})(Cp^{iPr5})]^{+}$ displaying an unprecedented blocking temperature of 80 K. Thus, bis-metallocenium cations are opening a new avenue for a further improvement in the case of Ln-based SIMs, and are currently under an intense study both experimental and theoretical.[183,279]

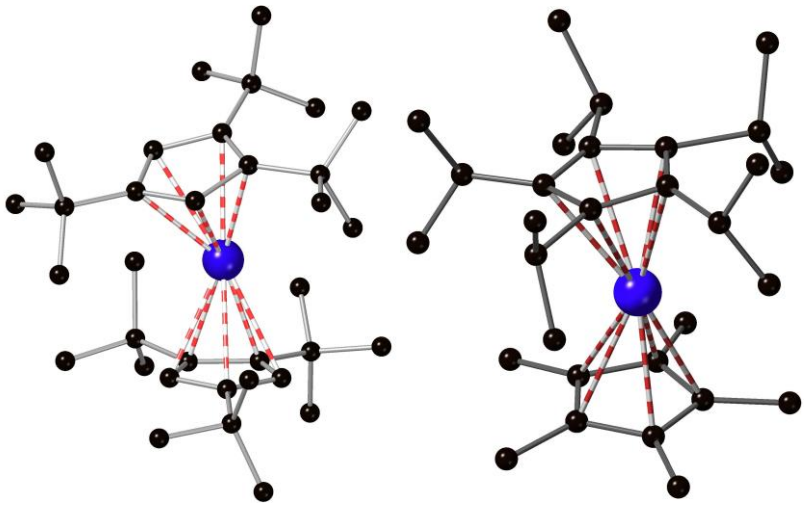

Fig. 32 $[Dy(Cp^{ttt})_2]^{+}$ (left) and $[Dy(Cp^{*})(Cp^{iPr5})]^{+}$ (right) molecular compounds where the angles $\measuredangle CpDyCp$ are 152.8º and 162.5º, resp. Dy: blue, C: black. H omitted for clarity.

By keeping these optimized metallocenium ligands into consideration, it is worth wondering now whether the overall magnet performance could be further improved by selecting other potential metal ions such as actinides as the next natural frontier to explore. Indeed, 5f orbitals in actinides are known to have a more diffuse electron density in space than 4f orbitals of lanthanides.[159] This initially gives rise to a stronger interaction between 5f orbitals and ligand p orbitals, which would enhance total zero field splittings and enable actinide ions as potential candidates to provide better SIMs.[280] For instance, this splitting could be larger in U^{3+} and even up to one order of magnitude higher in U^{4+} respect to lanthanides. Due to the majority radioactive behavior of actinides, there exist few candidates available with some very long-lived isotope able to produce stable molecular compounds. This fact excludes all actinide ions but the ones based on ^{232}Th, ^{238}U, ^{237}Np, ^{244}Pu, and ^{247}Cm, being ^{238}U the most popular as others either are present in an extremely low natural occurrence or

need to be synthesized in specialized labs. Herein, we will focus on $^{238}U^{3+}$ since it has a Russell-Saunders ground level $^{4}I_{9/2}$ (like Nd^{3+}) with the largest $J = 9/2$ quantum number compared to the ions $^{238}U^{4+}$ ($^{3}H_4$) and $^{238}U^{5+}$ ($^{2}F_{5/2}$). Indeed, while slow relaxation of magnetization has been observed in all these three ions,[159,280–282] $^{238}U^{3+}$-based molecular compounds seem to be more inclined towards SIM behavior as it has been detected in a range of ligand fields of vastly differing symmetries, although only with moderate energy barriers.[187,283–290]

Only very recently (2019), the $^{238}U^{3+}$ ion has been experimentally tested for the first time with one particular bis-metallocenium ligand, altogether also in the form of a cationic unsymmetrical compound with bending angle $\measuredangle CpUCp$ = 167.82º.[291] Contrary to expectations, a poor dynamic magnetic performance was measured with no detected slow relaxation at zero field and no reported hysteresis loop, and relaxation times only observable up to 6 K under an external static field of 1000 Oe. Theoretical calculations suggest that metal-ligand covalency leads to a partially quenched orbital angular momentum and fast magnetic relaxation at zero field via quantum tunneling. Therefore, it seems that unsymmetrical actinide metallocenes, unlike the lanthanide-based analogs, could be unlikely to produce exceptional SIMs. In this situation, a more suitable approach would be to enforce 5f orbital degeneracy by designing systems with strict high point symmetry and/or by decreasing the mixing with ligand orbitals.

In this section, we pursue two goals, one general and one particular. In the first place, as shown above, the first-principles evaluation of the spin-vibration coupling in molecular nanomagnets is still a hardly systematic task that involves many computationally demanding calculations.[164,165] Below, we will propose a novel *ab initio* methodology devoted to Ln- and U-based SIMs that relies on a single first-principles calculation, while the rest of calculations are inexpensive. Importantly, this method produces a drastic decrease in the computational time for the first time thus allowing a much faster exploration of potential candidates *in silico* before the lab stage. Moreover, it is able to identify low-frequency molecular vibrations that may assume the role of optical phonons in Orbach and Raman relaxation processes, which opens the path towards a rational re-design of ligands to suppress them and improve the magnet performance. In the second place, we intend to particularly rationalize the apparently limited performance of bis-metallocenium U^{3+}-based SIMs, as well as to compare them with other U^{3+}-based SIMs previously reported. For that purpose, the aforementioned

methodology will be applied to the hypothetical analog $[U(Cp^{ttt})_2]^+$ (hereafter referred to as **5**) of $[Dy(Cp^{ttt})_2]^+$ where Dy^{3+} is replaced by U^{3+}, which will also serve as a prediction.

In chapter 2, we have discussed the suitability of the Russell-Saunders coupling scheme to describe the low-lying electronic structure of Ln ions as building blocks of SIMs. Instead, this picture is not necessarily also valid for actinide ions,[174] since in this case the inter-electronic repulsion (~10^4 cm^{-1}), spin-orbit coupling (~10^3 cm^{-1}) and ligand field potential (~10^3 cm^{-1}) become similar in magnitude. Ultimately, this brings an important consequence in the modelling of actinide-based coordination compounds. Indeed, to properly describe this electronic situation, a new coupling scheme may be put at play, namely, the *J*-mixing scheme. This scheme is favorable when there can exist a significant enough mixing between the ground level $^{2S+1}L_J$ and excited ones if, for instance, the gap energy Δ between them is small, see **Fig. 3**. In other words, this ground level cannot be considered as isolated anymore and hence *J* is no longer a well-defined quantum number.

In particular, calculations have shown that, for $5f^2$, $5f^3$ and $5f^4$ configurations, the Russell-Saunders scheme can recover only up to an 80% of the ground state wave-function as determined from the *J*-mixing coupling scheme.[292,293] This percentage is even lower in the case of Am^{3+} (44.9%), which constitutes one of the worst scenarios. To complete the comparison, note the best situation for lanthanide ions with a 94% for Er^{3+}. In the case of the U^{3+} ion, with a $5f^3$ configuration, the Russell-Saunders scheme recovers around an 84.1% of the ground state wave-function. This accuracy is further lowered for U^{4+}, with a $5f^2$ configuration, where the percentage is around 77.5%.[294] These limitations in accuracy restrict the use of the package SIMPRE to lanthanides, which only considers the ground level $^{2S+1}L_J$ but neglects any excited one. For a proper description of U-based SIMs, one also has to include the excited *J* multiplets whose effects are now more important and not negligible at all. Thus, the Crystal Field Hamiltonian (Russell-Saunders + only ground $^{2S+1}L_J$) must be replaced by the full Hamiltonian $\hat{H}$ in **Fig. 3**, where kinetic energy, inter-electron repulsion, spin-orbit coupling and ligand field are treated explicitly along with the whole set of *J* multiplets. Since this coupling scheme is not included in SIMPRE yet, we will use the CONDON package which contains and diagonalizes $\hat{H}$.[174,295]

Preliminary equations and proposed methodology

The key tool to evaluate the spin relaxation dynamics is the so-called master equation, which determines the time evolution of the spin population flow through a set of Hamiltonian eigenstates from an initial situation. We use the well-established Pauli master equation, see **Eq. 45**, as commonly done in the case of single-ion molecular nanomagnets.[75,164]

$$\frac{dp_i(t)}{dt} = \sum_{f=1,\, f\neq i}^{2J+1} \left[\gamma_{f\to i} p_f(t) - \gamma_{i\to f} p_i(t)\right],\ i = 1,\ldots,2J+1 \qquad \textbf{Eq. 45}$$

In **Eq. 45**, J corresponds to the ground level $^{2S+1}L_J$ for Ln^{3+} ions, while for U^{3+} we use $J = 9/2$. On the other hand, $0 \le p_i(t) \le 1$ is the spin population present at the eigenstate $|i\rangle$ at a given time t, and all of them are such that $\sum_i p_i(t) = 1$. To solve the master equation, which means to calculate each $p_i(t)$ as a function of time, we will need to set the initial conditions $p_i(0)$ at $t = 0$. The transitions rates (probability per unit time) from a given $|i\rangle$ to any $|f\rangle$ and from $|f\rangle$ to $|i\rangle$ are $\gamma_{i\to f}$ and $\gamma_{f\to i}$, resp. Thus, $\gamma_{i\to f} p_i(t)$ and $\gamma_{f\to i} p_f(t)$ determine the outcoming and incoming flows respect to the given $|i\rangle$, resp. Their difference is the net flow in $|i\rangle$ and equals the variation of its spin population with time according to **Eq. 45**.

Besides the initial conditions $p_i(0)$, we also need to introduce the aforementioned transition rates as an input in the master equation. To determine the probability per unit time of driving a transition from a state characterized by the ket $|E_i, n_j\rangle$ -where $|E_i\rangle$ is a given initial eigenstate with energy E_i and the quantum number n_j describes the eigenstate of a given 1D harmonic vibrational mode j- to another state $|E_f, n_j \pm 1\rangle$ either by emitting or by absorbing a phonon -where E_f is the energy of a given final eigenstate $|E_f\rangle$- is common to proceed by employing the so-called Fermi Golden Rule.[75] This rule is usually prepared

to incorporate a given expression of the phonon density of states. For example, the most employed phonon density of states is that of the Debye model, where this density is proportional to the square of the phonon frequency. Then, one integrates the transition rate over this phonon frequency up to the Debye temperature, and the resultant expression depends on some parameters such as the crystal longitudinal and transverse sound velocities. Let us recall that the current main goal is the development of fully *ab initio* methodologies, in particular, by not assuming any specific form in the phonon density of states. This means being able to incorporate the vibrational spectrum as provided by first-principles calculations. In solid state systems, typical vibrational energies are close enough so that it is considered they form an energy continuum. That is why the phonon frequency in the Debye model appears as a continuous variable -not discrete- which is subsequently integrated over a given real interval. On the contrary, a first-principles software will always provide a finite number R of vibrational modes (each one with its harmonic frequency, reduced mass, force constant and displacement vector). These vibrations are the result of diagonalizing the so-called force matrix which has always a finite size. To incorporate this finite set of vibrations into the transition rates, we need to replace the standard integral of the phonon frequency over a real interval by a summation over this given set of vibrations. Thus, the transition rates we show below are the result of adapting the standard Fermi Golden Rule, where the integral over the phonon frequency have been substituted by a summation over all vibrational modes as proposed by Goodwin et al.[164] Since the spin-vibration coupling is calculated up to second order in perturbation theory, there no exist crossed interactions among different vibrational modes and the transition rate expressions are just a finite summation over non-interacting harmonic vibrations. Moreover, these transition rates have been derived under the so-called Born-Oppenheimer approximation whereby the electronic and nuclear dynamics are uncoupled thus resulting in non-adiabatic electronic transitions. Herein, we will work with the vibrationally-induced transition rates between given pairs of eigenstates corresponding to the Orbach and second-order Raman processes.

Orbach transition rates:

The Orbach relaxation process is a finite sequence of direct transitions $|i\rangle \to |f\rangle$ where each one of them is driven by only one resonant phonon with the energy difference $|E_f - E_i|$. The process starts in an initial eigenstate with unity population. Then, the spin is excited to higher intermediate eigenstates in the potential barrier through phonon absorption. Once the barrier has been crossed (either by overcoming the highest eigenstate or by tunneling), this is followed by a cascade of de-excitations until reaching a final eigenstate through phonon emission. The transition rates read as follows and depend on whether the transition $|i\rangle \to |f\rangle$ is driven through a phonon absorption or emission:

Absorption $$\gamma_{i\to f} = \frac{2\pi}{\hbar}\sum_{j=1}^{R}\left[\left|\langle i|\hat{H}_j|f\rangle\right|^2 \left|\langle n_j - 1|\varepsilon_j|n_j\rangle\right|^2 \rho_j\left(\left|E_i - E_f\right|\right)\right] \qquad \textbf{Eq. 46}$$

Emission $$\gamma_{i\to f} = \frac{2\pi}{\hbar}\sum_{j=1}^{R}\left[\left|\langle i|\hat{H}_j|f\rangle\right|^2 \left|\langle n_j + 1|\varepsilon_j|n_j\rangle\right|^2 \rho_j\left(\left|E_i - E_f\right|\right)\right] \qquad \textbf{Eq. 47}$$

Second-order Raman transition rates:

In the second-order Raman process, each transition $|i\rangle \to |f\rangle$ is not direct but driven through an intermediate eigenstate $|c\rangle$, and involves two resonant phonons with the energy differences $|E_c - E_i|$ and $|E_f - E_c|$. The first phonon j mixes $|i\rangle$ with $|c\rangle$, while the second one l mixes $|c\rangle$ with $|f\rangle$. Now, the case $E_i = E_f$ has a certain transition rate whose value is not necessarily zero. Given $|i\rangle$ and $|f\rangle$, the transition rate expression includes all intermediate eigenstates $|c\rangle$ but the ones with an energy E_c equal to both E_i and E_f. Thus, given $|i\rangle$ and $|f\rangle$, for each $|c\rangle$ only one of the following four options is possible: (i) $E_i < E_c > E_f$, (ii) $E_i > E_c < E_f$, (iii) $E_i > E_c > E_f$, (iv) $E_i < E_c < E_f$. The transition rate expression is as follows:

$$\gamma = \frac{2\pi}{\hbar} \sum_{\substack{c=1 \\ E_c \neq E_i, E_f}}^{2J+1} \sum_{j=1}^{R} \sum_{l=1}^{R} [\ ] \qquad \textbf{Eq. 48}$$

$$[\ ] = \frac{\left|\langle c|\hat{H}_j|i\rangle\right|^2 \left|\langle f|\hat{H}_l|c\rangle\right|^2}{|E_c - E_i||E_f - E_c|} \Theta(c,j)\Theta(c,l)\rho_j\left(|E_c - E_i|\right)\rho_l\left(|E_f - E_c|\right)$$

In case of (i), the phonon j is absorbed and the phonon l is emitted; hence $\Theta(c,j) = \left|\langle n_j - 1|\varepsilon_j|n_j\rangle\right|^2$ and $\Theta(c,l) = |\langle n_l + 1|\varepsilon_l|n_l\rangle|^2$. In case of (ii), the phonon j is emitted and the phonon l is absorbed; hence $\Theta(c,j) = \left|\langle n_j + 1|\varepsilon_j|n_j\rangle\right|^2$ and $\Theta(c,l) = |\langle n_l - 1|\varepsilon_l|n_l\rangle|^2$. In case of (iii), the phonon *j* is emitted and the phonon *l* is emitted; hence $\Theta(c,j) = \left|\langle n_j + 1|\varepsilon_j|n_j\rangle\right|^2$ and $\Theta(c,l) = |\langle n_l + 1|\varepsilon_l|n_l\rangle|^2$. In case of (iv), the phonon *j* is absorbed and the phonon *l* is absorbed; hence $\Theta(c,j) = \left|\langle n_j - 1|\varepsilon_j|n_j\rangle\right|^2$ and $\Theta(c,l) = |\langle n_l - 1|\varepsilon_l|n_l\rangle|^2$.

Strain tensor matrix elements:

$$\left|\langle n_j - 1|\varepsilon_j|n_j\rangle\right|^2 = \frac{1}{e^{\hbar\omega_j/k_BT} - 1} \qquad \left|\langle n_j + 1|\varepsilon_j|n_j\rangle\right|^2 = \frac{1}{1 - e^{-\hbar\omega_j/k_BT}} \qquad \textbf{Eq. 49}$$

These matrix elements describe the strain suffered by the lattice when the vibrational mode *j* absorbs or emits a phonon, where ε_j is the so-called strain tensor. The vibration bath is considered to be thermalized, i.e., its dynamics is much faster than that of the magnetic relaxation. Thus, these matrix elements are proportional to the Bose-Einstein statistics of the given vibrational mode *j*, and depend only on temperature.[75,296,297] Note that when temperature $T \to 0$ the left matrix element in **Eq. 49** vanishes, but not the right term which tends to 1.

This means that some transition rates do not necessarily vanish as $T \to 0$, and thus the spin may also relax even at very low temperature.

Distribution of phonon energies:

$$\rho_j(\hbar\omega) = \frac{1}{\sigma\sqrt{2\pi}} \exp\left(-\frac{1}{2}\left(\frac{\hbar\omega - \hbar\omega_j}{\sigma} \right)^2 \right) \quad j = 1, \ldots, R \qquad \textbf{Eq. 50}$$

There is another modification implemented in the above transition rates. The original expressions contain the Dirac delta function $\delta(\hbar\omega - \hbar\omega_j)$, where $\hbar\omega = |E_f - E_i|$ is the energy difference between final and initial eigenstates. The conservation of energy implies that $\hbar\omega$ must equal the phonon energy $\hbar\omega_j$ of a given vibrational mode *j*. Otherwise, both $\delta(\hbar\omega - \hbar\omega_j)$ and the corresponding transition rate vanish, i.e., there is no spin transition. As said above, first-principles packages provide a discrete vibrational spectrum. Thus, it is quite unlikely to find a vibrational mode whose phonon energy exactly matches a given energy difference $|E_f - E_i|$, and hence one would not observe any spin relaxation. To solve this issue, the Dirac delta function is replaced by a Gaussian convoluted spectrum around the phonon energy $\hbar\omega_j$ of the given vibrational mode *j*. In other words, the phonon energy is let to have an uncertainty width around its value $\hbar\omega_j$. This width is determined by the standard deviation parameter σ, and can be estimated by inspecting the experimental IR and Raman vibrational spectra (the full-width-half-maximum linewidth is twice as much as σ). This parameter has to be estimated carefully, since a too small value makes the Gaussian convoluted spectrum become too much similar to a delta function, and no relaxation is observed. On the contrary, a too large value means a continuously flat vibrational spectrum which is not observed for molecular systems.

Spin-vibration coupling matrix elements:

To model vibration-mediated spin relaxation in molecular nanomagnets, we are proposing a new methodology based on the following picture currently employed: an equilibrium electronic structure, in the form of a potential barrier where the spin is initially located at one side, perturbed by a set of harmonic vibrations that drive the spin through a set of Hamiltonian eigenstates. Prior to determine the equilibrium electronic structure, one first has to relax the molecular geometry. Then, the determination of the IR spectrum provides the set of vibrations with harmonic frequencies ν_j, reduced masses m_j and displacement vectors $\vec{u}_j$. The next step is to perform a CASSCF calculation on the experimental molecular geometry to extract the lowest $2J+1$ spin energies.[164] After setting the coordinate origin at the metal experimental position, the experimental positions of the metal-coordinating atoms are introduced in SIMPRE. As explained in chapter 3, this code first calculates the CFPs and then diagonalizes the $2J+1$-sized Crystal Field Hamiltonian corresponding to the ground level $^{2S+1}L_J$. The charge magnitudes and the metal-charge radial distances are varied to fit the CASSCF energies.[216,224] To speed up the fitting procedure, quite often it will be enough to use the same charge magnitude and radial distance variation in each coordinating atom. Thus, we project the CASSCF information onto the first coordination sphere via effective parameters. Of course, the CASSCF evaluation can be avoided if the low-lying experimental energies are available. In this case, the experimental structure used in SIMPRE should be determined at the same temperature as that of the experimental energies.

Now, the coordinating atom positions of the relaxed geometry are radially varied with the same fitting distance variations previously determined in SIMPRE. By using the same found charge values, SIMPRE calculates the equilibrium CFPs $\left\{\left(A_k^q\left\langle r^k\right\rangle\right)_{eq}\right\}_{k,q}$ in Stevens notation. As mentioned above, excited states beyond the ground J multiplet may also influence the low-lying electronic structure of actinide SIMs unlike lanthanide ions. Thus, in case of U^{3+}, to determine the charge magnitude and the radial distance variation, the energy fitting must be replaced by a fitting of the SIMPRE CFPs to the CFPs either CASSCF or experimental.

The diagonalization in SIMPRE of the equilibrium Crystal Field Hamiltonian $\hat{H}_{eq} = \sum_{k=2,4,6} \sum_{q=-k}^{k} \left(A_k^q \left\langle r^k \right\rangle \right)_{eq} a_k \hat{O}_k^q$ provides the equilibrium electronic structure, i.e., the lowest $2J+1$ equilibrium eigenstates and energies corresponding to the ground level $^{2S+1}L_J$. For the U^{3+} ion, the diagonalization is performed in CONDON, where the CFPs must be introduced in Wybourne notation as this software uses a rather different implementation of the ligand field operators. Then, the obtained eigenstates are truncated to the ordered basis set $\{|-J\rangle,...,|+J\rangle\}$ of the ground $J = 9/2$ multiplet and then renormalized.

The perturbing Hamiltonians $\left\{ \hat{H}_j = \sum_{k=2,4,6} \sum_{q=-k}^{k} \Delta\left(A_k^q \left\langle r^k \right\rangle \right)_j (T) a_k \hat{O}_k^q \right\}_j$, which are built in the same ordered basis set as the equilibrium eigenstates, account for the perturbation to the equilibrium electronic structure from each vibrational mode j. Their determination requires to estimate the temperature-dependent change $\Delta\left(A_k^q \left\langle r^k \right\rangle \right)_j (T)$ produced in $\left(A_k^q \left\langle r^k \right\rangle \right)_{eq}$ after activating each mode j. We use our model derived above which provides the following perturbative expression up to second-order in mode coordinate Q_j for $\Delta\left(A_k^q \left\langle r^k \right\rangle \right)_j (T)$:

$$\Delta\left(A_k^q \left\langle r^k \right\rangle \right)_j (T) = \frac{\hbar}{4\pi} \left(\frac{\partial^2 A_k^q \left\langle r^k \right\rangle}{\partial Q_j^2} \right)_{eq} \frac{1}{m_j \nu_j} \left(\left\langle n_j \right\rangle + \frac{1}{2} \right) \qquad \textbf{Eq. 51}$$

The determination of $\left(\partial^2 A_k^q \left\langle r^k \right\rangle / \partial Q_j^2 \right)_{eq}$ is as follows. For each mode j, several distorted geometries $\left\{ \overrightarrow{v_d^j} \right\}_d$ are generated around the relaxed geometry $\overrightarrow{v_{eq}}$ by following the corresponding displacement vector $\vec{u}_j$. Then, we run a SIMPRE calculation at each distorted geometry $\overrightarrow{v_j^d}$ to determine the set of CFPs $A_k^q \left\langle r^k \right\rangle$ in cm^{-1} by following the same procedure employed to determine $\left\{ \left(A_k^q \left\langle r^k \right\rangle \right)_{eq} \right\}_{k,q}$. Namely, we apply the same radial distance variations and charge magnitudes to the metal-coordinating atoms in these distorted geometries. Hence, for each

mode *j* and each CFP we have a set of pairs $\left\{\left(\left(A_k^q\left\langle r^k\right\rangle\right)_j^d, Q_j^d\right)\right\}_d$. By fitting each plot $\left(A_k^q\left\langle r^k\right\rangle\right)_j^d$ vs Q_j^d to a polynomial and evaluating its second derivative at $Q_j = 0$ we access $\left(\partial^2 A_k^q\left\langle r^k\right\rangle / \partial Q_j^2\right)_{eq}$. Then, by performing a simple vector-matrix-vector product, it is possible to compute each given spin-vibration coupling matrix element $\langle i|\hat{H}_j|f\rangle$. Note that for the first time we introduce a temperature dependence in these matrix elements through each boson number $\langle n_j\rangle$. In the case of U^{3+}, the Stevens coefficients to use in $\hat{H}_j$ are the same of the isoelectronic metal ion Nd^{3+}.

Crucially for our interests, the elements $\langle i|\hat{H}_j|f\rangle$, which compose the transition rates γ that connect the pairs of eigenstates $|i\rangle$ and $|f\rangle$, depend proportionally on **Eq. 86** through the perturbing Hamiltonians $\hat{H}_j$. Thus, we can state again the key role of **Eq. 51** regarding magnetic relaxation. Indeed, the evaluation of this relaxation depends on solving a master equation, which determines the time evolution of the spin population through several Hamiltonian eigenstates. This equation depends on the abovementioned transition rates and they consist in a summation of independent contributions each one accounting for a different vibrational mode. As mentioned, the key point is that each one of these contributions is proportional to the corresponding matrix element $\langle i|\hat{H}_j|f\rangle$. Hence, since $\hat{H}_j$ is proportional to **Eq. 51**, in order to suppress the transition rates and consequently magnetic relaxation, we need to unavoidably look for strategies aimed at canceling each $\Delta\left(A_k^q\left\langle r^k\right\rangle\right)_j(T)$. We already stated that some simple strategies may consist in increasing both the harmonic frequencies ν_j and reduced mass m_j. In addition, a complementary and beneficial effect is that of those modes that give a quasi-linear evolution in $A_k^q\left\langle r^k\right\rangle$ with Q_j around the relaxed geometry, since they will produce a rather negligible second derivative $\left(\partial^2 A_k^q\left\langle r^k\right\rangle / \partial Q_j^2\right)_{eq}$.

Application to $[U(Cp^{ttt})_2]^+$

The geometry relaxation and the vibrational spectrum calculation of **5** is conducted again via DFT in Gaussian09. As a starting geometry, we use the experimental one of $[Dy(Cp^{ttt})_2]^+$ where Dy^{3+} is replaced by U^{3+}. In this case, this geometry is relaxed in vacuum without any crystal environment. Of course, a more realistic relaxation would require to include it as did for **1**. Nevertheless, calculated relaxation times reasonably similar to the experimental ones were obtained for $[Dy(Cp^{ttt})_2]^+$ by relaxing its geometry in vacuum, i.e., by focusing only on gas-phase molecular vibrations. Just to illustrate the proposed methodology, we thus decided to follow the same approach with the beneficial side effect of avoiding to increase the computational cost. Since there is no experimental IR spectrum available for **5**, we use the same value of σ as in $[Dy(Cp^{ttt})_2]^+$, which is $\sigma = 10$ cm^{-1}.

According to our method, we should first perform a CASSCF evaluation on an experimental geometry of **5** to obtain $\left\{\left(A_k^q \left\langle r^k \right\rangle\right)_{eq}\right\}_{k,q}$. Since we lack this geometry, the adapted procedure relies on the equilibrium electronic structure of $[Dy(Cp^{ttt})_2]^+$ as a starting point which is projected onto **5**. Indeed, to determine the two REC model parameters that describe the ligand field produced by the two coordinating Cp^{ttt} rings in **5**, our starting point are the CASSCF energies determined by Goodwin *et al.* at the experimental geometry of $[Dy(Cp^{ttt})_2]^+$.[164] The experimental coordinates of the first coordination sphere of $[Dy(Cp^{ttt})_2]^+$ are used as an input in SIMPRE, and the REC parameters are varied to fit the aforementioned energies. The best fit, with an error $E = 0.03$ % in **Eq. 17**, results in $D_r = 1.313$ Å and $Z_i = 0.06806$. The calculated ground $J = 15/2$ multiplet energies (E_{fit}) by SIMPRE with these REC parameters are compared with the CASSCF ones (E_{ref}) in **Table. 5**.

Subsequently, we apply the calculated REC parameters to the DFT-relaxed coordinates of the coordinating atoms in **5**. This target compound has identical ligands as $[Dy(Cp^{ttt})_2]^+$ only differing in the metal ion. This allows us to transfer the REC parameters from $[Dy(Cp^{ttt})_2]^+$ to **5** as demonstrated in several previous works.[215,222–224] The input coordinates of the relaxed positions of the coordinating atoms in **5** and the most important calculated CFPs are reported in **Table. 6** and **Table. 7**, resp.

Table. 5 Ground J = 9/2 multiplet Kramers doublets determined by CASSCF calculations (E_{ref}) and REC model (E_{fit}) for $[Dy(Cp^{ttt})_2]^+$. $\Delta E = |E_{ref} - E_{fit}|$. Relative errors are < 2.6 %.

E_{ref} –CASSCF (cm^{-1})	E_{fit} –REC (cm^{-1})	ΔE (cm^{-1})
0	0	-
488.6	480.7	7.9
771.0	775.6	4.6
956.5	980.9	24.4
1122.2	1145.4	23.2
1277.5	1280.5	3.0
1399.3	1365.4	33.9
1476.1	1465.4	10.7

Table. 6 Relaxed input coordinates of the coordinating atoms in **5** after applying D_r = 1.313 Å to the radial spherical coordinate and using a charge magnitude of Z_i = 0.06806.

Label	R_i (Å)	θ_i (degrees)	φ_i (degrees)	Z_i
C1	1.302	16.97	170.79	0.06806
C2	1.306	15.43	349.02	0.06806
C3	1.391	39.05	39.80	0.06806
C4	1.490	49.27	80.81	0.06806
C5	1.374	40.50	122.08	0.06806
C6	1.302	163.04	63.04	0.06806
C7	1.306	164.55	244.76	0.06806
C8	1.391	140.94	194.02	0.06806
C9	1.491	130.73	153.01	0.06806
C10	1.375	139.51	111.74	0.06806

Table. 7 Most important calculated CFPs for **5** at the DFT-relaxed geometry in Stevens ($A_k^q \langle r^k \rangle$ and B_k^q) and Wybourne (B_{kq}) notation. The rest of CFPs are such that $|B_k^q| < 0.1$ cm^{-1}.

k	q	$A_k^q \langle r^k \rangle$ (cm^{-1})	B_k^q (cm^{-1})	B_{kq} (cm^{-1})
2	0	997.8	-6.414	1995.6
2	1	-1118.3	7.188	-456.5
2	-1	-568.0	3.651	-231.9
2	2	-47.1	0.303	-38.5
2	-2	-64.4	0.414	-52.6
4	1	-623.1	0.181	-557.3

Now, the CFPs in Wybourne notation calculated at the DFT-relaxed geometry of **5** are used as an input in CONDON to determine the equilibrium electronic structure of **5**, see **Table. 8** and **Fig. 33**.

Table. 8 Lowest five equilibrium Kramers doublets of **5** determined in CONDON. The wave-functions were truncated to the ten m_J components corresponding to the ground level of U^{3+} and then renormalized. m_J contributions below 10% are omitted.

E (cm^{-1})	Wave-function
0.0	$81.5\%\|\pm 9/2\rangle + 12.2\%\|\pm 3/2\rangle$
159.3	$40.7\%\|\mp 5/2\rangle + 17.7\%\|\mp 3/2\rangle + 17.6\%\|\pm 1/2\rangle + 13.5\%\|\mp 7/2\rangle$
331.0	$30.2\%\|\pm 3/2\rangle + 18.5\%\|\pm 1/2\rangle + 18.2\%\|\mp 5/2\rangle + 12.0\%\|\mp 7/2\rangle$
499.1	$26.9\%\|\mp 1/2\rangle + 25.6\%\|\mp 5/2\rangle + 15.7\%\|\pm 7/2\rangle + 12.4\%\|\mp 7/2\rangle + 10.3\%\|\mp 3/2\rangle$
638.3	$42.6\%\|\pm 7/2\rangle + 21.5\%\|\pm 3/2\rangle + 18.0\%\|\pm 1/2\rangle$

In the particular case of **5** we found that the contribution of excited *J* multiplets to the lowest 10 equilibrium eigenstates before truncation is rather negligible. Note that the zero field splitting ~640 cm^{-1} is relatively moderate and quite below the one observed in $[Dy(Cp^{ttt})_2]^+$ (~1400 cm^{-1}) and $[Dy(Cp^*)(Cp^{iPr5})]^+$ (~1900 cm^{-1}). Thus, the ground doublet of the first excited J multiplet in **5**, which lies around few thousands of cm^{-1}, is far from influencing the U^{3+} ground level. Of course, this is not necessarily the general situation for uranium-based coordination compounds. Whenever the ZFS becomes comparable to the spin-orbit coupling, excited *J* multiplets will show increasing contributions to the ground one.

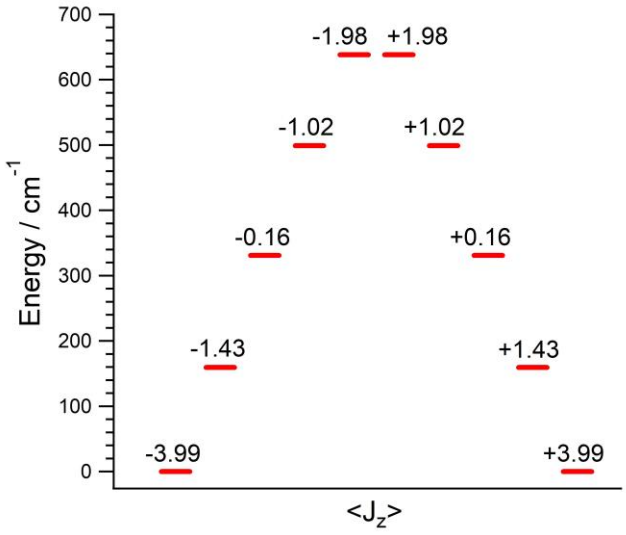

Fig. 33 Lowest $2J+1 = 10$ spin energies of the ground $J = 9/2$ multiplet of U^{3+} evaluated at the relaxed geometry of **5**, along with the corresponding $\hat{J}_z$ expectation values.

The resolution of the master equation in **Eq. 45** provides the temperature dependence of the relaxation time τ. Details are routine and are found elsewhere.[298] In **Fig. 34**, we show this calculated thermal evolution for **5** by employing the Orbach transition rates with initial conditions $p_{|-9/2\rangle}(t=0)=1$, $p_{|i\rangle}(t=0)=0$ for $i \neq$ -9/2. Indeed, since our current interest is the use of a molecular magnet as a classical memory storage, the initial spin population is all placed at one component of the ground doublet, which acts as the memory

bit. In an experiment, this corresponds to magnetize the sample and then to turn the magnetic field off. The relaxation time in the temperature range where the Orbach process dominates (above some few tens of Kelvin) is experimentally modeled by an Arrhenius-like law $\tau = \tau_0 \exp(U_{eff} T^{-1})$. In this process, the spin population does not necessarily reach the top of the barrier in **Fig. 33** before crossing it. Instead, it tunnels the barrier at an effective height given by U_{eff}. The Orbach prefactor τ_0^{-1} represents the number of attempts per unit time to tunnel the barrier. From **Fig. 34**, the fitting produces U_{eff} = 203 cm^{-1}, and τ_0 = $2.7 \cdot 10^{-8}$ s. As seen in **Fig. 33**, U_{eff} would be located around 40 cm^{-1} above the first excited doublet, and is much smaller than those found in $[Dy(Cp^{ttt})_2]^+$ (~1223 cm^{-1}) and $[Dy(Cp^*)(Cp^{iPr5})]^+$ (~1541 cm^{-1}). On the contrary, the estimated Orbach prefactor is at least three orders of magnitude larger than those found for $[Dy(Cp^{ttt})_2]^+$ (τ_0 = $2.0 \cdot 10^{-11}$ s) and $[Dy(Cp^*)(Cp^{iPr5})]^+$ (τ_0 = $4.2 \cdot 10^{-12}$ s). The attempt rate to cross the barrier seems thus to be much slower in **5**. Nevertheless, the comparison of previously reported uranium SIMs with **5** reveals that our calculated Orbach prefactor is found among the smallest ones.[223,290] Note that the calculated times τ at low temperatures in **Fig. 34** should be considered as an upper bound of the real ones since at these temperatures other different mechanisms are often dominant.

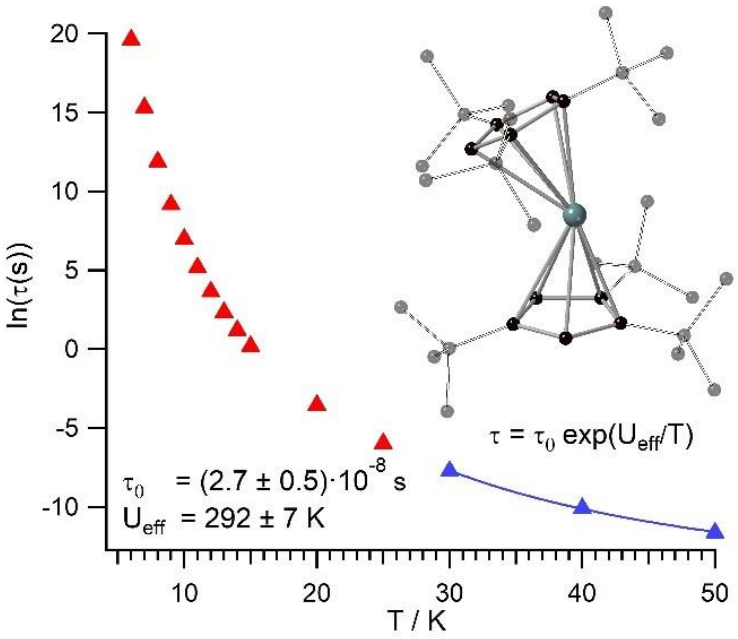

Fig. 34 Thermal evolution of the Orbach-based relaxation time τ, along with fit to determine both the Orbach prefactor τ_0 and the effective barrier U_{eff} in the thermally-activated regime ($T \geq 30$ K). Inset: visual representation of **5**.

We repeated the master equation resolution but by employing now the second-order Raman transitions rates. This mechanism is far from dominating relaxation in the explored temperature range as the calculated times τ are at least five orders of magnitude longer than the Orbach-based ones, see **Table. 9**. The reason to calculate the Orbach and second-order Raman relaxation times up to 50 K is because at this temperature the Orbach relaxation time reaches the standard experimental detection limit, which is around 10^{-6} s. We select 6 K (Orbach process) and 11 K (second-order Raman process) as lower bounds for temperature since below these values numerical noise becomes too important to produce reliable relaxation times.

Table. 9 Thermal evolution of the Orbach and second-order Raman relaxation times τ_O and τ_R for **5**.

T (K)	τ_O (s)	τ_R (s)
11	$1.8 \cdot 10^{2}$	$3.4 \cdot 10^{7}$
12	$3.9 \cdot 10^{1}$	$5.1 \cdot 10^{6}$
13	$1.0 \cdot 10^{1}$	$1.1 \cdot 10^{6}$
14	$3.3 \cdot 10^{0}$	$2.9 \cdot 10^{5}$
15	$1.2 \cdot 10^{0}$	$9.3 \cdot 10^{4}$
20	$2.9 \cdot 10^{-2}$	$1.7 \cdot 10^{3}$
25	$2.6 \cdot 10^{-3}$	$1.5 \cdot 10^{2}$
30	$4.5 \cdot 10^{-4}$	$2.9 \cdot 10^{1}$
40	$4.2 \cdot 10^{-5}$	$3.6 \cdot 10^{0}$
50	$9.0 \cdot 10^{-6}$	$1.0 \cdot 10^{0}$

A complementary information that can also be extracted from the master equation when using the Orbach transition rates is the Orbach-mediated relaxation pathway followed by the spin population, see **Fig. 35**. This can be accomplished by checking the pairs of eigenstates with the highest transition rates. Moreover, it is also possible to identify the vibrations that promote each relaxation step in this pathway. Indeed, as explained above, these rates depend proportionally on the non-interacting contributions from the several vibrational modes. We focus on those modes with the highest relative weight in each rate. Once the most contributing ones are identified, we can now visually inspect which atomic movements are involved. Then, chemical modifications on the molecular structure can be proposed to remove the relevant motions with the hope of further suppressing magnetic relaxation and improving the magnet performance.

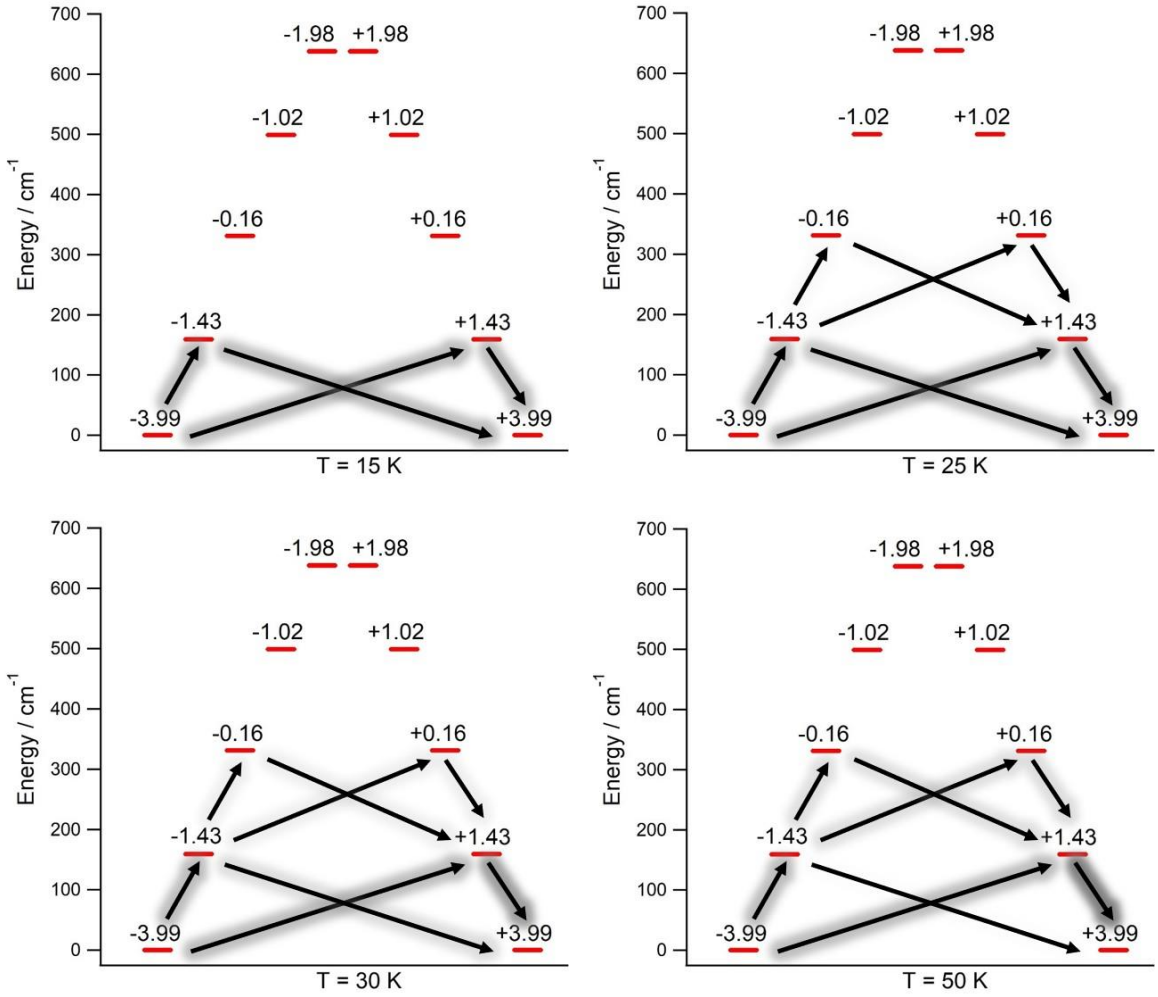

Fig. 35 Orbach-driven relaxation pathways of **5** starting at the $\langle J_z \rangle = -3.99$ equilibrium eigenstate with unity population at different temperatures. Arrow shades are proportional to the percentage of the transient spin population. The outcome population sum from a given eigenstate equals the income population sum to the same eigenstate. Transient populations lesser than 1.0% not shown. Note that there is no spin population transfer between degenerate states as no quantum tunneling processes are under consideration in the master equation.

Below 25 K, we find that only the ground and first excited doublets are populated and the spin tunnels the barrier through their components. Nevertheless, here we must recall again that we are only considering Orbach-driven magnetic relaxation. At low temperatures, alternative relaxation mechanisms can be at play and dominate, such as the case of the direct process where the spin tunnels the barrier through the ground doublet components

without populating any excited doublet (quantum tunneling of magnetization). Above 25 K, the Orbach process starts to dominate, this is the so-called thermally-activated regime where the number of available phonons is high enough to promote the spin to excited states. As temperature is raised, both the first and second excited doublets become populated, and an increasing spin population tunnels the barrier through their components. This is consistent with an effective barrier U_{eff} found in between these two excited doublets.

Above 30 K, the thermally activated relaxation is at play. The spin population flows through excited doublets by absorption and emission of phonons. We identify up to six molecular vibrations involved in this relaxation mechanism. These are the calculated vibrations 16, 17, 18, 19, 20 ,21, with harmonic frequencies ν_{16} = 135.0115 cm^{-1}, ν_{17} = 136.8658 cm^{-1}, ν_{18} = 170.0364 cm^{-1}, ν_{19} = 172.5580 cm^{-1}, ν_{20} = 175.4401 cm^{-1}, ν_{21} = 175.7696 cm^{-1}, where the last four frequencies closely match the gaps between the equilibrium ground and first excited doublets (159.3 cm^{-1}), and first and second excited doublets (171.7 cm^{-1}) in virtue of the selected value σ = 10 cm^{-1}. The vibration 16 is a rocking-like deformation of the two Cp^{ttt} rings: the two hydrogen atoms bounded to each Cp^{ttt} ring moves towards and away from the U^{3+} ion. As a side effect, there are also rigid movements of the terc-butyl substituents. This kind of vibration was also identified in $[Dy(Cp^{ttt})_2]^+$ as the one promoting the first step in the most likely relaxation pathway from the ground doublet to the first excited doublet. As mentioned above, it was proposed to substitute these two hydrogen atoms in the Cp^{ttt} rings by bulkier substituents in order to block this vibration thus producing $[Dy(Cp^*)(Cp^{iPr5})]^+$. This modification succeeded since this vibration is no longer observed and both blocking temperature and experimental effective barrier were increased by 20 K and around 300 cm^{-1}, resp. The vibration 17 involves kind of rigid movements in the terc-butyl substituents. The modes 18 and 21 are symmetric and antisymmetric breathing-like vibrations: the two rigid Cp^{ttt} rings moves towards and moves away from the U^{3+} ion at once and out of phase, resp., and are also found in $[Dy(Cp^*)(Cp^{iPr5})]^+$. This vibration could be hindered by bounding the two coordinating rings, such as it happens in stapled bis-phthalocyanines. The vibrations 19 and 20 involve methyl rotations in the terc-butyl substituents, which could be partially suppressed if one replaces the methyl groups $–CH_3$ by the heavier fluorinated analogs $–CF_3$. In general, since the frequencies of some of these six vibrations are close to match the gaps between the low-lying spin doublets, the magnet performance could be

improved by any structural modification that brought these vibrational modes out of resonance. Hence, there may be still room for further improvement in these bis-metallocenium-based SIMs, which seem to open more avenues in the pursuit of new highly-performing molecular magnets based on f-block elements.

Comparison with other systems

We also calculated the CFPs thermal evolution as shown in **Fig. 36**. As can be seen, important contributions from off-diagonal CFPs are clearly observed, which leads to the sizeable $|m_J\rangle$ mixing in the equilibrium eigenstates observed in **Table. 8**. This fact opposes a good SIM behavior, where the diagonal CFPs should largely dominate over the off-diagonal ones.

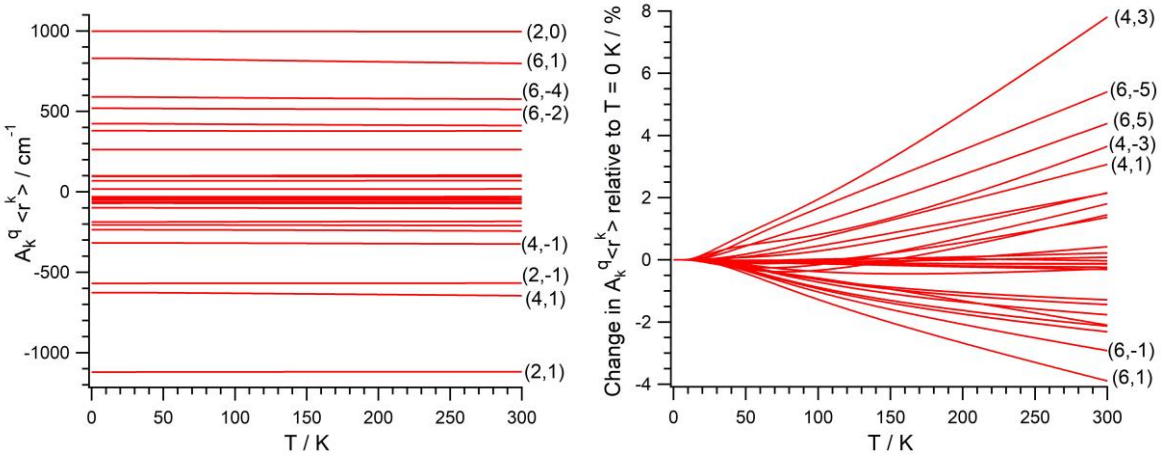

Fig. 36 Absolute (left) and relative to T = 0 K (right) thermal evolution of the CFPs. Some parameters are identified as (k,q), where k and q are the scripts k = 2, 4, 6 and q = -k,…,+k.

Importantly, this heavy mixing is also found in previously reported uranium SIMs even for very linear environments,[223,282,290] but not in the cutting-edge Dy-based SIMs $[Dy(Cp^{ttt})_2]^+$ and $[Dy(Cp^*)(Cp^{iPr5})]^+$ whose ligand coordination is in fact not strictly axial. This clearly constitutes a limitation of uranium SIMs compared to those based on the second half of the lanthanide series, namely, Tb^{3+}-, Dy^{3+}-, Ho^{3+}-, and Er^{3+}-based SIMs. Thus, the problem behind the somewhat disappointing results that have been reported so far in uranium SIMs

does not seem to be the lack of linearity but rather the activation of certain off-diagonal CFPs which can be additionally coupled strongly with vibrations. This common pattern does not seem to be an accidental consequence of particular molecular geometries, but rather a general feature caused by the low value J = 9/2 of the U^{3+} ground level. In particular, and this does depend on the molecular geometry, in the reported examples so far there are important m_J = ±3/2 mixings in the low-lying states. For instance, if there is a m_J = ±9/2 weight in the ground doublet, there is also at least some m_J = ±3/2 weight either in the ground doublet or in the first excited doublet. Similarly, if there is a m_J = ±7/2 weight in the ground doublet, there is also at least some m_J = ±1/2 weight either in the ground doublet or in the first excited doublet.

As mentioned, it seems that some off-diagonal CFPs, especially those of rank 3 such as B_4^3 in **Fig. 36**, are relevant for the majority of the existing uranium SIMs from the point of view both of molecular symmetries and of wave-function composition. This means that any variation in a rank 3 off-diagonal CFP is likely to produce remarkable m_J mixing thus facilitating fast spin relaxation. This fact needs to be considered for chemical design efforts since D_{3h} and nearly D_{3h} symmetries are quite often found in uranium coordination compounds. Indeed, whenever the first coordination shell is close to D_{3h}, all antisymmetric vibrations respect to the symmetry plane σ_h belonging to D_{3h} are expected to largely change rank 3 off-diagonal CFPs. Note that all of the reported uranium SIMs show U_{eff} ~ 20 − 30 K with 47.6 K as a record,[223,290,299] and magnetic hysteresis below 5 K in the best of the cases.[287] This contrasts with the obtained U_{eff} for some dysprosium complexes such as $[Dy(Cp^{ttt})_2]^+$ (1760 K), $[Dy(Cp^*)(Cp^{iPr5})]^+$ (2217 K), and $[Dy(O^tBu)_2(py)_5]^+$ (1815 K),[278] where magnetic hysteresis are measured up to 80 K for $[Dy(Cp^*)(Cp^{iPr5})]^+$.

A similar comparison can be done between the theoretical estimates of **5** and the available experimental data for $[Dy(Cp^{ttt})_2]^+$. In this case, there is a larger deviation from linearity in both cases but especially in the uranium analog: $\measuredangle CpDyCp$ = 152.6º versus $\measuredangle CpUCp$ = 142.4º, resp. This results in a less axial environment and, as mentioned, in a much more compressed low-lying energy scheme in **Fig. 33**. Also in **5**, the ground doublet is composed of 82%$|\pm 9/2\rangle$, and the m_J mixing further increases towards excited doublets. As discussed above, this extensive mixing coincides with what has also been calculated in previously

reported uranium-based SIMs and is assumed to facilitate spin relaxation. In fact, our calculations in **5** show that, in a predominantly Orbach-mediated relaxation, the spin population tunnels the barrier just a bit above the first excited doublet. These features are in sharp contrast with those exhibited by the dysprosocenium molecular nanomagnets $[Dy(Cp^{ttt})_2]^+$ and $[Dy(Cp^*)(Cp^{iPr5})]^+$ where (i) the low-lying spin states are much purer even with a non-strictly axial ligand coordination, and (ii) the effective barrier reaches the most excited doublets.[279] Thus, according to this electronic structure and the fact that calculated relaxation times in **5** are much shorter than those reported for $[Dy(Cp^{ttt})_2]^+$ and $[Dy(Cp^*)(Cp^{iPr5})]^+$, the experimental performance of **5** in terms of SIM behavior is expected to be worse than that of dysprosocenium nanomagnets. This seems to evidence the need to set up different design strategies for 5f SIMs since simple transmutation strategies -consisting in replacing dysprosium by the actinide ion in a carefully designed Dy^{3+}-based SIM- might not be enough to exploit the particular full potential of uranium.

On the other hand, there do seem to exist two significant advances in **5** respect to previous uranium SIMs, namely, (i) the effective barrier commonly measured appears in the range of dozens of kelvin as mentioned above, while the one calculated for **5** reaches several hundreds of kelvin (292 K), (ii) by assuming that the Orbach relaxation process dominates between 30 K – 50 K in **5**, the standard experimental detection limit ~10^{-6} s for the relaxation time τ would be found at 50 K. This upper bound is around one order of magnitude greater than that observed in the uranium-based nanomagnets reported so far.[223,290] In the case of $[Dy(Cp^{ttt})_2]^+$ and $[Dy(Cp^*)(Cp^{iPr5})]^+$, the detection limits are reached at 112 K and 138 K, resp. It is clear that **5** is far from outperforming $[Dy(Cp^{ttt})_2]^+$ and $[Dy(Cp^*)(Cp^{iPr5})]^+$ even employing bis-metallocenium ligands. As discussed, this can be unsurprising since, after all, these ligands seem to be optimal for Dy^{3+} while U^{3+} could need rather different requirements.

5

Magnetic Noise

This chapter is devoted to tackle the spin dephasing caused by an uncontrolled magnetic noise that surrounds and interacts with a given molecular spin qubit. In particular, we will focus on the mechanisms nuclear spin diffusion and instantaneous diffusion, which have already been described in chapter 2. In the first case, the noise arises when there is a nuclear spin bath surrounding the qubit, while in the second case the noise source is due to the magnetic nature of the involved molecules. Since single crystals are hard to achieve for some molecular systems, samples are often probed in EPR spectrometers in the form of microcrystalline powder or frozen solution. Thus, it is useful to develop a framework suited to estimate the phase memory time T_m in these samples. This is what we undertake in section 5.1, where a model developed by Witzel and Das Sarma and focused on nuclear spin diffusion is extended to deal with the aforementioned samples.[300] In section 5.2, we will develop a first-principles model to estimate T_m when instantaneous diffusion is the main dephasing mechanism. This novel approach will allow us reproducing the experimental T_m evolution as a function of both magnetic field magnitude and metal ion concentration -especially when the latter is high enough- in a challenging molecular system displaying atomic clock transitions and in a regular $S = 1/2$ spin qubit (section 5.3). On the contrary, in section 5.4 we will use this method to rule out instantaneous diffusion as the dominant decoherence source in a Gd^{3+}-based molecular spin qubit at the working experimental conditions. Then, we will discuss on the possible dephasing mechanisms that can be behind the discrepancy between our calculated T_m values and the ones experimentally measured.

5.1 $[Cu(mnt)_2]^{2-}$

In this section, we extend a model devoted to estimate the phase memory time due to nuclear spin diffusion in single crystal so that it can be used in microcrystalline powder or frozen solution.[300] This model was originally developed and applied to single localized electron spins in semiconductor quantum computer architectures, which are surrounded by a nuclear spin bath. In particular, a quantitative agreement was obtained when simulating experimental Hahn echo decays in phosphorus-doped silicon and quantum dots in GaAs. The model is fully quantum-mechanical and incorporates the nuclear spin flip-flop dynamics microscopically without making any phenomenological statistical (Markovian or otherwise) approximations. Herein, we first provide a summary of the original model along with its main assumptions and restrictions, and then we will describe our expansion which will be applied to **1**, i.e. $[Cu(mnt)_2]^{2-}$ (powder sample) as a case study, see **Fig. 15** in section 4.1.

As mentioned, the range of application is focused on those regimes where nuclear spin diffusion dominates as a dephasing mechanism. Hence, the Hahn echo decay follows a stretched exponential-like evolution $\exp(-(2\tau/T_m)^k)$ with a stretching factor $k > 2$. It is assumed that the Zeeman interaction in the effective spin doublet describing the qubit is much stronger than the magnetic interaction -modeled as dipolar- between the spin that encodes the qubit and each nuclear spin in the bath. The pair-wise interaction between nuclear spins is also modeled as dipolar and should also be much weaker than the abovementioned Zeeman interaction. Lastly, this Zeeman interaction is also assumed to be much stronger than the same interaction on each magnetic nuclei. We use the analytical solution found to calculate the Hahn echo decay $v(\tau)$ as a function of the pulse delay time τ, which is only available for $I = 1/2$ nuclear spins, namely, ^{1}H, ^{15}N, ^{13}C, ^{31}P, ^{183}W, ^{11}F. The working experimental conditions must be such that magnetic field magnitude B and temperature are above 0.1 T and 100 mK, resp. The model can be applied to general energy schemes arising from spin quantum numbers $J \geq 1/2$, provided one uses the effective Landé factor g working in the applied field direction and associated to the doublet that defines the qubit. The calculation of $v(\tau)$ requires to compute the following variables:

$$b_{nm} = -\frac{1}{2}\mu_0 \frac{\gamma_n}{2\pi}\frac{\gamma_m}{2\pi}\hbar \frac{1-3\cos^2(\theta_{nm})}{R_{nm}^3}, \quad \cos(\theta_{nm}) = \frac{\vec{B}\cdot\vec{R}_{nm}}{BR_{nm}} \qquad \textbf{Eq. 52}$$

$$A_n = -\mu_0 \frac{\gamma_n}{2\pi}\frac{\gamma}{2\pi}\hbar \frac{1-3\cos^2(\theta_n)}{R_n^3}, \quad \cos(\theta_n) = \frac{\vec{B}\cdot\vec{R}_n}{BR_n} \qquad \textbf{Eq. 53}$$

$$A_m = -\mu_0 \frac{\gamma_m}{2\pi}\frac{\gamma}{2\pi}\hbar \frac{1-3\cos^2(\theta_m)}{R_m^3}, \quad \cos(\theta_m) = \frac{\vec{B}\cdot\vec{R}_m}{BR_m} \qquad \textbf{Eq. 54}$$

$$c_{nm} = \frac{A_n - A_m}{4b_{nm}}, \quad \omega_{nm} = 2b_{nm}\sqrt{1+c_{nm}^2} \qquad \textbf{Eq. 55}$$

In **Eq. 52**, **Eq. 53**, **Eq. 54**, μ_0 is the vacuum permeability, $\gamma = \mu_B g / \hbar$ and $\gamma_i = \mu_N g_i / \hbar$ ($i = n, m$) are the gyromagnetic ratios of the effective spin doublet encoding the qubit and of the magnetic nuclei with nuclear Landé factor g_i, θ_{nm} is the angle between the magnetic field $\vec{B}$ and the vector $\vec{R}_{nm}$ (with magnitude $R_{nm} = |\vec{R}_{nm}|$) that joins the position of two nuclear spins n and m, θ_n and θ_m are the angles between the magnetic field $\vec{B}$ and the vectors $\vec{R}_n$ and $\vec{R}_m$ (with magnitudes $R_n = |\vec{R}_n|$ and $R_m = |\vec{R}_m|$) that join the position of the nuclear spins n and m with the point magnetic center that contains the qubit (e.g., a single localized electron, or a metal ion). Note that $\vec{R}_{nm} = \vec{R}_m - \vec{R}_n$. With all these ingredients, the Hahn echo $\nu(\tau)$ reads as follows:

$$\nu(\tau) = \exp\left(-\sum_{m<n} \frac{c_{nm}^2}{\left(1+c_{nm}^2\right)^2}\left(\cos(\omega_{nm}\tau) - 1\right)^2 \right) \qquad \textbf{Eq. 56}$$

If in the single crystals there exists a distribution in the Landé factor g, one would sample a large enough number N of values $\{g_j\}_j$. Then, after computing each $\nu_j(\tau)$ in **Eq. 56**, the average echo decay $\bar{\nu}(\tau) = \sum_j \nu_j(\tau)/N$ would be fitted to a stretched exponential function $f(\tau) = \exp(-(\tau/T_m)^k)$ to obtain T_m and k. Note that a similar procedure applies to powder samples and frozen solutions provided the set of resonant directions -where the EPR spectrometer irradiation frequency closely matches the qubit energy gap- is finite. In this case, while keeping the molecule and nuclear spin bath relative orientation, one will have to change the field direction accordingly to perform the $\nu_j(\tau)$ calculation at each one of these directions with the relevant effective g in each case.

To extend the model, we focus on the particular cases of either an axial effective Landé tensor with $g_\parallel \neq g_\perp$ where the resonance is produced in the circular region $g = g_\perp$, or an isotropic effective Landé tensor with $g_\parallel = g_\perp$ where the resonance is produced in the spherical region $g = g_\parallel = g_\perp$. For powder samples and frozen solutions, in the first case we will have to perform an integration over the circle $g = g_\perp$, while in the second case this integration will be conducted over the sphere $g = g_\parallel = g_\perp$. Note that in the case of the axial effective Landé tensor, no integration is required if the resonance is produced in the direction corresponding to $g_\parallel$.

Let us start with the first case. The diagonalization of the effective Landé tensor provides three eigenvectors, two of them, $\vec{u}_1$ and $\vec{u}_2$, associated to $g_\perp$ and the remaining one, $\vec{u}_3$, associated to $g_\parallel$. To facilitate the calculation, we use the following convention. We rotate the crystallographic molecular structure, along with the crystallographic positions of all magnetic nuclei, until $\vec{u}_1$, $\vec{u}_2$, $\vec{u}_3$ match the canonical Cartesian axes X, Y, Z resp. Now, the $g = g_\perp$ is contained in the XY plane while the axial axis coincides with the Z direction. The magnetic field is set to be contained in the XY plane in any given fixed direction no matter which one. With this fixed direction, the integration consists in rotating both the molecule and the nuclear spin bath -while keeping their relative orientation- 360 degrees around the Z axis. For that, we need first to

parameterize each nuclear position, i.e. the vectors $\vec{R}_n$ and $\vec{R}_m$, in terms of the rotation angle. Given the initial molecular orientation, the known position of each nucleus *n*, $\vec{R}_n = \left((R_n)_x, (R_n)_y, (R_n)_z \right)$, can be written in terms of spherical coordinates for some $\varepsilon_n \in [-\pi/2, \pi/2]$, $\alpha_n \in [0, 2\pi]$ such as:

$$\vec{R}_n = R_n \left(\cos\varepsilon_n \cos\alpha_n, \cos\varepsilon_n \sin\alpha_n, \sin\varepsilon_n \right) \qquad \textbf{Eq. 57}$$

$$\cos\varepsilon_n = \frac{\sqrt{(R_n)_x^2 + (R_n)_y^2}}{R_n}, \quad \sin\varepsilon_n = \frac{(R_n)_z}{R_n} \qquad \textbf{Eq. 58}$$

$$\cos\alpha_n = \frac{(R_n)_x}{\sqrt{(R_n)_x^2 + (R_n)_y^2}}, \quad \sin\alpha_n = \frac{(R_n)_y}{\sqrt{(R_n)_x^2 + (R_n)_y^2}} \qquad \textbf{Eq. 59}$$

Any rotation around the Z axis just adds an angle $\delta \in [0, 2\pi]$ to the azimuthal angle α_n. Hence, the new nuclear position is:

$$\left(\vec{R}_n\right)_\delta = R_n \left(\cos\varepsilon_n \cos(\alpha_n + \delta), \cos\varepsilon_n \sin(\alpha_n + \delta), \sin\varepsilon_n \right) \qquad \textbf{Eq. 60}$$

Likewise, a similar parameterization $\left(\vec{R}_m\right)_\delta$ in terms of δ is obtained for $\vec{R}_m$. We calculate $\left(\vec{R}_{nm}\right)_\delta$ as $\left(\vec{R}_{nm}\right)_\delta = \left(\vec{R}_m\right)_\delta - \left(\vec{R}_n\right)_\delta$. Note that $\left|\left(\vec{R}_{nm}\right)_\delta\right| = \left|\vec{R}_{nm}\right|$ since any rotation always conserve vector magnitudes. Thus, the integral to evaluate for each τ value is:

$$\bar{\nu}(\tau)=\frac{1}{2\pi}\int_0^{2\pi}\nu(\tau,\delta)d\delta \qquad \textbf{Eq. 61}$$

Since the above integral cannot be solved analytically, we proceed numerically. For that, we consider a finite number N of equally-spaced angles δ_i and estimate $\bar{\nu}(\tau)$ as the following average:

$$\bar{\nu}(\tau)\approx\sum_{i=1}^{N}\nu(\tau,\delta_i)/N\,,\quad \delta_i=2\pi(i-1)/N \qquad \textbf{Eq. 62}$$

By increasing N, the estimated Hahn echo on the right of **Eq. 62** should converge to a limiting curve. As mentioned above, the resulting curve is fitted to the stretched exponential function $f(\tau) = \exp(-(\tau/T_m)^k)$ to obtain T_m and k.

In the second case, since $g_{\parallel}=g_{\perp}$ there is no need to firstly rotate the molecule along with the surrounding nuclear spin bath. Indeed, any set of three mutually orthogonal unitary vectors work as eigenvectors of the effective Landé tensor and we consider again the three canonical Cartesian axes X, Y, Z. The magnetic field is set in a space direction no matter which one. Then, with this fixed direction, the integration is made by jointly rotating the molecule and the nuclear spin bath over the whole unitary sphere. As made above, we need now to parameterize each nuclear position $\vec{R}_n$. Let us recall that, given the initial molecular orientation, the known position of each nucleus *n*, $\vec{R}_n=\left((R_n)_x,(R_n)_y,(R_n)_z\right)$, can be written in terms of spherical coordinates for some $\varepsilon_n\in[-\pi/2,\pi/2]$, $\alpha_n\in[0,2\pi]$ as in **Eq. 57**. Now, an arbitrary rotation is described by two independent angles $\delta\in[-\pi/2,\pi/2]$, $\gamma\in[0,2\pi]$ and thus we have to find the new expression $\left(\vec{R}_n\right)_{\delta,\gamma}$ of $\vec{R}_n$ as a function of δ, γ. For that, according to the definition of δ and γ, we decompose the rotation into two elementary rotations. The first one is anti-clockwise with angle δ around the Z axis, thus producing $\left(\vec{R}_n\right)_{\delta}$ in **Eq. 60**; the second one is a rotation of $\left(\vec{R}_n\right)_{\delta}$ also

antic-clockwise with angle γ around the unitary vector $\vec{u}_\delta = \left[\left(\vec{R}_n\right)_\delta \times \vec{Z}\right]/M$ where $M = \left|\left(\vec{R}_n\right)_\delta \times \vec{Z}\right|$, which is contained in the XY plane and is also perpendicular to the plane generated by $\left(\vec{R}_n\right)_\delta$ and $\vec{Z} = (0,0,1)$. If $\left(\vec{R}_n\right)_\delta$ were parallel to $\vec{Z}$ (in this case, $\left(\vec{R}_n\right)_\delta$ would not be dependent on δ but rather coincident with $\vec{R}_n$), we would use $\vec{u}_\delta = (-\sin\delta, \cos\delta, 0)$. Thus, $\left(\vec{R}_n\right)_{\delta,\gamma}$ is found by performing the matrix-vector product $\left(\vec{R}_n\right)_{\delta,\gamma} = R\left(\vec{u}_\delta,\gamma\right)\left(\vec{R}_n\right)_\delta$, where $R\left(\vec{u}_\delta,\gamma\right)$ is the anti-clockwise rotation matrix of angle $\gamma \in [0,2\pi]$ around the unitary vector $\vec{u}_\delta = \left[\left(\vec{R}_n\right)_\delta \times \vec{Z}\right]/M = \left(u_{x,\delta}, u_{y,\delta}, 0\right)$ as follows:

$$R\left(\vec{u}_\delta,\gamma\right) = \begin{pmatrix} \cos\gamma + u_{x,\delta}^2\left(1-\cos\gamma\right) & u_{x,\delta}u_{y,\delta}\left(1-\cos\gamma\right) & u_{y,\delta}\sin\gamma \\ u_{x,\delta}u_{y,\delta}\left(1-\cos\gamma\right) & \cos\gamma + u_{y,\delta}^2\left(1-\cos\gamma\right) & -u_{x,\delta}\sin\gamma \\ -u_{y,\delta}\sin\gamma & u_{x,\delta}\sin\gamma & \cos\gamma \end{pmatrix} \qquad \textbf{Eq. 63}$$

The average echo $\bar{v}(\tau)$ is obtained by evaluating the following integral for each τ:

$$\bar{v}(\tau) = \frac{1}{4\pi}\int_{-\pi/2}^{\pi/2}\left(\int_0^{2\pi} v(\tau,\delta,\gamma)\left|\cos\gamma\right| d\gamma\right) d\delta \qquad \textbf{Eq. 64}$$

Since the above integral cannot be solved analytically either, we proceed in this case numerically by employing the so-called Lebedev rules. A given Lebedev rule of precision $p \in \mathbb{N}$ is characterized for producing the same result obtained by analytically integrating any polynomial with variables *x*, *y*, *z* for which the highest degree term $x^i y^j z^k$ satisfies $i + j + k \leq$ p. For each given rule, the approximation to the integral I of a function $f(x,y,z)$ over the unit sphere -where *x*, *y*, *z* are parameterized in terms of the angles δ and γ- consists in

using a set with a finite number N of arrays $(\delta_i, \gamma_i, w_i)$ to produce the following estimation:

$$I \approx 4\pi \sum_{i=1}^{N} w_i f(\delta_i, \gamma_i) \qquad \textbf{Eq. 65}$$

Importantly, the weights w_i are such that $\sum_i w_i = 1$. In our particular case, the estimation of $\bar{v}(\tau)$ is conducted with the following expression for each τ:

$$\bar{v}(\tau) \approx \sum_{i=1}^{N} w_i v(\tau, \delta_i, \gamma_i) \qquad \textbf{Eq. 66}$$

The arrays $(\delta_i, \gamma_i, w_i)$ are coded in SIMPRE for several precisions. By increasing p, the estimated Hahn echo on the right of **Eq. 66** should also converge to a limiting curve. Again, the resulting curve is fitted to the stretched exponential function $f(\tau) = \exp(-(\tau/T_m)^k)$ to obtain T_m and k.

We now apply the first case to **1**. The experimental determination of the phase memory time of **1** was conducted by K. Bader et al. in a non-deuterated powder sample with a molar ratio 99.999:0.001 at T = 7 K.[207] This measurement was performed in a Q-band EPR spectrometer in the circular region $g = g_\perp$ = 2.0227 of the axial Landé tensor, and provided T_m^{exp} = 9.23 μs, k^{exp} = 2.48. The Cartesian positions of the magnetic nuclei in a microcrystal were determined by X-ray crystallography.[207] Since the microcrystal contains a number of nuclei too large to be handled in a computer, we extract from the crystallographic structure several spherical clusters centered at a given copper ion. We then use the coordinates of all magnetic nuclei inside the cluster that have some I = 1/2 isotope, namely, ^{1}H, ^{15}N, ^{13}C, ^{31}P. Note that the relative occurrence of ^{15}N and ^{13}C is quite low (0.368 and 1.07%, resp.), and thus the main contribution comes from ^{1}H and ^{31}P with relative occurrence of ~100 and 100%. We used a radius of 40 Å and N = 72 angles in **Eq. 62**, which allows to produce the estimate T_m

= 9.15 μs and k = 2.69. The simulation is quite accurate in T_m with a relative error of 0.9%, while the prediction of k results in a larger relative error of 8.5%. We repeated the calculation by increasing both the cluster radius and N, but it does not improve the prediction significantly. Note that the much more abundant isotope ^{14}N with I = 1 and a relative occurrence of 99.632% is not being included as it requires a much more computationally demanding numerical treatment (let us recall that for I > 1/2 nuclei there is no analytical solution available for $v(\tau)$ in **Eq. 56**). Yet, the result in which only I = 1/2 magnetic nuclei are considered is sufficient to provide a quantitative prediction of T_m.

5.2 HoW_{10}

As we explained in chapter 2, there exist two important mechanisms that can collapse the quantum information saved in a molecular spin qubit, namely, the coupling of the spin qubit with lattice vibrations,[164,184,243,245] and the interaction of the qubit with surrounding nuclear and electron spins.[139] The standard method employed to suppress the second one consists in (i) placing qubit-carriers in nuclear-spin free environments or with little magnetic moments (e.g. by deuteration) and (ii) diluting these carriers among their diamagnetic analogues, where the magnetic entity is substituted by a diamagnetic one.[207] These strategies are well-established and have allowed reaching unprecedented phase memory times around one millisecond in V^{+4}-based molecular spin qubits.[196] Nevertheless, as also stated above, isolation of qubits is impractical at the stage of device design since the implementation of logical gates for quantum algorithms crucially relies on communication among close qubits.[137,301,302] We thus need to design qubits able to maintain their coherence at a high spatial concentration of qubit-carrier spins.

An appealing strategy that could overcome this drawback consists in looking for magnetic molecules where spin qubits can be defined in the form of atomic clock transitions, see **Fig. 37**.[303–306] These are avoided crossings between two spin states with a given energy gap Δ in which Zeeman effect vanishes up to first order in Δ, thus making qubit coherence become remarkably insensitive to surrounding magnetic noise. To obtain a clock transition, the spin Hamiltonian should involve off-diagonal CFPs that allow mixing different spin projections to produce an avoided crossing. Importantly, within molecule-based

spin qubits, this approach was recently demonstrated for the first time in $[Ho(W_5O_{18})_2]^{9-}$ (hereafter referred to as HoW_{10}), see **Fig. 38**. HoW_{10} is a magnetic molecule composed of a single Ho^{3+} ion that is coordinated by two polyoxometalate (POM) ligands $[W_5O_{18}]^{6-}$. In this system, long T_m values were reported at an unusual high Ho^{3+} concentration x as $[Ho_xY_{1-x}(W_5O_{18})_2]^{9-}$ in a close neighborhood of each given atomic clock transition.[206]

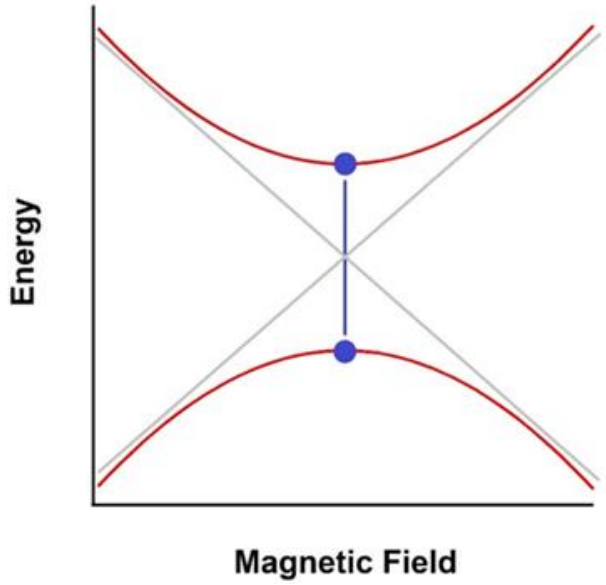

Fig. 37 Schematic representation of an atomic clock transition in blue at an avoided crossing between two energy states in red. Note the vanishing slopes at the transition field.

In fact, single spin qubits of molecular nature operating at atomic clock transitions could be ideal candidates for implementing logical gates as a part of scalable architectures.[148] Indeed, an important requirement to communicate single molecule spins via coplanar waveguides as described in chapter 2 is the attainment of the spin-photon strong coupling regime in the nano-constrictions. This regime is defined by the condition $gT_m/h>1$, where g is the coupling strength parameter. Hence, working at clock transitions becomes specially promising to enhance the spin-photon coupling, as they can provide sufficiently long phase memory times T_m. Moreover, in case of magnetic molecules with electron spin quantum number $J>1/2$ operating at these particular transitions,

the use of tunnel split $|\pm n\rangle$ spin states to define the qubit basis can provide not only a high qubit coherence,[206] but also rise the g magnitude by a factor of $2n$ respect to the simplest case $J = 1/2$. All in all, in order for a $J > 1/2$ molecular spin qubit to be a potential candidate in this regard, it must fulfil $2nT_m > 70$ μs, which seems nowadays to be within reach with $n = 4$.[206]

Herein, we aim to theoretically estimate T_m in samples where there is a high concentration of spin-qubit carriers provided instantaneous diffusion is the dominant dephasing mechanism. The case study is a single-crystal composed of many identical and equally-oriented copies of HoW_{10}. Four peculiar narrow regions appear in its experimental T_m magnetic field dependence, where T_m sharply increases up to a maximum value, see **Fig. 39**. To understand the origin of this limiting value, we firstly applied a state-of-the-art model that satisfactorily explained the experimental T_m evolution of a Cu^{2+}-based molecular qubit, see section 5.3, at increasing Cu^{2+} concentration.[254] However, this model overestimates the experimental T_m top values reached at the clock fields in HoW_{10} as we will see below. This motivated us to propose a new first-principles model, which relies on another model developed by Stamp and Tupitsyn devoted to estimate the phase memory time T_m^n induced by magnetic nuclei in case of non-stretched Hahn echo decays.[307] Our model does successfully reproduce the experimental height of T_m at the clock fields in HoW_{10}.

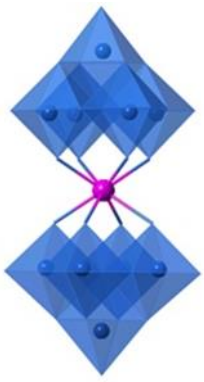

Fig. 38 HoW_{10}. Blue spheres: W, magenta sphere: Ho, polyhedron vertexes: O.

Model

The starting point is the abovementioned T_m^n-related model developed by Stamp and Tupitsyn, where the calculation of the off-diagonal element in the qubit reduced density matrix is conducted as a path integral over pairs of qubit trajectories.[307] From the derivation of this model it follows that the mentioned matrix element decays as a non-stretched exponential function $\exp\left(-\tau / T_m^n\right)$ with time τ (note that in general T_m is defined as the characteristic time for the decay of the aforementioned off-diagonal element). It is appropriate since our model is to be employed in an experimental regime where instantaneous diffusion dominates as a dephasing mechanism. This allows determining an expression for T_m^n which in turn is used to define a dimensionless dephasing rate γ_n whose expression is written for convenience as $\gamma_n \equiv 2\hbar / T_m^n \Delta$, being Δ the energy gap between the two spin states of the qubit.[139,307] Thus, the rate γ_n is dependent on the off-diagonal matrix element of the qubit reduced density matrix. By employing standard techniques developed for the spin-boson model, it is possible to find the simple expression $\gamma_n = 2\left(E_n / \Delta\right)^2$, where E_n is the magnetic nuclear contribution to the echo line half-width E. In fact, this equality is derived as a perturbative expression up to second order in E_n / Δ. For that, it is necessary to operate under the so-called high-field regime, which means $E_n \ll \Delta$.[139,254,307] This hypothesis is widely fulfilled in all systems and experimental conditions of our interest, since the working spin concentrations and field magnitudes in **Eq. 11**, which determine E_n and Δ resp., quite often lies inside this regime. As a last step, an expression for E_n -shown in section 5.3- is derived as a function of the magnetic nuclei positions as well as other variables.

Our model is intended to apply to coordination magnetic molecules, where only one qubit is defined, whose relevant energy scheme is described by the spin Hamiltonian in **Eq. 11**. Note that the parameters in this Hamiltonian are often determined via cw-EPR experiments. Nonetheless, whenever experimental data is not available, one can resort to first-principles codes such as MOLCAS and ORCA to estimate these parameters, see chapter 4. Now, we adapt the T_m^n-related model to estimate our dephasing rate $\gamma_e = 2\left(E_e / \Delta\right)^2$ resulting from the magnetic field produced by the ensemble of qubit-carrying molecules, where E_e is the corresponding contribution to the echo line half-

width and should also fulfil $E_e \ll \Delta$.[254] In particular, hereunder it is shown the procedure to calculate E_e based on that followed to derive E_n. Since the rates γ_n and γ_e are assumed to be additive,[139,307] the collective phase memory time reads as $T_m^{n+e} = 2\hbar / \left[\left(\gamma_n + \gamma_e \right) \Delta \right]$.

Firstly, one considers the dipolar magnetic field $\overrightarrow{B_j}$ that a given metal ion *j* generates at the position of another given metal ion *k*:

$$\overrightarrow{B_j}\left(\overrightarrow{r_{jk}}\right) = \frac{\mu_0}{4\pi}\frac{1}{r_{jk}^5}\left(3\left(\overrightarrow{m_j}\cdot\overrightarrow{r_{jk}}\right)\overrightarrow{r_{jk}} - r_{jk}^2\overrightarrow{m_j}\right) \qquad \textbf{Eq. 67}$$

The vector connecting these two ions is $\overrightarrow{r_{jk}}$, with a magnitude r_{jk}; and their magnetic moments are $\overrightarrow{m_j}$ and $\overrightarrow{m_k}$. This allows calculating their dipolar interaction energy as:

$$E_{jk} = -\overrightarrow{m_k}\cdot\overrightarrow{B_j}\left(\overrightarrow{r_{jk}}\right) = \frac{\mu_0}{4\pi}\frac{1}{r_{jk}^3}\left(\overrightarrow{m_j} - \frac{3\left(\overrightarrow{m_j}\cdot\overrightarrow{r_{jk}}\right)}{r_{jk}^2}\overrightarrow{r_{jk}}\right)\cdot\overrightarrow{m_k} \qquad \textbf{Eq. 68}$$

The diagonalization of **Eq. 11** provides $\left(2J+1\right)\left(2I+1\right)$ energies and wave-functions $\left\{E_l, \left|\psi_l\right\rangle\right\}_{l=1,\ldots,(2J+1)(2I+1)}$, where *J* and *I* correspond to the ground level $^{2S+1}L_J$ and the nuclear spin quantum number of the metal ion, resp. The wave-functions are expressed with complex coefficients $c\left(l\right)_i^n$ in the basis set $\left\{\left|m_J, m_I\right\rangle\right\}_{m_J=-J,\ldots,J;m_I=-I,\ldots,I}$ of the m_J and m_I projections as:

$$\left|\psi_l\right\rangle = \sum_{n=1}^{2J+1}\sum_{i=(n-1)(2I+1)+1}^{n(2I+1)} c\left(l\right)_i^n \left|n-1-J, i-\left(n-1\right)\left(2I+1\right)-1-I\right\rangle \qquad \textbf{Eq. 69}$$

We need now to calculate $\left\{\left\langle \hat{J}_{\alpha}^{2}\right\rangle_{l}=\left\langle \psi_{l}\left|\hat{J}_{\alpha}^{2}\right|\psi_{l}\right\rangle\right\}_{l=1,\ldots,(2J+1)(2I+1);\alpha=x,y,z}$, the expectation values of each component ($\alpha=x,y,z$) of the squared electron spin operator $\hat{J}^{2}$. After some algebra, one obtains:

$$\left\langle \hat{J}_{z}^{2}\right\rangle_{l}=\sum_{n=1}^{2J+1}\left(n-1-J\right)^{2}\sum_{i=(n-1)(2I+1)+1}^{n(2I+1)}\left|c\left(l\right)_{i}^{n}\right|^{2} \qquad \textbf{Eq. 70}$$

$$\left\langle \hat{J}_{x}^{2}\right\rangle_{l}=\frac{1}{4}\left\{2J\left(J+1\right)-2\left\langle \hat{J}_{z}^{2}\right\rangle_{l}+\ldots\right.$$

$$\ldots\sum_{n=1}^{2J-1}\left(J\left(J+1\right)-\left(n-1-J\right)\left(n-J\right)\right)^{1/2}\left(J\left(J+1\right)-\left(n+1-J\right)\left(n-J\right)\right)^{1/2} \qquad \textbf{Eq. 71}$$

$$\left.\ldots\sum_{i=(n-1)(2I+1)+1}^{n(2I+1)}\left[\left(c\left(l\right)_{i+2(2I+1)}^{n+2}\right)^{*}c\left(l\right)_{i}^{n}+\left(c\left(l\right)_{i}^{n}\right)^{*}c\left(l\right)_{i+2(2I+1)}^{n+2}\right]\right\}$$

$$\left\langle \hat{J}_{y}^{2}\right\rangle_{l}=J\left(J+1\right)-\left\langle \hat{J}_{z}^{2}\right\rangle_{l}-\left\langle \hat{J}_{x}^{2}\right\rangle_{l} \qquad \textbf{Eq. 72}$$

The asterisk stands for the conjugate complex number. As done in the T_{m}^{n}-related model with the nuclear spin bath, we also consider that the qubit is coupled to an ensemble of thermalized molecular spins at a given temperature *T*. Thus, the squared expectation values $\left\{\left\langle \hat{J}_{\alpha}^{2}\right\rangle_{l}\right\}_{l=1,\ldots,(2J+1)(2I+1);\alpha=x,y,z}$ of each α = *x*, *y*, *z* component are distributed according to the Boltzmann law, and this defines the Boltzmann-averaged squared expectation values $\overline{\left\langle \hat{J}_{\alpha}\right\rangle}^{2}$ as:

$$\left\{\overline{\left\langle \hat{J}_{\alpha}\right\rangle}^{2}=\sum_{l=1}^{(2J+1)(2I+1)}e^{-E_{l}/k_{B}T}\left\langle \hat{J}_{\alpha}^{2}\right\rangle_{l}/\sum_{l=1}^{(2J+1)(2I+1)}e^{-E_{l}/k_{B}T}\right\}_{\alpha=x,y,z} \qquad \textbf{Eq. 73}$$

Also in the T_m^n-related model, each magnetic nucleus *i* in the bath is described with an isotropic Zeeman Hamiltonian $\hat{H}_i = \mu_N g_N^i \vec{B} \cdot \vec{\hat{I}}_i$, where μ_N is the nuclear magneton, g_N^i is the nuclear Landé factor, $\vec{B}$ is the applied magnetic field and $\vec{\hat{I}}_i$ is the nuclear spin operator. The diagonalization of $\hat{H}_i$ provides a set of energies and wave-functions $\left\{E_{i,l}, \left|\psi_{i,l}\right\rangle\right\}_{l=1,\ldots,2I_i+1}$, where I_i is the nuclear spin quantum number. These wave-functions allows determining the expectation values $\left\{\left\langle \hat{I}_\alpha^2 \right\rangle_{i,l} = \left\langle \psi_{i,l} \left| \hat{I}_\alpha^2 \right| \psi_{i,l} \right\rangle\right\}_{\alpha=x,y,z;l=1,\ldots,(2I_i+1)}$ of the α = *x*, *y*, *z* components of $\hat{I}^2$, which are also distributed according to the Boltzmann law at a given temperature *T* and define $\left\{\overline{\left\langle \hat{I}_\alpha \right\rangle_i}^2 = \sum_{l=1}^{2I_i+1} e^{-E_{i,l}/k_BT} \left\langle \hat{I}_\alpha^2 \right\rangle_{i,l} / \sum_{l=1}^{2I_i+1} e^{-E_{i,l}/k_BT}\right\}_{\alpha=x,y,z}$. Since $\hat{H}_i$ is isotropic, each $\left\langle \hat{I}_\alpha^2 \right\rangle_{i,l}$ must be independent of the magnetic field direction. Thus, we can choose a direction at our convenience to calculate $\left\langle \hat{I}_\alpha^2 \right\rangle_{i,l}$. By considering the magnetic field in the *Z* axis direction, the wave-functions $\left\{\left|\psi_{i,l}\right\rangle\right\}_{l=1,\ldots,2I_i+1}$ become $\left\{\left|m_{I_i}\right\rangle\right\}_{m_{I_i}=-I_i,\ldots,I_i}$, where m_{I_i} are the several projections of I_i. Each $\left\langle \hat{I}_\alpha^2 \right\rangle_{i,l}$ can now be easily calculated, resulting in $\left\langle m_{I_i} \left| \hat{I}_z^2 \right| m_{I_i} \right\rangle = {m_{I_i}}^2$; while $\left\langle m_{I_i} \left| \hat{I}_x^2 \right| m_{I_i} \right\rangle$ and $\left\langle m_{I_i} \left| \hat{I}_y^2 \right| m_{I_i} \right\rangle$ are both equal to $\left(I_i(I_i+1) - {m_{I_i}}^2\right)/2$. At the working magnetic fields $\left|\vec{B}\right|$ < 0.5 T and temperatures $T \geq 3$ K, each nuclear Zeeman energy $E_{i,l}$ is still far from reaching the thermal energy k_BT, thus $\exp\left(-E_{i,l}/k_BT\right) \to 1$. Under this assumption, it is easy to prove that $\left\{\overline{\left\langle \hat{I}_\alpha \right\rangle_i}^2 = I_i(I_i+1)/3\right\}_{\alpha=x,y,z}$, and the nuclear magnetic moment is defined as $\vec{m_i} = \mu_N g_N^i \left(\overline{\left\langle \hat{I}_x \right\rangle_i}, \overline{\left\langle \hat{I}_y \right\rangle_i}, \overline{\left\langle \hat{I}_z \right\rangle_i}\right)$. In our case, we adapt this procedure to define the magnetic moments $\vec{m_j}$ and $\vec{m_k}$ of the metal ions *j*, *k* in terms of the electron Landé factors $\{g_\alpha\}_{\alpha=x,y,z}$ and $\overline{\left\langle \hat{J}_\alpha \right\rangle}$ as:

$$\vec{m} = \mu_B \left(g_x \overline{\left\langle \hat{J}_x \right\rangle}, g_y \overline{\left\langle \hat{J}_y \right\rangle}, g_z \overline{\left\langle \hat{J}_z \right\rangle}\right) \qquad \textbf{Eq. 74}$$

Note that both metal ions are modeled with the same spin Hamiltonian in **Eq. 11** and hence $\overrightarrow{m_j} = \overrightarrow{m_k}$, which are renamed as $\vec{m}$. Moreover, since the qubit is not being described as an effective spin doublet, we will use the free-ion value g both in **Eq. 11** and in the Landé factors $\{g_\alpha\}_{\alpha=x,y,z}$.

As mentioned, in the T_m^n-related model the qubit is coupled to a thermal nuclear spin bath. Each one of the two qubit states, symmetric *S* and antisymmetric *A*, generates a different dipolar magnetic field $\left\{\overrightarrow{B^T}\left(\vec{r}_i\right)\right\}_{T=S,A}$ at the position $\vec{r}_i$ of a given magnetic nucleus *i*. Thus, two different dipolar interaction energies are involved, namely, $\left\{E_i^T = \left(-\overrightarrow{B^T}\left(\vec{r}_i\right)\right)\cdot\overrightarrow{m_i}\right\}_{T=S,A}$. For a given qubit state either S or A, the three terms $\left\{\left(-\overrightarrow{B^T}\left(\vec{r}_i\right)\right)_\alpha\left(\overrightarrow{m_i}\right)_\alpha\right\}_{\alpha=x,y,z}$ whose summation amounts to E_i^T define the qubit-nucleus interaction vector as $\overrightarrow{E_i^T} = \left(\left(\overrightarrow{E_i^T}\right)_x, \left(\overrightarrow{E_i^T}\right)_y, \left(\overrightarrow{E_i^T}\right)_z\right)/2$ with $\left\{\left(\overrightarrow{E_i^T}\right)_\alpha = \left(-\overrightarrow{B^T}\left(\vec{r}_i\right)\right)_\alpha\left(\overrightarrow{m_i}\right)_\alpha\right\}_{\alpha=x,y,z}$. The contribution of the magnetic nucleus *i* to E_n is the magnitude $\left\|\overrightarrow{E_i^A} - \overrightarrow{E_i^S}\right\|$ of the difference between these two qubit-nucleus interaction vectors. By considering the whole nuclear spin bath, the square nuclear echo line half-width is found to be $E_n^2 = \sum_i \left\|\overrightarrow{E_i^A} - \overrightarrow{E_i^S}\right\|^2$.

Indeed, when the qubit is in a given state $\alpha|0\rangle + \beta|0\rangle$ with $|\alpha|^2 + |\beta|^2 = 1$, there exists an allowed set of $\prod_i (2I_i + 1)$ nuclear spin states in a finite nuclear spin bath. For a large enough bath, the density of states as a function of energy converges to a Gaussian distribution with a Gaussian line shape by virtue of the so-called Central Limit Theorem. The Gaussian line half-width is just E_n, and E_n^2 would be the corresponding variance associated to this distribution. Nevertheless, there may be some special situations in which the nuclear density of states largely deviates from a Gaussian-like line. This can be encountered when all $\left\|\overrightarrow{E_i^A} - \overrightarrow{E_i^S}\right\|$ have similar enough values, or when one qubit-nucleus

interaction dominates over the others. In this case, this model would not be valid anymore.

In our case, we propose to adapt this procedure to determine E_e as follows. From the dipolar interaction energy $E_{jk} = -\overrightarrow{m_k} \cdot \overrightarrow{B_j}\left(\overrightarrow{r_{jk}}\right)$ in **Eq. 68**, we consider the three terms $\left\{-\left(\overrightarrow{m_k}\right)_\alpha \left(\overrightarrow{B_j}\left(\overrightarrow{r_{jk}}\right)\right)_\alpha\right\}_{\alpha=x,y,z}$ whose summation amounts to E_{jk} and define the interaction vector between the metal ions *j*, *k* as $\overrightarrow{E_{jk}} = \left(\left(\overrightarrow{E_{jk}}\right)_x, \left(\overrightarrow{E_{jk}}\right)_y, \left(\overrightarrow{E_{jk}}\right)_z\right)/2$ with $\left\{\left(\overrightarrow{E_{jk}}\right)_\alpha = -\left(\overrightarrow{m_k}\right)_\alpha \left(\overrightarrow{B_j}\left(\overrightarrow{r_{jk}}\right)\right)_\alpha\right\}_{\alpha=x,y,z}$. We now define the contribution of the *j*, *k* pair to E_e as the magnitude $\left\|\overrightarrow{E_{jk}}\right\|$ which, after some algebra, reads as follows:

$$\left\|\overrightarrow{E_{jk}}\right\|^2 = \left(\frac{\mu_0 \mu_B^2}{8\pi r_{jk}^3}\right)^2$$

$$\ldots \sum_{\alpha=x,y,z} \left[g_\alpha \overline{\left\langle \hat{J}_\alpha \right\rangle} \left(\left(1 - 3\left(\frac{\left(\overrightarrow{r_{jk}}\right)_\alpha}{r_{jk}} \right)^2 \right) g_\alpha \overline{\left\langle \hat{J}_\alpha \right\rangle} - 3\frac{\left(\overrightarrow{r_{jk}}\right)_\alpha}{r_{jk}^2} \sum_{\substack{\beta=x,y,z \\ \beta\neq\alpha}} \left(\overrightarrow{r_{jk}}\right)_\beta g_\beta \overline{\left\langle \hat{J}_\beta \right\rangle} \right) \right]^2 \quad \textbf{Eq. 75}$$

To determine the squared electron echo line half-width E_e^2, we add all *j*, *k* pairs of metal ions and divide the result by the number N of these ions in the ensemble as done elsewhere:[254]

$$E_e^2 = \frac{1}{N} \sum_{j=1}^{N-1} \sum_{k>j}^{N} \left\|\overrightarrow{E_{jk}}\right\|^2 \quad \textbf{Eq. 76}$$

As thoroughly mentioned, the magnetic molecules of our interest encoding the qubit consist of a single metal ion coordinated by several ligands. Depending on the overlapping degree between the ion and ligand orbitals, part of the spin density in the ion may be deployed towards the ligands and lead to an effective

decrease in the ion spin magnitude. This effect reduces the dipolar interaction strength between metal ions (i.e. the surrounding magnetic noise), thus resulting in an increase of the qubit coherence, and can be described by the so-called covalency parameter $0<\varepsilon\leq 1$ as introduced and employed elsewhere.[254,308] This parameter can be estimated by first-principles methods routinely employed in computational quantum chemistry such as those based on DFT.[308] The limit value $\varepsilon=1$ corresponds to a spin density fully located at the metal ion. We incorporate ε as a correction to E_n and E_e. Hence, the corrected phase memory time reads as $T_m^{n+e}=\hbar\Delta/\left[\varepsilon^2\left(E_n^2+E_e^2\right)\right]$. The influence of metal-ligand covalency on the spin coherence was recently explored from the experimental side.[272] Indeed, the elongation of the spin-lattice relaxation time, which facilitates enabling longer T_m values, was correlated with a greater spin delocalization onto the ligand environment.

Our model will be applied to a single crystal composed of many equally-oriented copies of HoW_{10}. Each one of these copies is modeled with the same values for the spin Hamiltonian parameters and, hence, the calculated T_m^{n+e} is the same for all these copies. Nonetheless, the method can be readily extended to simulate experiments where different sets of spin Hamiltonian parameters are used to describe each copy. For instance, this situation can be encountered when there is a distribution of CFPs due to the presence of dislocations, defects, as well as other lattice strains in the crystal. In this case, one would first generate a sample of M sets of parameters according to the given distribution. Then, M decoherence times $\left(T_m^{n+e}\right)_i$ would be calculated in order to build the average spin echo $\sum_{i=1}^{M}\exp\left(-\tau/\left(T_m^{n+e}\right)_i\right)/M$. By plotting and fitting this average versus τ to an exponential function, we would obtain the overall phase memory time. Moreover, the same procedure described in section 5.1 applies to the case of powder samples and frozen solutions. In this situation, the echo expressions $\nu(\tau,\delta)$ and $\nu(\tau,\delta,\gamma)$ for effective axial and isotropic Landé tensors at given angles δ, γ are $\exp\left(-\tau/T_m^{n+e}(\delta)\right)$ and $\exp\left(-\tau/T_m^{n+e}(\delta,\gamma)\right)$. Then, the average echo curves are determined as in **Eq. 62** and **Eq. 66** to extract the overall phase memory time.

Results

Under the application of an external magnetic field $\vec{B}$, the Hamiltonian determining the wave-functions and spin energies of HoW_{10} in terms of the ground electron and nuclear spin quantum numbers $J = 8$, $I = 7/2$ is:[206]

$$\hat{H} = \sum_{k=2,4,6} B_k^0 \hat{O}_k^0 + B_4^4 \hat{O}_4^4 + \vec{\hat{I}} \cdot \mathbf{A} \cdot \vec{\hat{J}} + \mu_B \vec{B} \cdot g \cdot \vec{\hat{J}} \qquad \textbf{Eq. 77}$$

We focus on the ground $J = |L+S| = 8$ multiplet of the Ho^{3+} ion, which arises from the spin-orbit coupled quantum numbers $L = 6$ and $S = 2$. As determined via cw-EPR spectroscopy by Shiddiq et al., the CFPs are $B_2^0 = 0.601$ cm^{-1}, $B_4^0 = 6.96 \cdot 10^{-3}$ cm^{-1}, $B_6^0 = -5.10 \cdot 10^{-5}$ cm^{-1}, $B_4^4 = 3.14 \cdot 10^{-3}$ cm^{-1}; while the hyperfine coupling parameters are $A_z = 830$ MHz, $A_x = A_y = 0$.[206] The axial terms $B_2^0 \hat{O}_2^0$, $B_4^0 \hat{O}_4^0$, $B_6^0 \hat{O}_6^0$ result, in the case of HoW_{10}, in an isolated $m_J = \pm 4$ ground doublet separated from the first excited state (a $m_J = \pm 5$ doublet) by at least 20 cm^{-1}. This is a robust result that has been confirmed repeatedly over the years by methods that rely on different assumptions on the spin Hamiltonian as well as different experimental data derived from magnetic properties in the 2-300 K temperature range of a whole series of isostructural $Ln^{3+}W_{10}$ compounds,[175,226] multi-frequency EPR studies of the ground electronuclear multiplet of HoW_{10},[309] or the spectroscopic technique Inelastic Neutron Scattering.[310] Since this ground state is not being described as an effective spin doublet, g is set to be the free-ion value of 1.25 in **Eq. 77**. When combined with the eight nuclear spin projections of $I = 7/2$, the ground state $m_J = \pm 4$ gives rise to a low-lying multiplet of 16 states, see **Fig. 39**. The sizeable interaction B_4^4 generates an energy gap $\Delta \sim 9.18$ GHz at the clock fields, which can still be probed via X-band EPR spectroscopy and defines the long-lived spin qubit. We consider that all copies of HoW_{10} in the single crystal have their magnetic anisotropy axis pointing in the same direction, and it defines the direction of $\vec{B}$.

In the experimental work of HoW_{10},[206] it was established that its extreme uniaxial anisotropy results in a rather negligible sensitivity to the perpendicular component of the applied magnetic field $\vec{B}$. In other words, the effective

perpendicular Landé factor of the $m_J = \pm 4$ ground state is $g_{\perp,eff}$ < 0.01. Thus, since the focus is on this doublet as it defines the spin qubit, the Zeeman term $\mu_B \vec{B} \cdot g \cdot \vec{\hat{J}}$ is replaced by the scalar approximation $\mu_B g B_z \hat{J}_z$, where the *Z* direction is defined by the molecular magnetic anisotropy axis along which $\vec{B}$ is applied (hence, $B_z = \left|\vec{B}\right|$). Note that this does not mean that an axial Landé factor is being used in **Eq. 77** with g = 0 in $\mu_B B_x g \hat{J}_x$ and $\mu_B B_y g \hat{J}_y$ while g = 1.25 in $\mu_B B_z g \hat{J}_z$. Instead, the terms $\mu_B B_x g \hat{J}_x$ and $\mu_B B_y g \hat{J}_y$ are neglected after considering an isotropic factor g = 1.25. Nonetheless, the translation of this scalar approximation in terms of **Eq. 75** means to set g_z = 1.25, $g_x = g_y$ = 0. As lanthanide 4f-orbitals are internal enough not to deploy a significant spin density towards the ligands, we use $\varepsilon = 1$ for HoW_{10}.

In **Fig. 39**, T_m remarkably increases around the four clock fields, but only up to a maximum value. Since the experimental Hahn echoes decay as non-stretched exponential functions,[206] we firstly applied the T_m^n-related model to estimate the influence of magnetic nuclei dephasing on T_m. We found $T_m^n \sim 300$ μs at the valleys which is much above the experimental values in the whole magnetic field range explored. This agrees with the fact that this decoherence source might not be limiting qubit coherence, given the clear experimental dependence of T_m with the Ho^{3+} concentration.

Instead, our T_m^e calculation excellently agrees with the maximum experimental T_m values at the clock fields for the relevant Ho^{3+} concentrations, which span over one order of magnitude, see **Fig. 39**. In contrast, the state-of-the-art model by M. Warner et al. -with a rather different expression of $\left\|\overrightarrow{E_{jk}}\right\|^2$ in **Eq. 75**- overestimates the same T_m experimental values. In our calculations, the high-field regime holds as the highest $E_e \sim 0.05$ GHz << $\Delta \sim 9.18$ GHz (x = 10%). Since the calculated $\overline{\left\langle \hat{J}_x \right\rangle} = \overline{\left\langle \hat{J}_y \right\rangle} = 5.3$, $\overline{\left\langle \hat{J}_z \right\rangle} = 4.0$ in **Eq. 73** remain constant with B_z and are non-zero, E_e^2 in **Eq. 76** also takes a non-zero value. Hence, $T_m^e \propto 1/E_e^2$ cannot diverge and reach an arbitrarily high value at the clock fields. Note that the analog of **Eq. 75** in the T_m^n-related model (see section 5.3) is proportional to the expectation value differences $\left\{\left\langle \hat{J}_\alpha \right\rangle^A - \left\langle \hat{J}_\alpha \right\rangle^S\right\}_{\alpha=x,y,z}$ of the

electron spin operator components $\alpha = x, y, z$ evaluated at the symmetric S and antisymmetric A states of the qubit $\{|\psi_T\rangle\}_{T=A,S}$ instead of $\left\{\overline{\langle \hat{J}_\alpha \rangle}\right\}_{\alpha=x,y,z}$ in **Eq. 75**. It turns out that in a small neighborhood of the clock fields, each $\langle \hat{J}_\alpha \rangle^A - \langle \hat{J}_\alpha \rangle^S$ tends to zero and thus E_n^2 vanishes. Since $T_m^n \propto 1/E_n^2$, the T_m^n-related model wrongly predicts a divergence of T_m^n at the clock fields in contrast to the experimental behavior.

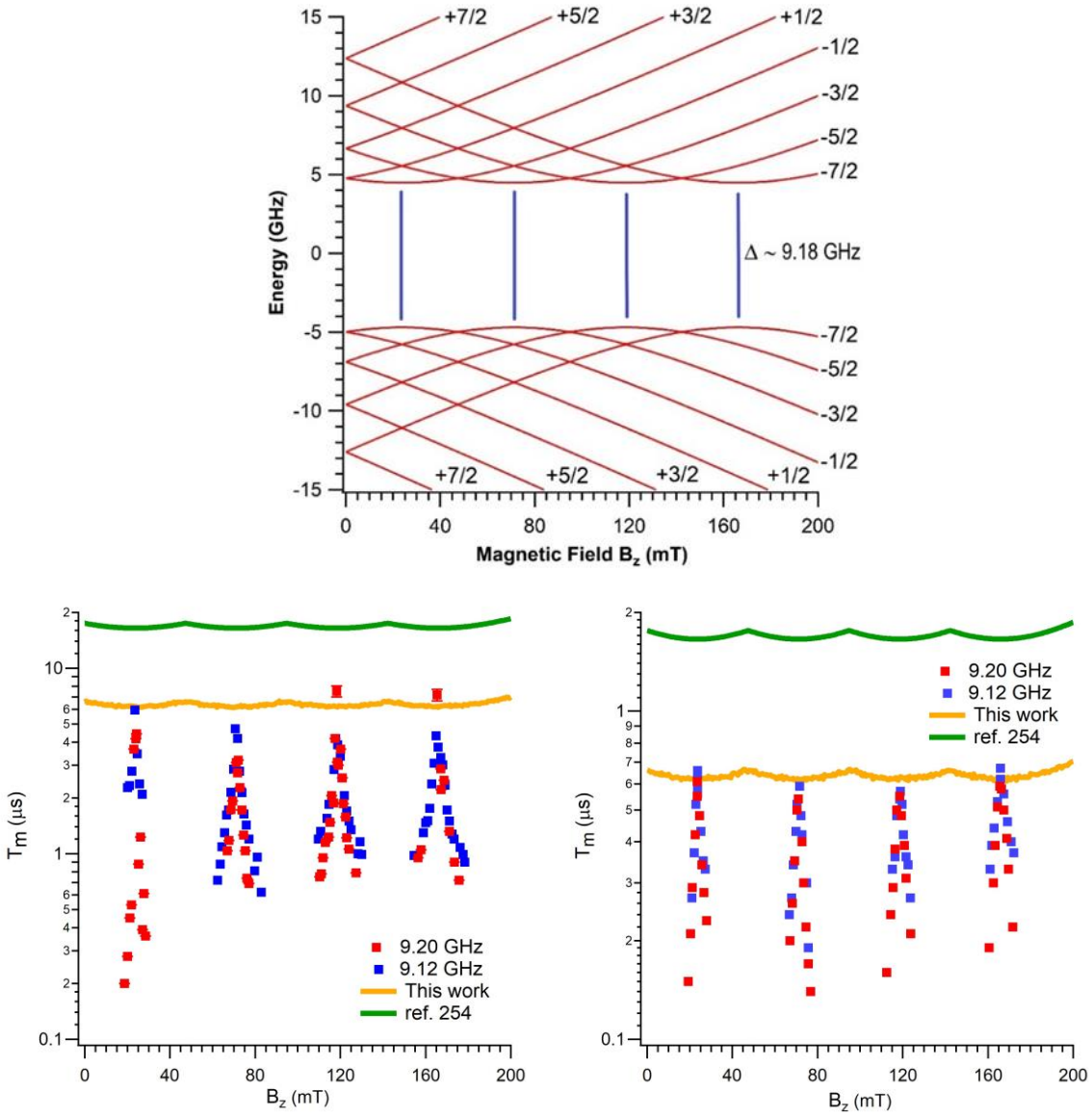

Fig. 39 Top: spin energy evolutions of HoW_{10} labeled with the m_I projections. Blue lines are clock energy gaps. Bottom: magnetic field dependence of T_m (logarithmic scale) in HoW_{10} at T = 5 K for two Ho^{3+} concentrations. Left: x = 1%. Right: x = 10%. Blue and red points are experimental T_m values at different microwave frequencies.[206] Green and orange curves are theoretical calculations using the model in ref. 254 and that of the present work, resp.

As mentioned, calculating E_e in **Eq. 76** requires to know the Cartesian positions of the metal ions in the single crystal. These positions were already determined via X-ray crystallography by Shiddiq et al.[206] Similarly to section 5.1, from the crystallographic structure we extract several spherical clusters of

increasing radius centered at a given Ho^{3+} ion, and then we save all the Ho^{3+} coordinates inside. Let us recall that the orientation of these clusters has to be such that $\vec{B}$ is applied along the magnetic anisotropy axis of HoW_{10}, which defines the *Z* axis direction. We used a radius of 700 Å as it was enough to produce a variation in T_m^e less than 0.01 μs, which assures that the sample-shape dependency of T_m^e is safely removed. The other important step is to simulate the desired Ho^{3+} concentration x according to $[Ho_xY_{1-x}(W_5O_{18})_2]^{9-}$ inside the cluster. Indeed, since this concentration is below 100%, a proper number of Ho^{3+} ions must be removed before calculating T_m^e. The selected values for x in the experiments are 0.01 (1%) and 0.1 (10%),[206] which means that we need to remove 99 and 90 Ho^{3+} ions out of 100, resp. For that purpose, we sweep all Ho^{3+} ions and, at each one, a random number p between 0 and 1 is generated. If $0 \leq p < 0.01$ or $0 \leq p < 0.1$ resp., we save the ion position; otherwise, we drop it. This results in a random dilution that matches the desired concentration. Of course, there does not exist a unique way to produce a dilution in the cluster with the desired concentration as in other attempts different Ho^{3+} positions will be dropped. We thus generate a finite set of L dilutions all of them with the same concentration -either 1% or 10%-, and calculate E_e^2 at each one. Since all of these dilutions are equally likely to occur, we use the arithmetic mean $\overline{E_e^2}$ to determine T_m^e as $T_m^e = \hbar\Delta / \varepsilon^2 \overline{E_e^2}$. To also produce a variation in T_m^e less than 0.01 μs, it was enough to use L = 90 for x = 0.01 and L = 1 for x = 0.1. In the application of the T_m^n-related model, we employed a cluster with a radius of 90 Å also centered at a given Ho^{3+} ion, which was enough to reach the limiting value in T_m^n. Here, we need to save the position of both the central Ho^{3+} ion and the magnetic nuclei. The nuclear spin bath is composed of all magnetic nuclei inside the cluster, namely ^{23}Na (counter-ions), ^{1}H (in surrounding water molecules), ^{17}O (both in surrounding water molecules and in POM cage), ^{183}W (only in POM cage), which are sampled according to their natural abundances.

Discussion

A striking feature of **Fig. 39** is the small variation in the calculated T_m^e with B_z. This is because $T_m^e \propto \Delta / E_e^2$ and E_e^2 is constant in HoW_{10}. The small rise in T_m^e arises from the slight increase in Δ at fields away from the clock transitions. Our model is only capturing a certain dephasing mechanism, namely instantaneous diffusion, which can be experimentally confirmed as the limiting one around these transitions given the non-stretched Hahn echo decays and the noticeable linear dependence of T_m with the relatively high Ho^{3+} concentrations.[206] Instead, out of the clock fields, other mechanisms might be at play and hence our model cannot recover the experimental T_m decay. Initially, the experimental conditions at the magnetic field range explored, namely a temperature of 5 K and a qubit energy gap Δ ~ 9.18 GHz, should discard a significant contribution from vibrational decoherence to the EPR linewidth.[139] As a matter of fact, the spin-lattice relaxation time T_1 measured at 5 K in the aforementioned field range is about ~20 μs. Besides being quite above T_m, note that this value is kept even out of the clock transitions where, on the contrary, T_m sharply falls. Hence, T_1-related phenomena should not be limiting qubit coherence in terms of T_m. In chapter 6, we will elaborate on a hypothesis with the aim of reproducing the T_m decay beyond the clock fields.

Whenever instantaneous diffusion dominates, tuning T_m^e needs to properly engineer Δ and E_e^2. The former depends on the electronic structure determined by **Eq. 77**, and the latter depends additionally on the metal ion concentration in the sample. The qubit energy gap Δ in HoW_{10} at the clock fields is set by the B_4^4 parameter, which is activated because of the deviation from the D_{4d} symmetry in the Ho-coordinating oxygen atoms set.[206] Simple calculations made by us reveal that Δ scales with B_4^4 as $\Delta(\text{GHz}) = 2.0\, B_4^4\ (\text{cm}^{-1}) + 926900 \left(B_4^4\right)^2\ (\text{cm}^{-2})$. Besides, we also checked that **Eq. 73** is unaffected by changing B_4^4 in a wide range around its value $3.14 \cdot 10^{-3}$ cm^{-1}. Thus, given a Ho^{3+} concentration, we expect that a rise in B_4^4 will increase Δ while keeping E_e^2 unaltered. Since $T_m^e \propto \Delta / E_e^2$, the phase memory should be consequently increased.

To understand how T_m^e scales with the metal ion concentration, let us fix the electronic structure with given values of Δ, g_α and **Eq. 73**. If we replace r_{jk} in

Eq. 75 by an average effective distance, E_e^2 becomes proportional to $(1/N)N(N-1)/2$. Since N is large, $T_m^e \propto 1/N$. To assess the validity of this expression, let us recall that T_m in HoW_{10} is ten-fold larger as Ho^{3+} concentration decreases by one order of magnitude. Thus, we expect $N_{10\%}/N_{1\%} = 10$. Indeed, given the cluster with 700 Å radius, the concentrations x = 10% and x = 1% are recovered by keeping the crystallographic positions of $N_{10\%} = 88259$, $N_{1\%} = 8832$ Ho^{3+} ions inside the cluster resp., and it turns out that $N_{10\%}/N_{1\%} = 9.993 \sim 10$.

5.3 CuPc

Our model accounts for qubit coherence in challenging systems displaying atomic clock transitions such as HoW_{10} but is not intrinsically tied to these particular transitions. Indeed, as a further test, we checked that our model is also able to reproduce the experimental T_m in regular $S = 1/2$-based molecular qubits. Herein, the case study is the Cu^{2+} phthalocyanine ($C_{32}H_{16}N_8Cu$, hereafter referred to as CuPc) shown in **Fig. 40**, which was experimentally probed via EPR spectroscopy by M. Warner et al.[254] In this case, we will reproduce its T_m evolution against an increasing Cu^{2+} concentration while keeping fixed the magnetic field magnitude. As in HoW_{10}, the recorded Hahn echoes in CuPc also decay as non-stretched exponential functions in the whole concentration range explored, see below.

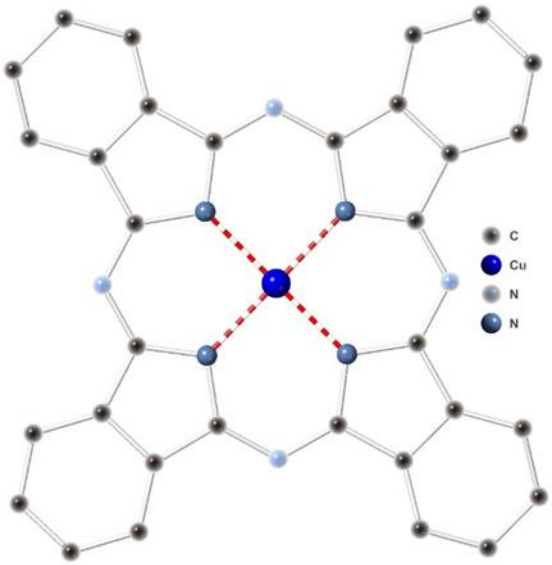

Fig. 40 CuPc. Black: C, blue: N, dark blue: Cu. Red dashed lines represent coordination Cu-N bonds. Hydrogen atoms are omitted for clarity.

CuPc is a magnetic molecule whose qubit is defined as the transition $\left|m_J=-1/2, m_I=-1/2\right\rangle \rightarrow \left|m_J=+1/2, m_I=-1/2\right\rangle$ between the relevant spin states that arise from the coupling between the Cu^{2+} electron and nuclear spin quantum numbers J = 1/2 and I = 3/2 according to the Hamiltonian:

$$\hat{H}=\vec{\hat{I}}\cdot\boldsymbol{A}\cdot\vec{\hat{J}}+\mu_B\vec{B}\cdot\boldsymbol{g}\cdot\vec{\hat{J}} \qquad \textbf{Eq. 78}$$

In **Eq. 78**, the hyperfine coupling parameters and electron Landé factors were determined via EPR spectroscopy and the values were found to be $A_{\parallel}=A_z$ = -648 MHz, $A_{\perp}=A_x=A_y$ = - 83 MHz, and $g_{\parallel}=g_z$ = 2.1577, $g_{\perp}=g_x=g_y$ = 2.0390 (the latter will be used in **Eq. 75** to calculate T_m^e). The Zeeman effect is due to an external magnetic field with a magnitude $\left|\vec{B}\right|$ = 311.5 mT, which is applied along the perpendicular direction to the molecular plane, namely, the magnetic anisotropy axis of CuPc. With these magnetic anisotropy parameters, the qubit energy gap is $\Delta \sim 9.73$ GHz.

To reproduce the experimental T_m evolution of CuPc against the increasing Cu^{2+} concentration, we have to apply both the T_m^n-related model and our model but first the former needs to be adapted to correctly account for the magnetic-nuclei-induced dephasing in CuPc. Indeed, in this aforementioned model the interaction between the molecular spin encoding the qubit and each given nucleus in the bath is modeled as a dipolar-like interaction. This is valid if the metal ion in the molecule and the given nucleus are far away enough. Instead, if they are close to each other, the interaction strength will now be much greater than the one predicted by the dipolar-like interaction. This stronger interaction is often known as contact hyperfine interaction since the magnetic nucleus is close to overlap with the orbitals of the metal ion in the molecule. The coupling constants that describe this contact interaction can be determined experimentally via cw-EPR spectroscopy. This simply means to expand the spin Hamiltonian by including as many terms of the form $\vec{\hat{I}}_i \cdot \boldsymbol{A}_i \cdot \vec{\hat{J}}$ as close nuclei i there are to the metal ion. Then, the coupling constants A_x^i, A_y^i, A_z^i can be determined by fitting the relevant cw-EPR spectrum provided one is able to resolve the relevant spin transitions involving both molecular and nuclear spins. This is what was done in the experimental work of CuPc by M. Warner et al. respect to the four copper-coordinating nitrogen atoms in **Fig. 40**. For all these four nitrogen atoms, the coupling parameters corresponding to their I = 1 nuclear spin (the most occurring isotope) were found to be A_x^N = 57 MHz, $A_y^N = A_z^N$ = 45 MHz. Whenever there is no experimental data available, these parameters could also be calculated by means of the standard first-principles codes routinely employed in quantum chemistry. The E_n^2 expression in the T_m^n-related model is $E_n^2 = \sum_i \left\| \overrightarrow{E_i^A} - \overrightarrow{E_i^S} \right\|^2$, where the sum incorporates all the magnetic nuclei in the bath and the squared qubit-nucleus interaction strength $\left\| \overrightarrow{E_i^A} - \overrightarrow{E_i^S} \right\|^2$ reads as follows:

$$\left\|\overrightarrow{E_i^A}-\overrightarrow{E_i^S}\right\|^2=\left(\frac{\mu_0\mu_B\mu_N g_N^i}{8\pi r_i^3}\right)^2\sum_{\alpha=x,y,z}\left[\left\langle\hat{I}_\alpha\right\rangle_i\left(\left(1-3\left(\frac{\left(\vec{r_i}\right)_\alpha}{r_i}\right)^2\right)g_\alpha\left(\left\langle\hat{J}_\alpha\right\rangle^A-\left\langle\hat{J}_\alpha\right\rangle^S\right)\right.\right.$$

$$\left.\left.\ldots-3\frac{\left(\vec{r_i}\right)_\alpha}{r_i^2}\sum_{\substack{\beta=x,y,z\\ \beta\neq\alpha}}\left(\vec{r_i}\right)_\beta g_\beta\left(\left\langle\hat{J}_\beta\right\rangle^A-\left\langle\hat{J}_\beta\right\rangle^S\right)\right)\right]^2 \qquad \textbf{Eq. 79}$$

In **Eq. 79**, besides the variables already described in section 5.2 such as $\left\{\overline{\left\langle\hat{I}_\alpha\right\rangle_i}\right\}_{\alpha=x,y,z}$, $\vec{r_i}$ is the vector connecting the metal ion and the nucleus *i*, r_i is the corresponding inter-distance, g_N^i is the nuclear Landé factor of the nucleus *i*, and $\left\{\left\langle\hat{J}_\alpha\right\rangle^T=\left\langle\psi_T\left|\hat{J}_\alpha\right|\psi_T\right\rangle\right\}_{T=A,S;\alpha=x,y,z}$ are the expectation values of the three Cartesian components of the electron spin operator $\hat{J}$ evaluated at the symmetric S and antisymmetric A states of the qubit $\left\{\left|\psi_T\right\rangle\right\}_{T=A,S}$ derived from the spin Hamiltonian of the relevant magnetic molecule. These two wave-functions are expressed in the $\left\{\left|m_J,m_I\right\rangle\right\}_{m_J=-J,\ldots,J;m_I=-I,\ldots,I}$ basis set of the m_J and m_I projections as:

$$\left|\psi_k\right\rangle=\sum_{j=1}^{2J+1}\sum_{i=(j-1)(2I+1)+1}^{j(2I+1)}c(k)_i^j\left|j-1-J,i-(j-1)(2I+1)-1-I\right\rangle \qquad \textbf{Eq. 80}$$

Thus, after some algebra, the corresponding expectation values are given by (here, $K=\sqrt{-1}$ stands for the imaginary unit, and the asterisk denotes the conjugate complex number):

$$\left\langle\hat{J}_z\right\rangle_k=\sum_{j=1}^{2J+1}(j-1-J)\sum_{i=(j-1)(2I+1)+1}^{j(2I+1)}\left|c(k)_i^j\right|^2 \qquad \textbf{Eq. 81}$$

$$\left\langle \hat{J}_x \right\rangle_k = \frac{1}{2}\sum_{j=1}^{2J}\sqrt{J(J+1)-\left(j-1-J\right)\left(j-J\right)}$$

$$\ldots \sum_{i=(j-1)(2I+1)+1}^{j(2I+1)}\left(\left(c(k)_{i+(2I+1)}^{j+1}\right)^{*} c(k)_i^{j} + \left(c(k)_i^{j}\right)^{*} c(k)_{i+(2I+1)}^{j+1}\right) \qquad \textbf{Eq. 82}$$

$$\left\langle \hat{J}_y \right\rangle_k = -\frac{K}{2}\sum_{j=1}^{2J}\sqrt{J(J+1)-\left(j-1-J\right)\left(j-J\right)}$$

$$\ldots \sum_{i=(j-1)(2I+1)+1}^{j(2I+1)}\left(\left(c(k)_{i+(2I+1)}^{j+1}\right)^{*} c(k)_i^{j} - \left(c(k)_i^{j}\right)^{*} c(k)_{i+(2I+1)}^{j+1}\right) \qquad \textbf{Eq. 83}$$

All in all, whenever there is a contact hyperfine interaction between the metal ion -i.e., the molecular spin- and a given magnetic nuclei, the expression $\left\|\overrightarrow{E_i^A} - \overrightarrow{E_i^S}\right\|^2$ in **Eq. 79** must be replaced by:[307]

$$\left\|\overrightarrow{E_i^A} - \overrightarrow{E_i^S}\right\|^2 = \frac{1}{4}\sum_{\alpha=x,y,z}\left[A_\alpha^i \overline{\left\langle \hat{I}_\alpha \right\rangle}_i \left(\left\langle \hat{J}_\alpha \right\rangle^A - \left\langle \hat{J}_\alpha \right\rangle^S\right)\right]^2 \qquad \textbf{Eq. 84}$$

Before applying **Eq. 75** and **Eq. 85**, we need to describe the geometrical form of the molecular and nuclear spin baths, see **Fig. 41**. Indeed, the samples used in the pulsed X-band EPR measurements of CuPc at 5 K were 400-nm thick films composed of ~50 nm diameter and nearly spherical CuPc granules. These granules present an *α*-phase-like brick-stack lattice structure. The films were grown on a layer of perylene-3,4,9,20-tetracarboxylic dianhydride by deposition of CuPc. This deposition forces the CuPc molecules to lie with their normal direction to the molecular plane pointing in a common direction that is almost perpendicular to the perylene surface. The magnetic field is applied in this common direction which, as mentioned above, coincides with the CuPc

magnetic anisotropy axis and defines the Z direction. A given Cu^{2+} concentration in the granules is achieved by co-deposition of the proper proportion of CuPc and H_2Pc molecules, where H_2Pc is the diamagnetic analogue of CuPc which lacks the Cu^{2+} ion in exchange for two extra hydrogen atoms.

Now, from the abovementioned lattice structure determined by X-ray crystallography, we extract a 50 nm diameter spherical cluster centered at a given Cu^{2+} ion, and then save all Cu^{2+} ion and magnetic nuclei positions inside. To simulate a given Cu^{2+} concentration c, we need to decide which Cu^{2+} positions are maintained and which ones are removed. Note that in the case of CuPc, the concentration c used in the experimental work holds a rather different definition than that of HoW_{10}. Indeed, let us calculate the probability $0 \leq p \leq 1$ to save the position of a given Cu^{2+} ion. Let M_p and M_d be the molar masses of CuPc and H_2Pc, resp. Let n_p and n_d be the moles of CuPc and H_2Pc inside the cluster for the given concentration. Thus, the masses of CuPc and H_2Pc are $m_p = M_p \cdot n_p$ and $m_d = M_d \cdot n_d$. Since the concentration c is expressed as the percentage of CuPc relative to H_2Pc by mass, we have $c = \left(m_p / m_d\right) \cdot 100 = \left(M_p \cdot n_p / M_d \cdot n_d\right) \cdot 100$, namely, $c \cdot M_d \cdot n_d = M_p \cdot n_p \cdot 100$. Now, let N_T the number of Cu^{2+} ions inside the cluster when there is a 100% concentration. After dilution, $N_p + N_d = N_T$, being N_p and N_d the number of Cu^{2+} ions that have been kept and removed, resp. Multiplying the equality $c \cdot M_d \cdot n_d = M_p \cdot n_p \cdot 100$ by the Avogadro's number N_A, we obtain: $c \cdot M_d \cdot N_d = M_p \cdot N_p \cdot 100$. If we replace N_d by $N_d = N_T - N_p$, we get the expression that determines the number of Cu^{2+} positions to save: $N_p = N_T / \left(\left(M_p / M_d\right) \cdot \left(100 / c\right) + 1\right) \leq N_T$. Thus, the probability p of saving a given Cu^{2+} ion is $p = 1 / \left(\left(M_p / M_d\right) \cdot \left(100 / c\right) + 1\right) \leq 1$, which increases with the concentration c. Then, we cover all Cu^{2+} ions by generating a random number $0 \leq r \leq 1$ at each one of them. Whenever $0 \leq r < p$, we keep the position; otherwise, we drop it. As in the case of HoW_{10}, this procedure generates a random dilution of Cu^{2+} ions in the granule with the desired concentration c, and E_e^2 is subsequently calculated with the Cartesian coordinates of each Cu^{2+} ion kept. Since other equally likely dilutions with the same concentration can

be generated by dropping different Cu^{2+} ions, we sample several granules and consider the arithmetic mean $\overline{E_e^2}$ to calculate T_m^e as $T_m^e = \hbar\Delta / \varepsilon^2 \overline{E_e^2}$. Again, the sampling size L must be large enough to achieve the converged value of $\overline{E_e^2}$, namely, L = 80.000 (c = 0.1%), L = 11.000 (c =1.0%), L = 300 (c = 5.0%), L = 30 (c = 10.0%).

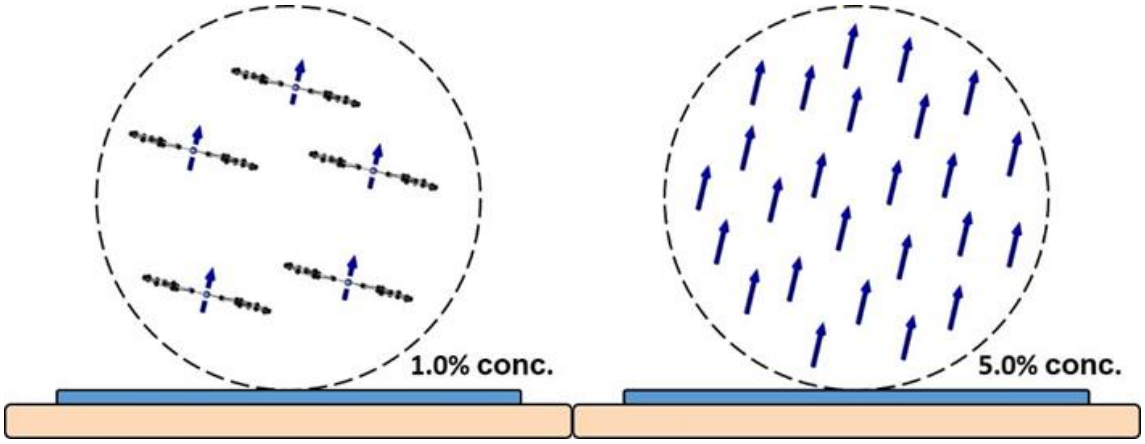

Fig. 41 Representation of the molecular spin bath (whose preferred magnetic anisotropy axis depicted as dark blue arrows is perpendicular to the CuPc plane) for two different Cu^{2+} concentrations, 1.0% (left) and 5.0% (right), inside the spherical granule deposited on top of the perylene surface (blue). Note that real number of molecular spins in the granules at these concentrations is much larger than that of this figure. CuPc molecules are only drawn in the picture on the left just to show their relative orientation to the perylene surface.

We first conducted the calculation of T_m^n by only considering the four copper-coordinating nitrogen atoms (**Eq. 84**). As determined elsewhere,[254] we set $\varepsilon = 0.74$ and then get T_m^n = 2.2 μs. The high-field approximation holds as E_n ~ 0.03 GHz << Δ ~ 9.73 GHz. In a second calculation, we added the rest of the nuclear spin bath (**Eq. 79**) but found that the calculated T_m^n value remains unchanged compared to the previous one. This fact confirms that the magnetic nuclei dephasing is limited by the nuclei of the four copper-coordinating nitrogen atoms. This is most likely due to the strong contact hyperfine coupling between the Cu^{2+} ion and these four surrounding nitrogen nuclei due to their proximity, and the fact that the closest hydrogen atoms are more than 5.5 angstroms away. This extreme proximity of magnetic nuclei to the metal ion is

not present in HoW_{10}. In this system, the Ho^{3+} ion is coordinated by eight oxygen atoms, but their most occurring isotope (^{16}O with a 99.8% abundance) has a non-magnetic nucleus.

Secondly, we evaluated T_m^e also with $\varepsilon = 0.74$ at the four different concentrations, namely, c = 0.1%, 1.0%, 5.0%, 10.0%. The high-field approximation holds again in the whole concentration range as the highest E_e ~ 0.06 GHz << Δ ~ 9.73 GHz (10% conc.). In **Fig. 42**, we show the calculated T_m^{n+e} values, which satisfactorily agree with the experimental T_m values. As expected, molecular-spin-induced dephasing in the form of instantaneous diffusion dominates as Cu^{2+} concentration becomes high, while dephasing induced by the nuclear spin bath dominates at low Cu^{2+} concentration. Let us recall that non-stretched exponential functions were satisfactorily used to fit the Hahn echo decays in the aforementioned concentration range. Note that we are able to reproduce the experimental T_m values of CuPc even though the working applied magnetic field does not correspond to any clock field. Moreover, the experimental T_1 values are now at least two order of magnitude above T_m. Hence, phonon-induced decoherence might have even a lesser influence compared with HoW_{10}.

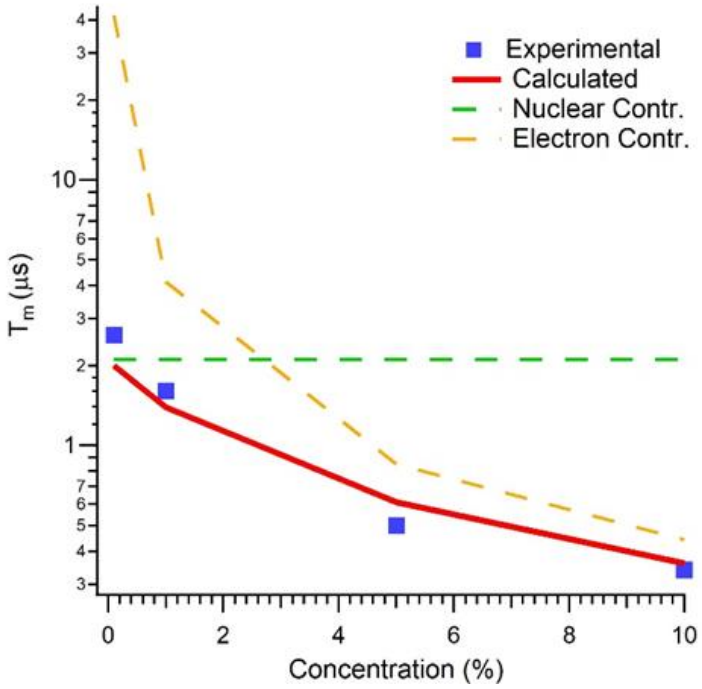

Fig. 42 Phase memory time evolution (logarithmic scale) of CuPc at T = 5 K with the Cu^{2+} concentration. The experimental blue points are from ref. 254. Green and orange dashed lines are the T_m^n and T_m^e contributions to T_m^{n+e} (red curve) calculated by our model.

To end up, it is interesting to unveil additional factors that can make T_m values be different between clock-transition-protected and simple S = 1/2 molecular spin qubits once instantaneous diffusion becomes the limiting dephasing mechanism. Indeed, at the highest Ho^{3+} and Cu^{2+} concentrations, the T_m^e values in HoW_{10} at the clock fields are appreciably higher than that of CuPc. To figure this difference out, let us fix x = 8.2% concentration in HoW_{10} (T_m^e ~ 0.57 μs), which is the equivalent to c = 10% in CuPc (T_m^e ~ 0.36 μs). The values of **Eq. 73** in CuPc are $\overline{\langle \hat{J}_x \rangle} = \overline{\langle \hat{J}_y \rangle} = \overline{\langle \hat{J}_z \rangle} = 0.5$, noticeably smaller than those of HoW_{10} at the clock fields: $\overline{\langle \hat{J}_x \rangle} = \overline{\langle \hat{J}_y \rangle} = 5.3$, $\overline{\langle \hat{J}_z \rangle} = 4.0$. As E_e^2 is initially proportional to $\left\{ \overline{\langle \hat{J}_\alpha \rangle} \right\}_{\alpha=x,y,z}$ in **Eq. 75**, we would expect a greater T_m^e value in CuPc. To explain the rather opposite behavior, we need to focus on the electron Landé factors of HoW_{10} and CuPc. Indeed, while all these factors are non-zero for CuPc in **Eq. 75**, only g_z is different from zero for HoW_{10} in the same equation. Let us recall

that, as mentioned, this fact is due to the particular extreme uniaxial anisotropy of HoW_{10}. Since **Eq. 75** is a three-term and non-negative sum proportional to g_α, E_e^2 takes a smaller value for HoW_{10}, which results in a larger T_m^e value since $T_m^e \propto 1/E_e^2$ for a similar qubit energy gap Δ. As a matter of fact, simple calculations conducted by us show that a decrease of g_x and g_y in CuPc rises T_m^e. This reveals the crucial role of having an axial electron Landé tensor in the spin doublet -either real or effective- defining the qubit, with rather negligible perpendicular components and a small parallel component.

5.4 GdW_{30}

As previously mentioned, the implementation of sophisticated quantum algorithms, which may involve a large number of logical gates, critically depends on our ability to entangle sets of qubits without damaging the encoded information. For this purpose, it is crucial to control both the position and the orientation of the relevant physical qubits in space so that they can properly communicate with each other. As far as this spatial organization is concerned, molecular spin qubits could become potential candidates.

Nevertheless, an alternative strategy to spatially arrange many copies of a given spin qubit is to design a magnetic molecule whose energy scheme allows defining more than one qubit in it. The implementation of *n* qubits requires 2^n isolated energy levels and, importantly, the transition between each pair of them must be addressable and distinguishable from the rest. Thus, it would be possible to perform a given quantum algorithm by using a single-molecule. In other words, the molecule itself becomes an autonomous and independent quantum processor. This is precisely what has recently been proposed by M. D. Jenkins et al. on a Gd^{3+}-based magnetic POM, namely $[Gd(H_2O)P_5W_{30}O_{110}]^{12-}$, hereafter referred to as GdW_{30}.[271] This molecule consists in a single Gd^{3+} ion entrapped inside a POM cage, whose metal-coordinating atom distribution (ten oxygen atoms and one apical water molecule H_2O) results in a 5-fold geometry around the magnetic ion, see **Fig. 43**. The Gd-O distance between Gd^{3+} and the oxygen atom of H_2O is 2.259 Å, which is compatible with a coordination bond. The other Gd-O distances lie between 2.6 and 2.8 Å. Its low-lying energy scheme consists in the eight isolated states of the ground $J = 7/2$ multiplet, and thus allows defining three qubits ($n = 3$) that can be probed by means of EPR spectroscopy.[138] As a matter of fact, there exist simple algorithms exactly involving three qubits, which could be implemented on GdW_{30} such as one of

the Shor's quantum error correction codes, see chapter 7. The potential of GdW_{30} was envisioned in 2013 when long-lived Rabi oscillations were observed under the so-called Hartmann-Hahn condition, i.e., by matching the Rabi frequency with the proton Larmor frequency.[138] Importantly, it allowed increasing the number of these oscillations by a factor of 10.

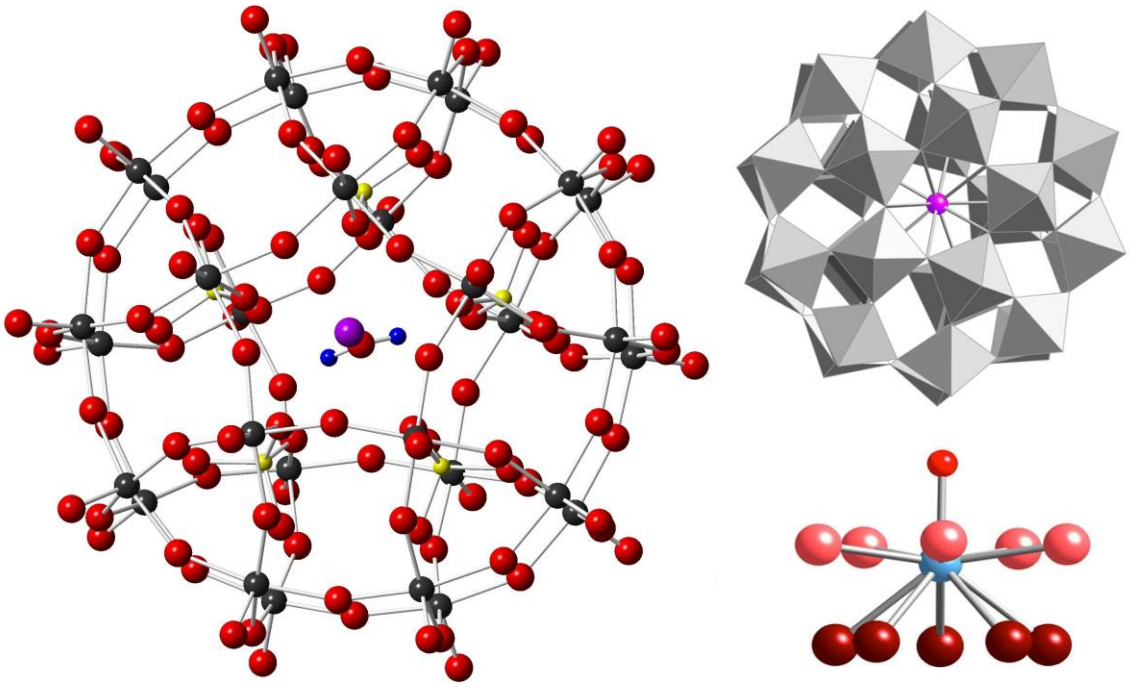

Fig. 43 Left: top view of GdW_{30}. Purple: Gd; dark grey: W; yellow: P; red: O; blue: H. Right top: alternative view of GdW_{30} where the polyhedron vertexes and centers represent the O and W atoms, resp. Right bottom: Gd^{3+} coordination sphere composed of eleven O atoms (with different colors).

Of course, the implementation of complex algorithms will require the interplay of an increasing number of qubits. In the case of GdW_{30}, this would generally mean to assemble several copies in close enough positions to allow qubit entanglement. Nonetheless, approaching magnetic molecules with the goal of communicating them also leads to an unavoidable detrimental effect. Indeed, as explained in other chapters, the nature of the involved molecular entities produces a magnetic field that is permanently covering all the space. This field results in a magnetic noise which will eventually destroy the information at play during the algorithm. The successful implementation of GdW_{30} in a device devoted to perform generic quantum algorithms will require

close enough copies of it to allow inter-qubit communication, but with a weak enough magnetic noise to keep quantum information -either stored or under processing- safe from decoherence.

Herein, we aim to calculate the effect of magnetic noise –present in a single crystal of many equally-oriented copies of GdW_{30} at a moderate Gd^{3+} concentration– in the form of instantaneous diffusion and nuclear spin bath. This will allow us checking whether these dephasing mechanisms are limiting the several T_m values of a given set of pairs of energy states in GdW_{30}. An estimate yet rough was already provided,[271] but now we will employ more sophisticated models such as the ones presented in section 5.2. The particular set of pairs of energy levels is composed of those pairs whose transitions are resonant with the microwave frequencies employed in an X-band EPR spectrometer (~9 – 10 GHz). We will compare our calculated values with the experimental ones reported by M. D. Jenkins et al. at T = 6 K,[271] and discuss on the presence of other T_m-limiting decoherence sources. The electronic structure of GdW_{30}, namely energies E_l and wave-functions $|\psi_l\rangle$ of the ground J = 7/2 multiplet is determined by the spin Hamiltonian in **Eq. 85**.

$$\hat{H} = D\left[\hat{J}_z^2 - \frac{1}{3}J(J+1)\right] + E\left(\hat{J}_x^2 - \hat{J}_y^2\right) + \mu_B g\vec{B}\cdot\vec{J} \qquad \textbf{Eq. 85}$$

The axial and rhombic zero-field splitting parameters D and E are related with B_2^0 and B_2^2 as $D = 3B_2^0$ and $E = B_2^2$. The values D = 1281 MHz and E = 294 MHz were determined by means of EPR spectroscopy while keeping g = 2 fixed.[271] Note that in the case of Gd^{3+}, where the 4f shell is half-filled, the first order contribution to the orbital angular momentum is L = 0. Thus, the total angular momentum J mainly arises from the spin angular momentum S = 7/2. This results in much smaller ZFS of the order of 1 cm^{-1}, and that is why the CFPs are between two and three orders of magnitude below those found for magnetic coordination compounds based on much more anisotropic Ln^{3+} ions such as Tb^{3+}, Dy^{3+} or Ho^{3+}. The diagonalization of **Eq. 85** is conducted in SIMPRE. The last important point is the direction of the applied magnetic field $\vec{B}$. The orientation of the single crystal in the EPR spectrometer was such that this direction coincides with the perpendicular axis to the molecular plane of GdW_{30}, see **Fig. 43** left, which defines the Z axis direction. Thus, when calculating the phase memory times, we apply the magnetic field in this

perpendicular axis which is common to all copies of GdW_{30} in the crystal since all of them are equally oriented. Thus, hereafter the magnitude $|\vec{B}|$ of the applied magnetic field will be referred to as B_z. The eight energy states E_l derived from **Eq. 85** as a function of a typical B_z range are plotted in **Fig. 44**.

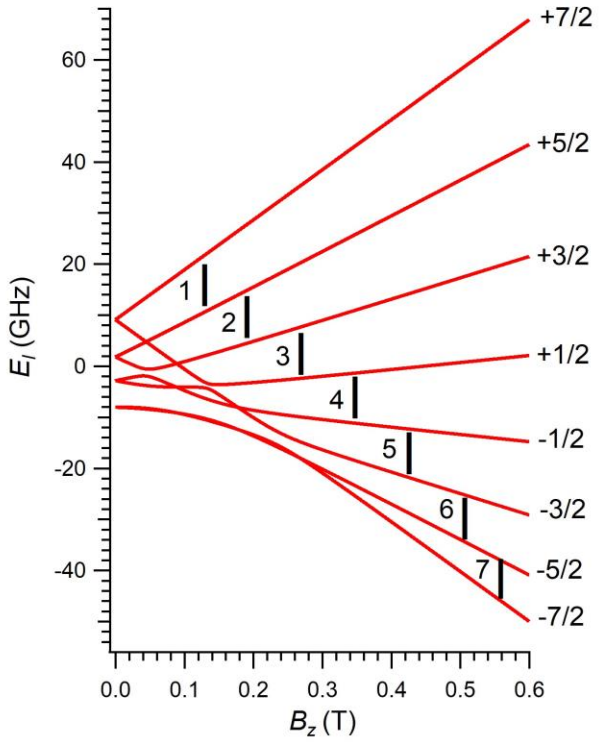

Fig. 44 Zeeman energy scheme of GdW_{30} as a function of the applied magnetic field, derived by diagonalizing **Eq. 85**. Each Zeeman curve is labeled with the corresponding m_J projection of the ground electron quantum number J = 7/2 of Gd^{3+}. Numbers 1 – 7 label each resonant transition with the working microwave frequency (~9 – 10 GHz).

The radius of the spherical cluster containing the crystallographic positions of the Gd^{3+} ions is of 400 Å, which was enough to converge the calculated T_m^e in each pair of energy levels explored. The simulated Gd^{3+} concentration x in $[Gd_xY_{1-x}(H_2O)P_5W_{30}O_{110}]^{12-}$ is x = 0.01 = 1%, which is achieved by randomly removing 99 out of 100 Gd^{3+} ions that are substituted by the chemically similar diamagnetic ion Y^{3+}. We also sample several random dilutions -all of them with the same concentration- to calculate the averaged T_m^e at each magnetic field. In

Fig. 45, we show the comparison between calculated T_m^e and experimental T_m values for the particular transitions depicted in .**Fig. 44**.

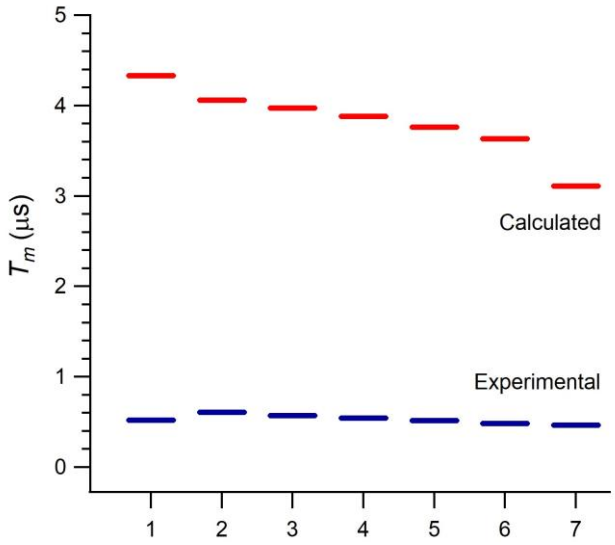

Fig. 45 Calculated T_m^e and experimental[271] T_m phase memory times of GdW_{30} at each one of the seven resonant transitions in the explored magnetic field range (1: 0.125 T, 2: 0.19 T, 3: 0.27 T, 4: 0.35 T, 5: 0.43 T, 6: 0.51 T, 7: 0.56 T).

A noticeable feature in **Fig. 45** is the monotonous decrease in the calculated T_m^e. Indeed, this is because E_e^2 is constant, while Δ monotonously decreases from the first to the seventh transition. This behavior is also observed in the experimental T_m, although with a slighter decrease and with the value of the first transition lying out of this trend possibly because of a larger experimental error. The calculated T_m^e values are around 3 µs above the experimentally reported T_m values. Unlike the rough estimate and despite using non-stretched exponential functions to extract T_m,[271] our results suggest that electron magnetic noise in the form of instantaneous diffusion is not the limiting decoherence source at x = 1%. Yet, due to the proximity between T_m^e and T_m, it could be limiting T_m but in competition with other mechanisms.

To check whether electron magnetic noise is among the dephasing mechanisms, it is useful to measure T_m at different Gd^{3+} ion concentrations as did elsewhere.[311] These measurements revealed that indeed T_m decreases as Gd^{3+} concentration increases, which means that electron magnetic noise might be limiting T_m. Nonetheless, it might only be partially in the light of the two

following reasons. First, as mentioned above, the theoretical estimates T_m^e do not match the experimental T_m values. Second, T_m does not scale with the Gd^{3+} concentration x as $T_m \propto 1/x$. This scaling characterizes electron magnetic noise and, in this case, establishes that a rise in x of one order of magnitude should divide T_m by 10 as seen in section 5.2.

A well-established strategy to reduce the effect of electron magnetic noise is by further dilution of the given single crystal. Nonetheless, as we mention elsewhere, this is not a useful method since it implies to move the Gd^{3+} ions away, which hence can result in an important alteration of the inter-qubit communication. Thus, one needs to choose a concentration that allows a robust qubit communication while keeping electron magnetic noise below a safe threshold. In a 100% concentrated single crystal of GdW_{30} the minimum distance between pairs of Gd^3 ions is around 17 Å, while in our 1% working concentration this minimum distance is increased up to ~37 Å. If this distance is still too large and further approach of Gd^{3+} ions is required to allow a safe inter-qubit communication, one should first identify and suppress the other decoherence sources before rising the single crystal concentration.

Let us recall that GdW_{30} is a charged molecule, which requires the presence of counter-ions to properly balance the overall charge. Thus, the single crystal is composed of several copies of GdW_{30} surrounded by water molecules and potassium cations acting as counter-ions, see **Fig. 46**. Importantly, the single crystal is composed of chemical elements that present a high occurrence of isotopes with magnetic nuclei. Namely, tungsten (14%, I = 1/2) and phosphorus (100%, I = 1/2) atoms in the POM cage, hydrogen atoms (100%, I = 1/2) in water molecules, and potassium cations (100%, I = 3/2), where I is the isotope nuclear spin quantum number. This bath of magnetic nuclei generates an extra magnetic noise which adds to that of the Gd^{3+} ion bath and, of course, can also limit T_m.

We also considered the model described in section 5.2 devoted to estimate the phase memory time T_m^n produced by a given nuclear spin bath. By applying this model to a single crystal of GdW_{30}, we subsequently conducted the calculation of T_m^n for each one of the seven selected transitions in **Fig. 44**. For that, we employed the crystallographic positions of all magnetic nuclei inside a spherical cluster of 40 Å radius, which was enough to converge each T_m^n. Our results show that T_m^n lies inside the range 51 – 68 μs, whose values are two orders of magnitude above the experimental T_m. Thus, magnetic nuclear

decoherence might not be among the decoherence mechanisms limiting T_m according to this model.

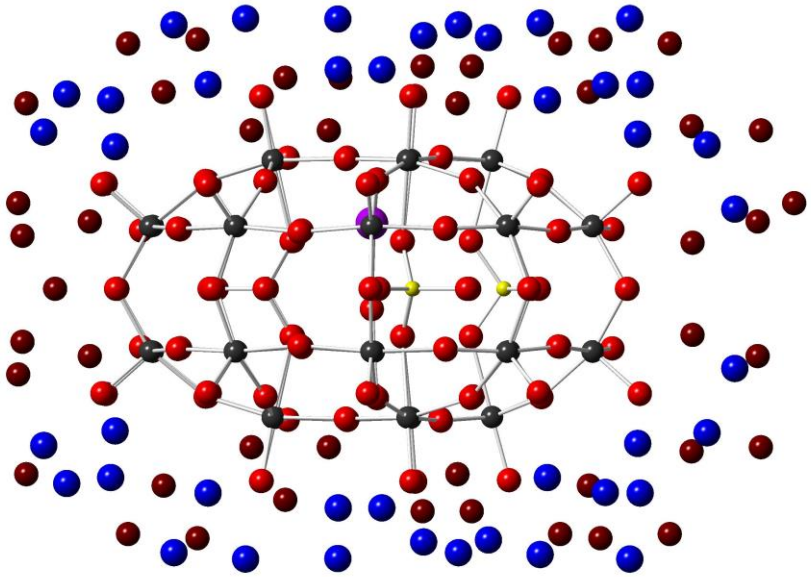

Fig. 46 Side view of GdW_{30} surrounded by the crystallographic positions of some K cations (blue) and water molecules (O atoms in dark red, H atoms omitted for clarity).

As discussed in chapter 4, molecular spin qubits can also couple to crystal vibrations at any temperature, and this constitutes another important decoherence mechanism that becomes more important as thermal energy is increased. At T = 6 K, the measurements at each one of the seven transitions led to T_1 values around 2.5 μs.[271] Note that this timescale is close to T_m, which suggests that lattice vibrations might be considered as another potential source of decoherence. Due to the relatively low working temperature, the vibrational states involved might be low in energy such as those from long-wavelength phonon modes and low-frequency molecular vibrations. In fact, the latter can be significantly coupled even if they are moderately populated at low temperature as found in section 4.1 of chapter 4. Since the spin-vibration coupling Hamiltonians are proportional to derivatives of the anisotropy parameters respect to distortion coordinates, the relevant vibrational modes to focus on may be found among those producing significant variations in these parameters. As shown, the determination of these evolutions involve many point calculations that can be computationally demanding and are beyond the

scope of this section. Higher energy modes should play a very limited role not significant at all because of their negligible thermal population.

At first sight, the apparent rigidity of the POM cage would prevent from a significant vibrational decoherence. While this observation could be true, we must not forget that the Gd^{3+} ion is coordinated by an apical water molecule, which is also embedded in the cage but not covalently bonded to it. This could result in a certain freedom of movement that allows the vibration of this water molecule with respect to the Gd^{3+} position. Thus, both independent and collective motions of Gd^{3+} ion and apical water molecule could be examples of significantly coupled low-frequency vibrations. In addition, there also exists another important decohering movement concerning rotations of magnetic nuclei. For instance, it is well known that rotation of methyl groups $-CH_3$ can couple to energy states encoding spin qubits.[203,210,312] In case of GdW_{30}, the rotation would take place in the coordinating water molecule, whose magnetic nuclei in the form of two hydrogen atoms would couple to the Gd^{3+} ion. Of course, this would deserve further investigation, since the forced removal of this apical water molecule could result in an enhanced coherence for the three qubits encoded in the energy scheme of GdW_{30}. In fact, a family of Ln-based POMs with a similar coordination environment but excluding the apical water molecule has recently been theoretically explored,[313] whose Gd^{3+} derivative could offer a promising platform to design more robust single-molecule qubits.

Block 3.

Current Challenges

6

Atomic Clock Transitions in HoW_{10}

This chapter is a follow-up to section 5.2 concerning the system HoW_{10}, and is broken down into three sections. In section 6.1 we will introduce an additional concept to the model presented in section 5.2, namely, the transition probability between the two energy states that define a spin qubit. First, we will propose how this transition probability affects and is related with T_m^e; then, we will explain how to calculate it. In section 6.2 we will show the results derived from the expanded model along with the input parameters employed to simulate the experimental T_m evolution against the applied magnetic field. In section 6.3 we will thoroughly discuss on these results and on the connection between this transition probability and the reported experiments of HoW_{10}.

6.1 Transition Probability

To manipulate a two-level system in magnetic molecules (e.g. a spin qubit), we need to excite the sample with radiation of a frequency that matches the energy gap between the two spin states. This energy gap will depend on the applied magnetic field via Zeeman effect. As a matter of fact, the irradiation frequency does not need to exactly match the energy gap to drive a transition between two spin states. This fact is derived from a fundamental principle in quantum mechanics: uncertainty, which in this case means that each one of these states has an uncertainty width in its energy. Of course, the closer the irradiation frequency is to the energy gap, the more likely a transition will be driven between the spin states. Thus, there might exist a transition probability involved in the manipulation of a given spin qubit. To the best of our

knowledge, decoherence models devoted to estimate the phase memory time T_m do not mention this probability and, whenever it is below 1, no effect is expected on T_m.

The picture we propose to introduce the transition probability P_{trans} and to relate it with T_m^e is as follows. As exposed in chapter 5, the expression of T_m^e is given by $T_m^e = \hbar\Delta / E_e^2$, where Δ is the energy gap between the two spin states of the qubit and E_e is the electron contribution to the echo line half-width. From this expression, an effectively infinite magnetic noise would be translated into an infinite value of E_e, which would give rise to $T_m^e = 0$. Thus, we propose to introduce P_{trans} as a new source of noise and define an effective electron contribution $E_{e,eff}$ to the echo line half-width such that $E_{e,eff}^2 = E_e^2 / P_{trans}$. The corrected phase memory time $T_m^{e,P}$ reads as $T_m^{e,P} = \hbar\Delta / E_{e,eff}^2$, i.e., $T_m^{e,P} = P_{trans} T_m^e$. Since $P_{trans} \leq 1$, $T_m^{e,P}$ will always be in general lesser or equal than T_m^e, i.e., $T_m^{e,P} \leq T_m^e$. Hence, the result of the action of P_{trans} is to make the qubit behave as if it was feeling an additional magnetic noise. Whenever $P_{\text{trans}} = 1$, there is no additional noise and $T_m^{e,P}$ equals T_m^e. In summary, a lower transition probability caused by a larger mismatch between the irradiation frequency and the qubit energy gap will lead to a lower T_m^e than expected.

The next step is to calculate P_{trans}. For this purpose, we will use time-dependent perturbation theory up to first order. First, we need to express the oscillating magnetic field $\overrightarrow{B_1}\left(t,\vec{r}\right) = \overrightarrow{B_1^0}\cos\left(\omega t - \vec{k}\cdot\vec{r}\right)$ that composes the microwave radiation applied in pulsed EPR spectroscopy. This field couples with the magnetic dipolar moment of the molecule and hence is responsible for driving a transition between two given spin states. It propagates along the direction determined by the wave-vector $\vec{k}$, which is orthogonal to the static magnetic field $\overrightarrow{B_0}$ applied by the same spectrometer. The angular frequency ω determines the irradiation frequency $\hbar\omega$ (~ 9 – 10 GHz in X-band EPR experiments), and t is the pulse length, i.e., the irradiation time (~10 ns). The constant vector $\overrightarrow{B_1^0}$ determines the polarization of $\overrightarrow{B_1}\left(t,\vec{r}\right)$, and $\left|\overrightarrow{B_1^0}\right|$ determines the magnitude (~1 mT) of this oscillating magnetic field. EPR spectrometers usually employ a resonant cavity designed to create a linearly polarized oscillating magnetic field

$\vec{B_1}$, see **Fig. 47**. Hence, since this is the case of the spectrometer employed to probe HoW_{10}, we will consider this model of polarization to calculate P_{trans}.

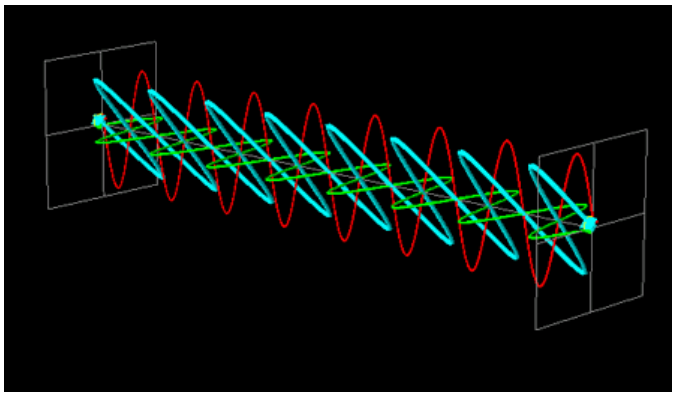

Fig. 47 Oscillating magnetic field linearly polarized in blue along with its decomposition according to two orthogonal axes in red and green.

In **Fig. 47**, let us imagine $\vec{B_0}$ pointing in vertical direction and use it to define the *Z* axis. On the other hand, let us use the propagation direction of $\vec{B_1}$ determined by $\vec{k}$ to define now the *X* axis. Note that $\vec{B_0}$ and $\vec{k}$ are orthogonal. If we define the *Y* axis as the axis orthogonal to the *X* and *Z* axes, $\vec{B_1^0}$ is hence contained in the *YZ* plane and is orthogonal to $\vec{k}$. Thus, $\vec{B_1^0}$ determines the constant direction of oscillation of $\vec{B_1}$ as colored in blue in **Fig. 47**. With this axes definition, $\vec{B_1^0}$ forms an angle $-90^o \leq \delta \leq 90^o$ with the *Y* axis, which is called polarization angle, see **Fig. 48**. Since this angle is an input for our model, we can cover in particular the experiments performed both in parallel ($\delta = 90^o$) and in perpendicular ($\delta = 0^o$) mode.

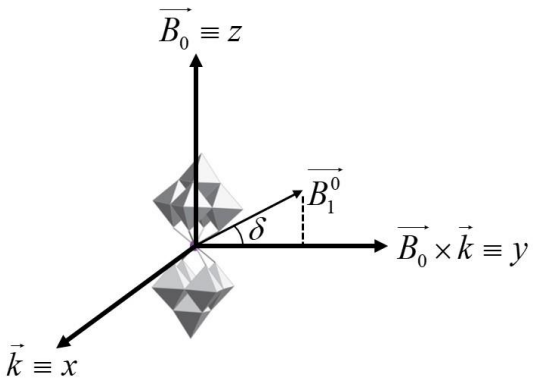

Fig. 48 Definition of Cartesian axes in an EPR spectrometer. The static magnetic field $\overrightarrow{B_0}$ defines the *Z* axis, the wave-vector $\vec{k}$ defines the X axis, and the cross product $\overrightarrow{B_0} \times \vec{k}$ defines the *Y* axis. The angle δ between the *Y* axis and the polarization vector $\overrightarrow{B_1^0}$ is the polarization angle.

The next step is to apply the so-called long wavelength approximation in the expression $\overrightarrow{B_1}\left(t,\vec{r}\right) = \overrightarrow{B_1^0}\cos\left(\omega t - \vec{k}\cdot\vec{r}\right)$. Since the wavelength λ of $\overrightarrow{B_1}$ is much larger than the molecular dimensions, i.e. $\left|\vec{r}\right|/\lambda \ll 1$, the term $\vec{k}\cdot\vec{r}$ is rather negligible since $\left|\vec{k}\cdot\vec{r}\right| \sim 2\pi\left|\vec{r}\right|/\lambda \sim \left|\vec{r}\right|/\lambda \ll 1$. For instance, the wavelength in X- and Q-band EPR spectrometers are ~30 and ~9 mm, while the typical molecular dimension is ~1 nm. Thus, $\overrightarrow{B_1}$ is approximated as $\overrightarrow{B_1}\left(t,\vec{r}\right) \approx \overrightarrow{B_1^0}\cos\left(\omega t\right)$. The calculation of P_{trsns} requires to solve the time-dependent Schrödinger equation. To keep a fluent reading, we will avoid the technical details in the resolution of this equation and just give a general scheme of the procedure. These details are routine and can be found in any basic course on time-dependent perturbation theory up to first order.

The starting point is the time-dependent wave-function $\left|\Psi(t)\right\rangle$ in **Eq. 86** that describes the time evolution of a (magnetic) system with a given set of (spin) states characterized by (spin) energies E_k and eigenfunctions $\left|\psi_k\right\rangle$.

$$\left|\Psi\left(t\right)\right\rangle = \sum_k c_k\left(t\right)\exp\left(-itE_k/\hbar\right)\left|\psi_k\right\rangle \qquad \textbf{Eq. 86}$$

E_k and $|\psi_k\rangle$ are obtained by diagonalizing a given (spin) Hamiltonian $\hat{H}$. In the case of HoW_{10}, $\hat{H}$ is the one presented in section 5.2. To determine the time evolution of the coefficients $c_k(t)$, $|\Psi(t)\rangle$ is plugged into the time-dependent Schrödinger equation in **Eq. 87**:

$$\left(\hat{H}+\hat{V}(t)\right)|\Psi(t)\rangle = i\hbar\frac{\partial}{\partial t}|\Psi(t)\rangle \qquad \textbf{Eq. 87}$$

In **Eq. 87**, $\hat{V}(t) = -\overrightarrow{\hat{\mu}_J}\cdot\vec{B}_1(t)$ is the time-dependent interaction potential that describes the coupling between $\vec{B}_1$ and the magnetic dipolar moment $\overrightarrow{\hat{\mu}_J} = -(\mu_B/\hbar)\left(g_x\hat{J}_x, g_y\hat{J}_y, g_z\hat{J}_z\right)$ of the molecule. In the expression of $\overrightarrow{\hat{\mu}_J}$, g_α are the electron Landé factors and $\hat{J}_\alpha$ are the Cartesian components of the electron spin operator $\hat{\boldsymbol{J}}$. Note that in the resolution of **Eq. 87** we are considering $\hat{V}(t)$ as a perturbation; hence, its magnitude has to be small enough as compared to $\hat{H}$. Indeed, $\left|\overrightarrow{B_1^0}\right|$ is found around 1 mT or even below, while $\left|\overrightarrow{B_0}\right|$, which determines the dominant interaction in $\hat{H}$, i.e. the Zeeman effect, usually lies inside the range of some hundreds of mT. In addition, $\hat{V}(t)$ is working only for a few tens of ns, which is much shorter than the standard timescale T_m found in common molecular spin qubits (above one microsecond). This allows to assume that the system in a given eigenfunction at $t = 0$ will be driven as a closed system without significant decohering effects and hence this evolution can be described with **Eq. 87**.

After working out **Eq. 87**, an uncoupled set of differential equations is obtained. These equations can be readily solved to get the coefficients $c_k(t)$. They are expressed in terms of the initial conditions $c_k(t=0)$, i.e., the coefficients $c_k(t)$ evaluated at $t = 0$. Since we want to calculate the transition probability between the two qubit states $|0\rangle$ and $|1\rangle$, let us set the molecule to be initialized at $t = 0$ in one of them. For instance, say $|0\rangle$ with label n. Thus,

$c_n(t=0)=1$ and $c_k(t=0)=0$ for every $k \neq n$. This allows calculating the transition probability $P_{n\to m}(t)$ from $|0\rangle$ to $|1\rangle$ with label *m*. Likewise, we can also proceed the other way around, i.e., to initialize the molecule in $|1\rangle$ at $t = 0$ and to calculate the transition probability $P_{m\to n}(t)$ from $|1\rangle$ to $|0\rangle$. We propose to define the working transition probability P_{trans} as in **Eq. 88**.

$$P_{trans} = \frac{P_{n\to m}(t) + P_{m\to n}(t)}{2} \qquad \textbf{Eq. 88}$$

The irradiation time *t* in **Eq. 88**, which will depend on $\left|\overrightarrow{B_1^0}\right|$, is the one corresponding to a π-pulse, i.e., the right time to drive the system from $|0\rangle$ to $|1\rangle$ or vice versa. Before showing the expression of $P_{n\to m}(t)$, we need first to rename the coefficients $c_k(t)$. Indeed, once a given label *n* is fixed to describe the initial eigenstate at $t = 0$, the system will eventually be driven to the rest of eigenstates with label *k*. Thus, we rename $c_n(t)$ as $c_{n\to n}(t)$ -which determines the probability of remaining in the eigenstate *n* at a given $t > 0$-; and also rename $c_k(t)$ as $c_{n\to k}(t)$ which determines the probability of driving the system to an eigenstate *k* at a given $t > 0$. In particular, $c_{n\to m}(t)$ determines the transition probability from the eigenstate *n*, i.e. $|0\rangle$, to the eigenstate *m*, i.e. $|1\rangle$. The expression of $P_{n\to m}(t)$ is given in **Eq. 89**.

$$P_{n\to m}(t) = \frac{\left|c_{n\to m}(t)\right|^2}{\sum_{\substack{k \\ E_k \neq E_n \\ or, k=n}} \left|c_{n\to k}(t)\right|^2} \qquad \textbf{Eq. 89}$$

The sum in **Eq. 89** includes the *n* eigenstate ($k = n$) as well as the eigenstates *k* with energy E_k different from E_n, where the particular case $k = m$ is included.

We consider that the transition from the eigenstate *n* to any other eigenstate with the same energy E_n is negligible compared to the transitions to eigenstates *k* with energy $E_k \neq E_n$. Thus, all the eigenstates with energy E_n but the eigenstate *n* are excluded. This sum acts as a normalization constant so that $P_{n\to m}(t) \leq 1$ and $\sum_m P_{n\to m}(t) = 1$, where the label *m* is such that $E_m \neq E_n$ or *m* = *n*. The square modulus of the coefficients $c_k(t)$ are given in **Eq. 90**, **Eq. 91**, **Eq. 92**.

$$\left|c_{n\to n}(t)\right|^2 = 1 + \left|\overrightarrow{\hat{\mu}_J^{nn}} \cdot \overrightarrow{B_1^0}\right|^2 \left(\frac{\sin(\omega t)}{\hbar\omega}\right)^2 \qquad \textbf{Eq. 90}$$

$$\text{If } E_k > E_n \Rightarrow \left|c_{n\to k}(t)\right|^2 = \left|\overrightarrow{\hat{\mu}_J^{kn}} \cdot \overrightarrow{B_1^0}\right|^2 \left(\frac{\sin\left(\left(E_k - E_n - \hbar\omega\right)t/2\hbar\right)}{E_k - E_n - \hbar\omega}\right)^2 \qquad \textbf{Eq. 91}$$

$$\text{If } E_k < E_n \Rightarrow \left|c_{n\to k}(t)\right|^2 = \left|\overrightarrow{\hat{\mu}_J^{kn}} \cdot \overrightarrow{B_1^0}\right|^2 \left(\frac{\sin\left(\left(E_k - E_n + \hbar\omega\right)t/2\hbar\right)}{E_k - E_n + \hbar\omega}\right)^2 \qquad \textbf{Eq. 92}$$

The term $\left|\overrightarrow{\hat{\mu}_J^{kn}} \cdot \overrightarrow{B_1^0}\right|^2$ (transition rule) describes the coupling strength between $\overrightarrow{B_1}$ and $\overrightarrow{\hat{\mu}_J}$, where $\overrightarrow{\hat{\mu}_J^{kn}} = \langle\psi_k|\overrightarrow{\hat{\mu}_J}|\psi_n\rangle$ connects the eigenstates *n* and *k*. In other words, $\left|\overrightarrow{\hat{\mu}_J^{kn}} \cdot \overrightarrow{B_1^0}\right|^2$ determines how able $\overrightarrow{B_1}$ is to drive a transition between the eigenstates *n* and *k*. $\overrightarrow{\hat{\mu}_J^{nn}} = \langle\psi_n|\overrightarrow{\hat{\mu}_J}|\psi_n\rangle$ is just the expectation value of $\overrightarrow{\hat{\mu}_J}$ under the eigenfunction $|\psi_n\rangle$. The terms $E_k - E_n - \hbar\omega$ and $E_k - E_n + \hbar\omega$ account for the resonance in energy between $|E_k - E_n|$ and $\hbar\omega$. Analogously, an expression for $P_{m\to n}(t)$ is also derived as given in **Eq. 93**.

$$P_{m\to n}(t)=\frac{\left|c_{m\to n}(t)\right|^2}{\sum\limits_{\substack{k\\ E_k\neq E_m\\ or,k=m}}\left|c_{m\to k}(t)\right|^2} \qquad \textbf{Eq. 93}$$

6.2 Results

In the application to HoW_{10} of the picture described in section 6.1 we are only considering the 8th and 9th spin states as sorted by energy for each value of the applied magnetic field, which define the two states of the qubit with an energy gap $\Delta = E_9 - E_8$ that depends on this field. Thus, n = 8, m = 9, and the working transition probability is $P_{trans} = \left(P_{8\to 9}(t) + P_{9\to 8}(t)\right)/2$ where $P_{8\to 9}(t)$, $P_{9\to 8}(t)$ are given in **Eq. 94**.

$$P_{8\to 9}(t)=\frac{\left|c_{8\to 9}(t)\right|^2}{\left|c_{8\to 8}(t)\right|^2+\left|c_{8\to 9}(t)\right|^2} \qquad P_{9\to 8}(t)=\frac{\left|c_{9\to 8}(t)\right|^2}{\left|c_{9\to 9}(t)\right|^2+\left|c_{9\to 8}(t)\right|^2} \qquad \textbf{Eq. 94}$$

We could have considered the full set of the 16 low-lying spin states of HoW_{10}, but because of the large difference between $|E_k - E_8|$, $|E_k - E_9|$ and $\hbar\omega$, the transitions 8→k, 9→k with $k \neq 8, 9$ are rather unlikely. The employed input parameters are: $\hbar\omega$ = 9.1765 GHz, t = 32 ns, $\left|\overrightarrow{B_1^0}\right|$ = 0.5 mT, δ = 90º (i.e., the $\overrightarrow{B_1^0}$ direction coincides with that of $\overrightarrow{B_0}$). In section 6.3 we will explain the choice of these numerical values.

In **Fig. 49**, we show the calculated T_m^e and $T_m^{e,P}$ along with the experimental T_m against the applied magnetic field B_z at a Ho^{3+} concentration of 10% (T = 5 K). The maximum transition probability $P_{trans}^{\max} \sim 0.93$ is reached at each clock transition (Δ = 9.1765 – 9.1768 GHz), while the minimum probability $P_{trans}^{\min} \sim 10^{-3}$ is located right at the middle of the valleys ($\Delta \sim 9.75$ GHz).

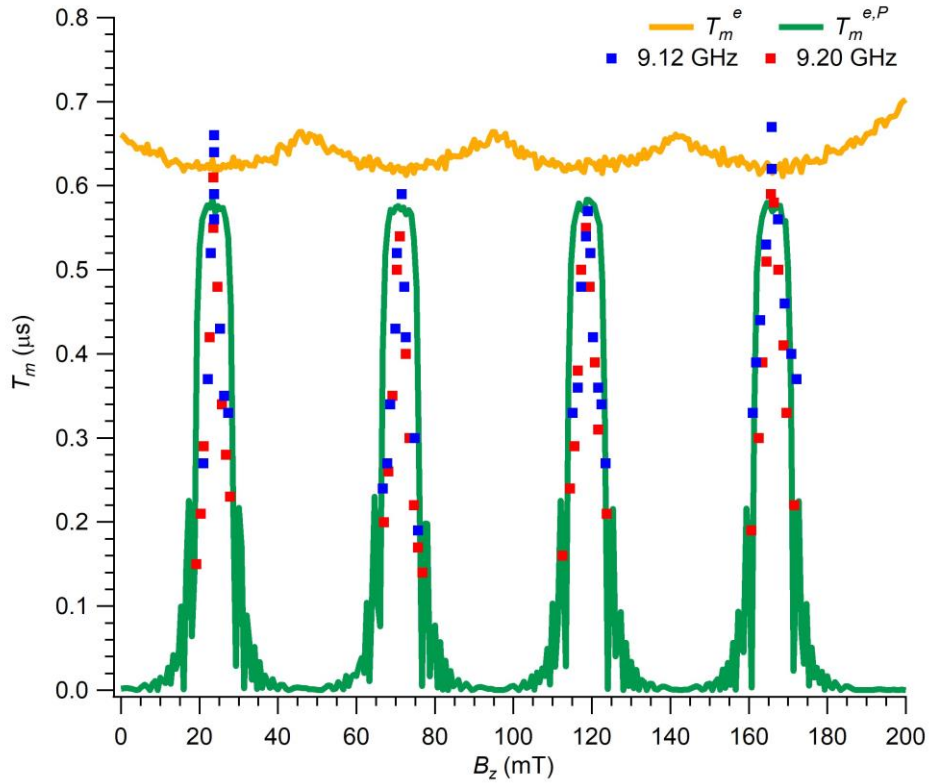

Fig. 49 T_m evolution against the applied magnetic field B_z at a Ho^{3+} concentration of 10% in the experimentally-probed single crystal (T = 5 K). Non-corrected T_m^e in orange, corrected $T_m^{e,P}$ in green. Blue and red points are experimental T_m values at two different $\hbar\omega$. The highest experimental errors in T_m are found around the clock transition fields.

At the much lower concentration of 1% (T = 5 K), instantaneous diffusion is expected not to be the limiting decoherence mechanism anymore, since high enough metal ion concentrations are required for this mechanism to be dominant. This agrees with the fact that the calculated $T_m^{e,P}$ is now somewhat higher than the experimental T_m as shown in **Fig. 50**. Yet, both the qualitative behavior and the order of magnitude of the experimental T_m are recovered.

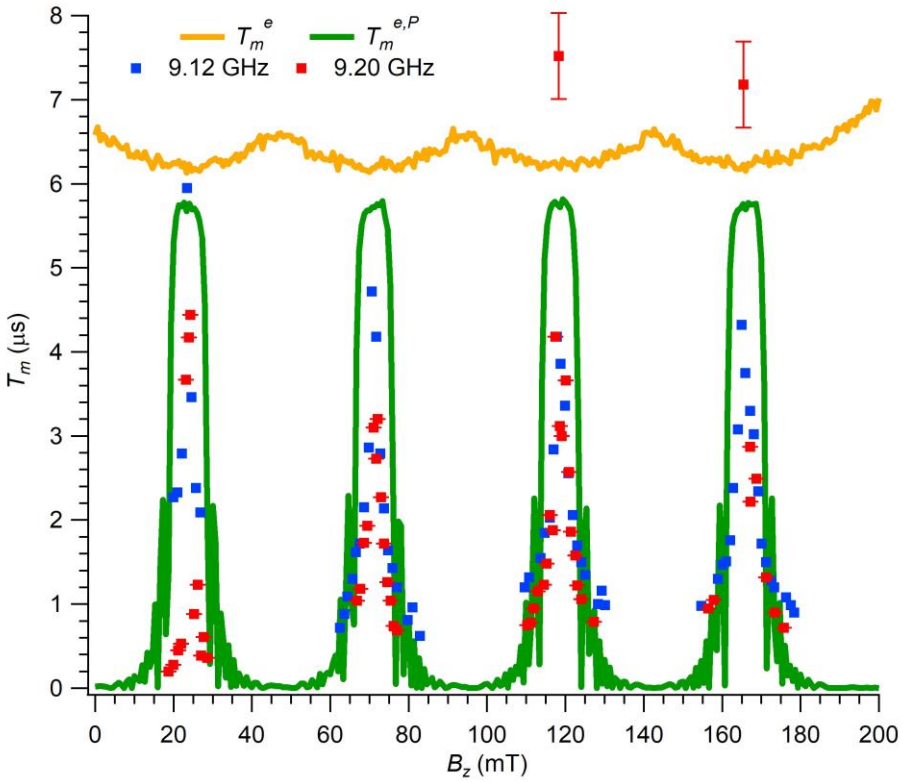

Fig. 50 T_m evolution against the applied magnetic field B_z at a Ho^{3+} concentration of 1% in the experimentally-probed single crystal (T = 5 K). Non-corrected T_m^e in orange, corrected $T_m^{e,P}$ in green. Blue and red points are experimental T_m values at two different $\hbar\omega$. The highest experimental errors in T_m are found around the clock transition fields.

6.3 Discussion

Let us start by discussing on the evidence which may support the fact that transitions probabilities are at play in the reported experiments of HoW_{10}. First, we will put the focus on **Fig. 51**, which depicts the ESE (Electron Spin Echo) detected spectra determined by Shiddiq et al. at different $\hbar\omega$ for a Ho^{3+} concentration of 1% and around the clock transition located at 165.4 mT.[206] These spectra record a peak at the magnetic fields in which a resonance between Δ and $\hbar\omega$ is produced.

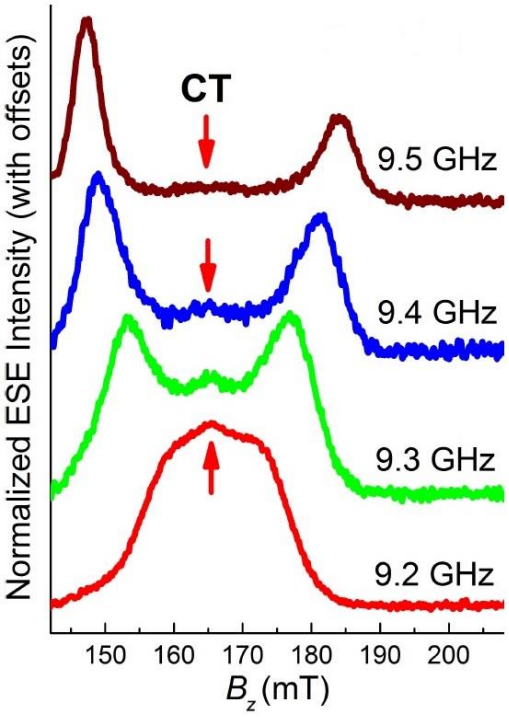

Fig. 51 ESE (Electron Spin Echo) detected spectra at different $\hbar\omega$ for a Ho^{3+} concentration of 1% around a clock transition (CT) as determined by Shiddiq et al.[206]

The qubit energy gap Δ is 9.1768 GHz at 165.4 mT. Thus, it is reasonable to detect a high ESE intensity at this magnetic field for $\hbar\omega$ = 9.20 GHz. As we use a $\hbar\omega$ more and more different from Δ = 9.1768 GHz, the detected ESE intensity at 165.4 mT is noticeably reduced. This fact agrees with the picture of a decreasing transition probability at play as $\hbar\omega$ moves away from the value Δ = 9.1768 GHz. In other words, there exists a lesser probability to drive the transition 8 ↔ 9 and a lesser number of molecules is excited.

In second place, **Fig. 52** shows field-swept T_m measurements for a Ho^{3+} concentration of 0.1% at different $\hbar\omega$ as also determined by Shiddiq et al.[206] It is important to note that these measurements are beyond the clock transition located at 165.4 mT, and correspond to the so-called normal EPR transitions, i.e., $m_J = -4$ to $m_J = +4$ transitions where the dependence of spin energy with the applied magnetic field approaches the linear regime, see **Fig. 39**. Note that because of the small concentration of 0.1%, the model presented in section 5.2 cannot reproduce the experimental T_m in **Fig. 52** as it requires instantaneous

diffusion to be the limiting decoherence mechanism, i.e., high enough metal ion concentrations.

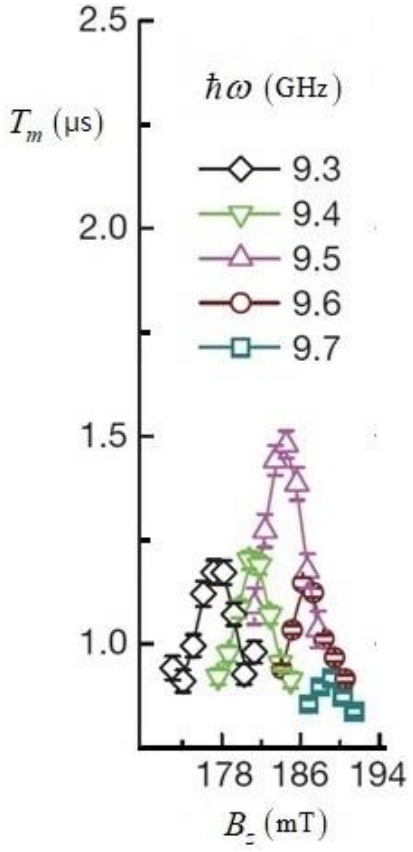

Fig. 52 Field-swept T_m measurements for a Ho^{3+} concentration of 0.1% at different $\hbar\omega$ as determined by Shiddiq et al.[206]

These normal transitions do not follow the definition of a real clock transition and qubit coherence becomes more limited. In other words, although T_m is moderately peaked, the sharp divergences seen at the four clock transitions are clearly absent. In fact, as soon as the Ho^{3+} concentration is increased up to 1.0%, the experimental T_m values at the normal transitions become much shorter (~100 ns) since the ESE intensity can hardly be detected. A further increase in the Ho^{3+} concentration leads to a total suppression of T_m as the ESE signal can no longer be detected.

Of course, this is consistent with the fact that dipolar magnetic noise increases with increasing metal ion concentration, which results in shorter T_m values. Nevertheless, here we are not focusing on the T_m evolution with Ho^{3+} concentration, but on the T_m evolution with the applied magnetic field once both Ho^{3+} concentration and $\hbar\omega$ are fixed. Indeed, even though we are not around the position of a clock transition, this does not preclude observing the same qualitative evolution of T_m: firstly T_m increases up to a maximum value and then decreases monotonically as the applied magnetic field is increased. In a small neighborhood of each clock transition, see **Fig. 39**, the two Zeeman curves that define the two qubit energies follow a non-monotonic evolution as the applied magnetic field is increased: they first approach each other until reaching a gap minimum at the clock transitions, and then move away from each other. This behavior is nicely correlated with that of T_m as T_m also reaches an extreme value right at the clock transitions. Nevertheless, at the normal transitions each one of the two Zeeman curves follow a monotonic evolution with the applied magnetic field; yet, the T_m evolution is non-monotonic as mentioned above.

To explain this fact, we might consider the mismatch between Δ and the given $\hbar\omega$ as a key variable, since this mismatch does follow a non-monotonic evolution by reaching a minimum value when Δ approaches the given $\hbar\omega$. This mismatch is precisely related with the transition probability, see **Eq. 90**, **Eq. 91**, **Eq. 92**, in the sense that the smaller the mismatch is the greater the transition probability is and vice versa. Thus, the non-monotonic evolution of this transition probability could explain the non-monotonic evolution of T_m both at the clock transitions and at the normal transitions, either in case the two qubit energies follow a non-monotonic evolution or not with the applied magnetic field.

To elaborate further, let us note that in **Fig. 52** the peaks are sorted from left to right by increasing values of $\hbar\omega$. This fact is consistent with our approach. Indeed, as recently mentioned, Δ increases monotonically as the applied magnetic field is increased in this range. When this increasing Δ approaches the given $\hbar\omega$, the transition probability reaches its maximum value and a peak in T_m is observed. Thus, the larger Δ is, the larger $\hbar\omega$ has to be in order to observe a new peak in T_m, and this would explain why the peaks in **Fig. 52** are sorted from left to right by increasing $\hbar\omega$. The calculation of Δ right at the magnetic

fields where the T_m peaks are observed gives: Δ = 9.3 GHz at 178 mT, Δ = 9.4 GHz at 182 mT, Δ = 9.5 GHz at 185 mT, Δ = 9.6 GHz at 187 mT, Δ = 9.7 GHz at 189 mT, which indeed coincide with the corresponding employed $\hbar\omega$ values as expected. These T_m peaks are thus located at a transition probability maximum; hence, the divergences in T_m could be the result of the modulation of this probability with the applied magnetic field.

Let us now comment on our choice of the numerical values *t* = 32 ns, $\left|\overrightarrow{B_1^0}\right|$ = 0.5 mT and $\hbar\omega$ = 9.1765 GHz. We used these values to calculate each point of the green curves in **Fig. 49** and **Fig. 50**. Nonetheless, since each experimental determination of T_m was initially independent from the rest, the values of these parameters could be somewhat different depending on the given determination. Of course, the best choice for us would be to use the specific set of values that was employed to determine each T_m. Unfortunately, ref. 206 only provides these values either at the clock transitions or inside a bounded range; yet, our values are very close or even equal to these experimental values. An important limitation to bear in mind is the fact that the parameters B_2^0, B_4^0, B_6^0, B_4^4 and $A_{\|}$ in the Hamiltonian $\hat{H}$ of HoW_{10} arise from a fitting to a cw-EPR spectrum. It is important to check how good this fitting is since Δ critically depends on these parameters, and hence both calculations and conclusions. A poor fitting would probably lead to use unrealistic values for *t*, $\left|\overrightarrow{B_1^0}\right|$ and $\hbar\omega$ when simulating the experimental results. Fortunately, this does not seem to be the present case.

Concerning *t*, it is the length of a π-pulse. According to ref. 206, a Rabi frequency of 15.6 MHz was determined for 0 dB attenuation at the clock transitions, which resulted in a π/2-pulse length of 16 ns. Thus, we use *t* = 32 ns. The magnitude $\left|\overrightarrow{B_1^0}\right|$ of the oscillating magnetic field was independently measured under the same conditions via the Rabi oscillation frequency of a spin-1/2 EPR standard, namely, an organic radical. The values varied from 4 G (0.4 mT) at 9.1 GHz, to 9 G (0.9 mT) at 9.75 GHz. Since the irradiation frequencies $\hbar\omega$ involved in **Fig. 49** and **Fig. 50** are 9.12 GHz and 9.20 GHz, a value of $\left|\overrightarrow{B_1^0}\right|$ = 5 G = 0.5 mT might be reasonable and realistic enough.

Special attention needs to be focused on the $\hbar\omega$ value. Let us take into account that, so far, we have not included the distribution of the B_4^4 parameter in our method. Hence, only one value of Δ is found at each clock transition, namely, Δ = 9.1765 GHz (23.6 mT), Δ = 9.1765 GHz (70.9 mT), Δ = 9.1767 GHz (118.1 mT), Δ = 9.1768 GHz (165.4 mT), which is determined by the value B_4^4 = $3.14 \cdot 10^{-3}$ cm^{-1}. Based on our experience with these calculations, the transition probability strongly depends on how close $\hbar\omega$ and Δ are. Thus, this probability will quickly fall as soon as $\hbar\omega$ moves away from the given values of Δ, and that is the reason why we need to set $\hbar\omega$ = 9.1765 GHz to reproduce the experimental evolution of T_m around the clock transitions. Yet, it is possible to vary $\hbar\omega$ a bit around 9.1765 GHz and get essentially the same green curves as in **Fig. 49** and **Fig. 50** provided the $\left|\overrightarrow{B_1^0}\right|$ value is accordingly increased. For example, a value of $\hbar\omega$ = 9.185 GHz requires $\left|\overrightarrow{B_1^0}\right|$ = 0.57 mT. The need to increase $\left|\overrightarrow{B_1^0}\right|$ as $\hbar\omega$ moves away from the given value of Δ in order to keep the transition probability high is consistent with the following statement mentioned in ref. 206: "The ESE intensity does peak at 9.2 GHz (with reference to **Fig. 51**), above which it decays, although not as rapidly as one may expect purely on the basis of the gap distribution. This is due to the increasing B_1 field of the spectrometer, which enables excitation of more spins and hence the generation of stronger echoes at higher frequencies.".

Of course, the values to employ in $\hbar\omega$ should be the experimental values 9.12 GHz and 9.20 GHz. Let us recall that, at the current level of approximation, as soon as $\hbar\omega$ becomes different enough from the given value of Δ, the transition probability will rapidly fall. Since Δ = 9.1765 GHz – 9.1768 GHz at the clock transitions, the use of 9.12 GHz or 9.20 GHz in $\hbar\omega$ produces a fall in $T_m^{e,P}$ that impedes reproducing the experimental T_m values around these transitions. Yet, it is possible to recover again the experimental T_m evolution provided $\left|\overrightarrow{B_1^0}\right|$ is properly increased. This rise in $\left|\overrightarrow{B_1^0}\right|$ offsets the non-inclusion of the distribution in Δ (via the Gaussian distribution in B_4^4) in our method.

Nevertheless, this rise may lead to unrealistic $\left|\overrightarrow{B_1^0}\right|$ values and/or bad results. For example, when using $\hbar\omega$ = 9.12 GHz, a value of $\left|\overrightarrow{B_1^0}\right|$ = 3.9 mT is required to keep a high enough transition probability at the clock transitions that allows reproducing the maximum experimental value reached by T_m. Unfortunately, several fast oscillations appear in the rest of the calculated T_m curve due to the non-negligible mismatch between $\hbar\omega$ and Δ. At this point, it is useful to recall the sinus function in **Eq. 90**, **Eq. 91**, **Eq. 92**. On the other hand, when using $\hbar\omega$ = 9.20 GHz, it is enough to set $\left|\overrightarrow{B_1^0}\right|$ = 0.51 mT since 9.20 GHz is much closer to Δ = 9.1765 GHz – 9.1768 GHz. In spite of it, a medium size oscillation still appears right at each clock transition in the calculated T_m curve. Certainly, by forcing the numerical value of $\left|\overrightarrow{B_1^0}\right|$, we are trying to offset an effect not yet considered, namely, the distribution in Δ via the Gaussian distribution in B_4^4.

Fortunately, this distribution, with a mean value $\overline{B_4^4}$ = 3.14·10^{-3} cm^{-1} and a standard deviation $\sigma_{B_4^4}$ = 2.1·10^{-5} cm^{-1}, can be easily incorporated in our method. According to ref. 206, this distributes Δ with a mean value $\overline{\Delta}$ = 9.177 GHz and a standard deviation σ_Δ = 123 MHz, and up to one standard deviation it opens a range of ±0.17 GHz around 9.177 GHz where the experimental values 9.12 GHz and 9.20 GHz of $\hbar\omega$ are included. Thus, there exist molecules whose values of Δ at the clock transitions are equal or close enough both to 9.12 GHz and to 9.20 GHz. This of course will remove the need of artificially increasing $\left|\overrightarrow{B_1^0}\right|$ to keep reproducing the experimental evolution of T_m around the clock transitions. Instead, it will possible to keep using the realistic values of $\left|\overrightarrow{B_1^0}\right|$ reported for HoW_{10}.

As mentioned above, the inclusion of the Gaussian distribution in B_4^4 is really simple. First, we need to generate a large enough random sample $\left\{\left(B_4^4\right)_i\right\}_i$ of B_4^4 values obeying the given distribution. Then, the corrected phase memory time $T_m^{e,P}\left(B_4^4\right)_i$ is calculated at each $\left(B_4^4\right)_i$ value to build the Hahn-echo curves $\exp\left(-2\tau / T_m^P\left(B_4^4\right)_i\right)$ for $\tau > 0$. The experimental Hahn-echo decay is nothing but

the superposition of these individual echoes, i.e., $\sum_i \exp\left(-2\tau / T_m^P \left(B_4^4\right)_i\right)$. After plotting this sum against 2τ, it is fitted to an exponential function $f(x) = a \cdot \exp\left(-x / \overline{T_m^P}\right)$ to extract the overall phase memory time $\overline{T_m^{e,P}}$. This process is now repeated in the whole magnetic field range with the same random sample of B_4^4. We will undertake this task in a future work. Of course, besides the distribution in B_4^4 -generally, in the spin Hamiltonian parameters- produced by the existence of slightly different copies of the same molecule, there can exist other factors that also distribute the energy gap Δ but are not included in the present model. For instance, the magnetic field is not necessarily homogeneous in the whole sample and hence each molecule could feel a rather different magnitude. This can be due to imperfections in the applied field or internal fields in the sample. Another related issue is the microwave radiation, which is not perfectly monochromatic. This will depend on the pulse length -e.g., long pulses have better well-defined energies- but also on technical details about the cavity such as the intensity distribution against frequency.

According to ref. 206, ESE-envelope (ESEE) modulations are detectable in the recorded Hahn-echo decay curves corresponding to the T_m values determined out of the clock transitions. These modulations consist in several Hahn-echo oscillations at short times. In particular, ESEE modulations are observed at the normal transitions and enough of them are detected to confirm that they are due to the coupling of the Ho^{3+} electron spin with the protons present in the single crystal. Importantly, these ESEE modulations vanish at the clock transitions. As argued, this might mean that the Ho^{3+} electron spin is decoupled from the nuclear magnetic noise at these transitions, and this is the reason used in ref. 206 to infer that, in fact, the Ho^{3+} electron spin is decoupled from all magnetic noise, both nuclear and electronic. This fact would explain the fast rise of T_m as $B_z \to B_{CT}$, where B_{CT} is the magnetic field of a given clock transition.

Let us recall from section 5.2 that T_m should not be limited by the nuclear magnetic noise in the whole magnetic field range. In other words, ESEE modulations may be changing the Hahn-echo decay from a simple exponential to an exponential plus some oscillations, but cannot be affecting the echo global decay which is what determines the value of T_m. Hence, if the disappearance of

the ESEE modulations at the clock transitions is not really an evidence that allows asserting that the qubit is decoupled from the nuclear magnetic noise, we should not consider this disappearance as an evidence to infer that the same qubit is also decoupled from the electron magnetic noise either. Given the close match between the experimental and calculated T_m values in **Fig. 49** and **Fig. 50**, especially at 10% concentration where instantaneous diffusion dominates, the experimental rise of T_m could rather be attributed to the fast rise of the transition probability close to the clock transitions, instead of the fact that decoherence is dominated by a magnetic noise that vanish at first order as $B_z \to B_{CT}$. As a proof of concept, experiments on simple spin-1/2 magnetic molecules with negligible strains in the Hamiltonian parameters, which would consist in checking whether T_m peaks as $\hbar\omega$ is changed for a given resonant magnetic field, could also help to probe transitions probabilities and assess the validity of this hypothesis.

7

Quantum Error Correction

In previous chapters, we have elaborated on the idea of developing design strategies to create spin qubits with increasing protection against decoherence.[135] While maintaining coherence for long enough is important, quantum algorithms can also suffer from errors that should be accordingly corrected. As a matter of fact, here one finds a complementary effort: we need quantum error correction codes but also highly-coherent qubits as the success of these codes rely on robust logical gates. In classical computing, error correction is based on encoding information in redundant bits that will help to detect and correct errors. Indeed, after sending several copies of a given bit through a noisy channel, a majority vote is taken to discard altered bits. However, in quantum computing, according to the non-cloning theorem,[314] it is not possible to build a machine able to produce an exact copy of a quantum system in state superposition, i.e., without previously measuring the state of the given system. Copying a quantum state implies measuring it and, hence, destroying the information saved in the form of quantum superposition.

In 1995 and 1996, Shor and Steane introduced quantum error correction codes for the first time.[315,316] Nonetheless, several objections regarding the implementation of these codes arose,[317] and most of them were focused on two points. First, decoherence could destroy the information contained in quantum states faster than the error correction speed but, moreover, even if working fast, errors could also be introduced if each manipulation is not conducted with a proper enough fineness. Second, a given quantum state is specified by a set of complex numbers, which suggests that decoherence-induced errors are produced in a non-finite variety. Shor and Steane proved that these two objections are not necessarily a matter of concern.

Indeed, the first objection only applies whenever the decoherence rate is high enough to overwhelm error-correction codes, i.e., only if errors occur faster than they can be corrected. Fortunately, in virtue of the so-called threshold theorem, errors can be corrected as they occur provided the error rate is below a certain threshold.[318–322] To remove the second objection, let us note that generic errors occurring on a single qubit $|\Psi\rangle = \alpha|0\rangle + \beta|1\rangle$ can be decomposed into simpler errors, namely, bit flip error and phase flip error, see section 8.2. The former consists in a change of the qubit value from $|0\rangle$ to $|1\rangle$ or vice versa, while the latter happens whenever there is a change of relative sign between $|0\rangle$ and $|1\rangle$. Note that in classical computing only bit flip errors are possible. Thus, it is enough to act on these simpler errors when it comes to correcting more complex errors occurring on a single qubit. Of course, there could also exist errors affecting more than qubit at once. In this case, one should try to look for a clever assignment of the qubit labels $|...a_i...\rangle$ ($a_i = 0,1$) to the several spin states such that only errors on single qubits correspond to non-forbidden transitions. A complementary option is to minimize the likelihood of single qubit errors, which hence further decreases the likelihood of multi-qubit errors.

Now, let us consider that an information -or logical- qubit is sent through a noisy channel or stored for a given time, and then an error is produced on this qubit. The key goal is to detect and correct such error without at the same time spoiling the information encoded in the logical qubit. To correct this error, Shor and Steane considered the quantum equivalent of redundancy. As a given logical qubit cannot be cloned, quantum error correction codes employ ancillary qubits which are initialized as a function of the logical qubit state before the error occurs. The proper manipulation of these ancillary qubits after the error is produced leads to the error correction. Of course, these manipulations will not alter the logical qubit state whenever it does not suffer from any error. These error correction codes were successfully implemented firstly by means of NMR techniques,[17,323] and then with trapped ions,[324,325] linear optics,[326] superconducting qubits,[327] and nitrogen-vacant centers in diamond.[328]

7.1 Quantum Algorithms and Logical Gates

A quantum algorithm consists in a finite number of unitary transformations, also known as quantum logical gates,[329] which act on a finite number of qubits with the purpose of producing an outcome. Of course, quantum algorithms of increasing complexity will require a larger number of logical gates. The optimal implementation is when the smallest possible number of gates is used to run a given algorithm, which is important for two reasons. First, running times can become shorter than decoherence timescale and, second, the error occurrence is minimized. In practice, there is no need to know how to implement all the required logical gates since any of them can be approximated with a safe enough accuracy by a finite sequence composed of a minimal set of elementary gates. This set is employed to approximate any logical gate, and is called universal set of quantum gates.[330]

A universal set of logical gates is always selected to be finite. Nevertheless, combining a finite set of elementary gates can only produce a finite set of composed gates, while the number of gates in practice is of course non-finite. As mentioned above, this drawback can be satisfactorily solved by approximating any given logical gate as a finite sequence of universal gates with an accuracy as high as desired, which is guaranteed by the so-called Solovay-Kitaev theorem.[99,331] Two important examples of universal sets are those composed of (i) the three gates Hadamard, CNOT, $\pi/8$,[99] and (ii) the three-qubit Deutsch gate $D(\theta)$.[332] On one hand, (i) means that universal quantum computation can be achieved by combining only two-qubit gates.[330,333] In other words, to conduct any quantum algorithm it is enough to implement logical gates acting only on two qubits. On the other hand, the Toffoli gate itself defines a universal set of gates for classical computing and coincides with $D(\theta=\pi/2)$, which proves that all classical gates can be realized in a quantum computer.

As defined above, a quantum algorithm consists in a sequence of unitary transformations $\{\hat{U}_i\}_{i\geq 1}$ -also known as logical gates- acting on a reduced number of qubits. The physical implementation of each given gate requires to identify a proper Hamiltonian $\hat{H}_i$ that generates the corresponding transformation as $\hat{U}_i=\exp(it\hat{H}/\hbar)$. Then, the quantum device should designed so that $\hat{H}_i$ can be turned on at time $t=t_{i-1}$ and then turned off at time $t=t_i$ with $t_{i-1}<t_i$. The key

goal for experimentalists is to provide high-fidelity gates, i.e., able to produce a result as close as possible to the expected ideal result. A promising experimental setup for quantum computing is nowadays the cold ion trap approach proposed by Cirac and Zoller.[5] As a matter of fact, some logical gates have already been implemented in this setup,[334–337] among which one finds the paradigmatic CNOT gate.[6,338,339] On the other hand, the molecular approach has also produced several proof-of-concept systems with two magnetically-distinguishable metal centers involving both transition and lanthanide ions, which are used to implement two-qubit quantum gates such as CNOT, SWAP, √SWAP, √iSWAP, and CZ.[81,137,301,302,340,341]

7.2 Shor's Quantum Error Correction Code

Let us start by introducing the logical gates that compose the original Shor's error correction algorithm. The controlled-NOT gate, briefly CNOT, is a two-qubit gate that changes the state of the target qubit depending on the state of the control qubit, which remains unaltered in any case. Any logical gate is also a linear transformation, and hence it is enough to state how it acts on a two-qubit basis set, for instance, $|00\rangle,|01\rangle,|10\rangle,|11\rangle$, in the particular case of two-qubit gates. In this basis set, the first position corresponds to the control qubit, and the second position stands for the target qubit. The action is such that the value of the target qubit is flipped whenever the value of the control qubit is 1. Otherwise, the target qubit value is not changed. Thus, $|00\rangle \rightarrow |00\rangle$, $|01\rangle \rightarrow |01\rangle$, $|10\rangle \rightarrow |11\rangle$, $|11\rangle \rightarrow |10\rangle$. The flipping of the target qubit corresponds to a 180 degrees rotation in the Bloch sphere along the coordinate line $\varphi = 0$, see **Fig. 7** in section 2.2. These rules allow us determining the result in the most general case when both control and target qubits are in a state superposition $(\alpha|0\rangle + \beta|1\rangle)\otimes(\gamma|0\rangle + \delta|1\rangle)$, where $|0\rangle\otimes|0\rangle = |00\rangle$, $|0\rangle\otimes|1\rangle = |01\rangle$, $|1\rangle\otimes|0\rangle = |10\rangle$, $|1\rangle\otimes|1\rangle = |11\rangle$. This gate is represented with the symbol in **Fig. 53**, where the black and white circles stand for the control and target qubits, resp.

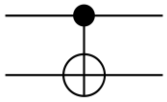

Fig. 53 Symbol of controlled-NOT (CNOT) quantum logical gate. The black dot represents the control qubit, while the white circle stands for the target qubit. They both are linked by a vertical straight line.

The Hadamard gate, whose symbolic representation is depicted in **Fig. 54**, is a one-qubit gate that is useful to transform the qubit state into a state superposition. Let us consider the one-qubit basis set $|0\rangle$, $|1\rangle$. Then, the action of this gate is such that $|0\rangle \rightarrow (|0\rangle + |1\rangle)/\sqrt{2}$ and $|1\rangle \rightarrow (|0\rangle - |1\rangle)/\sqrt{2}$. In the Bloch sphere, this consists in a 90 degrees rotation around the Y axis along the coordinate line $\varphi = 0$. For the general case $\alpha|0\rangle + \beta|1\rangle$, the result is $\left[(\alpha+\beta)|0\rangle + (\alpha-\beta)|1\rangle\right]/\sqrt{2}$.

Fig. 54 Symbol of Hadamard quantum logical gate.

The Toffoli or controlled-controlled-not gate, briefly CCNOT, is a three-qubit gate that changes the state of the target qubit depending on the state of the two control qubits, which remain unaltered in any case, see **Fig. 55**. Let us consider now the three-qubit basis set $|000\rangle$, $|001\rangle$, $|010\rangle$, $|011\rangle$, $|100\rangle$, $|101\rangle$, $|110\rangle$, $|111\rangle$, where the two first positions correspond to the two control qubits and the third position is for the target qubit. The action is such that the value of the target qubit is flipped whenever the value of both control qubits is 1. This flipping also corresponds to a 180 degrees rotation in the Bloch sphere. Otherwise, the target qubit value is not changed. Thus, $|000\rangle \rightarrow |000\rangle$, $|001\rangle \rightarrow |001\rangle$, $|010\rangle \rightarrow |010\rangle$, $|011\rangle \rightarrow |011\rangle$, $|100\rangle \rightarrow |100\rangle$, $|101\rangle \rightarrow |101\rangle$, $|110\rangle \rightarrow |111\rangle$, $|111\rangle \rightarrow |110\rangle$.

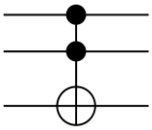

Fig. 55 Symbol of Toffoli or controlled-controlled-not (CCNOT) quantum logical gate. The black dots represent the control qubits, while the white circle stands for the target qubit. They all are linked by a vertical straight line.

With these ingredients, we can now introduce the Shor's quantum error correction code depicted in **Fig. 56**. The relevant information to be protected is encoded in the logical qubit in the form of quantum superposition $|\Psi\rangle = \alpha|0\rangle + \beta|1\rangle$. Eight ancillary qubits are all of them initialized at the $|0\rangle$ state before starting the algorithm. The circuit in **Fig. 56** must be read from left to right, where each horizontal line represents the evolution path of each qubit. The top line corresponds to the logical qubit, while the remaining ones correspond to the ancillary qubits. Before sending all qubits through a noise channel E, several CNOT and Hadamard gates are applied as can be seen. The present code is useful under the following important assumption: only one qubit at most can suffer from an error, which can be either logical or ancillary. In other words, the error must affect to a single qubit at most. As mentioned above, the error can be a bit flip, a phase flip, or a combination of both. This means that the Shor's code can correct any kind of error always affecting a single qubit. Indeed, an error acting on a given qubit can be modeled as a 2x2-sized unitary transform U. Since the identity and Pauli matrices I, σ_x, σ_y, σ_z form a basis set for the 2x2-sized unitary matrices, U can be expressed as the linear combination $U = c_0 I + c_x\sigma_x + c_y\sigma_y + c_z\sigma_z$ with complex coefficients. If $U = I$, there is no error. If $U = \sigma_x$, there is a bit flip error. If $U = \sigma_z$, there is a sign flip error. If $U = i\sigma_y$, there is a combination of both bit and sign flip errors. Hence, due to the linearity property of quantum-mechanical operators, it follows that the Shor code is able to correct any single-qubit error. Further gates are applied after the channel E, which detect the error and recover the initial state of the logical qubit. Interestingly, by measuring the state of the ancillary qubits it is possible

to know which error occurred without disturbing the logical qubit. Of course, to restart the algorithm the ancillary qubits must be initialized again.

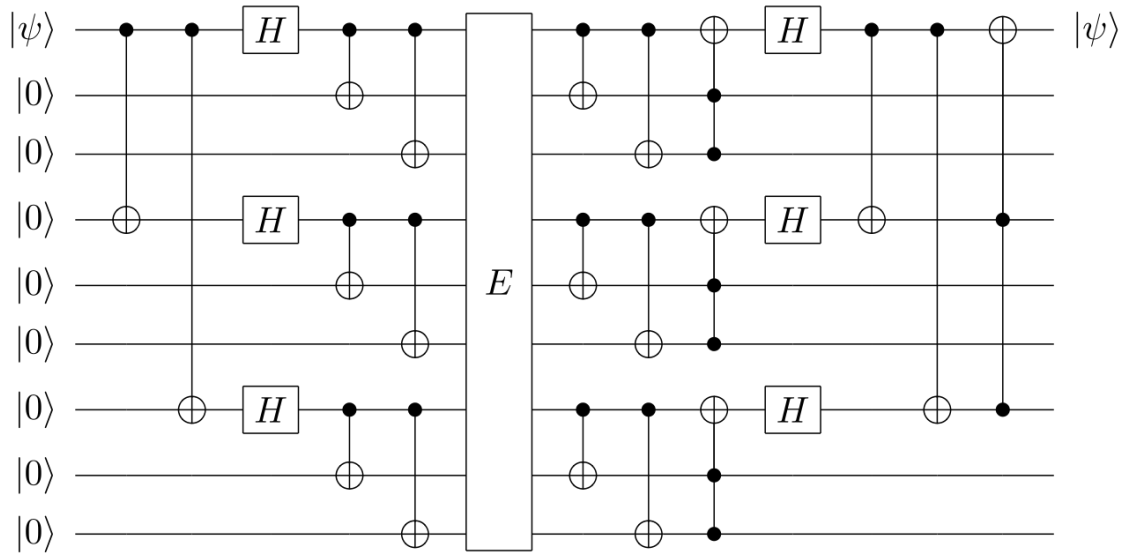

Fig. 56 Circuit of the Shor's error correction code. The logical qubit encodes quantum information in the form of state superposition $|\Psi\rangle = \alpha|0\rangle + \beta|1\rangle$. The ancillary qubits are initialized at the $|0\rangle$ state before executing the algorithm.

Subsequently, Steane developed a code able to perform the same task as the Shor's code but by using only seven qubits.[316,342] This number was further reduced to five qubits by Laflamme and collaborators in the smallest quantum algorithm that can correct all one-qubit errors.[343] Single-qubit bit and phase flip errors can also be corrected separately by using simpler algorithms which involve only two ancillary qubits, see **Fig. 57** and **Fig. 58** respectively. Both five-qubit and phase flip error corrections codes have already been experimentally implemented by means of NMR techniques.[17,323,344,345]

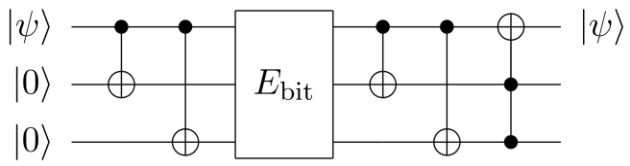

Fig. 57 Quantum circuit of the bit-flip error correction code. CC BY-SA 3.0. Credits to https://en.wikipedia.org/wiki/File:Quantum_error_correction_of_bit_flip_using_three_qubits.svg

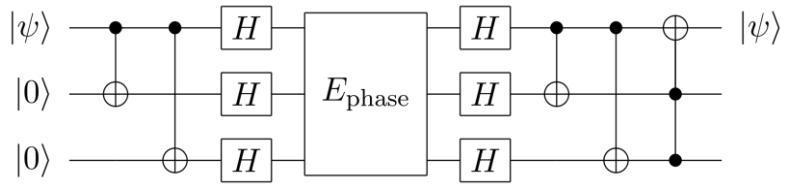

Fig. 58 Quantum circuit of the phase-flip error correction code. CC BY-SA 3.0. Credits to https://en.wikipedia.org/wiki/File:Quantum_error_correction_of_phase_flip_using_three_qubits.svg

In this chapter, we study the possibility of implementing the Shor's quantum error correction code on a magnetic molecule where the nine qubits are encoded in the low-lying 2^9 electronuclear spin states. Then, we derive the relationship between spin states and qubit labels $|...a_i...\rangle$ ($a_i = 0,1$). Importantly, our quantum fidelity calculations reveal that the wave-functions can be safely replaced by the tensor product between the electron and nuclear parts in an ample realistic parameter range, which greatly simplifies the elaboration of such relationship. The relationship we select offers the important advantage of favoring the so-called non-correlated noise. Indeed, one unfortunate simplification in quantum error correction consists in assuming that errors affecting different qubits are independent. This restriction is useful at an abstract level as it makes theoretical developments easier but not necessarily realistic. Our relationship favors this restriction to be fulfilled in practice as it is built in such a way that it ensures transitions flipping more than one qubit to be forbidden transitions. We also propose specific molecular candidates that could be adequate to implement the Shor's code and show they lie inside the parametric range explored. In the last section we discuss on the most appropriate experimental techniques that could be used to conduct the algorithm.

7.3 Selection and Modeling of Quantum Hardware

Our general scheme is to consider a molecular system with three exchange-coupled magnetic ions M in linear connectivity M-M-M. Let us now assume that the ground electron state of M can be mapped onto an effective spin doublet, which would contribute one qubit per ion. To reach the required nine qubits, we consider the nuclear spin states of M which should have a nuclear spin quantum number $I = 3/2$. Hence, each M with $2I+1 = 4 = 2^2$ would contribute with two additional qubits. All in all, the combination between the three electron doublets and the three nuclear quadruplets provides a $2^3 \cdot 4^3 = 2^9$ dimensional Hilbert space, i.e., a computational basis set for 9 qubits. A potential candidate M can be the $^{159}Tb^{3+}$ ion, which has a nuclear spin quantum number $I_{Tb} = 3/2$ with 100% natural isotopic purity, provided the ground electron state is a spin doublet with a large enough energy gap to the excited states. Alternatively, one could use the $^{63}Cu^{2+}$ (or $^{65}Cu^{2+}$) ion also with $I_{Cu} = 3/2$ and a natural spin doublet $J_{Cu} = 1/2$ as a ground electron state. More transition metal candidates exist, but are more problematic from the point of view of experimental synthesis.

The ground electron spin doublet of each $^{159}Tb^{3+}$ ion can be modeled in many different ways. Of course, the simplest approach could be to use an effective spin $J = 1/2$. Nevertheless, this imposes a severe restriction at zero field, namely, in virtue of the so-called Kramers' theorem the use of an effective spin $J = 1/2$ would lead to a degenerate doublet in the absence of other interactions that could lift this degeneracy. In order not to lose this degree of freedom at zero field, which is in fact a physical property of the systems proposed in section 8.4, we propose to use an effective spin $J = 1$ with a large enough negative value (-1000 cm^{-1}) in the axial zero-field splitting parameter D. This guarantee isolating two components of $J = 1$ as a ground electron spin doublet, and allows removing their degeneracy at zero field by introducing the rhombic zero-field splitting parameter E. On the other hand, the zero-field splitting in lanthanide coordination compounds largely exceeds the exchange coupling magnitude. Thus, standard experiments do not allow to resolve a possible anisotropy in this coupling to include such a physical richness in the spin Hamiltonian. Hence, in order to avoid over-parametrization, we will consider an isotropic exchange.

All in all, the Hamiltonian we employ to model the low-lying energy spectrum composed of the lowest and well-isolated $2^9 = 512$ electronuclear spin states is found in **Eq. 95**.

$$\hat{H} = -2J_{ex}\left(\hat{J}_1\hat{J}_2 + \hat{J}_2\hat{J}_3\right) + \sum_{i=1}^{3}\left(D\hat{J}_{z,i}^2 + E\left(\hat{J}_{x,i}^2 - \hat{J}_{y,i}^2\right)\right) + \sum_{i=1}^{3}\left(A\hat{J}_i\hat{I}_i + P\hat{I}_{z,i}^2 + B_z\left(\mu_B g\hat{J}_{z,i} + \mu_I g_I\hat{I}_{z,i}\right)\right) \quad \textbf{Eq. 95}$$

In **Eq. 95**, $\hat{J}_i$ are the electron spin operators of each magnetic metal ion i = 1, 2, 3, $\hat{I}_i$ are the corresponding nuclear spin operators, J_{ex} is the isotropic magnetic exchange between electron spins, D and E are the axial and rhombic zero-field splitting parameters, A is the isotropic hyperfine coupling between electron and nuclear spins, P is the isotropic nuclear quadrupole parameter, g is the effective electron Landé factor associated to the ground doublet of J = 1, g_I is the nuclear Landé factor, μ_B and μ_I are the Bohr and nuclear magneton, and B_z is the magnitude of the magnetic field applied in the Z-axis direction, which is defined by the molecular anisotropy axis (note that both D and P act on the z-component of $\hat{J}_{z,i}^2$ and $\hat{I}_{z,i}^2$ for each i). We consider that the magnetic exchange between nuclear spins is negligible enough not to include any direct coupling between them in **Eq. 95**. Of course, **Eq. 95** could be expanded to incorporate both anisotropic magnetic exchanges and anisotropic hyperfine couplings.

In the case of $^{159}Tb^{3+}$, we take typical values A = 0.1038 cm^{-1}, P = 0.01 cm^{-1}, g_I = 0.00073 as found in the literature.[346–348] Since the typical value of g for lanthanide spin doublets modeled as an effective J = 1/2 is around 18, we select g = 9 in **Eq. 95** because the magnitude of the effective electron spin we use is as much as twice J = 1/2 (i.e. J = 1). We will explore realistic ranges for J_{ex} , E, and B_z, as these parameters can be varied with relative ease either by chemical or experimental design. In particular, we explore the three-dimensional parametric space defined by $-1.0 \leq 2J_{ex} \leq -0.2$ cm^{-1}, $0.0 \leq 2E \leq 1.0$ cm^{-1}, $0.00 \leq B_z \leq 0.25$ T.[349] In fact, we simplified this exploration by reducing it into a two-dimensional parametric space such that, for each value of J_{ex}, B_z is chosen so

that the energy gap between the ground and first excited spin states when $A = 0$ closely matches the irradiation frequencies around 95 GHz employed in W-band EPR spectrometers. This corresponds to $0.09 \leq B_z \leq 0.22$ T. Of course, other spin transitions would require non-standard experimental setups to drive them. **Eq. 95** is diagonalized by using the software package Magpack.[350,351]

In a second independent exploration, we replace $^{159}Tb^{3+}$ by Cu^{2+} and expand **Eq. 95** to include an axial hyperfine coupling with components $A_{\parallel} = A_z$, $A_{\perp} = A_x = A_y$. This allows us exploring a different parametric space but typical in Cu^{2+} complexes given by $0.005 \leq A_{\parallel} \leq 0.030$ cm^{-1}, $-10.00 \leq J_{ex} \leq -1.00$ cm^{-1}, where the following parameters are kept fixed $A_{\perp} = 0.002$ cm^{-1}, $P = 0.00127$ cm^{-1}, $g = 2.1$, and $g_I = 0.00081$.[352–358] The parametric space is also simplified as explained above by applying magnetic fields with a magnitude around 2.25 T. Now that in this case $D = E = 0$ since $J_{Cu} = 1/2$.

7.4 Spin States Labelling

Since the Shor's code involves nine qubits, the $2^9 = 512$ lowest electronuclear spin states must be labeled as $|a_1a_2a_3a_4a_5a_6a_7a_8a_9\rangle$ with $a_i = 0,1$. For the sake of a simpler analysis, let us formally consider that the first three positions in these kets correspond to the three electron spin qubits and the rest stand for the six nuclear spin qubits. Of course, the electron and nuclear degrees of freedom appear together in **Eq. 95**. Nevertheless, if they both could be essentially decoupled, we could factorize the wave-functions describing each spin state as the tensor product between an electron part and a nuclear part. This would bring the important advantage of facilitating the search for a spin-qubit labeling with the desired properties mentioned above. Indeed, after rewriting the kets as $|a_1a_2a_3\rangle \otimes |a_4a_5a_6a_7a_8a_9\rangle$, it would be enough to assign $|a_1a_2a_3\rangle$ to the $2^3 = 8$ electron spin states and to assign $|a_4a_5a_6a_7a_8a_9\rangle$ to the $2^6 = 64$ nuclear spin states. In both cases, the number of spin states to deal with is considerably reduced from 512 to 8 and 64 resp.

To factorize the wave-functions as explained above, we need to compare the actual wave-functions with the ones obtained by cancelling the hyperfine coupling A, and then check whether these two groups are essentially the same.

The measure we consider to compare two given wave-functions and decide how similar they are is the so-called quantum fidelity. Given two (normalized) wave-functions $|\Psi_1\rangle = \sum_{i=1}^{N} x_i |\varphi_i\rangle$ and $|\Psi_2\rangle = \sum_{i=1}^{N} y_i |\varphi_i\rangle$ expressed in a orthonormal basis set $\{|\varphi_i\rangle\}_{i=1}^{N}$, where x_i and y_i are complex coefficients, the quantum fidelity F_{12} between $|\Psi_1\rangle$ and $|\Psi_2\rangle$ is defined in **Eq. 96**.

$$F_{12} = |\langle \Psi_1 | \Psi_2 \rangle|^2 = \left| \sum_{i=1}^{N} x_i y_i \right|^2 \qquad \textbf{Eq. 96}$$

We calculate F_{AC} between the actual wave-function $|\Psi_A\rangle$ and the wave-function $|\Psi_C\rangle$ obtained by cancelling A in $^{159}Tb^{3+}$ and both $A_{\parallel}$ and $A_{\perp}$ in Cu^{2+}, for example, by giving a rather negligible value of 10^{-6} cm^{-1}. Since cancelling the hyperfine coupling may change the energy sorting of the wave-functions, we match each $|\Psi_A\rangle$ with the $|\Psi_C\rangle$ that maximizes F_{AC}. Given a fixed set of parameters, we calculate the 512 fidelities and consider the lowest one F_{lowest}. Then, we plot $\log(1-F_{lowest})$ as a function of J_{ex} and E for $^{159}Tb^{3+}$, and as a function of J_{ex} and $A_{\parallel}$ for Cu^{2+}. As seen in **Fig. 59**, the calculated fidelities are high enough both in $^{159}Tb^{3+}$ ($F_{lowest} \geq 0.9999$) and in Cu^{2+} ($F_{lowest} \geq 0.999999$) for wide parametric areas, which allows the safe factorization of the wave-functions.

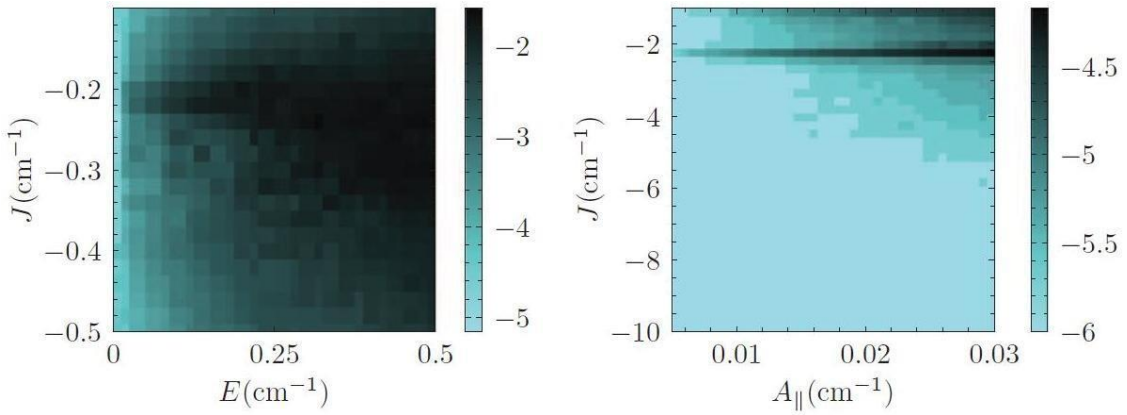

Fig. 59 $\log\left(1-F_{lowest}\right)$ as a function of J_{ex} and E for $^{159}Tb^{3+}$ (left), and as a function of J_{ex} and $A_{\|}$ for Cu^{2+} (right).

In **Table. 10**, we label the $2^3 = 8$ spin states corresponding to the electron part of the wave-function in terms of the three electron spin qubits $\left|a_1 a_2 a_3\right\rangle$. Let us recall that these states arise from the coupling of three electron spin doublets, either the two well-isolated lowest components of the effective $J = 1$ in the case of $^{159}Tb^{3+}$, or the two components of $J = 1/2$ in the case of Cu^{2+}. Hence, these states are expressed in terms of the spin up-down basis set $\left|\uparrow\uparrow\uparrow\right\rangle$, $\left|\uparrow\uparrow\downarrow\right\rangle$, $\left|\uparrow\downarrow\uparrow\right\rangle$, $\left|\uparrow\downarrow\downarrow\right\rangle$, $\left|\downarrow\uparrow\uparrow\right\rangle$, $\left|\downarrow\uparrow\downarrow\right\rangle$, $\left|\downarrow\downarrow\uparrow\right\rangle$, $\left|\downarrow\downarrow\downarrow\right\rangle$. The coupling of three spin doublets results in two doublets $J = 1/2$ and one quadruplet $J = 3/2$; we label the spin states according to the quantum numbers J and m_J.

Table. 10 Selected spin-qubit labeling of the eight states that arise from coupling three spins doublets, which results in two doublets J = 1/2 and one quadruplet J = 3/2. A > a, and the exact values depend on J_{ex}. We omit normalization constants.

$\lvert a_1 a_2 a_3 \rangle$	J	m_J	$\lvert \Psi \rangle$
$\lvert 111 \rangle$	1/2	-1/2	$A\lvert\downarrow\uparrow\downarrow\rangle - a\left(\lvert\uparrow\downarrow\downarrow\rangle + \lvert\downarrow\downarrow\uparrow\rangle\right)$
$\lvert 011 \rangle$	1/2	+1/2	$A\lvert\uparrow\downarrow\uparrow\rangle - a\left(\lvert\downarrow\uparrow\uparrow\rangle + \lvert\uparrow\uparrow\downarrow\rangle\right)$
$\lvert 101 \rangle$	1/2	-1/2	$\lvert\downarrow\downarrow\uparrow\rangle - \lvert\uparrow\downarrow\downarrow\rangle$
$\lvert 001 \rangle$	1/2	+1/2	$\lvert\downarrow\uparrow\uparrow\rangle - \lvert\uparrow\uparrow\downarrow\rangle$
$\lvert 100 \rangle$	3/2	-3/2	$\lvert\downarrow\downarrow\downarrow\rangle$
$\lvert 110 \rangle$	3/2	-1/2	$\lvert\downarrow\uparrow\downarrow\rangle + \lvert\downarrow\downarrow\uparrow\rangle + \lvert\uparrow\downarrow\downarrow\rangle$
$\lvert 010 \rangle$	3/2	+1/2	$\lvert\uparrow\downarrow\uparrow\rangle + \lvert\uparrow\uparrow\downarrow\rangle + \lvert\downarrow\uparrow\uparrow\rangle$
$\lvert 000 \rangle$	3/2	+3/2	$\lvert\uparrow\uparrow\uparrow\rangle$

The correspondence was built in such a way that: (a) all spin- and symmetry-allowed transitions correspond to single-qubit errors and can hence be corrected by the Shor's code, and (b) the state of the logical qubit (first position in $\lvert a_1 a_2 a_3 a_4 a_5 a_6 a_7 a_8 a_9 \rangle$) can be unequivocally read from a measurement determining the value of m_S. As mentioned, by assuming that the error will occur in the electron spin part of the wave-function, we can choose among many valid spin-qubit mappings for the nuclear spin states. Note that quantum algorithms often assume independent spin qubits to produce trivial mappings like $\lvert\uparrow\rangle = \lvert 0 \rangle$ and $\lvert\downarrow\rangle = \lvert 1 \rangle$. This can be unrealistic in many solid-state implementations with sizeable magnetic interactions. Indeed, as we have shown, the coupling between spins forces a non-trivial spin-qubit labeling. This situation, known as "always-on coupling", is usually the general rule in dense solid- state systems.

7.5 Molecular Systems as Candidates

Coordination chemistry is known for its versatility of designing and synthesizing molecular candidates devised for an ample set of purposes.[71,160,161,177,231] In particular, potential candidates that would be appropriate to implement the Shor's code can come either in the form of discrete molecules or in the form of single-ion molecular entities connected with each other via supramolecular interactions such as hydrogen bonds. For instance, **Fig. 60** (top) shows a Tb^{3+}-based discrete molecular trimer, $Tb_3(OQ)_9$.[359] The magnetic exchange J_{ex} can be controllably weakened from this discrete situation to the supramolecular case exemplified in **Fig. 60** (bottom), $[\{Tb(TETA)\}_2Tb(H_2O)_8]^+$.[360]

Instead, the case of Cu^{2+} may present experimental complications such as the difficulty to magnetically isolate each trimer from the rest. Indeed, since the Shor's code only needs a single trimer to be implemented, it is important to isolate each one of them to avoid interferences. The standard procedure to accomplish this isolation would consist in synthesizing the diamagnetic analog of the Tb^{3+}/Cu^{2+}-based trimer, where the Tb^{3+}/Cu^{2+} ions are replaced by a non-magnetic ion such as Y^{3+}/Zn^{2+}, resp. Once these diamagnetic analogs were synthesized, they would be mixed with the magnetic trimers in a small enough proportion to assure that the latter are far enough away with each other. In the case of lanthanide ions, 4f-orbitals are quite internal and hardly participate in the ligand bonding. Thus, since the main change is produced in these orbitals, in the form of a different number of electrons, lanthanide ions acquire a certain chemical indistinguishability that allows them forming compounds with the same ligand set. On the contrary, 3d orbitals in metal transition compounds do participate in the ligand bonding and, of course, their electron content also depends on the metal ion. Thus, after producing the magnetic trimer, there does not exist a safe certainty to guarantee that synthesizing the Zn^{2+}-based diamagnetic analog is also possible. Hence, we will focus the next discussion on the Tb^{3+}-based trimer $Tb_3(OQ)_9$ as a case study.

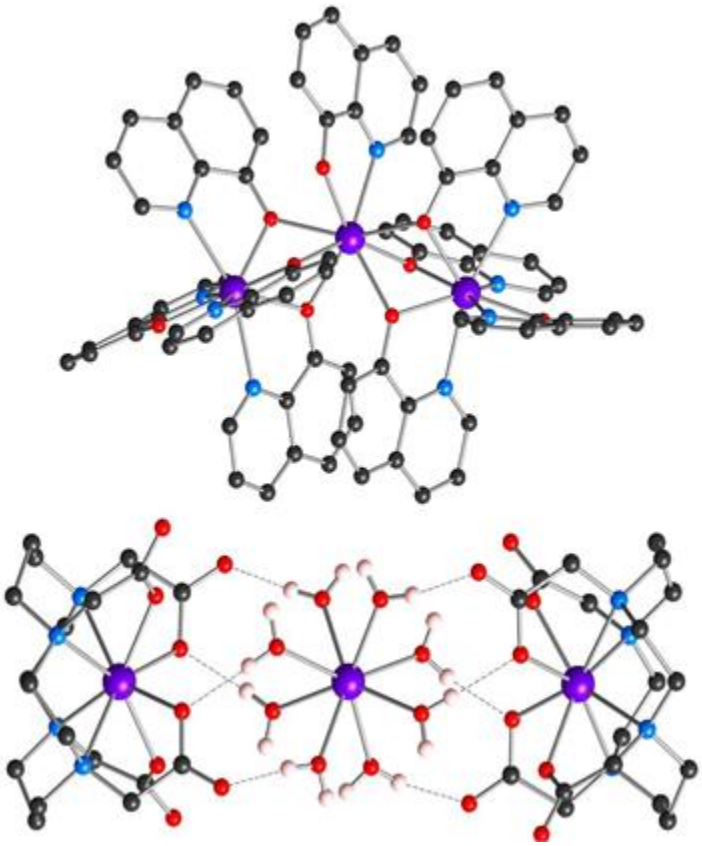

Fig. 60 Molecular candidates for the implementation of the Shor's code. Top: $Tb_3(OQ)_9$, (OQ=Quinoline). Bottom: $[\{Tb(TETA)\}_2Tb(H_2O)_8]^+$, (TETA=Triethylenetetramine). Purple: Tb, Black: C, Blue: N, Red: O, White: H.

We studied the low-lying electronic structure of $Tb_3(OQ)_9$ with the software package SIMPRE.[213,214] This structure consists in the crystal field splitting of the $2J+1$ components corresponding to the ground electron spin quantum number J of the given lanthanide ion. The calculated two lowest electron spin states $|\Psi_i\rangle$, energy gap Δ between these two states, energy gap Ω between the first and second excited electron spin states, and electron Landé factors associated to the two lowest electron spin states for $Tb_3(OQ)_9$ are found in **Table. 11**. These results reveal that each Tb^{3+} ion shows a well-isolated ground electron spin doublet with a high effective Landé factor such as we needed. Of course, the set of molecular trimers in linear connectivity is too broad to explore. Nevertheless, we could expect that similar compounds synthesized with a similar chemistry will produce values for the relevant parameters in **Table. 11** in the order of magnitude that we need to satisfy our assumptions.

Table. 11 Single-ion characterization of $^{159}Tb^{3+}$ in $Tb_3(OQ)_9$ with (i) composition of the two lowest electron spin states $|\Psi_i\rangle$ in terms of the basis set $|m_J\rangle$ of the m_J components of the Tb^{3+} ground electron spin quantum number $J = 6$, (ii) energy gap Δ between the two lowest electron spin states, (iii) energy gap Ω between the first and second excited electron spin states, and (iv) effective electron Landé factors associated to the two lowest electron spin states.

Ion	$\|\Psi_i\rangle$	Δ (cm^{-1})	Ω (cm^{-1})	g_z	g_x	g_y
Tb_1	$96\%\|\pm6\rangle$	0.86	89.7	17.11	0.95	1.10
Tb_2	$96\%\|\pm6\rangle$	0.92	191.2	17.20	0.54	0.72
Tb_3	$96\%\|\pm6\rangle$	1.28	83.7	16.81	0.95	1.13

7.6 Experimental Implementation

The first step would consist in encoding the quantum information as a state superposition in the logical qubit. This would require to initialize the molecule in its spin state corresponding to the label $|000000000\rangle$, whose electronic part has been intentionally assigned to the ground wave-function $|\uparrow\uparrow\uparrow\rangle$ in **Table. 10**. Then, a rotation from $|000000000\rangle$ to $|100000000\rangle$ will result in the desired state superposition $|\alpha 0+\beta 1\rangle|00000000\rangle$. Since the logical qubit is encoded in the electronic part of the wave-function, according to **Table. 10** this would require a coherent transition with a proper pulse length from the spin state $|\uparrow\uparrow\uparrow\rangle$ to $|\downarrow\downarrow\downarrow\rangle$ while preserving the nuclear part.

In the case of the Tb^{3+}-based trimers, given the magnitude ~0.10 cm^{-1} = 0.14 K employed in the hyperfine coupling *A*, this initialization could be achieved by cooling the sample to mK temperatures. There exist alternative options such as pumping through excited states and the so-called algorithmic cooling. In the first case,[361] an accurate irradiation of the sample allows promoting the spin population to excited states with much shorter spontaneous deexcitation rates towards the ground state. These excited states may lie outside the computational

Hilbert space, and the irradiation time should not be extended for too long since otherwise the increasing thermal energy would deploy ground state population towards excited states. This drawback restricts the accuracy in the irradiation frequency and hence it would be desirable for the molecule not to contain states too close in energy. In the second case,[362–366] one first performs a projective measurement inside the computational Hilbert space. Then, depending on this projected state, a different pulse sequence is applied to drive the spin population towards the ground state. Of course, the time taken in this procedure must be added to the overall computational time in which the molecule still keeps its coherence.

To execute the Shor's code, the circuit in **Fig. 56** needs to be translated into an EPR pulse sequence. The experimental implementation will require the ability to apply pulses of many different frequencies to drive the relevant transitions between spin states. This could be achieved by means of an Arbitrary Waveform Generator operating inside an appropriate energy range.[367–369] For instance, in the case of $Tb_3(OQ)_9$ and in the light of the energy gaps shown in **Table. 11**, a driving frequency of up to some tens of GHz could be required as in Q-band EPR spectroscopy. Note that the action of a CNOT gate whenever the value of the control qubit is 1 is to flip the value of the target qubit. Thus, this gate can be seen as a full transition or a π pulse between those spin states whose labels only differ in the value of the target qubit. On the other hand, a Hadamard gate consists in transforming $|0\rangle$ into $(|0\rangle+|1\rangle)/\sqrt{2}$ and $|1\rangle$ into $(|0\rangle-|1\rangle)/\sqrt{2}$. Thus, this gate can be seen as a half transition or a $\pi/2$ pulse between those spin states whose labels only differ in the value of the relevant qubit. In this regard, ENDOR/ELDOR-based techniques have already been applied to molecular ensembles -where qubits are encoded in electronuclear spin states- in order to implement these gates and thus conduct quantum algorithms.[370] Moreover, complementary techniques have also been proposed to minimize systematic errors that may arise in spin rotation operations and hence limit the usefulness of pulsed magnetic spectroscopy for quantum computing applications.[371]

A minimalistic alternative to the full Shor's code would consist in implementing either the bit flip or phase flip error correction code in **Fig. 57** and **Fig. 58**, where only three qubits are required. In particular, **Fig. 61** shows the pulse sequence that should be driven to run the bit flip correction code. This

could be done with no interference from nuclear spin states by using molecular trimers with no nuclear spin. For instance, either with lanthanides such as $^{164}Dy^{3+}$ and $^{166}Er^{3+}$, or with transition metals such as low-spin $^{56}Fe^{3+}$.

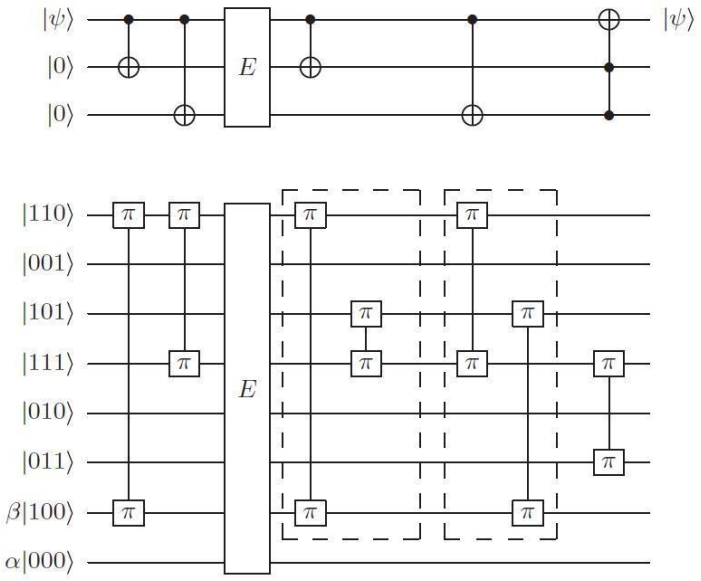

Fig. 61 Translation of the Shor's bit-flip error correction code (top) into an EPR pulse sequence (bottom). The quantum information is encoded in the logical qubit $|\Psi\rangle$ at the beginning of the code in the form of state superposition $\alpha|000\rangle + \beta|100\rangle = |\alpha 0 + \beta 1\rangle|00\rangle$.

It is equally important to implement an experimental mechanism to readout the computation result as required by the Di Vincenzo's criteria. Interestingly, in our chosen spin-qubit labelling it is possible to measure the value of the logical qubit just by determining the sign of the quantum number m_S. While this could be experimentally tricky, there exist recent proposals more feasible to implement.[148] As previously indicated, this possibility consists in placing the target molecules in resonant nano-constrictions, which are connected with each other through a net of superconducting coplanar waveguides. Under the so-called dispersive regime, the difference in the energy level spacing of the molecule-resonator depends on the logical qubit state, and this would allow performing a non-demolition measurement by probing the molecule with a proper pulse energy. The ability to measure and initialize such logical qubit can be used, after a series of swap operations, to measure and initialize the ancillary

qubits instead. This would preserve the state superposition of the logical qubit and allow restarting the error correction code. In general, a potential molecular candidate devised to implement a given quantum algorithm should also fulfill the following two important requirements: (a) to have a low-lying energy scheme -determined by cw-EPR spectroscopy- with good enough isolation from the rest of the energy spectrum and (b) to show distinguishable and well-resolved pulsed-EPR signals with sufficiently long relaxation times to allow observing Rabi oscillations.

Resumen

No hay duda de que hoy en día vivimos todos inmersos en la llamada era de la información. Cada día, grandes ficheros de datos fluyen por todo el mundo a una velocidad que habría sido inconcebible solo unas pocas décadas atrás. Junto con la necesidad de almacenar y transportar grandes cantidades de información, existe también un creciente interés por lograr un mayor poder computacional capaz de satisfacer los más exigentes desafíos de interés actual para la sociedad y la industria. Entre estos desafíos, uno puede encontrar por ejemplo la simulación de nuevos materiales tanto para dispositivos tecnológicos como para aeronaves espaciales, o la simulación *in-silico* de nuevos medicamentos que ayuden a controlar y curar las enfermedades que afectan a los seres humanos. Estas necesidades siguen vigentes y lo seguirán estando mientras no sean resueltas.

El aumento en la capacidad de computación de ordenadores estándar durante las últimas décadas ha sido posible según la tecnología ha sido capaz de fabricar transistores cada vez más pequeños para disponer un número más grande de ellos en un chip de procesamiento. Para hacerse una idea, cada dos años el número de transistores en un microprocesador se multiplica aproximadamente por dos. Esto es lo que se conoce como Ley de Moore, nombrada así por el cofundador Gordon Moore de Intel, quien estableció esta observación empírica en 1965. No obstante, es evidente que esta incesante miniaturización de los componentes electrónicos acabará por alcanzar la nanoescala, donde la física clásica ya no es válida y entran en juego las leyes de la física cuántica en su lugar.

Dentro de este contexto, vale la pena preguntarse si las propiedades de los sistemas cuánticos podrían ser aprovechadas para construir un procesador cuántico y así procesar información. En efecto, esta idea ya fue propuesta primero por P. Benioff en 1980 y luego por R. P. Feynman en la primera conferencia de Física de la Computación en el Instituto Tecnológico de Massachusetts en 1981. Estas propuestas habrían quedado en una simple anécdota de no ser porque, en 1994, P. Shor ideó el primer algoritmo cuántico capaz de llevar a cabo factorizaciones en números primos de grandes números enteros en tiempo polinomial, lo cual mejora con creces el tiempo exponencial

que requieren los ordenadores clásicos. Este hecho representó la prueba de concepto de las enormes ventajas que un ordenador cuántico podría traer respecto a la computación clásica, y desde entonces ello ha atraído la atención de un número creciente de investigadores de todo el mundo interesados en contribuir al desarrollo de la computación cuántica.

El siguiente paso natural es preguntarse qué tipo de hardware debería ser empleado ya sea para almacenar información en éste o para implementar un algoritmo cuántico dado que la procese. Mientras que por el momento ciertos sistemas físicos pueden ser identificados como potenciales candidatos, es igualmente esencial perseguir este objetivo sobre una amplia base de enfoques que colaboren entre sí permitiendo la interacción de distintas disciplinas físicas (por ejemplo, óptica cuántica, física atómica y física del estado sólido). Algunas de las propuestas para hardware más comúnmente estudiadas son aquellas basadas en: trampas de iones fríos, resonancia magnética nuclear, electrodinámica cuántica de cavidades, óptica lineal, puntos cuánticos, dadores de fósforo en silicio, uniones de Josephson, fulerenos endohédricos, y centros nitrógeno-vacante. De hecho, el emergente campo de la nanociencia y la nanotecnología también está proporcionando más aproximaciones alternativas. En este caso, las piezas básicas son las que han constituido la materia de estudio en esta tesis: los llamados nanoimanes moleculares y los qubits de espín molecular. Los primeros podrían ser usados como memorias clásicas para el almacenamiento de información, mientras que los segundos constituirían la unidad más elemental de procesamiento cuántico.

A pesar de existir un sinfín de candidatos prometedores para hardware, el objetivo de construir ordenadores cuánticos multipropósito capaces de resolver, de manera eficiente, problemas intratables por ordenadores clásicos parece estar hoy en día aún fuera del alcance. Antes de lograr este objetivo, varios desafíos tanto fundamentales como tecnológicos deberán primero ser resueltos, siendo la decoherencia y la escalabilidad dos de los más representativos. El primero tiene que ver con el hecho de ser bastante difícil desacoplar un sistema mecano-cuántico dado de su entorno, de manera que ciertas interacciones no controladas con dicho entorno dañarán, dentro de una escala temporal, la información codificada en forma de qubits. Éstos son las piezas más básicas de cualquier procesador cuántico, y han sido presentados en el capítulo 2. Por otra parte, la ejecución de algoritmos capaces de realizar tareas de complejidad creciente requerirá la interacción de un número de qubits también mayor mientras se

mantiene la información cuántica intacta. Esto es a lo que la escalabilidad se refiere. Sí existen ya varios prototipos a pequeña escala que funcionan con un número reducido de qubits, los cuales están demostrando que la computación cuántica de la información se está convirtiendo en realidad. No obstante, solo la consecución de un procesador cuántico capaz de incorporar un número de qubits lo bastante grande hará de la computación cuántica una herramienta a la que merezca la pena prestar atención a la hora de resolver problemas de interés para la sociedad y la industria.

Actualmente en el campo de los qubits de espín molecular, uno de los objetivos clave es desvelar el rol de los distintos mecanismos de decoherencia que actúan sobre los qubits de esta naturaleza particular, con el fin de establecer reglas sintéticas generales y racionales que puedan ser empleadas en el laboratorio de manera rutinaria, así alcanzando tiempos de memoria de fase lo bastante largos. Este tiempo característico determina la escala temporal dentro de la cual la información cuántica puede mantenerse intacta, y ha sido introducido en el capítulo 2. En la consecución de este objetivo, el enfoque teórico está demostrando ser una herramienta indispensable sobre cómo adquirir un creciente conocimiento. Así, uno de los objetivos principales de esta tesis ha sido proporcionar un marco de trabajo de primeros principios destinado a proveer primero una estimación cuantitativa del impacto de algunos de los mecanismos de decoherencia más importantes sobre el tiempo de memoria de fase; y luego una guía de modificaciones químicas sobre las estructuras geométricas de moléculas dadas que resulten en un incremento de dicho tiempo. En conjunto, el objetivo clave consiste en desvelar la relación explícita estructura-propiedad en qubits de espín molecular, donde la estructura es de la molécula que codifica el qubit y la propiedad es su tiempo de memoria de fase, con el fin de elaborar una receta general que permita conocer cómo construir un qubit de espín molecular con el tiempo de memoria de fase deseado.

Otros sistemas magnéticos importantes que han sido objeto de estudio son los nanoimanes moleculares mononucleares basados en lantánidos y uranio. El mecanismo de relajación estudiado en estos sistemas ha sido el que se deriva del acoplamiento espín-vibración, el cual contribuye a destruir la información guardada en forma de bit a temperaturas lo bastante altas. Motivados por el hecho de que los métodos teóricos actuales son demasiado exigentes computacionalmente, el segundo objetivo principal ha sido desarrollar una metodología barata de aplicar y de primeros principios que permite una

evaluación generalizada y eficiente del acoplamiento espín-vibración y de la relajación de espín en nanoimanes moleculares mononucleares basados en lantánidos y uranio. Esta metodología también ha logrado ser capaz de proporcionar conocimiento sobre cómo la estructura geométrica de uno de estos nanoimanes tiene que ser modificada químicamente para mejorar el rendimiento del imán en cuestión.

Para asegurar una aplicación sistemática y práctica de los métodos aquí desarrollados, el tercer objetivo principal ha sido construir un marco de trabajo computacional en forma de paquete de software en el que todos estos métodos han sido programados. Este código ha sido usado en un conjunto representativo de qubits de espín molecular y nanoimanes moleculares potenciales. Por último, pero no menos importante, el cuarto objetivo principal ha sido presentar y discutir sobre el diseño de distintas estrategias moleculares que permitan usar qubits de espín para construir arquitecturas escalables destinadas a implementar algoritmos cuánticos tales como códigos de corrección cuántica de errores.

Esta tesis se ha presentado desglosada en tres bloques principales como sigue:

El primer bloque "Computational Development" describe el marco de trabajo computacional en forma de un software práctico y útil que pueda ser proporcionado a cualquier investigador interesado. Todos los modelos presentados en el segundo bloque son actualizaciones que han sido implementadas sobre el código original SIMPRE desarrollado con anterioridad a esta tesis. La primera versión actualizada de este código que fue desarrollada y publicada dentro del presente trabajo es SIMPRE1.2, y es presentada en el capítulo 3. Además, en este mismo capítulo, también se presenta la versión más reciente de este paquete computacional, SIMPRE2.0. El código en cuestión ha sido escrito en el lenguaje de programación FORTRAN, y requiere de la librería LAPACK de subrutinas sobre álgebra lineal para ser compilado y ejecutado. En aras de buscar una mejor organización, el código está estructurado de forma modular, esto es, las distintas funcionalidades se disponen en varias subrutinas independientes que son llamadas a conveniencia del usuario. Esto permite utilizar solamente aquellas cuya ejecución es requerida, reduciendo así el tiempo computacional empleado. Del mismo modo, el input se reparte en varios ficheros de manera que solo se usan aquellos que pertenezcan a las subrutinas requeridas. Así, se facilita la tarea al usuario ya que éste solo necesitará preparar

aquellos que se vayan a utilizar. Igualmente, con el fin de que su manejo sea tan cómodo como sea posible, el output del programa también se reparte en varios ficheros. Hay uno de ellos que siempre se producirá y que contiene el resultado de la diagonalización del Hamiltoniano de espín, esto es, energías, funciones de onda, y los valores esperados de los operadores de espín electrónico y nuclear. El resto de ficheros output se producirán en función de si las subrutinas a las que pertenecen han sido requeridas o no. La ventaja principal de SIMPRE es su capacidad de conducir a una amplia variedad de resultados sin por ello consumir un excesivo tiempo computacional. En particular, el código original anterior a este trabajo ya incorpora el llamado modelo “Radial Effective Charge” (REC), que permite una estimación barata de los parámetros de campo cristalino. Todo ello sin renunciar a producir predicciones satisfactorias respecto a datos experimentales e incluso al nivel de aquellas derivadas de cálculos de primeros principios. Los métodos dedicados a simular la relajación de espín y estimar sus parámetros característicos -trabajo realizado en esta tesis- también conllevan una rápida ejecución y, sobre todo, son sencillos de aplicar ya que en la gran mayoría de casos solo se requiere conocer las coordenadas atómicos en un cristal molecular, algo que rutinariamente se realiza mediante cristalografía de rayos X.

El segundo bloque "Theoretical Development and Applications" se centra en presentar los modelos teóricos desarrollados en esta tesis. Éstos han sido ideados para desvelar el impacto de algunos de los mecanismos de relajación de espín más importantes que actúan sobre qubits de espín molecular y nanoimanes moleculares mononucleares basados en lantánidos y uranio, a saber, "Spin-vibration Coupling" en el capítulo 4 y "Magnetic Noise" en el capítulo 5. Estos modelos han sido aplicados a varios qubits de espín molecular y nanoimanes moleculares potenciales de interés actual, con el fin de extraer una lista de modificaciones químicas sobre las estructuras moleculares que puedan ayudar a mejorar el rendimiento de estos sistemas en el laboratorio. En el capítulo 4, se estudia la relajación de espín mediada por vibraciones, ya sean deslocalizadas en la red cristalina o localizadas en la misma molécula. Para ello, se ha desarrollado primero un modelo de primeros principios capaz de cuantificar la influencia de dichas vibraciones sobre los estados de energía de espín en función de la temperatura. Además de la evolución termal de dichos estados, también es posible dar una medida del acoplamiento de cada vibración, de manera que el efecto conjunto consiste en un balance entre cuán acoplada y

cuán poblada está una vibración dada a una cierta temperatura. Posteriormente, combinando este enfoque con el modelo REC, ha sido posible llegar a un marco teórico general y barato computacionalmente que permite calcular tiempos de relajación magnética y determinar los caminos de relajación más probables en nanoimanes moleculares mononucleares basados en lantánidos y uranio. Estos modelos desarrollados en este capítulo han sido aplicados tanto a un nanoiman molecular basado en U^{3+} como a un conjunto de qubits de espín molecular potenciales basados en Cu^{2+} y V^{4+}. En cada ejemplo, ha sido posible determinar aquellas vibraciones más propensas a influir las energías magnéticas, así como de promover la relajación de espín. Son por tanto las vibraciones que deberían eliminarse en un rediseño de las moléculas en el laboratorio con el fin de mejorar el rendimiento de las mismas, tal y como se perseguía en los objetivos.

En el capítulo 5, en primer lugar, se ha extendido un modelo que estima el tiempo de memoria de fase cuando la difusión de espín nuclear es el mecanismo de decoherencia dominante al caso en que la muestra se presenta en forma de polvo microcristalino o disolución congelada. Esta extensión del modelo, basada en las llamadas reglas de Lebedev, se ha aplicado a un qubit de espín molecular de Cu^{2+}, proporcionando resultados que están de acuerdo con el experimento. De igual modo y con el mismo objetivo, se ha extendido también otro modelo destinado esta vez a estimar el tiempo de memoria de fase que resulta de un baño de espines nucleares. Esta extensión ha sido testada al aplicarse a los qubits de espín moleculares basados en Gd^{3+} presentados en el capítulo 7. Por último, en este capítulo se ha desarrollado un modelo centrado en calcular el tiempo de memoria de fase debido a un baño de espines electrónicos cuando la difusión instantánea es el mecanismo que domina como fuente de decoherencia. Importantemente, dicho modelo ha permitido reproducir y explicar el tiempo de memoria de fase de un qubit basado en Ho^{3+} y definido en un entorno de una transición atómica de reloj, donde otros modelos anteriores y recientes fallan.

En el tercer y último bloque "Current Challenges" algunos problemas abiertos y desafíos actuales de amplio interés en el campo de los qubits de espín molecular son presentados y discutidos. En el capítulo 6 "Atomic Clock Transitions in HoW_{10}" hemos propuesto un enfoque novedoso basado en la introducción de probabilidades de transición que ha permitido reproducir satisfactoriamente la dependencia con el campo magnético del tiempo de memoria de fase de un qubit de espín molecular basado en Ho^{3+}. Dado que el

modelo funciona una vez la difusión instantánea es la fuente de decoherencia dominante, las predicciones resultan tanto mejores según la concentración de espines electrónicos es más alta. Se ha discutido también con detalle sobre la presencia real de estas probabilidades en base a hechos experimentales que puedan sustentar dicha hipótesis. En el capítulo 7, "Scalability", discutimos sobre la potencial aplicación de qubits de espín molecular para ser espacialmente organizados y así construir arquitecturas escalables capaces de implementar algoritmos cuánticos. Aquí hemos presentado dos propuestas concretas basadas en (i) sujetar qubits de espín molecular a una clase específica de biomoléculas conocidas como "Lanthanide Binding Tags", (ii) incorporarlos dentro de estructuras tridimensionales llamadas "Metal-Organic Frameworks". En ambos casos, la parte desarrollada en esta tesis ha consistido primero en estimar los parámetros de campo cristalino en base a experimentos de espectroscopía EPR. A continuación, se han determinado los esquemas de estados de energía, lo que a su vez ha permitido estimar los tiempos de memoria de fase según los modelos presentados previamente. En estos sistemas, el hecho de que dichas estimaciones sean superiores a los valores experimentales, hace pensar que están en juego otros mecanismos de decoherencia no considerados. En el capítulo 8 "Quantum Error Correction" hemos estudiado moléculas magnéticas polinucleares de coordinación basadas en Tb^{3+}, cuyos esquemas de energía permiten definir hasta 9 qubits. Luego, hemos discutido sobre la posibilidad de implementar en ellas algunos algoritmos tales como los códigos de corrección cuántica de errores de Shor de 3 y 9 qubits. Si bien el punto crítico a superar es a menudo que los tiempos de memoria de fase sean lo bastante largos respecto a los tiempos de puerta lógica, los ejemplos aquí estudiados sí sientan un buen precedente que anime a buscar otros sistemas más prometedores en el futuro.

References

1. Benioff, P. The computer as a physical system: A microscopic quantum mechanical Hamiltonian model of computers as represented by Turing machines. *J. Stat. Phys.* **22**, 563–591 (1980).

2. Feynman, R. P. Simulating physics with computers. *Int. J. Theor. Phys.* **21**, 467–488 (1982).

3. Shor, P. W. Algorithms for quantum computation: discrete logarithms and factoring. *Proceedings 35th Annual Symposium on Foundations of Computer Science* 124–134 (IEEE Comput. Soc. Press). doi:10.1109/SFCS.1994.365700

4. Vandersypen, L. M. K. *et al.* Experimental realization of Shor's quantum factoring algorithm using nuclear magnetic resonance. *Nature* **414**, 883–887 (2001).

5. Cirac, J. I. & Zoller, P. Quantum Computations with Cold Trapped Ions. *Phys. Rev. Lett.* **74**, 4091–4094 (1995).

6. Monroe, C., Meekhof, D. M., King, B. E., Itano, W. M. & Wineland, D. J. Demonstration of a Fundamental Quantum Logic Gate. *Phys. Rev. Lett.* **75**, 4714–4717 (1995).

7. Turchette, Q. A., Hood, C. J., Lange, W., Mabuchi, H. & Kimble, H. J. Measurement of Conditional Phase Shifts for Quantum Logic. *Phys. Rev. Lett.* **75**, 4710–4713 (1995).

8. Turchette, Q. A. *et al.* Deterministic Entanglement of Two Trapped Ions. *Phys. Rev. Lett.* **81**, 3631–3634 (1998).

9. Lu, Y. *et al.* Global entangling gates on arbitrary ion qubits. *Nature* **572**, 363–367 (2019).

10. Lekitsch, B. *et al.* Blueprint for a microwave trapped ion quantum computer. *Sci. Adv.* **3**, (2017).

11. Arrazola, I. *et al.* Pulsed dynamical decoupling for fast and robust two-qubit gates on trapped ions. *Phys. Rev. A* **97**, (2018).

12. Gershenfeld, N. A. & Chuang, I. L. Bulk Spin-Resonance Quantum Computation. *Science* **275**, 350–6 (1997).

13. Cory, D. G., Fahmy, A. F. & Havel, T. F. Ensemble quantum computing

by NMR spectroscopy. *Proc. Natl. Acad. Sci. U. S. A.* **94**, 1634–9 (1997).

14. Chuang, I. L., Vandersypen, L. M. K., Zhou, X., Leung, D. W. & Lloyd, S. Experimental realization of a quantum algorithm. *Nature* **393**, 143–146 (1998).

15. Chuang, I. L., Gershenfeld, N. & Kubinec, M. Experimental Implementation of Fast Quantum Searching. *Phys. Rev. Lett.* **80**, 3408–3411 (1998).

16. Laflamme, R., Knill, E., Zurek, W. H., Catasti, P. & Mariappan, S. V. S. NMR Greenberger–Horne–Zeilinger states. *Philos. Trans. R. Soc. London. Ser. A Math. Phys. Eng. Sci.* **356**, 1941–1948 (1998).

17. Cory, D. G. *et al.* Experimental Quantum Error Correction. *Phys. Rev. Lett.* **81**, 2152–2155 (1998).

18. Vandersypen, L. M. K. *et al.* Experimental Realization of an Order-Finding Algorithm with an NMR Quantum Computer. *Phys. Rev. Lett.* **85**, 5452–5455 (2000).

19. Xin, T., Wei, S. J., Pedernales, J. S., Solano, E. & Long, G. L. Quantum simulation of quantum channels in nuclear magnetic resonance. *Phys. Rev. A* **96**, (2017).

20. Xin, T. *et al.* Nuclear magnetic resonance for quantum computing: Techniques and recent achievements. *Chinese Physics B* **27**, (2018).

21. Singh, A., Arvind & Dorai, K. Witnessing nonclassical correlations via a single-shot experiment on an ensemble of spins using nuclear magnetic resonance. *Phys. Rev. A* **95**, (2017).

22. Domokos, P., Raimond, J. M., Brune, M. & Haroche, S. Simple cavity-QED two-bit universal quantum logic gate: The principle and expected performances. *Phys. Rev. A* **52**, 3554–3559 (1995).

23. Chuang, I. L. & Yamamoto, Y. Simple quantum computer. *Phys. Rev. A* **52**, 3489–3496 (1995).

24. Haroche, S. *et al.* Step by step engineered entanglement with atoms and photons in a cavity. in *AIP Conference Proceedings* **551**, 143–157 (AIP, 2001).

25. Yang, C.-P., Chu, S.-I. & Han, S. Possible realization of entanglement, logical gates, and quantum-information transfer with superconducting-

quantum-interference-device qubits in cavity QED. *Phys. Rev. A* **67**, 042311 (2003).

26. Kaluzny, Y., Goy, P., Gross, M., Raimond, J. M. & Haroche, S. Observation of Self-Induced Rabi Oscillations in Two-Level Atoms Excited Inside a Resonant Cavity: The Ringing Regime of Superradiance. *Phys. Rev. Lett.* **51**, 1175–1178 (1983).

27. Brune, M. *et al.* Quantum Rabi Oscillation: A Direct Test of Field Quantization in a Cavity. *Phys. Rev. Lett.* **76**, 1800–1803 (1996).

28. Zou, X., Pahlke, K. & Mathis, W. Generation of an entangled state of two three-level atoms in cavity QED. *Phys. Rev. A* **67**, 044301 (2003).

29. Allen, J. L., Kosut, R., Joo, J., Leek, P. & Ginossar, E. Optimal control of two qubits via a single cavity drive in circuit quantum electrodynamics. *Phys. Rev. A* **95**, (2017).

30. Armata, F., Calajo, G., Jaako, T., Kim, M. S. & Rabl, P. Harvesting Multiqubit Entanglement from Ultrastrong Interactions in Circuit Quantum Electrodynamics. *Phys. Rev. Lett.* **119**, (2017).

31. Ross, M. & Oskin, M. Quantum computing. *Commun. ACM* **51**, 12 (2008).

32. Bandyopadhyay, S. & Roychowdhury, V. Computational Paradigms in Nanoelectronics: Quantum Coupled Single Electron Logic and Neuromorphic Networks. *Jpn. J. Appl. Phys.* **35**, 3350–3362 (1996).

33. Loss, D. & DiVincenzo, D. P. Quantum computation with quantum dots. *Phys. Rev. A* **57**, 120–126 (1998).

34. Burkard, G., Loss, D. & DiVincenzo, D. P. Coupled quantum dots as quantum gates. *Phys. Rev. B* **59**, 2070–2078 (1999).

35. Yoneda, J. *et al.* A quantum-dot spin qubit with coherence limited by charge noise and fidelity higher than 99.9%. *Nat. Nanotechnol.* **13**, 102–106 (2018).

36. Nichol, J. M. *et al.* High-fidelity entangling gate for double-quantum-dot spin qubits. *npj Quantum Inf.* **3**, (2017).

37. Hensgens, T. *et al.* Quantum simulation of a Fermi-Hubbard model using a semiconductor quantum dot array. *Nature* **548**, 70–73 (2017).

38. Li, R. *et al.* A crossbar network for silicon quantum dot qubits. *Sci. Adv.*

4, (2018).

39. Harvey-Collard, P. *et al.* Coherent coupling between a quantum dot and a donor in silicon. *Nat. Commun.* **8**, (2017).

40. Kane, B. E. A silicon-based nuclear spin quantum computer. *Nature* **393**, 133–137 (1998).

41. Morello, A. Donor qubits in silicon: Electrical control of nuclear spins. *Nature Nanotechnology* **12**, 937–938 (2017).

42. Laucht, A. *et al.* A dressed spin qubit in silicon. *Nat. Nanotechnol.* **12**, 61–66 (2017).

43. Watson, T. F. *et al.* A programmable two-qubit quantum processor in silicon. *Nature* **555**, 633–637 (2018).

44. Sigillito, A. J., Tyryshkin, A. M., Schenkel, T., Houck, A. A. & Lyon, S. A. All-electric control of donor nuclear spin qubits in silicon. *Nat. Nanotechnol.* **12**, 958–962 (2017).

45. Tosi, G. *et al.* Silicon quantum processor with robust long-distance qubit couplings. *Nat. Commun.* **8**, (2017).

46. Orlando, T. P. *et al.* Superconducting persistent-current qubit. *Phys. Rev. B* **60**, 15398–15413 (1999).

47. Pashkin, Y. A. *et al.* Quantum oscillations in two coupled charge qubits. *Nature* **421**, 823–826 (2003).

48. Yamamoto, T., Pashkin, Y. A., Astafiev, O., Nakamura, Y. & Tsai, J. S. Demonstration of conditional gate operation using superconducting charge qubits. *Nature* **425**, 941–944 (2003).

49. Nakamura, Y., Pashkin, Y. A. & Tsai, J. S. Coherent control of macroscopic quantum states in a single-Cooper-pair box. *Nature* **398**, 786–788 (1999).

50. Nakamura, Y., Pashkin, Y., Yamamoto, T. & Tsai, J. Charge Echo in a Cooper-Pair Box. *Phys. Rev. Lett.* **88**, 047901 (2002).

51. Nakamura, Y., Pashkin, Y. A. & Tsai, J. S. Rabi Oscillations in a Josephson-Junction Charge Two-Level System. *Phys. Rev. Lett.* **87**, 246601 (2001).

52. Martinis, J. M., Nam, S., Aumentado, J. & Urbina, C. Rabi Oscillations in

a Large Josephson-Junction Qubit. *Phys. Rev. Lett.* **89**, 117901 (2002).

53. Han, S. *et al.* Time-Resolved Measurement of Dissipation-Induced Decoherence in a Josephson Junction. *Science* **293**, 1457–1459 (2001).

54. Yu, Y., Han, S., Chu, X., Chu, S.-I. & Wang, Z. Coherent temporal oscillations of macroscopic quantum states in a Josephson junction. *Science* **296**, 889–92 (2002).

55. Benjamin, S. C. *et al.* Towards a fullerene-based quantum computer. *J. Phys. Condens. Matter* (2006). doi:10.1088/0953-8984/18/21/S12

56. Harneit, W., Meyer, C., Weidinger, A., Suter, D. & Twamley, J. Architectures for a spin quantum computer based on endohedral fullerenes. *Physica Status Solidi (B) Basic Research* (2002). doi:10.1002/1521-3951(200210)233:3<453::AID-PSSB453>3.0.CO;2-N

57. Harneit, W. Fullerene-based electron-spin quantum computer. *Phys. Rev. A - At. Mol. Opt. Phys.* (2002). doi:10.1103/PhysRevA.65.032322

58. Yang, W. L., Xu, Z. Y., Wei, H., Feng, M. & Suter, D. Quantum-information-processing architecture with endohedral fullerenes in a carbon nanotube. *Phys. Rev. A - At. Mol. Opt. Phys.* (2010). doi:10.1103/PhysRevA.81.032303

59. Ju, C., Suter, D. & Du, J. An endohedral fullerene-based nuclear spin quantum computer. *Phys. Lett. Sect. A Gen. At. Solid State Phys.* (2011). doi:10.1016/j.physleta.2011.02.031

60. Weber, J. R. *et al.* Quantum computing with defects. *Proc. Natl. Acad. Sci.* **107**, (2010).

61. Childress, L. & Hanson, R. Diamond NV centers for quantum computing and quantum networks. *MRS Bulletin* (2013). doi:10.1557/mrs.2013.20

62. Acosta, V. & Hemmer, P. Nitrogen-vacancy centers: Physics and applications. *MRS Bull.* (2013). doi:10.1557/mrs.2013.18

63. Yang, W. L., Yin, Z. Q., Hu, Y., Feng, M. & Du, J. F. High-fidelity quantum memory using nitrogen-vacancy center ensemble for hybrid quantum computation. *Phys. Rev. A - At. Mol. Opt. Phys.* (2011). doi:10.1103/PhysRevA.84.010301

64. Prawer, S. & Greentree, A. D. Diamond for Quantum Computing. *Science* **320**, (2008).

65. Wood, A. A. *et al.* Quantum measurement of a rapidly rotating spin qubit in diamond. *Sci. Adv.* **4**, (2018).

66. Abobeih, M. H. *et al.* One-second coherence for a single electron spin coupled to a multi-qubit nuclear-spin environment. *Nat. Commun.* **9**, (2018).

67. Sohn, Y. I. *et al.* Controlling the coherence of a diamond spin qubit through its strain environment. *Nat. Commun.* **9**, (2018).

68. Dréau, A., Tcheborateva, A., Mahdaoui, A. El, Bonato, C. & Hanson, R. Quantum Frequency Conversion of Single Photons from a Nitrogen-Vacancy Center in Diamond to Telecommunication Wavelengths. *Phys. Rev. Appl.* **9**, (2018).

69. Myers, B. A., Ariyaratne, A. & Jayich, A. C. B. Double-Quantum Spin-Relaxation Limits to Coherence of Near-Surface Nitrogen-Vacancy Centers. *Phys. Rev. Lett.* **118**, (2017).

70. Sorace, L., Benelli, C. & Gatteschi, D. Lanthanides in molecular magnetism: old tools in a new field. *Chem. Soc. Rev.* **40**, 3092 (2011).

71. Rinehart, J. D. & Long, J. R. Exploiting single-ion anisotropy in the design of f-element single-molecule magnets. *Chem. Sci.* **2**, 2078 (2011).

72. Benelli, C. & Gatteschi, D. Magnetism of Lanthanides in Molecular Materials with Transition-Metal Ions and Organic Radicals. (2002). doi:10.1021/CR010303R

73. Dei, A. & Gatteschi, D. Molecular (Nano) Magnets as Test Grounds of Quantum Mechanics. *Angew. Chemie Int. Ed.* **50**, 11852–11858 (2011).

74. Sessoli, R. & Powell, A. K. Strategies towards single molecule magnets based on lanthanide ions. *Coordination Chemistry Reviews* **253**, 2328–2341 (2009).

75. Gatteschi, D., Sessoli, R. & Villain, J. *Molecular nanomagnets*. (Oxford University Press, 2006).

76. *Molecular Nanomagnets and Related Phenomena*. **164**, (Springer Berlin Heidelberg, 2015).

77. *Molecular Magnets*. (Springer Berlin Heidelberg, 2014). doi:10.1007/978-3-642-40609-6

78. Dreiser, J. Molecular lanthanide single-ion magnets: from bulk to

submonolayers. *J. Phys. Condens. Matter* **27**, 183203 (2015).

79. Wernsdorfer, W. Quantum dynamics in molecular nanomagnets. *Comptes Rendus Chim.* **11**, 1086–1109 (2008).

80. Luis, F. *Revista española de física*. *Revista Española de Física* **30**, ([La Sociedad], 1987).

81. Aromí, G., Aguilà, D., Gamez, P., Luis, F. & Roubeau, O. Design of magnetic coordination complexes for quantum computing. *Chem. Soc. Rev.* **41**, 537–546 (2012).

82. Clemente-Juan, J. M., Coronado, E. & Gaita-Ariño, A. Magnetic polyoxometalates: from molecular magnetism to molecular spintronics and quantum computing. *Chem. Soc. Rev.* **41**, 7464 (2012).

83. Moreno-Pineda, E., Godfrin, C., Balestro, F., Wernsdorfer, W. & Ruben, M. Molecular spin qudits for quantum algorithms. *Chem. Soc. Rev.* **47**, 501–513 (2018).

84. Troiani, F. & Affronte, M. Molecular spins for quantum information technologies. *Chem. Soc. Rev.* **40**, 3119 (2011).

85. Molecular spintronics and quantum computing. *J. Mater. Chem.* **19**, 1670 (2009).

86. Leuenberger, M. N. & Loss, D. Quantum computing in molecular magnets. *Nature* **410**, 789–793 (2001).

87. Stepanenko, D., Trif, M. & Loss, D. Quantum computing with molecular magnets. *Inorganica Chim. Acta* **361**, 3740–3745 (2008).

88. van Hoogdalem, K., Stepanenko, D. & Loss, D. Molecular Magnets for Quantum Information Processing. 275–296 (2014). doi:10.1007/978-3-642-40609-6_11

89. Lehmann, J., Gaita-Ariño, A., Coronado, E. & Loss, D. Quantum computing with molecular spin systems. *J. Mater. Chem.* **19**, 1672–1677 (2009).

90. Cerletti, V., Coish, W. A., Gywat, O. & Loss, D. Recipes for spin-based quantum computing. *Nanotechnology* **16**, R27–R49 (2005).

91. Stamp, P. C. E. & Gaita-Ariño, A. Spin-based quantum computers made by chemistry: hows and whys. *J. Mater. Chem.* **19**, 1718–1730 (2009).

92. Ding, Y.-S. *et al.* The Rise of Single-Ion Magnets as Spin Qubits. *Magnetochemistry* **2**, 40 (2016).

93. Ghirri, A. *et al.* Molecular Spins in the Context of Quantum Technologies. *Magnetochemistry* **3**, 12 (2017).

94. Gaita-Ariño, A., Luis, F., Hill, S. & Coronado, E. Molecular spins for quantum computation. *Nat. Chem.* **11**, 301–309 (2019).

95. Dicarlo, L. *et al.* Demonstration of two-qubit algorithms with a superconducting quantum processor. *Nature* (2009). doi:10.1038/nature08121

96. Monz, T. *et al.* 14-qubit entanglement: Creation and coherence. *Phys. Rev. Lett.* (2011). doi:10.1103/PhysRevLett.106.130506

97. Turing, A. M. On Computable Numbers, with an Application to the Entscheidungsproblem. *Proc. London Math. Soc.* **s2-42**, 230–265 (1937).

98. Eckert, J. P. & Mauchly, J. W. Electronic numerical integrator and computer. (1947). doi:patents.google.com/patent/US3120606A/en

99. Nielsen, M. A. & Chuang, I. L. *Quantum computation and quantum information*. (Cambridge University Press, 2000).

100. Wiesner, S. Simulations of Many-Body Quantum Systems by a Quantum Computer. (1996).

101. Zalka, C. Simulating quantum systems on a quantum computer. *Proc. R. Soc. London. Ser. A Math. Phys. Eng. Sci.* **454**, 313–322 (1998).

102. Jané, E., Vidal, G., Dür, W., Zoller, P. & Cirac, J. I. Simulation of quantum dynamics with quantum optical systems. (2002).

103. Tseng, C. H. *et al.* Quantum simulation of a three-body-interaction Hamiltonian on an NMR quantum computer. *Phys. Rev. A* **61**, 012302 (1999).

104. Lloyd, S. Universal Quantum Simulators. *Science* **273**, 1073–1078 (1996).

105. Friedenauer, A., Schmitz, H., Glueckert, J. T., Porras, D. & Schaetz, T. Simulating a quantum magnet with trapped ions. *Nat. Phys.* **4**, 757–761 (2008).

106. Abrams, D. S. & Lloyd, S. Simulation of Many-Body Fermi Systems on

a Universal Quantum Computer. *Phys. Rev. Lett.* **79**, 2586–2589 (1997).

107. Cirac, J. I. & Zoller, P. Goals and opportunities in quantum simulation. *Nat. Phys.* **8**, 264–266 (2012).

108. Buluta, I. & Nori, F. Quantum simulators. *Science* **326**, 108–11 (2009).

109. Georgescu, I. M., Ashhab, S. & Nori, F. Quantum simulation. *Rev. Mod. Phys.* **86**, 153–185 (2014).

110. Somaroo, S., Tseng, C. H., Havel, T. F., Laflamme, R. & Cory, D. G. Quantum Simulations on a Quantum Computer. *Phys. Rev. Lett.* **82**, 5381–5384 (1999).

111. Lu, D. *et al.* Simulation of Chemical Isomerization Reaction Dynamics on a NMR Quantum Simulator. *Phys. Rev. Lett.* **107**, 020501 (2011).

112. Aspuru-Guzik, A., Dutoi, A. D., Love, P. J. & Head-Gordon, M. Simulated quantum computation of molecular energies. *Science* **309**, 1704–7 (2005).

113. Wu, L.-A., Byrd, M. S. & Lidar, D. A. Polynomial-Time Simulation of Pairing Models on a Quantum Computer. *Phys. Rev. Lett.* **89**, 057904 (2002).

114. Leibfried, D. *et al.* Trapped-Ion Quantum Simulator: Experimental Application to Nonlinear Interferometers. *Phys. Rev. Lett.* **89**, 247901 (2002).

115. Gauger, E. M., Rieper, E., Morton, J. J. L., Benjamin, S. C. & Vedral, V. Sustained Quantum Coherence and Entanglement in the Avian Compass. *Phys. Rev. Lett.* **106**, 040503 (2011).

116. Wiesner, S. & Stephen. Conjugate coding. *ACM SIGACT News* **15**, 78–88 (1983).

117. Bennett, C. H. & Brassard, G. Quantum cryptography: Public key distribution and coin tossing. *Theor. Comput. Sci.* **560**, 7–11 (2014).

118. Bennett, C. H., Brassard, G. & Ekert, A. K. Quantum Cryptography. *Scientific American* **267**, 50–57 (1992).

119. Bennett, C. H. & Brassard, G. An Update on Quantum Cryptography. *Advances in Cryptology* 475–480 (Springer Berlin Heidelberg, 1984). doi:10.1007/3-540-39568-7_39

120. Bennett, C., Bessette, F., Brassard, G., Salvail, L. & Smolin, J. Experimental quantum cryptography. *J. Cryptol.* **5**, 3–28 (1992).

121. Ribordy, G., Brendel, J., Gautier, J.-D., Gisin, N. & Zbinden, H. Long-distance entanglement-based quantum key distribution. *Phys. Rev. A* **63**, 012309 (2000).

122. Hughes, R. J., Nordholt, J. E., Derkacs, D. & Peterson, C. G. Practical free-space quantum key distribution over 10 km in daylight and at night. *New J. Phys.* **4**, 43–43 (2002).

123. Stucki, D., Gisin, N., Guinnard, O., Ribordy, G. & Zbinden, H. Quantum key distribution over 67 km with a plug&play system. *New J. Phys.* **4**, 341 (2002).

124. Bernstein, D. J., Heninger, N., Lou, P. & Valenta, L. Post-quantum RSA. 311–329 (Springer, Cham, 2017). doi:10.1007/978-3-319-59879-6_18

125. Grover, L. K. A fast quantum mechanical algorithm for database search. (1996).

126. Boyer, M., Brassard, G., Høyer, P. & Tapp, A. Tight Bounds on Quantum Searching. *Fortschritte der Phys.* **46**, 493–505 (1998).

127. Godfrin, C. *et al.* Operating Quantum States in Single Magnetic Molecules: Implementation of Grover's Quantum Algorithm. *Phys. Rev. Lett.* **119**, (2017).

128. DiVincenzo, D. P. The Physical Implementation of Quantum Computation. *Fortschritte der Phys.* **48**, 771–783 (2000).

129. Preskill, J. Quantum Computing in the NISQ era and beyond. (2018). doi:10.22331/q-2018-08-06-79

130. O'Brien, C., Lauk, N., Blum, S., Morigi, G. & Fleischhauer, M. Interfacing superconducting qubits and telecom photons via a rare-earth-doped crystal. *Phys. Rev. Lett.* **113**, (2014).

131. Zurek, W. H. Decoherence and the transition from quantum to classical -- REVISITED. (2003).

132. Haroche, S. & Raimond, J. Quantum Computing: Dream or Nightmare? *Phys. Today* **49**, 51–52 (1996).

133. Unruh, W. G. Maintaining coherence in quantum computers. *Phys. Rev. A* **51**, 992–997 (1995).

134. Ramanathan, C., Sinha, S., Baugh, J., Havel, T. F. & Cory, D. G. Selective coherence transfers in homonuclear dipolar coupled spin systems. *Phys. Rev. A* **71**, 020303 (2005).

135. Chuang, I. L., Laflamme, R., Shor, P. W. & Zurek, W. H. Quantum computers Quantum Computers, Factoring, and Decoherence. *Science* **270**, 1633–1635 (1995).

136. Wedge, C. J. *et al.* Chemical Engineering of Molecular Qubits. *Phys. Rev. Lett.* **108**, 107204 (2012).

137. Luis, F. *et al.* Molecular prototypes for spin-based CNOT and SWAP quantum gates. *Phys. Rev. Lett.* **107**, (2011).

138. Baldoví, J. J. *et al.* Coherent manipulation of spin qubits based on polyoxometalates: the case of the single ion magnet $[GdW_{30}P_5O_{110}]^{14-}$. *Chem. Commun.* **49**, 8922 (2013).

139. Takahashi, S. *et al.* Decoherence in crystals of quantum molecular magnets. *Nature* **476**, 76–79 (2011).

140. Morton, J. J. L. & Lovett, B. W. Hybrid Solid-State Qubits: The Powerful Role of Electron Spins. *Annu. Rev. Condens. Matter Phys.* **2**, 189–212 (2011).

141. Timco, G. A. *et al.* Engineering the coupling between molecular spin qubits by coordination chemistry. *Nat. Nanotechnol.* **4**, 173–178 (2009).

142. Candini, A. *et al.* Entanglement in supramolecular spin systems of two weakly coupled antiferromagnetic rings (purple-Cr_7Ni). *Phys. Rev. Lett.* **104**, (2010).

143. Bonizzoni, C., Ghirri, A. & Affronte, M. Coherent coupling of molecular spins with microwave photons in planar superconducting resonators. *Advances in Physics: X* **3**, (2018).

144. Bonizzoni, C. *et al.* Coherent coupling between Vanadyl Phthalocyanine spin ensemble and microwave photons: Towards integration of molecular spin qubits into quantum circuits. *Sci. Rep.* **7**, (2017).

145. Jenkins, M. D. *et al.* Nanoscale constrictions in superconducting coplanar waveguide resonators. *Appl. Phys. Lett.* **105**, (2014).

146. Wisby, I. *et al.* Coupling of a locally implanted rare-earth ion ensemble to a superconducting micro-resonator. *Appl. Phys. Lett.* **105**, 102601 (2014).

147. Jenkins, M. *et al.* Coupling single-molecule magnets to quantum circuits. *New J. Phys.* **15**, (2013).

148. Jenkins, M. D. *et al.* A scalable architecture for quantum computation with molecular nanomagnets. *Dalt. Trans.* **45**, 16682–16693 (2016).

149. Wingfield, P. T. Overview of the Purification of Recombinant Proteins. in *Current Protocols in Protein Science* 6.1.1-6.1.35 (John Wiley & Sons, Inc., 2015). doi:10.1002/0471140864.ps0601s80

150. Sternberg, S. H. & Doudna, J. A. Expanding the Biologist's Toolkit with CRISPR-Cas9. *Molecular Cell* **58**, 568–574 (2015).

151. Tørring, T., Voigt, N. V., Nangreave, J., Yan, H. & Gothelf, K. V. DNA origami: A quantum leap for self-assembly of complex structures. *Chemical Society Reviews* **40**, 5636–5646 (2011).

152. Schreiber, R., Santiago, I., Ardavan, A. & Turberfield, A. J. Ordering Gold Nanoparticles with DNA Origami Nanoflowers. *ACS Nano* **10**, 7303–7306 (2016).

153. Lakshmanan, A., Zhang, S. & Hauser, C. A. E. Short self-assembling peptides as building blocks for modern nanodevices. *Trends in Biotechnology* **30**, 155–165 (2012).

154. Sevdalina, L. *et al.* Multifrequency pulsed electron paramagnetic resonance on metalloproteins. *Acc. Chem. Res.* **43**, 181–189 (2010).

155. Lloyd, S. A potentially realizable quantum computer. *Science* **261**, 1569–1571 (1993).

156. Benjamin, S. C. Schemes for parallel quantum computation without local control of qubits. *Phys. Rev. A - At. Mol. Opt. Phys.* **61**, 4 (2000).

157. Morita, Y. *et al.* Triple-stranded metallo-helicates addressable as LLoyds electron spin qubits. *J. Am. Chem. Soc.* **132**, 6944–6946 (2010).

158. Schlipf, L. *et al.* A molecular quantum spin network controlled by a single qubit. *Sci. Adv.* **3**, (2017).

159. Layfield, R. & Murugesu, M. *Lanthanides and Actinides in Molecular Magnetism.* (Wiley, 2015).

160. Ishikawa, N., Sugita, M., Ishikawa, T., Koshihara, S.-y., and & Youkoh, K. Lanthanide Double-Decker Complexes Functioning as Magnets at the Single-Molecular Level. *J. Am. Chem. Soc.* **125**, 8694–8695 (2003).

161. AlDamen, M. A., Clemente-Juan, J. M., Coronado, E., Martí-Gastaldo, C. & Gaita-Ariño, A. Mononuclear Lanthanide Single-Molecule Magnets Based on Polyoxometalates. *J. Am. Chem. Soc.* **130**, 8874–8875 (2008).

162. Sessoli, R., Gatteschi, D., Caneschi, A. & Novak, M. A. Magnetic bistability in a metal-ion cluster. *Nature* **365**, 141–143 (1993).

163. Sessoli, R. Materials science: Magnetic molecules back in the race. *Nature* **548**, 400–401 (2017).

164. Goodwin, C. A. P., Ortu, F., Reta, D., Chilton, N. F. & Mills, D. P. Molecular magnetic hysteresis at 60 kelvin in dysprosocenium. *Nature* **548**, 439–442 (2017).

165. Guo, F. S. *et al.* Magnetic hysteresis up to 80 kelvin in a dysprosium metallocene single-molecule magnet. *Science* (2018). doi:10.1126/science.aav0652

166. Rudowicz, C. & Chung, C. Y. The generalization of the extended Stevens operators to higher ranks and spins, and a systematic review of the tables of the tensor operators and their matrix elements. in *Journal of Physics Condensed Matter* (2004). doi:10.1088/0953-8984/16/32/018

167. Malrieu, J. P., Durand, P. H. & Daudey, J. P. Intermediate Hamiltonians as a new class of effective Hamiltonians. *J. Phys. A. Math. Gen.* (1985). doi:10.1088/0305-4470/18/5/014

168. Durand, P. Theory of effective Hamiltonians and molecular applications. *J. Mol. Struct. THEOCHEM* (1985). doi:10.1016/0166-1280(85)85138-1

169. Maurice, R. *et al.* Universal theoretical approach to extract anisotropic spin hamiltonians. *J. Chem. Theory Comput.* (2009). doi:10.1021/ct900326e

170. Ishikawa, N. *et al.* Determination of Ligand-Field Parameters and f-Electronic Structures of Double-Decker Bis(phthalocyaninato)lanthanide Complexes. *Inorg. Chem.* **42**, 2440–2446 (2003).

171. Cucinotta, G. *et al.* Magnetic anisotropy in a dysprosium/DOTA single-molecule magnet: Beyond simple magneto-structural correlations. *Angew. Chemie - Int. Ed.* **51**, 1606–1610 (2012).

172. Sessoli, R. & Luzón, J. Lanthanides in molecular magnetism: so fascinating so challenging. *Dalt. Trans.* (2012). doi:10.1039/C2DT31388J

173. Perfetti, M. *et al.* Angular-Resolved Magnetometry Beyond Triclinic Crystals Part II: Torque Magnetometry of Cp*ErCOT Single-Molecule Magnets. *Chem. - A Eur. J.* **20**, 14051–14056 (2014).

174. van Leusen, J., Speldrich, M., Schilder, H. & Kögerler, P. Comprehensive insight into molecular magnetism via CONDON: Full vs. effective models. *Coordination Chemistry Reviews* **289**–**290**, 137–148 (2015).

175. AlDamen, M. A. *et al.* Mononuclear lanthanide single molecule magnets based on the polyoxometalates $[Ln(W_5O_{18})_2]^{9-}$ and $[Ln(\beta_2\text{-}SiW_{11}O_{39})_2]^{13-}$ (Ln^{III} = Tb, Dy, Ho, Er, Tm, and Yb). *Inorg. Chem.* (2009). doi:10.1021/ic801630z

176. Cardona-Serra, S. *et al.* Lanthanoid single-ion magnets based on polyoxometalates with a 5-fold symmetry: The series $[LnP_5W_{30}O_{110}]^{14-}$ (Ln^{3+} = Tb, Dy, Ho, Er, Tm, and Yb). *J. Am. Chem. Soc.* (2012). doi:10.1021/ja305163t

177. Baldoví, J. J. *et al.* Rational Design of Single-Ion Magnets and Spin Qubits Based on Mononuclear Lanthanoid Complexes. *Inorg. Chem.* **51**, 12565–12574 (2012).

178. Liu, J. L. *et al.* Switching the anisotropy barrier of a single-ion magnet by symmetry change from quasi-D_{5h} to quasi-O_h. *Chem. Sci.* (2013). doi:10.1039/c3sc50843a

179. Habib, F. *et al.* Significant enhancement of energy barriers in dinuclear dysprosium single-molecule magnets through electron-withdrawing effects. *J. Am. Chem. Soc.* (2013). doi:10.1021/ja404846s

180. Liu, J. *et al.* A Stable Pentagonal Bipyramidal Dy(III) Single-Ion Magnet with a Record Magnetization Reversal Barrier over 1000 K. *J. Am. Chem. Soc.* (2016). doi:10.1021/jacs.6b02638

181. Chen, Y. C. *et al.* Symmetry-Supported Magnetic Blocking at 20 K in Pentagonal Bipyramidal Dy(III) Single-Ion Magnets. *J. Am. Chem. Soc.* (2016). doi:10.1021/jacs.5b13584

182. Rechkemmer, Y. *et al.* A four-coordinate cobalt(II) single-ion magnet with coercivity and a very high energy barrier. *Nat. Commun.* (2016). doi:10.1038/ncomms10467

183. Randall McClain, K. *et al.* High-temperature magnetic blocking and magneto-structural correlations in a series of dysprosium(iii)

metallocenium single-molecule magnets. *Chem. Sci.* (2018). doi:10.1039/c8sc03907k

184. Escalera-Moreno, L., Baldoví, J. J., Gaita-Ariño, A. & Coronado, E. Spin states, vibrations and spin relaxation in molecular nanomagnets and spin qubits: A critical perspective. *Chemical Science* (2018). doi:10.1039/c7sc05464e

185. Liddle, S. T. & van Slageren, J. Improving f-element single molecule magnets. *Chem. Soc. Rev.* **44**, 6655–6669 (2015).

186. Pointillart, F. *et al.* Magnetic Memory in an Isotopically Enriched and Magnetically Isolated Mononuclear Dysprosium Complex. *Angew. Chemie Int. Ed.* **54**, 1504–1507 (2015).

187. Moro, F., Mills, D. P., Liddle, S. T. & van Slageren, J. The Inherent Single-Molecule Magnet Character of Trivalent Uranium. *Angew. Chemie Int. Ed.* **52**, 3430–3433 (2013).

188. Ungur, L. & Chibotaru, L. F. Magnetic anisotropy in the excited states of low symmetry lanthanide complexes. *Phys. Chem. Chem. Phys.* **13**, 20086 (2011).

189. Ungur, L., Thewissen, M., Costes, J.-P., Wernsdorfer, W. & Chibotaru, L. F. Interplay of Strongly Anisotropic Metal Ions in Magnetic Blocking of Complexes. *Inorg. Chem.* **52**, 6328–6337 (2013).

190. Eaton, S. S. & Eaton, G. R. Relaxation Times of Organic Radicals and Transition Metal Ions. in 29–154 (2000). doi:10.1007/0-306-47109-4_2

191. Hoffmann, S. K. & Lijewski, S. Phonon spectrum, electron spin–lattice relaxation and spin–phonon coupling of Cu^{2+} ions in BaF_2 crystal. *J. Magn. Reson.* **252**, 49–54 (2015).

192. Schweiger, A. (Arthur) & Jeschke, G. *Principles of pulse electron paramagnetic resonance*. (Oxford University Press, 2001).

193. Stoll, S. & Schweiger, A. EasySpin, a comprehensive software package for spectral simulation and analysis in EPR. *J. Magn. Reson.* **178**, 42–55 (2006).

194. Lehmann, J., Gaita-Arino, A., Coronado, E. & Loss, D. Spin qubits with electrically gated polyoxometalate molecules. *Nat. Nanotechnol.* (2007). doi:10.1038/nnano.2007.110

195. George, R. E., Edwards, J. P. & Ardavan, A. Coherent spin control by electrical manipulation of the magnetic anisotropy. *Phys. Rev. Lett.* (2013). doi:10.1103/PhysRevLett.110.027601

196. Zadrozny, J. M., Niklas, J., Poluektov, O. G. & Freedman, D. E. Millisecond coherence time in a tunable molecular electronic spin qubit. *ACS Cent. Sci.* **1**, 488–492 (2015).

197. Berliner, L. J., Eaton, G. R. & Eaton, S. S. *Distance measurements in biological systems by EPR*. (Kluwer Academic, 2002).

198. Takahashi, S. *et al.* Coherent Manipulation and Decoherence of S = 10 Single-Molecule Magnets. *Phys. Rev. Lett.* **102**, 087603 (2009).

199. Antosik, S., Brown, N. M. D., McConnell, A. A. & Porte, A. L. The effects of axial interactions on electron paramagnetic resonance spectra of copper(II) chelates: weak complexes of copper(II) chelates and chloroform. *J. Chem. Soc. A Inorganic, Phys. Theor.* 545 (1969). doi:10.1039/j19690000545

200. Morton, J. J. L. *et al.* Environmental effects on electron spin relaxation in N@ C_{60}. *Phys. Rev. B* **76**, 085418 (2007).

201. Matsushita, M., Momose, T. & Shida, T. Internal rotation of the methyl group in the radical cation of dimethyl ether. *J. Chem. Phys.* **92**, 4749–4758 (1990).

202. Kubota, S. *et al.* Internal Rotation of the Methyl Groups in the t -Butyl Radical as Studied by ESR . *Bull. Chem. Soc. Jpn.* **68**, 140–145 (1995).

203. Lin, C. Y., Ngendahimana, T., Eaton, G. R., Eaton, S. S. & Zadrozny, J. M. Counterion influence on dynamic spin properties in a V(iv) complex. *Chem. Sci.* **10**, 548–555 (2019).

204. Bader, K. Spin dynamics in transition metal compounds: towards nuclear-spin-free molecular quantum bits. (2016). doi:http://dx.doi.org/10.18419/opus-9097

205. Klauder, J. R. & Anderson, P. W. Spectral Diffusion Decay in Spin Resonance Experiments. *Phys. Rev.* **125**, 912–932 (1962).

206. Shiddiq, M. *et al.* Enhancing coherence in molecular spin qubits via atomic clock transitions. *Nature* **531**, 348–351 (2016).

207. Bader, K. *et al.* Room temperature quantum coherence in a potential

molecular qubit. *Nat. Commun.* **5**, 5304 (2014).

208. Lenz, S., Bader, K., Bamberger, H. & van Slageren, J. Quantitative prediction of nuclear-spin-diffusion-limited coherence times of molecular quantum bits based on copper(II). *Chem. Commun.* **53**, 4477–4480 (2017).

209. de Sousa, R. & Das Sarma, S. Theory of nuclear-induced spectral diffusion: Spin decoherence of phosphorus donors in Si and GaAs quantum dots. *Phys. Rev. B* **68**, 115322 (2003).

210. Zecevic, A., Eaton, G. R., Eaton, S. S. & Lindgren, M. Dephasing of electron spin echoes for nitroxyl radicals in glassy solvents by non-methyl and methyl protons. *Mol. Phys.* **95**, 1255–1263 (1998).

211. Yu, C.-J. *et al.* Long Coherence Times in Nuclear Spin-Free Vanadyl Qubits. *J. Am. Chem. Soc.* **138**, 14678–14685 (2016).

212. Graham, M. J., Yu, C.-J., Krzyaniak, M. D., Wasielewski, M. R. & Freedman, D. E. Synthetic Approach To Determine the Effect of Nuclear Spin Distance on Electronic Spin Decoherence. *J. Am. Chem. Soc.* **139**, 3196–3201 (2017).

213. Baldoví, J. J. *et al.* SIMPRE: A software package to calculate crystal field parameters, energy levels, and magnetic properties on mononuclear lanthanoid complexes based on charge distributions. *J. Comput. Chem.* **34**, 1961–1967 (2013).

214. Baldoví, J. J., Clemente-Juan, J. M., Coronado, E., Gaita-Ariño, A. & Palii, A. An updated version of the computational package SIMPRE that uses the standard conventions for Stevens crystal field parameters. *J. Comput. Chem.* **35**, 1930–1934 (2014).

215. Baldoví, J. J. *et al.* Rational Design of Lanthanoid Single-Ion Magnets: Predictive Power of the Theoretical Models. *Chem. - A Eur. J.* (2016). doi:10.1002/chem.201601741

216. Baldoví, J. J., Borrás-Almenar, J. J., Clemente-Juan, J. M., Coronado, E. & Gaita-Ariño, A. Modeling the properties of lanthanoid single-ion magnets using an effective point-charge approach. *Dalton Transactions* **41**, 13705 (2012).

217. Cardona-Serra, S. *et al.* SIMPRE1.2: Considering the hyperfine and quadrupolar couplings and the nuclear spin bath decoherence. *J. Comput.*

Chem. **37**, 1238–1244 (2016).

218. Stevens, K. W. H. Matrix elements and operator equivalents connected with the magnetic properties of rare earth ions. *Proc. Phys. Soc. Sect. A* **65**, 209–215 (1952).

219. Edvardsson, S. & Klintenberg, M. Role of the electrostatic model in calculating rare-earth crystal-field parameters. *J. Alloys Compd.* **275**–**277**, 230–233 (1998).

220. Karbowiak, M. & Rudowicz, C. Software package SIMPRE - Revisited. *J. Comput. Chem.* **35**, 1935–1941 (2014).

221. Rudowicz, C. & Karbowiak, M. Disentangling intricate web of interrelated notions at the interface between the physical (crystal field) Hamiltonians and the effective (spin) Hamiltonians. *Coordination Chemistry Reviews* **287**, 28–63 (2015).

222. Baldoví, J. J., Clemente-Juan, J. M., Coronado, E. & Gaita-Ariño, A. Molecular anisotropy analysis of single-ion magnets using an effective electrostatic model. *Inorg. Chem.* **53**, 11323–11327 (2014).

223. Baldoví, J. J., Cardona-Serra, S., Clemente-Juan, J. M., Coronado, E. & Gaita-Ariño, A. Modeling the properties of uranium-based single ion magnets. *Chem. Sci.* **4**, 938–946 (2013).

224. Baldoví, J. J., Gaita-Ariño, A. & Coronado, E. Modeling the magnetic properties of lanthanide complexes: relationship of the REC parameters with Pauling electronegativity and coordination number. *Dalton Trans.* **44**, 12535–8 (2015).

225. Qian, K. *et al.* Does the thermal evolution of molecular structures critically affect the magnetic anisotropy? *Chem. Sci.* **6**, 4587–4593 (2015).

226. Baldoví, J. J. *et al.* Construction of a general library for the rational design of nanomagnets and spin qubits based on mononuclear f-block complexes. The polyoxometalate case. *Inorg. Chem.* **53**, 9976–80 (2014).

227. Bogle, G. S., Duffus, H. J. & Scovil, H. E. D. The nuclear electric quadrupole moment of erbium 167. *Proceedings of the Physical Society. Section A* **65**, 760–761 (1952).

228. Abragam, A. & Bleaney, B. *Electron Paramagnetic Resonance of Transition Ions*. (Dover Publications, 1986).

229. Du, J.-L., Eaton, G. R. & Eaton, S. S. Electron Spin Relaxation in Vanadyl, Copper(II), and Silver(II) Porphyrins in Glassy Solvents and Doped Solids. *J. Magn. Reson. Ser. A* **119**, 240–246 (1996).

230. Zhou, Y., Bowler, B. E., Eaton, G. R. & Eaton, S. S. Electron Spin Lattice Relaxation Rates for S = 1/2 Molecular Species in Glassy Matrices or Magnetically Dilute Solids at Temperatures between 10 and 300 K. *J. Magn. Reson.* **139**, 165–174 (1999).

231. Graham, M. J. *et al.* Influence of Electronic Spin and Spin–Orbit Coupling on Decoherence in Mononuclear Transition Metal Complexes. *J. Am. Chem. Soc.* **136**, 7623–7626 (2014).

232. Zadrozny, J. M. & Freedman, D. E. Qubit Control Limited by Spin-Lattice Relaxation in a Nuclear Spin-Free Iron(III) Complex. *Inorg. Chem.* **54**, 12027–12031 (2015).

233. Walker, C. B. X-ray study of lattice vibrations in aluminum. *Phys. Rev.* **103**, 547–557 (1956).

234. Hoffmann, S. K., Hilczer, W. & Goslar, J. EPR, electron spin-lattice relaxation, and debye temperature of Cu(II)-doped triglycine selenate crystal. *J. Magn. Reson. - Ser. A* **122**, 37–41 (1996).

235. Shrivastava, K. N. Phonon-Induced Corrections to the Ground-State Splitting of S -State Ions in Cubic Crystals. *Phys. Rev.* **187**, 446–450 (1969).

236. Shrivastava, K. N. Splitting of states of Eu^{2+} by phonons in CaF_2: A novel correction to the spin-hamiltonian. *Phys. Lett. A* **31**, 454–455 (1970).

237. Shrivastava, K. N. Splitting of states by electron phonon interaction: Cr^{3+} in alums. *Chem. Phys. Lett.* **22**, 622–624 (1973).

238. Shrivastava, K. N. Lattice-dynamical contributions to g-values. *J. Phys. C Solid State Phys.* **15**, 3869–3876 (1982).

239. Atzori, M. *et al.* Quantum Coherence Times Enhancement in Vanadium(IV)-based Potential Molecular Qubits: the Key Role of the Vanadyl Moiety. *J. Am. Chem. Soc.* **138**, 11234–11244 (2016).

240. Lunghi, A., Totti, F., Sanvito, S. & Sessoli, R. Intra-molecular origin of the spin-phonon coupling in slow-relaxing molecular magnets. *Chem. Sci.* **8**, 6051–6059 (2017).

241. Fielding, A. J. *et al.* Electron Spin Lattice Relaxation of V(IV) Complexes in Glassy Solutions between 15 and 70 K. in 364–375 (2007). doi:10.1021/bk-2007-0974.ch026

242. Fielding, A. J. *et al.* Electron spin relaxation of copper(II) complexes in glassy solution between 10 and 120 K. *J. Magn. Reson.* **179**, 92–104 (2006).

243. Escalera-Moreno, L., Suaud, N., Gaita-Ariño, A. & Coronado, E. Determining Key Local Vibrations in the Relaxation of Molecular Spin Qubits and Single-Molecule Magnets. *J. Phys. Chem. Lett.* **8**, 1695–1700 (2017).

244. Atzori, M. *et al.* Room-Temperature Quantum Coherence and Rabi Oscillations in Vanadyl Phthalocyanine: Toward Multifunctional Molecular Spin Qubits. *J. Am. Chem. Soc.* **138**, 2154–2157 (2016).

245. Lunghi, A., Totti, F., Sessoli, R. & Sanvito, S. The role of anharmonic phonons in under-barrier spin relaxation of single molecule magnets. *Nat. Commun.* **8**, 14620 (2017).

246. Frisch G.W.; Schlegel, H. B.; Scuseria, G. E.; Robb, M. A.; Cheeseman, J. R.; Scalmani, G.; Barone, V.;Mennucci, B.; Petersson, G. A.; Nakatsuji, H.; Caricato, M.; Li, X.; Hratchian, H. P.; Izmaylov, A. F.; Bloino, J.; Zheng, G.; Sonnenber, D. J, M. J. . T. Gaussian 09. *Gaussian, Inc. Wallingford CT* 2–3 (2009).

247. Ordejón, P. Linear Scaling ab initio Calculations in Nanoscale Materials with SIESTA. *Phys. status solidi* **217**, 335–356 (2000).

248. Soler, J. M. *et al.* The SIESTA method for ab initio order-N materials simulation. *J. Phys. Condens. Matter* **14**, 2745–2779 (2002).

249. Neese, F. The ORCA program system. *Wiley Interdiscip. Rev. Comput. Mol. Sci.* **2**, 73–78 (2012).

250. Neese, F. Software update: the ORCA program system, version 4.0. *Wiley Interdiscip. Rev. Comput. Mol. Sci.* **8**, (2018).

251. Karlström, G. *et al.* MOLCAS: A program package for computational chemistry. in *Computational Materials Science* **28**, 222–239 (2003).

252. Aquilante, F., Pedersen, T. B., Veryazov, V. & Lindh, R. MOLCAS-a software for multiconfigurational quantum chemistry calculations. *Wiley Interdiscip. Rev. Comput. Mol. Sci.* **3**, 143–149 (2013).

253. Aquilante, F. *et al.* Molcas 8: New capabilities for multiconfigurational quantum chemical calculations across the periodic table. *J. Comput. Chem.* **37**, 506–541 (2016).

254. Warner, M. *et al.* Potential for spin-based information processing in a thin-film molecular semiconductor. *Nature* **503**, 504–508 (2013).

255. Weidinger, A., Waiblinger, M., Pietzak, B. & Almeida Murphy, T. Atomic nitrogen in C60:N@C_{60}. *Appl. Phys. A Mater. Sci. Process.* **66**, 287–292 (1998).

256. Morton, J. J. L. *et al.* The N@C_{60} nuclear spin qubit: Bang-bang decoupling and ultrafast phase gates. in *Physica Status Solidi (B) Basic Research* **243**, 3028–3031 (2006).

257. Paoletti, A. M. *et al.* Titanium and ruthenium phthalocyanines for NO_2 sensors: A mini-review. *Sensors* **9**, 5277–5297 (2009).

258. Kaminski, D. *et al.* Quantum spin coherence in halogen-modified Cr_7Ni molecular nanomagnets. *Phys. Rev. B - Condens. Matter Mater. Phys.* **90**, (2014).

259. Cooper, F., Khare, A. & Sukhatme, U. *Supersymmetry in Quantum Mechanics*. (World Scientific, 2001). doi:10.1142/4687

260. Secrest, D. Kratzer oscillator functions as a diatomic molecule basis set. *J. Chem. Phys.* **89**, 1017–1018 (1988).

261. Dahl, J. P. & Springborg, M. The Morse oscillator in position space, momentum space, and phase space. *J. Chem. Phys.* **88**, 4535–4547 (1988).

262. Tuzun, R. E. & Secrest, D. Numerical evaluation of Kratzer oscillator matrix elements. *Comput. Phys. Commun.* **70**, 362–370 (1992).

263. De Lima, E. F. & Hornos, J. E. M. Matrix elements for the morse potential under an external field. *J. Phys. B At. Mol. Opt. Phys.* **38**, 815–825 (2005).

264. Gallas, J. A. C. Some matrix elets for Morse oscillators. *Phys. Rev. A* **21**, 1829–1834 (1980).

265. Aquilante, F. *et al.* Software news and update MOLCAS 7: The next generation. *J. Comput. Chem.* **31**, 224–247 (2010).

266. Suaud, N., Ruamps, R., Guihéry, N. & Malrieu, J. P. A strategy to determine appropriate active orbitals and accurate magnetic couplings in organic magnetic systems. *J. Chem. Theory Comput.* **8**, 4127–4137

(2012).

267. Suaud, N., Ruamps, R., Malrieu, J. P. & Guihéry, N. Singly occupied MOs in mono- and diradical conjugated hydrocarbons: Comparison between variational single-reference, π-fully correlated and Hückel descriptions. *J. Phys. Chem. A* **118**, 5876–5884 (2014).

268. Bolvin, H. An alternative approach to the g-matrix: Theory and applications. *ChemPhysChem* **7**, 1575–1589 (2006).

269. Yancoillie, S. & Pierloot, K. Multiconfigurational g tensor calculations as a probe for the covalency of the copper-ligand bonds in copper(II) complexes: $[CuCl_4]^{2-}$, $[Cu(NH_3)_4]^{2+}$, and plastocyanin. *J. Phys. Chem. A* **112**, 4011–4019 (2008).

270. Vancoillie, S., Malmqvist, P. Å. & Pierloot, K. Calculation of EPR g tensors for transition-metal complexes based on multiconfigurational perturbation theory (CASPT2). *ChemPhysChem* **8**, 1803–1815 (2007).

271. Jenkins, M. D. *et al.* Coherent manipulation of three-qubit states in a molecular single-ion magnet. *Phys. Rev. B* **95**, (2017).

272. Fataftah, M. S. *et al.* Metal-ligand covalency enables room temperature molecular qubit candidates. *Chem. Sci.* **10**, 6707–6714 (2019).

273. Jackson, C. E., Lin, C.-Y., Johnson, S. H., van Tol, J. & Zadrozny, J. M. Nuclear-spin-pattern control of electron-spin dynamics in a series of V(IV) complexes . *Chem. Sci.* (2019). doi:10.1039/c9sc02899d

274. The electrical and thermal conductivities of monovalent metals. *Proc. R. Soc. London. Ser. A. Math. Phys. Sci.* **226**, 436–454 (1954).

275. Assour, J. M., Goldmacher, J. & Harrison, S. E. Electron Spin Resonance of Vanadyl Phthalocyanine. *J. Chem. Phys.* **43**, 159–165 (1965).

276. Singh, S. K., Eng, J., Atanasov, M. & Neese, F. Covalency and chemical bonding in transition metal complexes: An ab initio based ligand field perspective. *Coordination Chemistry Reviews* **344**, 2–25 (2017).

277. Liu, J. L. *et al.* A six-coordinate ytterbium complex exhibiting easy-plane anisotropy and field-induced single-ion magnet behavior. *Inorg. Chem.* **51**, 8538–8544 (2012).

278. Ding, Y. S., Chilton, N. F., Winpenny, R. E. P. & Zheng, Y. Z. On Approaching the Limit of Molecular Magnetic Anisotropy: A Near-

Perfect Pentagonal Bipyramidal Dysprosium(III) Single-Molecule Magnet. *Angew. Chemie - Int. Ed.* **55**, 16071–16074 (2016).

279. Guo, F. S. *et al.* A Dysprosium Metallocene Single-Molecule Magnet Functioning at the Axial Limit. *Angew. Chemie - Int. Ed.* **56**, 11445–11449 (2017).

280. Meihaus, K. R. & Long, J. R. Actinide-based single-molecule magnets. *Dalton Transactions* **44**, 2517–2528 (2015).

281. King, D. M. *et al.* Single-molecule magnetism in a single-ion triamidoamine uranium(V) terminal mono-oxo complex. *Angew. Chemie - Int. Ed.* **52**, 4921–4924 (2013).

282. Antunes, M. A. *et al.* A Mononuclear Uranium(IV) Single-Molecule Magnet with an Azobenzene Radical Ligand. *Chem. - A Eur. J.* **21**, 17817–17826 (2015).

283. Rinehart, J. D. & Long, J. R. Slow magnetic relaxation in a trigonal prismatic uranium(III) complex. *J. Am. Chem. Soc.* **131**, 12558–12559 (2009).

284. Rinehart, J. D., Meihaus, K. R. & Long, J. R. Observation of a secondary slow relaxation process for the field-induced single-molecule magnet $U(H_2BPz_2)_3$. *J. Am. Chem. Soc.* **132**, 7572–7573 (2010).

285. Rinehart, J. D. & Long, J. R. Slow magnetic relaxation in homoleptic trispyrazolylborate complexes of neodymium(iii) and uranium(iii). in *Dalton Transactions* **41**, 13572–13574 (2012).

286. Antunes, M. A. *et al.* $[U(Tp^{Me2})_2(bipy)]^+$: A cationic uranium(III) complex with single-molecule-magnet behavior. *Inorg. Chem.* **50**, 9915–9917 (2011).

287. Coutinho, J. T. *et al.* Single-ion magnet behaviour in $[U(Tp^{Me2})_2I]$. in *Dalton Transactions* **41**, 13568–13571 (2012).

288. Coutinho, J. T., Antunes, M. A., Pereira, L. C. J., Marçalo, J. & Almeida, M. Zero-field slow magnetic relaxation in a uranium(iii) complex with a radical ligand. *Chem. Commun.* **50**, 10262–10264 (2014).

289. Pereira, L. C. J. *et al.* Single-molecule-magnet behavior in mononuclear homoleptic tetrahedral uranium(III) complexes. *Inorg. Chem.* **53**, 11809–11811 (2014).

290. Coutinho, J. T. *et al.* Spectroscopic Determination of the Electronic Structure of a Uranium Single-Ion Magnet. *Chem. - A Eur. J.* **25**, 1758–1766 (2019).

291. Guo, F., Chen, Y., Tong, M., Mansikkamäki, A. & Layfield, R. A. Uranocenium: Synthesis, Structure, and Chemical Bonding. *Angew. Chemie* **131**, 10269–10273 (2019).

292. Grunzweig-Genossar, J., Kuznietz, M. & Friedman, F. Magnetic properties of uranium compounds with elements of the VA and VIA groups. I. Compounds of UX type. *Phys. Rev.* **173**, 562–573 (1968).

293. *The Actinides: Electronic Structure and Related Properties*. (Academic Press, 1974).

294. Moore, K. T. & Van Der Laan, G. Nature of the 5f states in actinide metals. *Rev. Mod. Phys.* **81**, 235–298 (2009).

295. Speldrich, M., Schilder, H., Lueken, H. & Kögerler, P. A computational framework for magnetic polyoxometalates and molecular spin structures: CONDON 2.0. *Israel Journal of Chemistry* **51**, 215–227 (2011).

296. Dove, M. T. *Introduction to lattice dynamics*. (Cambridge University Press, 1993).

297. Orbach, R. Spin-Lattice Relaxation in Rare-Earth Salts. *Proc. R. Soc. A Math. Phys. Eng. Sci.* **264**, 458–484 (1961).

298. Escalera-Moreno, L., Baldoví, J. J. & Coronado, E. Design of high-temperature f-block molecular nanomagnets through the control of vibration-induced spin relaxation. (2019). arXiv:1905.06989

299. Meihaus, K. R. *et al.* Influence of pyrazolate vs N -heterocyclic carbene ligands on the slow magnetic relaxation of homoleptic trischelate lanthanide(III) and uranium(III) complexes. *J. Am. Chem. Soc.* **136**, 6056–6058 (2014).

300. Witzel, W. M. & Das Sarma, S. Quantum theory for electron spin decoherence induced by nuclear spin dynamics in semiconductor quantum computer architectures: Spectral diffusion of localized electron spins in the nuclear solid-state environment. *Phys. Rev. B - Condens. Matter Mater. Phys.* **74**, (2006).

301. Ferrando-Soria, J. *et al.* A modular design of molecular qubits to implement universal quantum gates. *Nat. Commun.* **7**, (2016).

302. Aguilà, D. *et al*. Heterodimetallic [LnLn'] lanthanide complexes: Toward a chemical design of two-qubit molecular spin quantum gates. *J. Am. Chem. Soc.* **136**, 14215–14222 (2014).

303. Wolfowicz, G. *et al.* Atomic clock transitions in silicon-based spin qubits. *Nat. Nanotechnol.* **8**, 561–564 (2013).

304. Fraval, E., Sellars, M. J. & Longdell, J. J. Method of Extending Hyperfine Coherence Times in Pr^{3+}:Y_2SiO_5. *Phys. Rev. Lett.* **92**, (2004).

305. Zhong, M. *et al.* Optically addressable nuclear spins in a solid with a six-hour coherence time. *Nature* **517**, 177–180 (2015).

306. Zadrozny, J. M., Gallagher, A. T., Harris, T. D. & Freedman, D. E. A Porous Array of Clock Qubits. *J. Am. Chem. Soc.* **139**, 7089–7094 (2017).

307. Stamp, P. C. E. & Tupitsyn, I. S. Coherence window in the dynamics of quantum nanomagnets. *Phys. Rev. B - Condens. Matter Mater. Phys.* **69**, (2004).

308. Finazzo, C., Calle, C., Stoll, S., Van Doorslaer, S. & Schweiger, A. Matrix effects on copper(II)phthalocyanine complexes. A combined continuous wave and pulse EPR and DFT study. *Phys. Chem. Chem. Phys.* **8**, 1942–1953 (2006).

309. Ghosh, S. *et al.* Multi-frequency EPR studies of a mononuclear holmium single-molecule magnet based on the polyoxometalate $[Ho^{III}(W_5O_{18})_2]^{9-}$. in *Dalton Transactions* **41**, 13697–13704 (2012).

310. Vonci, M. *et al.* Magnetic Excitations in Polyoxotungstate-Supported Lanthanoid Single-Molecule Magnets: An Inelastic Neutron Scattering and ab Initio Study. *Inorg. Chem.* **56**, 378–394 (2017).

311. Martínez-Pérez, M. J. *et al.* Gd-based single-ion magnets with tunable magnetic anisotropy: Molecular design of spin qubits. *Phys. Rev. Lett.* **108**, (2012).

312. Eaton, G. R. & Eaton, S. S. Solvent and Temperature Dependence of Spin Echo Dephasing for Chromium(V) and Vanadyl Complexes in Glassy Solution. *J. Magn. Reson.* **136**, 63–68 (1999).

313. Baldoví, J. J. & Kondinski, A. Exploring high-symmetry lanthanide-functionalized polyoxopalladates as building blocks for quantum computing. *Inorganics* **6**, (2018).

314. Wootters, W. K. & Zurek, W. H. A single quantum cannot be cloned. *Nature* **299**, 802–803 (1982).

315. Shor, P. W. Scheme for reducing decoherence in quantum computer memory. *Phys. Rev. A* **52**, R2493–R2496 (1995).

316. Steane, A. M. Error Correcting Codes in Quantum Theory. *Phys. Rev. Lett.* **77**, 793–797 (1996).

317. Steane, A. M. Quantum computer architecture for fast entropy extraction. (2002). arXiv:quant-ph/0203047

318. Steane, A. M. Overhead and noise threshold of fault-tolerant quantum error correction. *Phys. Rev. A* **68**, 042322 (2003).

319. Knill, E. Quantum computing with realistically noisy devices. *Nature* **434**, 39–44 (2005).

320. Aliferis, P., Gottesman, D. & Preskill, J. Quantum accuracy threshold for concatenated distance-3 codes. (2005). arXiv:quant-ph/0504218

321. Cross, A. W., DiVincenzo, D. P. & Terhal, B. M. A comparative code study for quantum fault-tolerance. (2007). arXiv:0711.1556

322. Knill, E. Scalable quantum computing in the presence of large detected-error rates. *Phys. Rev. A* **71**, 042322 (2005).

323. Knill, E., Laflamme, R., Martinez, R. & Negrevergne, C. Benchmarking Quantum Computers: The Five-Qubit Error Correcting Code. *Phys. Rev. Lett.* **86**, 5811–5814 (2001).

324. Chiaverini, J. *et al.* Realization of quantum error correction. *Nature* **432**, 602–605 (2004).

325. Schindler, P. *et al.* Experimental repetitive quantum error correction. *Science* **332**, 1059–61 (2011).

326. Pittman, T. B., Jacobs, B. C. & Franson, J. D. Demonstration of quantum error correction using linear optics. *Phys. Rev. A* **71**, 052332 (2005).

327. Reed, M. D. *et al.* Realization of three-qubit quantum error correction with superconducting circuits. *Nature* **482**, 382–385 (2012).

328. Waldherr, G. *et al.* Quantum error correction in a solid-state hybrid spin register. *Nature* **506**, 204–207 (2014).

329. Deutsch, D. Quantum Theory, the Church-Turing Principle and the

Universal Quantum Computer. *Proc. R. Soc. A Math. Phys. Eng. Sci.* **400**, 97–117 (1985).

330. Barenco, A. *et al.* Elementary gates for quantum computation. *Phys. Rev. A* **52**, 3457–3467 (1995).

331. Dawson, C. M. & Nielsen, M. A. The Solovay-Kitaev algorithm. (2005). arXiv:quant-ph/0505030

332. Deutsch, D. Quantum Computational Networks. *Proc. R. Soc. A Math. Phys. Eng. Sci.* **425**, 73–90 (1989).

333. DiVincenzo, D. P. Two-bit gates are universal for quantum computation. *Phys. Rev. A* **51**, 1015–1022 (1995).

334. Sørensen, A. & Mølmer, K. Quantum Computation with Ions in Thermal Motion. *Phys. Rev. Lett.* **82**, 1971–1974 (1999).

335. Haljan, P. C. *et al.* Entanglement of trapped-ion clock states. *Phys. Rev. A* **72**, 062316 (2005).

336. Leibfried, D. *et al.* Experimental demonstration of a robust, high-fidelity geometric two ion-qubit phase gate. *Nature* **422**, 412–415 (2003).

337. Home, J. P. *et al.* Deterministic entanglement and tomography of ion–spin qubits. *New J. Phys.* **8**, 188–188 (2006).

338. Schmidt-Kaler, F. *et al.* Realization of the Cirac–Zoller controlled-NOT quantum gate. *Nature* **422**, 408–411 (2003).

339. Monroe, C. *et al.* Resolved-Sideband Raman Cooling of a Bound Atom to the 3D Zero-Point Energy. *Phys. Rev. Lett.* **75**, 4011–4014 (1995).

340. Boulon, M. E. *et al.* Measuring Spin···Spin Interactions between Heterospins in a Hybrid [2]Rotaxane. *Angew. Chemie - Int. Ed.* **56**, 3876–3879 (2017).

341. Atzori, M. *et al.* A two-qubit molecular architecture for electron-mediated nuclear quantum simulation. *Chem. Sci.* **9**, 6183–6192 (2018).

342. Multiple-particle interference and quantum error correction. *Proc. R. Soc. London. Ser. A Math. Phys. Eng. Sci.* **452**, 2551–2577 (1996).

343. Laflamme, R., Miquel, C., Paz, J. P. & Zurek, W. H. Perfect Quantum Error Correcting Code. *Phys. Rev. Lett.* **77**, 198–201 (1996).

344. Moussa, O., Baugh, J., Ryan, C. A. & Laflamme, R. Demonstration of

Sufficient Control for Two Rounds of Quantum Error Correction in a Solid State Ensemble Quantum Information Processor. *Phys. Rev. Lett.* **107**, 160501 (2011).

345. Boulant, N., Viola, L., Fortunato, E. M. & Cory, D. G. Experimental Implementation of a Concatenated Quantum Error-Correcting Code. *Phys. Rev. Lett.* **94**, 130501 (2005).

346. Paramagnetic resonance in some lanthanon ethyl sulphates. *Proc. R. Soc. London. Ser. A. Math. Phys. Sci.* **245**, 156–174 (1958).

347. Easley, W. C., Barclay, J. A. & Shirley, D. A. Nuclear moments of Tb157, Tb158, and Tb160 by electron paramagnetic resonance and nuclear alignment. *Phys. Rev.* **170**, 1083–1088 (1968).

348. Bleaney, B., Pfeffer, J. Z. & Wells, M. R. Magnetic properties of terbium vanadate. *J. Phys. Condens. Matter* **9**, 7469–7475 (1997).

349. Morita, T. *et al.* Comparison of the Magnetic Anisotropy and Spin Relaxation Phenomenon of Dinuclear Terbium(III) Phthalocyaninato Single-Molecule Magnets Using the Geometric Spin Arrangement. *J. Am. Chem. Soc.* **140**, 2995–3007 (2018).

350. J. J. Borrás-Almenar, J. M. Clemente-Juan, E. Coronado, and & B. S. Tsukerblat. High-Nuclearity Magnetic Clusters: Generalized Spin Hamiltonian and Its Use for the Calculation of the Energy Levels, Bulk Magnetic Properties, and Inelastic Neutron Scattering Spectra. (1999). doi:10.1021/IC990915I

351. Borrás-Almenar, J. J., Clemente-Juan, J. M., Coronado, E. & Tsukerblat, B. S. MAGPACK A package to calculate the energy levels, bulk magnetic properties, and inelastic neutron scattering spectra of high nuclearity spin clusters. *J. Comput. Chem.* **22**, 985–991 (2001).

352. Gersmann, H. R. & Swalen, J. D. Electron paramagnetic resonance spectra of copper complexes. *J. Chem. Phys.* **36**, 3221–3233 (1962).

353. Larsen, S. C., Aylor, A., Bell, A. T. & Reimex, J. A. Electron paramagnetic resonance studies of copper ion-exchanged ZSM-5. *J. Phys. Chem.* **98**, 11533–11540 (1994).

354. Kolks, G., Lippard, S. J., Waszczak, J. V. & Lilienthal, H. R. Magnetic Exchange in Imidazolate-Bridged Copper(II) Complexes. *J. Am. Chem. Soc.* **104**, 717–725 (1982).

355. Glerup, J., Goodson, P. A., Hodgson, D. J. & Michelsen, K. Magnetic Exchange through Oxalate Bridges: Synthesis and Characterization of (μ-Oxalato)dimetal(II) Complexes of Manganese, Iron, Cobalt, Nickel, Copper, and Zinc. *Inorg. Chem.* **34**, 6255–6264 (1995).

356. Hyde, J. S. & Froncisz, W. The role of microwave frequency in EPR spectroscopy of copper complexes. *Annual review of biophysics and bioengineering* **11**, 391–417 (1982).

357. Tang, J. A. *et al.* Solid-state ^{63}Cu and 65Cu NMR spectroscopy of inorganic and organometallic copper(I) complexes. *J. Am. Chem. Soc.* **129**, 13049–13065 (2007).

358. Menger, E. M. & Veeman, W. S. Quadrupole effects in high-resolution phosphorus-31 solid-state NMR spectra of triphenylphosphine copper(I) complexes. *J. Magn. Reson.* **46**, 257–268 (1982).

359. Artizzu, F. *et al.* Ln_3Q_9 as a Molecular Framework for Ion-Size-Driven Assembly of Heterolanthanide (Nd, Er, Yb) Multiple Near-Infrared Emitters. *Chem. - A Eur. J.* **21**, 3882–3885 (2015).

360. Zhu, X. *et al.* Formation of a sandwich-type supercomplex through second-sphere coordination of functionalized macrocyclic polyamines. *CrystEngComm* **10**, 19–22 (2008).

361. Jacques, V. *et al.* Dynamic Polarization of Single Nuclear Spins by Optical Pumping of Nitrogen-Vacancy Color Centers in Diamond at Room Temperature. *Phys. Rev. Lett.* **102**, 057403 (2009).

362. Brassard, G., Elias, Y., Mor, T. & Weinstein, Y. Prospects and limitations of algorithmic cooling. *Eur. Phys. J. Plus* **129**, 258 (2014).

363. Zaiser, S., Masatth, B., Rao, D. D. B., Raeisi, S. & Wrachtrup, J. Experimental Saturation of the Heat-Bath Algorithmic Cooling bound. (2018).

364. Boykin, P. O., Mor, T., Roychowdhury, V., Vatan, F. & Vrijen, R. Algorithmic cooling and scalable NMR quantum computers. *Proc. Natl. Acad. Sci.* **99**, 3388–3393 (2002).

365. Park, D. K. *et al.* Heat Bath Algorithmic Cooling with Spins: Review and Prospects. in 227–255 (Springer, New York, NY, 2016). doi:10.1007/978-1-4939-3658-8_8

366. Park, D. K. *et al.* Hyperfine spin qubits in irradiated malonic acid: heat-

bath algorithmic cooling. *Quantum Inf. Process.* **14**, 2435–2461 (2015).

367. McPeak, J. E., Quine, R. W., Eaton, S. S. & Eaton, G. R. An x-band continuous wave saturation recovery electron paramagnetic resonance spectrometer based on an arbitrary waveform generator. *Rev. Sci. Instrum.* **90**, 024102 (2019).

368. Tseitlin, M., Quine, R. W., Rinard, G. A., Eaton, S. S. & Eaton, G. R. Digital EPR with an arbitrary waveform generator and direct detection at the carrier frequency. *J. Magn. Reson.* **213**, 119–125 (2011).

369. Jeschke, G., Pribitzer, S. & Doll, A. Coherence Transfer by Passage Pulses in Electron Paramagnetic Resonance Spectroscopy. *J. Phys. Chem. B* **119**, 13570–13582 (2015).

370. Sato, K. *et al.* Molecular electron-spin quantum computers and quantum information processing: pulse-based electron magnetic resonance spin technology applied to matter spin-qubits. *J. Mater. Chem.* **19**, 3739 (2009).

371. Morton, J. J. L. *et al.* High Fidelity Single Qubit Operations Using Pulsed Electron Paramagnetic Resonance. *Phys. Rev. Lett.* **95**, 200501 (2005).